# Hyphae-on-a-chip: A microfluidic platform for the study of zoospore germination and protrusive forces in hyphal invasion


**Yiling Sun**

Department of Electrical and Computer Engineering

University of Canterbury

A thesis submitted in partial fulfilment of
the requiremnt for the degree of

*Doctor of Philosophy*

July 2020

# Acknowledgements

The work presented in this thesis was carried out at the Nanofabrication Laboratory in the Department of Electrical and Computer Engineering and at the School of Biological Sciences at the University of Canterbury in Christchurch, New Zealand. This collaboration offered me the advantage of acquiring expertise from both institutes. Financial support was provided by Marsden Grant UOC1504, the Brian Mason Trust and the Biomolecular Interaction Centre.

I would like to express my sincere gratitude to my supervisors Associate Professors Volker Nock and Ashley Garrill for their patience, motivation and experience. Volker's guidance and continuous support was an immense help during the time of research and thesis writing. His encouragement and trust gave me the confidence for research in microfabrication and Lab-on-a-Chip technology. Ashley I have to thank for introducing me to the world of microorganisms and the biology laboratory, for his expert advice on all things fungi and oomycetes. I could not have imagined having a better team of mentors for my PhD study.

I would also like to express my thanks to all the people who helped me in so many ways, in particular Gary Turner and Helen Devereux for training me in the use of facilities in the Nanofabrication Laboratory; Deborah Erueti for helping me with all the paperwork. Special thanks have to be given to Dr Ayelen Tayagui for her support with cells-culture and zoospore induction. My colleagues and fellow labmates Dr Rebecca Soffe, Dr Azadeh Hashemi, Dr Louise Orcheston-Findlay, Linda Chen, Sevgi Onal, Caixia Hou, Stephanie Dijkstra and Elizabeth Dunn for all the help and suggestions around the lab, for all the fun we have had in last three years.

Last but not the least, I would like to thank my family, my husband Cheng Su and my parents Meifang Lin and Guoqiang Sun, for always being there for me and their endless love.

# Abstract

Fungal and oomycete pathogens have a significant influence on species extinctions, food security, ecosystem disturbances, and even human health. The large diversity of pathogenic fungi and oomycetes, and their acquired resistance to most antifungal agents, make treatment extremely difficult. Therefore, the aim of this work was to develop a lab-on-a-chip platform for high-throughput screening on individual spores and hyphae of fungi and oomycetes. This will help investigating and understanding the mechanisms of their invasive growth, and the development of antifungal compounds to control them.

The ability of invasive growth of fungal and oomycete hyphae to penetrate through host tissue is essential for pathogenicity. Given the importance of protrusive force, which is considered as the force generated by hyphae to grow invasively, this thesis introduces two Lab-on-a-Chip (LOC) platforms with elastomeric micropillars as force sensors for the study of underlying mechanisms enabling force generation. In the first case, an existing mycelial LOC platform was improved to contain single free-bending micropillars in channel constrictions, which enabled the measurement of protrusive forces exerted by individual hyphal tips of fungi and oomycetes. The platform design, fabrication process and photoresist optimization required to adapt the microfluidic platform to different hyphae sizes and corresponding high aspect-ratio micropillars are reported. To demonstrate the applicability of the platform, oomycete *Achlya bisexualis* and fungus *Neurospora crassa* were cultured on the devices and the forces exerted by individual hyphae measured.

For the second case, this thesis described the development of a novel monolithic LOC platform enabling high-throughput screening of different lifecycle stages and parameters of fungi and oomycetes, including spore germination, growth of resulting hyphae and their protrusive force generation. The platform integrates single zoospore capture and culture function with micropillar force sensing, allowing for investigations on an individual organism level. This is achieved by introducing hydrodynamic

trapping of single cells and pneumatic membrane valves for compartmentalization. Single zoospores of oomycete *A. bisexualis* were demonstrated to be successfully captured in the trap sites via constriction structures in the parallel measurement channels, and the trapping and germination efficacies of two types of constrictions were tested. Two types of pneumatic membrane valves, normally-open and normally-closed microvalves, were implemented and evaluated for quality of compartmentalization in this thesis. Normally-closed microvalves with individual control for each measurement channel showed more effective single spore capture and compartmentalization. Using these valves, germinated hyphae from trapped oomycete *A. bisexualis* zoospores were observed to extend along measurement channels of the LOC platform, impacting with the force sensing micropillars, allowing for their growth rate and protrusive forces to be evaluated.

In addition to the two LOC platforms, this thesis presents a number of other improvements on and contributions to device fabrication and experimentation, including high-resolution alignment marks for two-layer photoresist master; PDMS chip alignment and assembly for producing platforms with membrane valves, especially normally-closed microvalves; experimental setup for independent and precise control of channels with liquid or air, and in-depth characterization of flow on the platform during operation of normally-closed microvalves.

UNIVERSITY OF CANTERBURY
*Te Whare Wānanga o Waitaha*
CHRISTCHURCH NEW ZEALAND

Deputy Vice-Chancellor's Office
Postgraduate Research Office

# Co-Authorship Form

This form is to accompany the submission of any thesis that contains research reported in co-authored work that has been published, accepted for publication, or submitted for publication. A copy of this form should be included for each co-authored work that is included in the thesis. Completed forms should be included at the front (after the thesis abstract) of each copy of the thesis submitted for examination and library deposit.

| Please indicate the chapter/section/pages of this thesis that are extracted from co-authored work and provide details of the publication or submission from the extract comes: |
|---|
| A. Tayagui, Y. Sun, D. A. Collings, A. Garrill, and V. Nock, "An elastomeric micropillar platform for the study of protrusive forces in hyphal invasion", Lab on a Chip, vol. 17, no. 21, pp. 3643-3653, 2017.<br>Chapter 3 shows the fabrication and modification of the LOC platform. |

| Please detail the nature and extent (%) of contribution by the candidate: |
|---|
| 20% of writing, 40% of research and analysis |

**Certification by Co-authors:**
If there is more than one co-author then a single co-author can sign on behalf of all
The undersigned certifies that:

- The above statement correctly reflects the nature and extent of the Doctoral candidate's contribution to this co-authored work
- In cases where the candidate was the lead author of the co-authored work he or she wrote the text

Name: *Volker Nock* Signature: V. Nock Date: *24.03.2020*

UNIVERSITY OF CANTERBURY
*Te Whare Wānanga o Waitaha*
CHRISTCHURCH NEW ZEALAND

Deputy Vice-Chancellor's Office
Postgraduate Research Office

# Co-Authorship Form

This form is to accompany the submission of any thesis that contains research reported in co-authored work that has been published, accepted for publication, or submitted for publication. A copy of this form should be included for each co-authored work that is included in the thesis. Completed forms should be included at the front (after the thesis abstract) of each copy of the thesis submitted for examination and library deposit.

| Please indicate the chapter/section/pages of this thesis that are extracted from co-authored work and provide details of the publication or submission from the extract comes: |
|---|
| Y. Sun, A. Tayagui, A. Garrill and V. Nock, "Fabrication of In-Channel High- Aspect Ratio Sensing Pillars for Protrusive Force Measurements on Fungi and Oomycetes", Journal of Microelectromechanical Systems, vol. 27, no. 5, pp. 827-835, 2018.<br>Chapter 3 shows the fabrication and modification of the LOC platform, and proof-of-concept experiments on fungi and oomycetes. |

| Please detail the nature and extent (%) of contribution by the candidate: |
|---|
| 80% of writing, 85% of research and analysis |

**Certification by Co-authors:**
If there is more than one co-author then a single co-author can sign on behalf of all
The undersigned certifies that:

- The above statement correctly reflects the nature and extent of the Doctoral candidate's contribution to this co-authored work
- In cases where the candidate was the lead author of the co-authored work he or she wrote the text

Name: *Volker Nock* Signature: Volker Nock Date: *24.03.2020*

# Table of contents

# Chapter 1

# Introduction

## 1.1 Pathogenic fungi and oomycetes

Fungi and oomycetes are crucial components of most ecosystems and play key roles in the degradation of organic matter and nutrient recycling [1, 2]. However, some species can be pathogenic and can cause significant diseases in plants, animals and humans [3, 4]. In the last two decades in particular, the number of infectious diseases caused by fungi and fungal oomycetes has increased and led to severe die-offs and extinctions [5].

Probably the most well-known oomycete pathogen is *Phytophthora infestans*, which causes potato late blight. The epidemic outbreaks of *P. infestans* in Ireland from 1845 to 1849 caused significant crop failures. About one million people died and a million more emigrated from Ireland, a period referred to as The Great Famine [4]. Similar to potatoes, other crops are also attacked by fungal and oomycete diseases. For instance, rice blast caused by *Magnaporthe oryzae* [6], wheat stem rust by *Puccinia graminis* [7] and soybean rust by *Phakopsora pachyrhizi* [8] threaten major food crops. As such, the emerging infectious diseases caused by fungi and oomycetes not only lead to direct economic losses, but also pose a worldwide threat to food security [9].

Fungal and oomycete infections have driven high risks of biodiversity losses for both animal-host and plant-host species [9]. *Batrachochytrium dendrobatidis*, which causes chytridiomycosis in amphibians, can infect over 350 amphibians species on all continents except Antarctica, and has driven the severe decline of over 200 of these species [10]. An example of this in plants is ash dieback caused by *Hymenoscyphus pseudoalbidus*, which affects ash trees of all age classes [11]. The high mortality levels of ash trees are likely to have major ecological effect on European biodiversity and forest ecosystems. In New Zealand in particular, kauri dieback disease, caused by the

oomycete pathogen *Phytophthora agathidicida*, is threatening kauri trees, which are one of the world's largest and longest-living conifer species [12]. Kauri are now identified in New Zealand as a "Threatened – Nationally Vulnerable" species in regards to their conservation status, mainly due to the continued spread of kauri dieback disease and no known cure of infected trees [13].
Fungal infections can also affect human health. The most common of such fungal diseases are the superficial mycotic infections of the skin and nails that affect more than 20-25 % of the world's population [14]. Invasive fungal diseases cause unacceptably high mortality rates and kill about one and a half million people every year, more than killed by tuberculosis or malaria [15]. Cryptococcosis for example caused by *Cryptococcus neoformans*, usually attacks the lungs or the central nervous system of people who have weakened immune systems. According to a report from the Center for Disease Control and Prevention (CDC), one million cases of brain infections due to *Cryptococcus* occur among people with HIV/AIDS worldwide each year, resulting in nearly 625,000 deaths [16].
Human activity has contributed to the spread of fungal disease by trade and transport, and also to accelerated evolution of virulence in pathogenic fungi and oomycetes by modifying natural environments [9]. Furthermore, global climate change is altering the distribution of fungal infections through increasing water or temperature stresses on plants [17], and can enable increased survival of pathogens outside their historic occurrence ranges [18]. All of this is compounded by the fact that fungal and oomycete infections are difficult to treat because of their diversity and rapid evolution of resistance to antifungal drugs [19]. In addition, antifungal agents can also compromise human cells when treating human fungal infection. Resistance of fungal pathogens to most, or all antifungal agents has been reported, which impedes mankind's ability to control infections [20]. The latter in particular demonstrates an urgent need for the discovery of novel treatments for infectious fungal and oomycete diseases, a cause this thesis aims to contribute to.

## 1.2 Aim of research

Given the increasingly serious impact of fungal and oomycete pathogens on human health, food security and ecosystem resilience, development of novel targets, antifungal drugs and treatment methods are needed [3]. Therefore, it is important to strengthen and expand investigations that help our understanding of the molecular mechanisms that underline the invasive growth of fungi and oomycetes and their increasing drug

resistance. The aim of this research is to develop a lab-on-a-chip platform, which is capable of parallelized screening on individual hyphae of fungi and oomycetes, taking into account cellular heterogeneity, nuclear distribution and dynamics at the sub-hyphal level in response to exposure to various biocontrol strategies.

## Objective 1: Optimize the existing mycelial Lab-on-a-Chip platform containing elastomeric micro-pillars for force sensing

In many cases the capability of extending tips of fungal and oomycete hyphae to penetrate throughout host tissue and the resulting protrusive force are essential for pathogenicity [21]. Previous work demonstrated the growth of the hyphal oomycete *A. bisexualis* on PDMS devices and the possibility of protrusive force measurement by the use of integrated elastomeric micro-pillars [22, 23]. This thesis aimed to optimize the micro-channel structure, which guides individual hyphal growth from a transplanted mycelium, and miniaturize the force sensing pillars to increase the flexibility of the platform. This was demonstrated by engineering species-specific microfluidic platforms, which extend the applicability of the technique to fungi and oomycetes with hyphal diameters in the 5 to 30 $\mu$m range.

## Objective 2: Develop a monolithic Lab-on-a-Chip platform integrating single zoospore capture and germination with protrusive force sensing

The germination of hyphae from either zoospores or conidia is a crucial stage, leading to new infections and penetration into a plant or animal [4]. Therefore, this thesis aimed to combine in-channel high-aspect ratio sensing pillars for protrusive force measurements with zoospore trapping, on-chip germination and maintenance. Moreover, pneumatic membrane microvalves were to be introduced for high-throughput compartmentalization of individual zoospores or conidia. This would allow investigation of the effects of cell-to-cell variability and heterogeneity on hyphal growth and protrusive forces generated by these microorganisms.

## Objective 3: Characterize zoospore capture, maintenance, germination and germling force generation on-chip

The characteristics of capture, maintenance and germination of zoospores of the oomycete *A. bisexualis* were to be evaluated on the platform. Trap site design and

micro-valves were to be optimized in order to improve the trapping and germination efficiency. Zoospore germination and resulting hyphal growth were to be characterized. Finally, the platform was to be used to measure protrusive forces exerted by germ tubes and hyphae originating from the trapped zoospores.

## 1.3 Thesis contributions

The most significant contributions this thesis makes is in developing and optimizing a platform capable of screening the tip growth and protrusive force generation of individual hyphae of fungi and oomycetes. Variations of the platforms developed in this process are capable of maintenance of hyphae originating from both mycelium and zoospores. In particular, the zoospore version combines for the first time hydrodynamic trapping and zoospore compartmentalization with single hypha force sensing. Other major contributions include:

1. *In-channel fabrication of high aspect-ratio sensing micropillars [24].* A novel approach to fabricate single high aspect-ratio elastomeric micropillars *in-situ* in constrictions inside microchannels was developed. The devices were adapted for force measurements on hyphae from different species that had differing diameters.

2. *Combination of single zoospore capture with force sensing [25].* Hydrodynamic flow-assisted single cell trapping was combined with micropillar force sensing. This enabled the on-chip observation of zoospore germination and force measurements on resulting germlings/hyphae.

3. *Compartmentalization based on pneumatic membrane microvalves.* Hydrodynamic flow-assisted trapping and force sensing were expanded towards single zoospore compartmentalization by integration of pneumatic membrane microvalves. Independent control of microvalves integrated into each trapping channel facilitated the first high-throughput trapping, germination and force sensing on germlings.

In addition, other minor contributions were made by this thesis, including the improvement of alignment marks for two-layer photoresist masters; the use of dyes to improve visualization and tracking of integrated micropillars; demonstration of PDMS chip alignment and assembly for the multilayer platform; development of an experimental setup for independent control of multiple inlet/outlet ports and flow characteristics of

the platform. These may benefit platform design and fabrication for others in the future.

The following publications have resulted from this work:

Journal articles

1. Y. Sun, A. Tayagui, A. Garrill and V. Nock, "An integrated microfluidic platform for zoospore germination and hyphal force sensing", In Draft.

2. Y. Sun, A. Tayagui, A. Garrill and V. Nock, "Fabrication of In-Channel High-Aspect Ratio Sensing Pillars for Protrusive Force Measurements on Fungi and Oomycetes", *Journal of Microelectromechanical Systems*, vol. 27, no. 5, pp. 827-835, 2018.

3. A. Tayagui, Y. Sun, D. A. Collings, A. Garrill, and V. Nock, "An elastomeric micropillar platform for the study of protrusive forces in hyphal invasion", *Lab on a Chip*, vol. 17, no. 21, pp. 3643-3653, 2017.

Conference proceedings

1. Y. Sun, A. Tayagui, A. Garrill, and V. Nock, "A Monolithic Polydimethylsiloxane Platform for Zoospore Capture, Germination and Single Hypha Force Sensing", in *20th IEEE International Conference on Solid-State Sensors, Actuators and Microsystems (Transducers)*, pp. 409-412, 2019.

2. Y. Sun, A. Tayagui, H. Shearer, A. Garrill, and V. Nock, "A Microfluidic Platform with Integrated Sensing Pillars for Protrusive Force Measurements on *Neurospora crassa*", in *31st IEEE International Conference on Micro Electro Mechanical Systems (MEMS)*, pp. 1116-1119, 2018.

The work described in this thesis has also been presented in various forms:

1. V. Nock, Y. Sun, A. Tayagui, D. Sarkar and A. Garrill, "Using Lab-on-a-Chip technology to reduce complexity in plant-fungi interaction studies", *Queenstown Research Week 2019*, Queenstown, New Zealand, 2019. (Oral Presentation)

2. Y. Sun, A. Tayagui, A. Garrill, and V. Nock, "A Monolithic Polydimethylsiloxane Platform for Zoospore Capture, Germination and Single Hypha Force Sensing", in 20th IEEE International Conference on Solid-State Sensors, Actuators and Microsystems (Transducers), Berlin, Germany, 2019. (Oral Presentation)

3. Y. Sun, A. Tayagui, A. Garrill and V. Nock, "Trapping and Maintenance of Individual Zoospores On-Chip for Single Cell Protrusive Force Measurements", in *9th International Conference on Advanced Materials and Nanotechnology (AMN9)*, Wellington, New Zealand, 2019. (Oral Presentation)

4. A. Tayagui, Y. Sun, V. Nock and A. Garrill, "The use of Lab-on-a-Chip devices to study the invasive growth of oomycetes", in *20th Oomycete Molecular Genetics Network Annual Meeting*, Oban, Scotland, 2019. (Oral Presentation)

5. Y. Sun, A. Tayagui, H. Shearer, A. Garrill, and V. Nock, "A Microfluidic Platform with Integrated Sensing Pillars for Protrusive Force Measurements on *Neurospora crassa*", in *31st IEEE International Conference on Micro Electro Mechanical Systems (MEMS)*, Belfast, UK, 2018. (Poster Presentation)

6. V. Nock, A. Tayagui, Y. Sun and A. Garrill, "Characterization of protrusive forces generated by individual hyphal tips of *Achlya bisexualis* on a lab-on-a-chip platform", in *15th International Congress of Mycology and Eukarotic Microbiology (IUMS 2017)*, Singapore, 2017. (Oral Presentation)

## 1.4 Thesis structure

In this thesis, a monolithic PDMS platform based on LOC technology is introduced, which provides a new tool to help understand the molecular processes that underlie protrusive growth of fungi and oomycetes on a single cell/hyphal level. The platform and associated technologies developed as part of this thesis may present new ways to tackle the pathogenic growth of these organisms.
In addition to this introduction, the thesis consists of six main chapters, as shown in Fig. 1.1, with each covering the following content:

**Chapter 2:** Overview of existing models for mechanisms underlying the invasive growth of fungal and oomycete hyphae; summary of established measurement methods for protrusive forces; and review of LOC devices designed to maintain and study tip-growing cells.

**Chapter 3:** Modification and optimization of the existing mycelial LOC platform. The optimized version places single elastomeric micropillars in each measurement channel, instead of micropillar arrays, and improves pillar hit rates by means of reducing geometrical tolerances. This allows the measurement of protrusive forces exerted by individual fungal and oomycete hyphae. Chip design

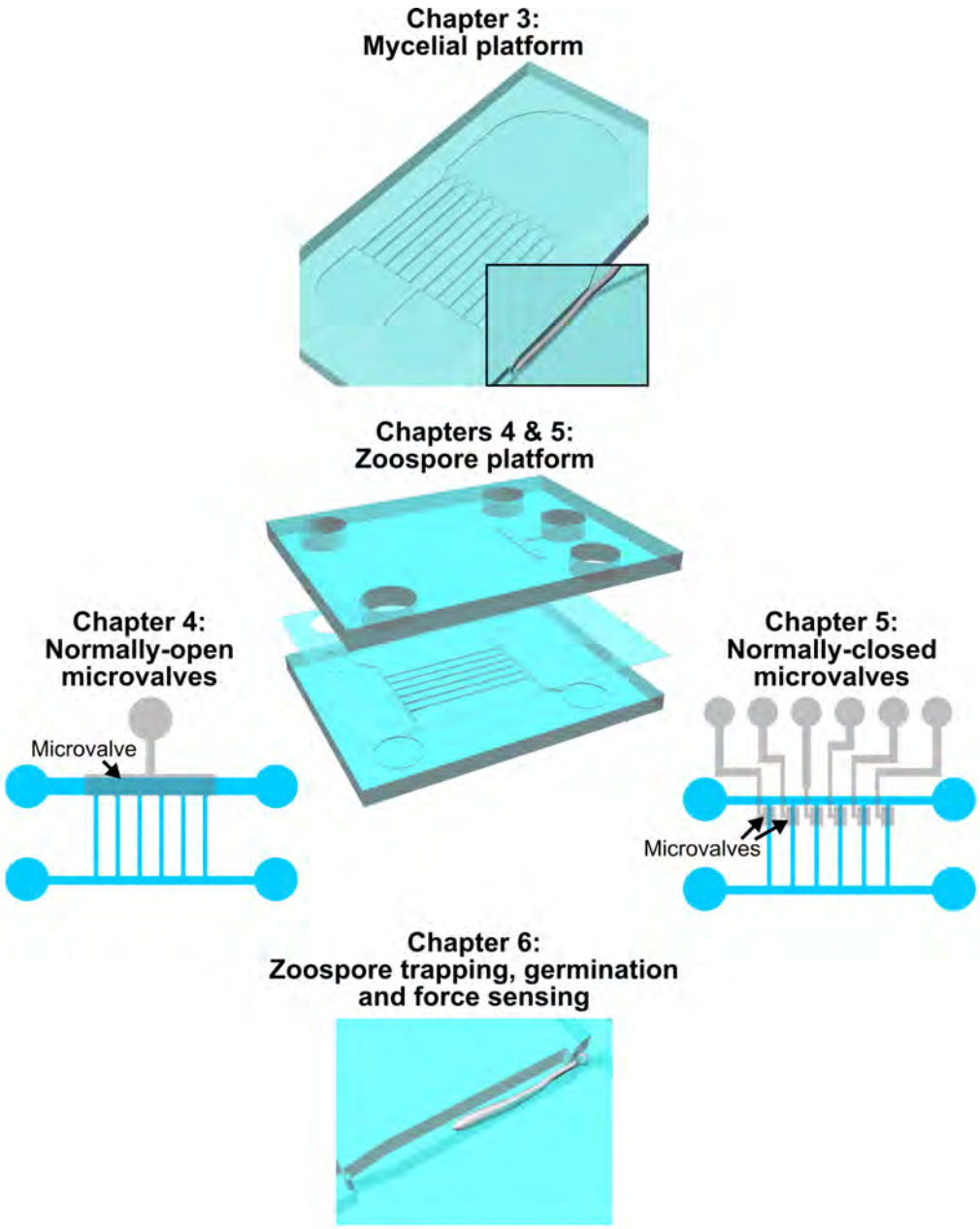


Figure 1.1: Outline of this thesis.

for specific organisms, fabrication processes for two-layer resist master and PDMS chip production, including novel photoresist optimization and platform application, are covered.

**Chapter 4:** Force sensing developed for the mycelial platform is combined with zoospore capture in a monolithic platform. Hydrodynamic trapping is introduced to parallelize zoospore loading. This enables the observation of on-chip zoospore germination and single hypha force generation. The design of hydrodynamic trap sites, fabrication of the two-layer PDMS platform with normally-open sieve microvalves, zoospore maintenance and germination, as well as proof-of-concept force sensing are described.

**Chapter 5:** Integration of the normally-closed microvalves to overcome the limitations of sieve microvalves. Compartmentalization of trapped zoospores and measurement channels is optimized by preventing back-growth of hyphae with the help of normally-closed microvalves. The chapter describes the design of the platform with normally-closed microvalves, the fabrication processes for integration of independently controlled microvalves, the optimization of microvalve air chambers and comprehensive characterization of fluid flow during operation of the platform.

**Chapter 6:** Demonstration of single zoospore capture and force sensing on individual germ tubes. The zoospore platform containing normally-closed microvalves is used to trap and maintain zoospores on-chip for demonstration of hyphal growth and force sensing. Zoospore trapping, maintenance to germination, characterization of germling and germ tube development and proof-of-concept force measurement on the platform with normally-closed microvalves are described in this chapter.

**Chapter 7:** Conclusions and future work. This final chapter provides a summary of the work presented in this thesis and recommendations for future research.

# Chapter 2

# Background

This chapter describes the infection strategies of pathogenic fungi and oomycetes, and the mechanism underlying their invasive growth. Together, these point to protrusive force generation as being an essential mechanism for fungal and oomycete hyphae to penetrate through host tissue. Thus, given the importance of force, the chapter then reviews existing methods for protrusive force measurement, such as optical tweezers and strain gauges. Finally, more recent approaches to characterize hyphal and other tip-growing microorganisms with lab-on-a-chip (LOC) techniques are summarized. The chapter finishes by concluding that further developments in LOC devices, such as described in this thesis, have the potential to help improve the understanding of the fundamental biology related to hyphal organisms.

## 2.1 Fungi and oomycetes

Fungi are organisms that secrete enzymes into the surrounding environment, digest organic matter, and absorb the nutrients back via tubular hyphae [1]. They belong to the group Opisthokonta, which are phylogenetically more related to animals than to plants [26]. Fungi are immensely diverse, currently estimated to have 2.2 to 3.8 million species [27], and play important roles in nutrient recycling. In addition to this crucial role in ecosystems they also impact humans many ways. In addition to edible fungi, such as mushrooms and ingredients for production of bread and alcoholic drinks [28], fungi are used to produce medicines [29], in paper manufacturing [30], washing detergents [31] and many other applications. In plants, positive plant-fungal interactions are found ubiquitously, especially in plant roots [32]. Beneficial symbiotic fungi for example enhance water and mineral nutrient uptake of plants from the soil, and help with plant defences to pests and diseases. While doing so, fungi rely on their

plant hosts for carbohydrate acquisition. Mycorrhizal fungi also benefit terrestrial ecosystems via regulation of nutrient and carbon cycles, litter decomposition, soil formation and aggregation [33].
Oomycetes resemble fungi, however, they are grouped within the Stramenopiles, which are phylogenetic relatives of brown algae [34]. Oomycetes have approximately 500 recognized species in freshwater and terrestrial environments, and include saprophytes and pathogens [35]. Several of these are well known as crop and plant pathogens, such as potato late blight disease and kauri dieback disease, as mentioned in Chapter 1. Most oomycetes have similar modes of nutrition and ecological roles to fungi by producing networks of hyphae, which secrete enzymes to breakdown complex nutrients and take up the resulting simple sugars and amino acids [36]. Differences in their respective biochemistries mean that oomycetes and fungi are sensitive to conventional fungicides, for example the Azole group of fungicides [37].

## 2.2 Pathogenic fungi and oomycetes

Although only a small minority of fungi and oomycetes are pathogenic, they have a rich diversity and widespread impact on human health, dwellings, agriculture, plants and animals [38]. In addition, the wide-spread use of antifungal agents for prophylaxis and treatment of fungal and oomycete infections has facilitated the emergence of drug-resistant fungal pathogens [39]. In New Zealand alone, researchers recorded the arrival of 466 new fungal pathogen species on 131 host plants from 1881 to 2012 [40]. These data show that, while fungal pathogen arrival rates have declined or remained steady for pasture, crop, and fruit tree species in recent decades, those for forestry species have continually increased. As a result of the latter, and due to the profound effect of kauri dieback, as an exemplar disease, has been having in New Zealand, this thesis aimed to specifically develop LOC devices for the study of root attacking pathogens (i.e. *Phytophthora* species). Due to biosecurity restrictions however, all proof-of-concept experiments were performed with the oomycete *Achlya bisexualis* and fungus *Neurospora crassa* as model organisms because of their relative safety and ease in handling.

### 2.2.1 Fungi and oomycete infection strategies

Despite evolutionary distance between fungi and oomycetes [34], they both produce mycelia, form spores for asexual and sexual reproduction, and share a range of infection strategies [41].

Reproduction of fungal and oomycete spores and dispersal capacity are critical for successful colonization in a new environment [42]. Durable fungal and oomycete spores can survive independently outside their hosts for long durations and in extreme conditions ranging from cold and heat to drought [4, 9]. As shown in Fig. 2.1, asexual spores of some oomycetes (sporangia) are able to germinate directly, forming invasive hyphae in the process, whereas sporangia of most oomycetes germinate indirectly, releasing motile zoospores [43]. In plant pathogens, zoospores and fungal spores (conidia) secrete adhesive material to firmly attach themselves to the plant surface before penetration [45]. Then, when supplied with the appropriate nutrients and moisture, germination of spores occurs, which includes swelling of the spores and initiation of polarized growth (germlings) [46]. Resulting germlings grow across the plant surface, navigating chemotropically towards a suitable penetration site. In some fungal and oomycete pathogens, such as the oomycete grape downy mildew *Plasmopara viticola*, the germlings/hyphae enter the host via natural openings, such as the stomata on plant leaves [47]. Others secrete toxins and/or enzymes, apply mechanical force, or subvert cellular processes of the host to penetrate its cell walls [48]. This is often accompanied by a morphological change, such as producing invasive hyphae and/or specialized infection structures, so called appressoria. Following penetration of the epidermis, for a biotrophic lifestyle or during the biotrophic phase of the hemibiotrophs, fungi and oomycetes generate vegetative hyphae that grow intercellularly and form spherical or lobed structures (haustoria), which penetrate the adjacent plant cells [44]. Haustoria are the key structures related to nutrient uptake of fungi and oomycete from host plants for foliar and root pathogens.

Infective fungi and oomycetes reproduce mitotically within the host as part of the disease cycle, which usually occurs after establishment of infections and development of lesions [48]. In the case of fungal pathogens, the ability for sexual reproduction is important for lineage survival because it can promote genetic variation and rapid evolution [49]. However, sexual reproduction of many species is rarely found in nature [50]. In contrast, sexual reproduction is more significant component of the life cycle of oomycetes [51]. In addition to benefits to genetic variation, sexual reproduction also produces the more robust, thick-walled sexual spores, called oospores. Figure 2.2 shows an example of the life cycle of oomycete plant pathogens. In both homothallic

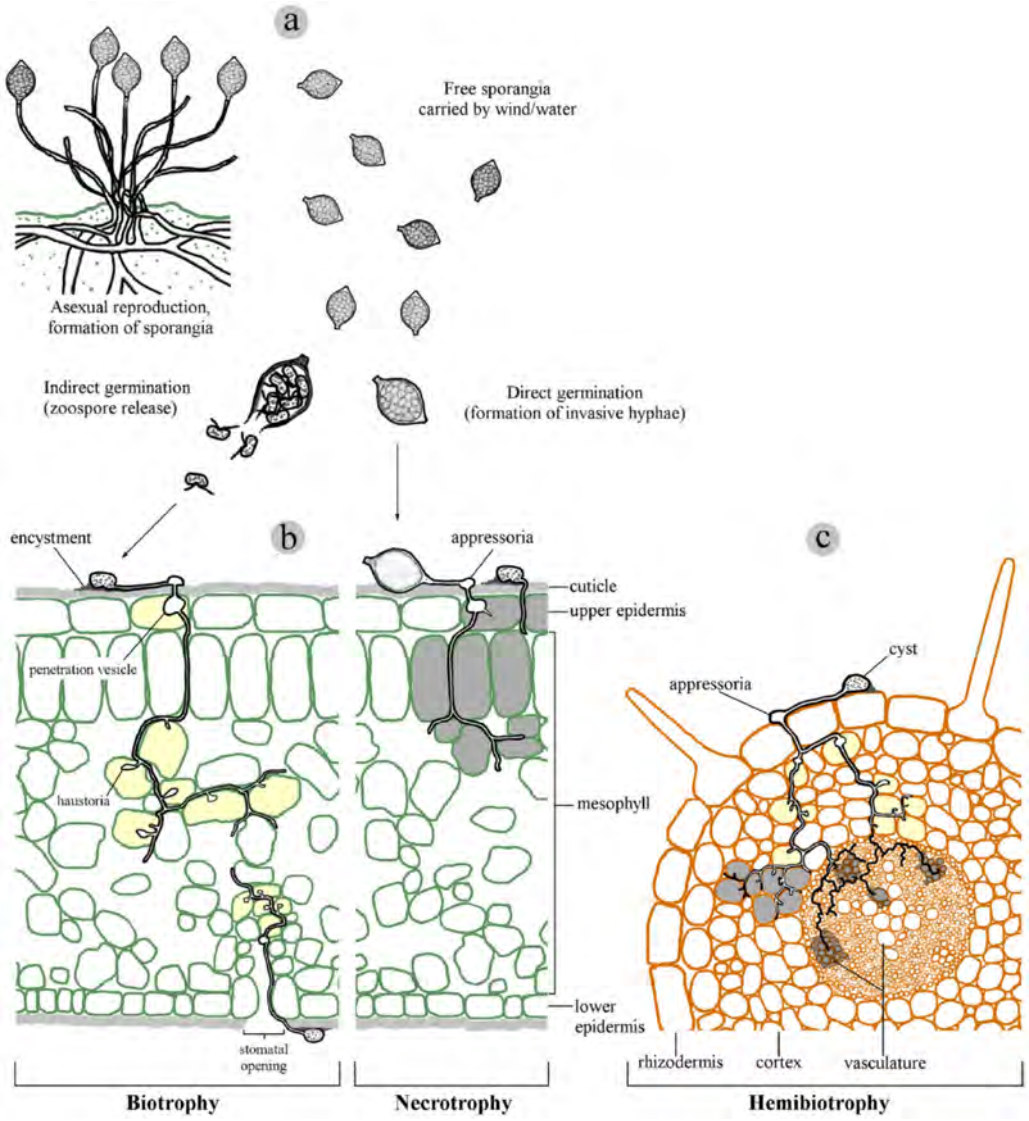


Figure 2.1: Infection strategies and lifestyles of selected oomycetes. (a) Typical asexual Phytophthora dispersal structures. Sporangia are able to germinate indirectly via zoospore release or directly via formation of invasive hyphae. (b) Leaf colonization via encystment or the formation of appressoria. (c) Root colonization by a cyst via formation of an appressoria. Reproduced with permission from Fawke et al. [44].

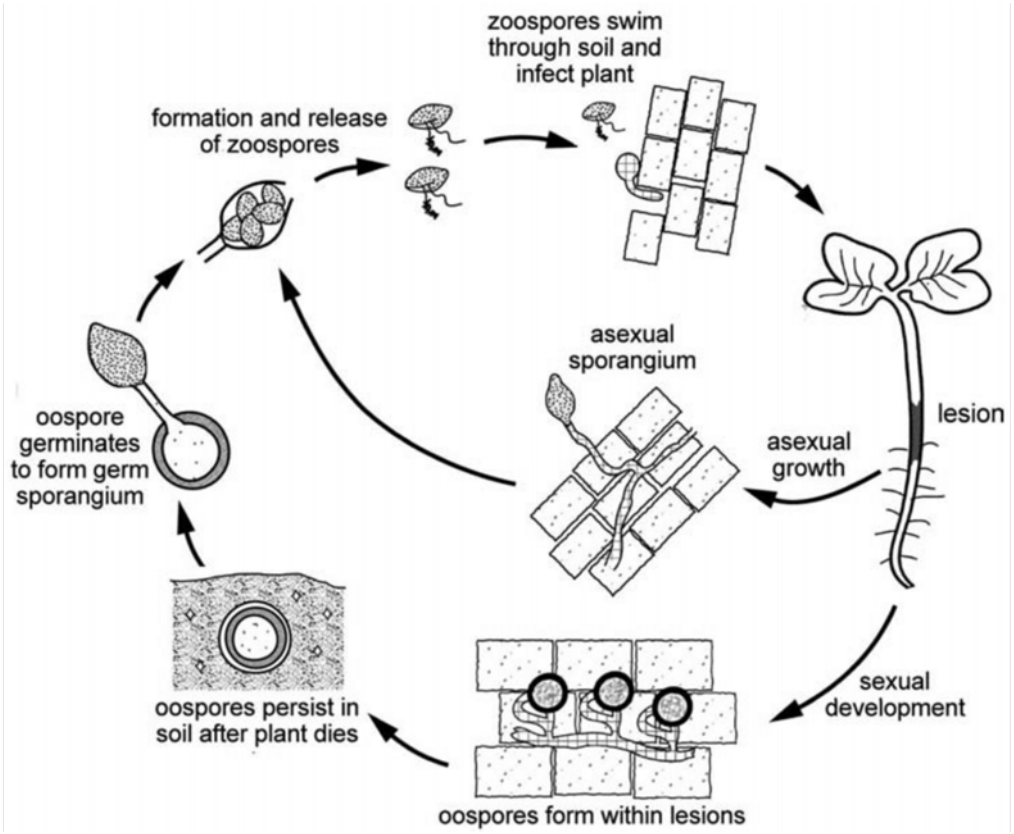


Figure 2.2: Simplified life cycle of homothallic oomycete plant pathogens. Reproduced with permission from Judelson [51].

and heterothallic species of oomycetes, male and female gametangia develop at hyphal tips, pair and form oospores between or within lesions [52]. The oospores then grow germ tubes and form germ sporangia, which are structurally similar to asexual conidia or sporangia. The occurrence of sexual and asexual sporulation can vary in pathogen and host species, climate and other issues [53]. However, in many pathosystems of oomycete plant pathogens, oospores incorporate into soil or plant debris, survive the winter and cause the outbreaks of disease in a new growing season, while zoospores typically form on plant surfaces and lead to subsequent secondary infections [4, 51].

### 2.2.2 Mechanisms underlying the invasive growth of fungal and oomycetes hyphae

Pathogenic fungi and oomycetes acquire nutrients via invasive growth, in which hyphae penetrate and branch throughout host tissue [54, 55]. Long, branching filamentous hyphae are the main structures vegetative in both microorganisms [56]. Hyphae consist of one or more cells surrounded by a tubular cell wall. The major structural polymer of the fungal cell walls is chitin, whereas oomycetes have predominantly cellulosic cell walls [57]. In most fungi, hyphae are divided into cells by internal cross-walls (septa), whereas oomycetes tend to form aseptate structures [41]. Septa in fungi are typically perforated by pores large enough for ribosomes, mitochondria and sometimes nuclei to transfer between cells. Depending on the species, hyphae can range in diameter from 2 to 30 $\mu$m [58].

Invasion of a host by fungi and oomycetes is thought to be guided by a complex interplay of secretion of lytic enzymes and application of mechanical force driven by internal hydrostatic pressure (turgor) [21]. Enzymes are likely to contribute to this process by reducing host tissue resistance. Particularly for some pathogenic fungi and oomycetes that directly produce mycelium or only exhibit minor morphogenetic changes during penetration, cell wall–degrading enzymes may be the primary mechanism in the infection process [59]. This was suggested in experiments where the *SNF1* gene of the maize pathogen *Cochliobolus carbonum*, which is required for expression of catabolite-repressed genes, was inactivated [60]. The results showed that in the *SNF1* mutants, activities of secreted enzymes were reduced and they were much less virulent on susceptible maize, while at the same time retaining their normal morphology. This view was also supported by comparing the pressures exerted by hyphae with the resistance of skin tissue [61, 62]. Microprobes attached to strain gauges were utilized to measure substrate resistance by monitoring the forces required to pierce tissues [61]. The experiments showed that a mean resistance of 24 MPa was

necessary to penetrate human skin from fresh cadavers, while the maximum pressure of single hyphal apices of pathogen *Pythium insidiosum* was 0.3 MPa.

Turgor is one of the major forces which provides mechanical support for free-standing structures and drives cellular expansion, substrate penetration and other processes [63, 64]. It is generated by osmosis, the influx of water driven by a concentration difference of osmotically active substances between the inside of the cell and the surrounding medium or substrate [65]. The first direct measurement of hyphal turgor pressure was reported using a micropipette-based pressure probe [66]. When the micropipette tip was inserted into the growing hypha, the oil meniscus (an oil/cytosol interface) was moved into the micropipette by turgor pressure. The pressure that had to be applied to force the oil meniscus back to the tip of the micropipette was measured as turgor of the hypha. This method has since been used for turgor measurement experiments on both oomycetes and fungi, with, for instance, 0.7 MPa recorded for *Achlya bisexualis* [67] and 0.45 MPa for *Neurospora crassa* [68]. While turgor exerts an equal force over every portion of inner surface of the cell wall, only the apical cell wall or a branch site of a hypha is compliant. Thus, a hypha exerts the highest proportion of its turgor against the substrate in contact with their growing tips [69, 70], as shown in Fig. 2.3.

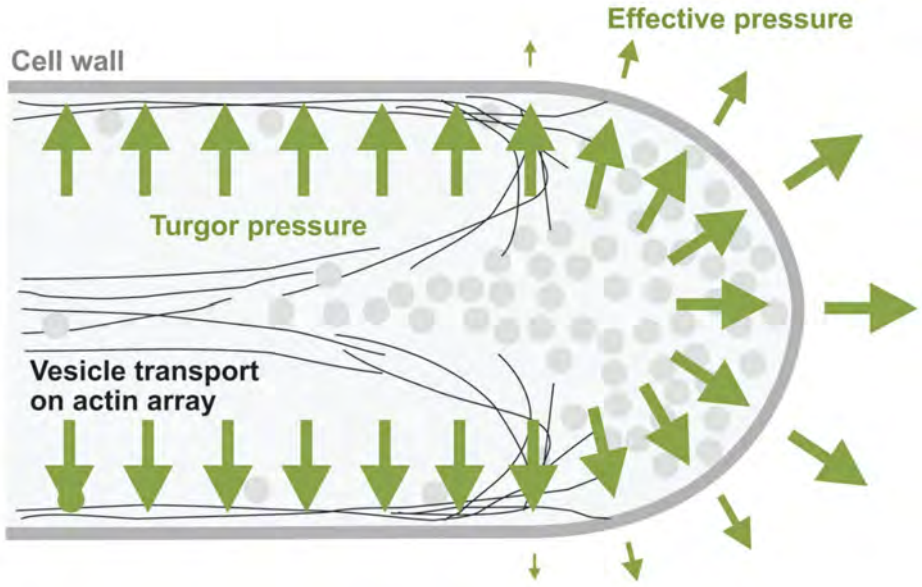


Figure 2.3: Force generation in tip-growing plant and fungal cells. The actin cytoskeleton is responsible for transporting cell wall material to the apical cell wall. The pushing force is generated by the turgor. Only where the cell wall is compliant, is this pressure felt as effective force outside of the cell (green arrows). Reproduced with permission from Nezhad and Geitmann [65].

The magnitude of protrusive force, the actual force generated by fungal and oomycete hyphae to grow invasively, is thought to arise from a balance between turgor pressure and tip yielding [71, 72]. According to experiments comparing F-actin depleted zones and turgor in the oomycete *A. bisexualis* and fungi *N. crassa* while these were growing either invasively and non-invasively, decreases in F-actin at actively extending tips may result in protrusive force increases in the absence of turgor increases.

## 2.3 High-throughput screening for antifungal agent discovery

Given the significant diseases caused by fungi and oomycetes and the emergence of antifungal resistance, the efficient identification of new or alternative antifungal agents is of high priority. To this end, High-Throughput Screening (HTS) of small molecules from libraries of synthetic compounds and natural products, originally developed for the pharmaceutical industry [73], has been used for antifungal drug discovery [74–76]. By combining with HTS technology, the processes of phenotype-based and target-based drug discovery approaches could be sped-up and hit rates increased, owing to screening of a multitude of small molecules [75]. For instance, Watamoto et al. tested a library of 1280 pharmacologically-active compounds using HTS with antifungal susceptibility tests in 96-well plates. They used this technique to identify antifungal agents with activity against the fungus *Candida albicans*, the major fungal pathogen in humans, particularly in immunocompromised individuals [77]. Out of the 1280 compounds, only 35 inhibited the metabolic activity of *C. albicans* by over 50 %. Among these, five compounds exhibited strong fungicidal effects, inhibiting the metabolic activity of *C. albicans* by over 90 %, while only one compound, CV-3988, showed no cytotoxicity to human cells at a fungicidal concentration.
More recently, Lawrence et al. screened root and leaf extracts of four New Zealand native plants likely to produce anti-*Phytophthora* compounds [78]. Crude extracts were screened to evaluate their effects on zoospore motility, zoospore germination, and mycelial growth of the oomycetes *Phytophthora agathidicida* and *Phytophthora cinnamomi*. Only extracts of the kānuka leaf and root were found to inhibit zoospore motility of both species within less than 5 mins. The same extracts completely eliminated germination of *P. agathidicida* zoospores, reduced zoospore germination of *P. cinnamomi* by more than 50 % and inhibited mycelial growth for both species. Furthermore, flavanones,which had not previously been reported as anti-*Phytophthora* compounds, were purified from the kānuka leaf and demonstrated to have identical

effects on these three lifecycle stages.
While promising, natural limitations of HTS in relation to fungal assays have so far led to the discovery of only a very limited number of new compounds. In HTS studies reported to date, fungi and selected compounds were cultured and screened in well plates, which made screening more difficult, especially for the morphologic evaluation of spores for example. Progress has been hampered by the ununified spore concentrations in each well, difficulties with spore immobilization and observation of their germination. More importantly though, being predominantly well-based, HTS approaches have been difficult to combine with other methods aimed at understanding possible alternative and under-examined angles of attack for antifungal agents, such as the protrusive force generation during hyphal invasion.

## 2.4 Protrusive force measurement and Lab-on-a-Chip techniques

### 2.4.1 Conventional measurements of the protrusive force

One of the simplest methods to measure protrusive force is to grow fungi and oomycetes on substrates with a range of known surface hardness, such as agar medium with yeasts [55] and non-biodegradable Mylar membranes [79]. Observation of agar penetration has for example demonstrated that an increase in agar medium from 2 to 8 % w/v slowed down the rate of fungal substrate invasion by the human pathogen *Wangiella dermatitidis* [55]. However, the application of this method is limited by the relatively low medium gel strength, since even the hardest agar at 8 % only exhibits a mechanical strength of around 0.1 $\mu$N/$\mu$m$^2$.
To circumvent the reliance on the substrate properties, optical tweezer techniques have been used to measure the growth forces of hyphae [80]. In this technique, force measurement is facilitated by the placement of optically trapped beads in front of the hyphal tips. Since the trapping forces are known, hyphal forces can be deduced from the translocation of the beads. Trapping force increases linearly with increasing incident laser power, and can be estimated by dragging a bead at an increasing velocity until it escapes from the trap. Even at the highest output laser power (70 mW), a leading hypha of *N. crassa* easily pushed a 4 $\mu$m bead out of a trap. This led to the conclusion that the growth forces of the hypha analyzed were in the pico-Newton range. When similar experiments were carried out on a germ tube, the same-sized bead was moved forward, but not expelled out of the trap [81]. In fact, the tip of the

germ tube was observed to swell and stop growing, with growth restarting again after removal of the bead. Based on this observation, it was concluded that the growth force generated by a germ tube is much smaller than that of a leading hypha. However, similar to the agar penetration method, the technique can be critiqued for growth force measurements on most fungi and oomycetes, mainly due to its weak trapping forces (ranging from 1 to 19 pN), but also as the intense laser light required might affect hyphal growth and thus skew experimental results [81, 82].

Given these limitations, the majority of currently available measurements of protrusive forces exerted by single hyphae of fungi and oomycetes have been made by using miniature silicon bridge strain gauges [61, 83, 84]. In these experiments, strain gauges were manually positioned with a motorized micromanipulator in a liquid-filled well close to leading hyphae. Forces were measured in proportion to the deformation of the silicon beam with an electrical-resistive element, when hyphae grew from solid medium into broth and against the strain gauge. The measurements from a variety of hyphae of basidiomycete, ascomycete, zygomycete and chytridiomycete species showed that species with larger diameter hyphae were able to exert greater forces than those with smaller diameters [84]. However, no significant difference between species was observed with respect to applied pressure, the force generated per unit area, which ranged from 0.04 MPa (*Sordaria*) to 0.09 MPa (*Neurospora*). Oomycete hyphae generated similar pressures from 0.01 to 0.17 MPa, which corresponded to a maximum of 54 % of their turgor pressure. Measurement of forces exerted by oomycete *A. bisexualis* revealed that the fluctuations in force had similar periodicity as that of extension rates of hyphae growing in agar medium [83]. The strain gauge technique risks underestimating forces exerted by invasive hyphae because these have to emerge from solid media into liquid before they can displace the transducer. In addition, it was observed that their tips change shape when they push silicon beams, which typically have a flat surface [70]. Finally, and most importantly, experiments with strain gauges can be technically challenging as the silicon beam of the gauges are typically 0.1 mm in thickness and 10 mm in width, while the diameter of hyphal tips is in the tens of micrometers range at the most.

As a result of these limitations and due to advances in microfabrication and device integration, newer devices and platforms for handling of fungi and oomycetes have predominantly been based on microfluidics and LOC technology. The next sections will summarize recent developments in both, general, as well as specific force sensing platforms for microorganisms exhibiting tip growth.

### 2.4.2 Lab-on-a-Chip device for tip-growing organisms

Microelectromechanical systems (MEMS) and LOC technologies have recently been used to study the biomechanics of tip-growing cells and organisms, such as plant pollen tubes, filamentous fungi and root hairs [85–89]. Microfluidic platforms provide several advantages over traditional culture and observation techniques when applied to microorganisms. These platforms enable stable, long-term culture, co-culture and compartmentalization in well-defined microenvironments, facilitate high-resolution observation and analysis, increase throughput and allow for precise manipulation at cellular and sub-cellular levels [90, 91].

A "Plant-on-a-chip" platform was reported by Meier et al. [92], which successfully grew live roots of *Arabidopsis thaliana* in microchannels with improved spatial and temporal resolution. The control of the local chemical environment around live roots was achieved using multi-laminar flow, and the effects of chemical stimulation on auxin transport and root hair growth were observed. This work was further extended by Parashar and Pandey to investigate root-pathogen interactions between *Arabidopsis* plants and sugarbeet nematode (SBN) or the oomycete *Phytophthora sojae* [93]. Physically, the platform consisted a set of parallel microchannels with individual inlet/outlet ports for plant seedlings and inoculation of pathogens. Motile zoospores swam randomly in the microchannels and then started to settle close to the root tip in the first 2 h after inoculation. After settling, zoospores germinated and extended hyphae towards the roots, with some areas of the root tips dying a few days later.

Platforms with three-dimensional microfluidic maze-like structures, mimicking aspects of the natural environment, have been developed to evaluate the growth behavior and analyze hyphal space-searching mechanisms of fungi [94–96]. Observations of basidiomycete hyphae before and after entering the microstructured areas showed that growth rates were not changed by confinement or obstacles, continuing to average 2.0 $\mu$m/min. In contrast, hyphal branching rates were almost twice as high within microstructures (1.5 branches per 100 $\mu$m) as compared to in unconfined areas [94]. Similarly, hyphae of the fungus *N. crassa* responded rapidly to geometrically confined microstructures, the dimensions of which were similar to the hyphal diameter [96]. Hyphae responded without any detectable temporal delay or spatial adjustment, while their growth behaviour depended on the complexity of structures they encountered. This indicated that the space-searching strategies did not exclusively rely on physical contact.

Several microfluidic platforms have been proposed for screening and monitoring of morphogenesis during spore germination and germ tube growth [97–100]. Grunberger

et al. utilized a microfluidic cultivation device with time-lapse live cell imaging to analyze spore swelling rates and hyphal/mycelium growth rates of the fungus *Penicillium chrysogenum* [99]. The average swelling rate in spore volume and growth rate of the mycelium were estimated as $\mu = 0.077 \pm 0.036$ and $0.046 \pm 0.031\ h^{-1}$, respectively, both showing significant heterogeneity within a population. Demming et al. fabricated a parallel microbioreactor for evaluation of fungal spore germination of *Aspergillus ochraceus* under different pH and temperatures [97]. The germination rate of *A. ochraceus* conidia was revealed to be 3.5 times higher (25 %) in pH 5.5 medium after 9 hours at 24 °C, compared to 8 and 6 % in pH 3.5 and 7.5 medium, respectively. Meanwhile, spore germination was observed to increase by 60 % in the temperature range of 26 - 30 °C. Although the use of LOC techniques in these examples facilitated parallelizing the investigation of fungal morphogenesis at single-cell resolution and under defined environmental conditions, most of the studies introduced spore suspensions into a microchamber for cultivation. This made it difficult to control the distribution of spores inside the chamber and immobilize organisms during media exchanges or the addition of other liquid reagents.

To address these problems, droplet microfluidics have also been used in conjunction with spore handling. Droplet microfluidics constituted a practical method for the encapsulation of single cells, allowing for chemical isolation and thus quantitative control of reagent concentrations [101]. Discrete droplets are generated by two co-flowing immiscible fluids, one of which becomes the dispersed phase (water/media) and is surrounded by the second fluid (oil) [102]. The volume of formed droplets can be adjusted from dozens of picoliters to hundreds of nanoliters by changing the channel sizes and flow rates, actively tailoring the control volumes for single cells of varying sizes and culture durations [103–105]. A study for phenotypic screening of an anti-oomycete candidate chemical was reported by Yang et al., in which motile zoospores of the oomycete plant pathogen *Phytophthora sojae* and metalaxyl were encapsulated into microdroplets using a simple T-junction droplet generator platform [106]. Zoospore germination and germling growth at different chemical concentrations inside droplets was tracked. At metalaxyl concentration 1.0 mg/mL, the germling length was reduced by 18 %. Furthermore, zoospore germination could be fully inhibited when the metalaxyl concentration was increased above 2.0 mg/mL. Beneyton et al. developed a high-throughput screening platform for large filamentous fungi, which combined droplet microfluidics with fluorescence-activated dielectrophoretic (DEP) sorting [105]. The spores of the fungus *Aspergillus niger* were encapsulated individually in 10 nL droplets with an $\alpha$-amylase fluorogenic enzyme substrate. Droplets with fungi were sorted according to fluorescence intensity after 24 h at 30°C, allowing

for spore germination, enzyme secretion and substrate digestion within the droplets. The platform was able to screen approximately $5 \times 10^4$ droplets in 90 min and sort around 750 droplets of these (1.45 %), corresponding to a 196-fold enrichment for those containing fungi. However, droplet volumes produced with droplet microfluidics techniques were too small for long-term culture of fungi and oomycetes. This meant that observations were restricted to the phases of spore germination or germling growth.

In order to implement compartmentalization and immobilization of fungi and oomycete spores for screening in long-term culture, hydrodynamic flow-assisted manipulation has been used to trap spores in a designated place [107–109]. A microfluidic channel array was employed that enabled observations of tip growth of *N.crassa* conidia which had a diameter of 3 to 8 $\mu$m [109]. An efficiency of 70 % for single cell trapping was achieved using hydrodynamic flow-assisted manipulation. Moreover, a specific structure of confined shallow channels in the trapping site was designed allowing only a single hypha to grow into a channel even if several conidia accumulated at one site. Hyphal growth and morphology in various glucose concentrations and channel geometry conditions, nuclear organization and migration, long-term gene expression dynamics were monitored and analyzed. The hyphal growth rate of *N.crassa* did not show significant change in the channels with various widths ranging from 5 to 20 $\mu$m, while the hyphae generated numerous branches in wider channels (12.5 to 20 $\mu$m). The nuclei were observed to continuously move towards the tip along with the hyphal elongation and keep a nuclear exclusion zone from the hyphal apex.

In the meantime, efforts, especially on the flow control methods, have been done to improve the ease of usage of microfluidic devices for point-of-care (POC) analyses and better incorporation into traditional biology [110, 111]. Millet et al. described a unique protocol of assembly, sterilization and self-priming of devices for ready-to-use microfluidics to end-user [111]. Three microfluidic platforms were shown enabling pre-priming, filling, and shipping of hydrated devices, with or without cultures. The fungus *Laccaria bicolor* was inoculated prior to sealing and kept growing during shipment. Transgenic bacteria, *Pseudomonas fluorescens*, were then introduced and observed with high-resolution imaging for bacterial-fungal interactions by collaborators. Additionally, *Arabidopsis thaliana* seeds were vacuum packaged on chip for 14 days storage to test packaging influences on the seed germination process. One hundred percent of the seeds germinated within 3 days after opening the package and filling with culture medium, and their growth rates showed no difference from the no-vacuum control.

### 2.4.3 Microfluidic platforms for invasive growth force studies

Despite the number of existing platforms designed to probe the morphogenesis of hyphal growth, reports on the characterization and quantification of forces exerted by tip-growing cells during invasion events remain scarce, in particular for use with fungi and oomycetes.

Examples of the latter include a polydimethylsiloxane (PDMS) array containing 10,000 cylindrical microchambers, which were employed as force sensors to measure the extension mechanics of single cells of the rod-shaped fission yeast *Schizosaccaromyces pombe* [112]. The elasticity (Young's modulus) of the PDMS microchambers ranged from 0.1 to 1.5 MPa. Single fission yeast cells were introduced into chambers, which were longer than the seeded cells, and left to extend until they pushed against the wall of chambers, as shown in Figure 2.4. By analyzing the growth of the cells and the deformation of the chambers, internal effective turgor pressure of $0.85 \pm 0.15$ MPa and the force-velocity relationships could be obtained. The microchambers were deformed from a round shape into an oval shape with the increase of exerted force, resulting in a gradual decrease in growth rates of yeast cells. Additionally, the growth force was shown to be dependent on turgor pressure using $\Delta$gpd1 mutant cells, which were

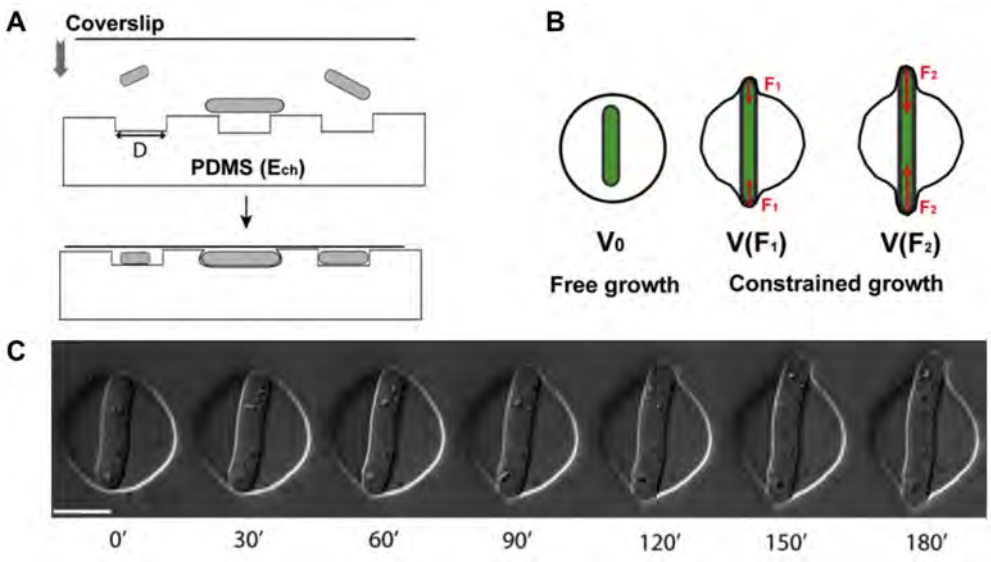


Figure 2.4: Microfabricated chambers as single-cell force sensors for studying the mechanical properties of fission yeast cells. (A) Schematic showing the placement of yeast cells into the PDMS chambers. (B) Schematic illustrating the basis of the experiments. As the cell deforms the chamber, the observable force increases ($F_2 > F_1$). (C) Time-lapse sequence of a fission yeast cell growing in and deforming a chamber made of soft PDMS (elastic modulus, Ech = 0.16 MPa). Scale bar represents 10 $\mu$m. Reproduced with permission from Minc et al. [112].

defective in turgor-pressure regulation. $\Delta$gpd1 mutants incubated in media of higher concentrations of sorbitol (0.05 M) were observed to grow significantly slower and produce less force. However, in this work the growth force measurement was based on the hypothesis that both tip-shaped sides of the cells pushed against the wall of microchambers with the same force, which may not be easily transferable to other filamentous fungi and oomycetes. Furthermore, cells had to be manually inserted into the well and were able to deform along their length due to the round shape of the wells. The majority of other LOCs developed for tip-growing cells to date have been used in the study of pollen tubes. While some of these could in principle be used with fungi and oomycetes due to the similar cell shapes, major changes are likely to be required to measure protrusive forces. For example, based on the deformation of elastic PDMS, a microfluidic device was developed to measure penetrative forces exerted by pollen tubes of *Camellia japonica* [113]. Pollen grains were transported through a distribution chamber and trapped at the entrances of microchannels (see Fig. 2.5). Pollen tubes were then guided to grow through the microchannels, which contained a sequential array of four narrowing gaps, ranging from 17 to 10 $\mu$m. The cells applied a penetrative force deforming the sidewalls of moderately-sized gaps (pollen tube diameter/gap size ratio $\leq$ 1.20) and constricted themselves when passing

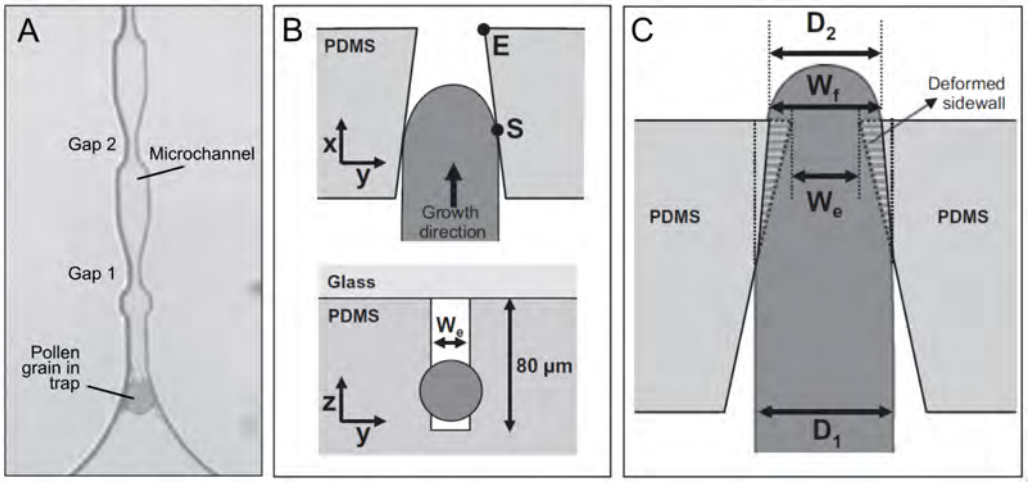


Figure 2.5: Experiments on the exposure of pollen tubes to microgaps and geometry of interaction. (A) Micrograph of the geometry of a microchannel comprising the channel entrance with a trapped pollen grain and subsequent gaps. (B) Simplified schematic views of the interaction between an elongating pollen tube (dark gray) and a microgap. (C) The passing pollen tube deforms the PDMS sidewalls of the gap to change the gap width at the narrowest section. Reproduced with permission from Nezhad et al. [113].

through narrower gaps (ratio between 1.20 and 1.33). The pressure when the tube reached the narrowest region of the gap was estimated to be 0.15 MPa using finite element methods. From this, the dilating force was estimated to be 14.7 $\mu$N at the moment of maximum contact. The results revealed that the pollen tubes regulated cell wall compliance to meet increasing mechanical impedance, resulting in a change in exerted force. However, the tapered shape of the microgaps and the interaction between the pollen tube and the sidewalls, resulting in a combination of deformation of the sidewalls and an apparent reduction in pollen tube diameter, meant finite element simulations rather than an analytical model had to be used to derive the applied force. Furthermore, the fact that forces were measured via the deflection of the sidewall of microscopic gap means that, when used with fungi or oomycete, squeezing forces, rather than penetrative forces, would be measured due to different contact points with the obstacles.

More recently, Burri et al. combined a LOC device with a MEMS-based capacitive force sensor to quantify the force exerted by pollen tubes [114]. The force-sensing plate of the sensor was scaled-down to 50 $\times$ 50 $\mu$m, providing a high force resolution

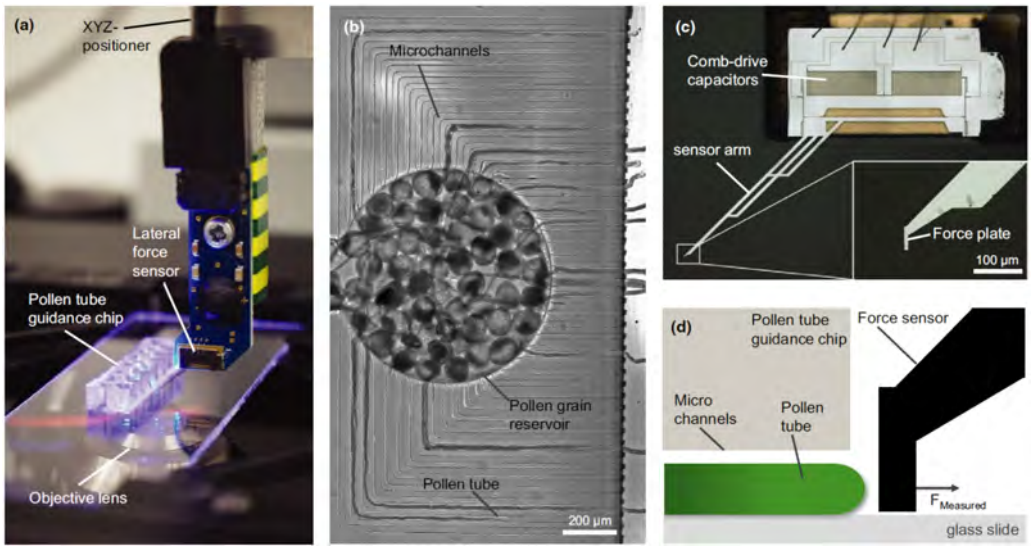


Figure 2.6: System configuration to simulate the natural environment of pollen tubes *in vitro* with integrated force readout. (a) The experimental system combines a LOC device with a capacitive force sensor. (b) An optical image of a LOC loaded with pollen grains in the inner reservoir. (c) Capacitive force sensor measuring lateral forces at the force-sensing plate. (d) Schematic side-view of the experimental setup where the force-sensing plate is placed in front of the tubes emerging from the microchannels. Reproduced with permission from Burri et al. [114]

of 0.18 $\mu$N. Pollen grains were injected into the inner reservoir and the resulting pollen tubes were guided to grow along parallel microchannels, as shown in Fig. 2.6, to ensure a perpendicular contact with the force-sensing plate placed at the channel exit. After the initial contact of the pollen tubes with the sensor plate, a sharp force increase was observed and measured up to a mean value of $9.6 \pm 1.6$ $\mu$N for *Lilium longiflorum* and $3.0 \pm 0.6$ $\mu$N for *Arabidopsis thaliana*. After that point, the pollen tubes were observed to stop growing for a few seconds, they then adjusted their apical growth direction to avoid obstacles and then resumed growth. By placing the force-sensing plate close to the exit of the microchannels, gaps with various widths and lengths could be formed. It was observed that, the narrower and longer the gap the pollen tube had to penetrate through, the larger the measured force, with a maximum of 85 $\mu$N. However, because the capacitive force sensor, with sensor arm and force plate on the front-end, was mounted on a piezoelectric xyz-positioner, only one measurement could be made at a time which limited the throughput of the system, even though multiple pollen tubes grew simultaneously in the parallel microchannels. This, combined with the fact that pollen tubes had to exit the LOC and bridge a gap, mean invasive conditions for fungi and oomycetes would be difficult to generate. Nonetheless, the work demonstrates that with continuing sensor miniaturization and improvements in MEMS techniques, experiments similar to the original silicon strain gauge work may yet have a place in the study of force generation.

In summary however, these examples demonstrate that, despite the inherent suitability of LOCs for the maintenance of fungi and oomycete cells, there exists a distinct technological gap. To overcome some of the limitations of current LOC platforms for force measurements and adapt them especially for fungi and oomycete, our group recently introduced the use of elastomeric micropillars as protrusive force sensors. These and their integration into microfluidic devices will be described in detail in the next chapter.

# Chapter 3

# Optimization of the Mycelial Force Sensing Platform

In this chapter, the optimization and enhancement of the existing, proof-of-concept mycelial Lab-on-a-Chip platform are presented. The improved platform contains single elastomeric micropillars in channel constrictions, achieving measurement of protrusive forces exerted by individual fungal hyphae. The chip design, fabrication process, and photoresist optimization required to adapt the microfluidic platforms to different species of oomycete and fungi are reported. Further miniaturization of sensing pillars and measurement channels is demonstrated to accommodate smaller hyphal sizes, as are efforts to improve pillar tracking. To show the applicability of the devices, the oomycete *Achlya bisexualis* and the fungus *Neurospora crassa* are cultured on the PDMS chips and the forces exerted by single hyphae from the organisms are measured.

## 3.1 Previous work

As described in the previous chapter, LOC platforms for force measurements have predominately focused on tip-growing organisms. Very few have been developed to specifically study fungal and oomycete pathogens and none had capabilities to measure protrusive force. To address this, our group recently introduced a LOC force sensing platform for fungi and oomycetes based on micropillar arrays that had originally been used for locomotion studies in nematodes. These nematode LOC devices integrated a matrix of elastomeric PDMS micropillars into microchambers and microchannels, as shown in Fig. 3.1, to investigate continuous forces and locomotion patterns (speed, amplitude and wavelength) of the nematode *Caenorhabditis elegans*, as influenced by

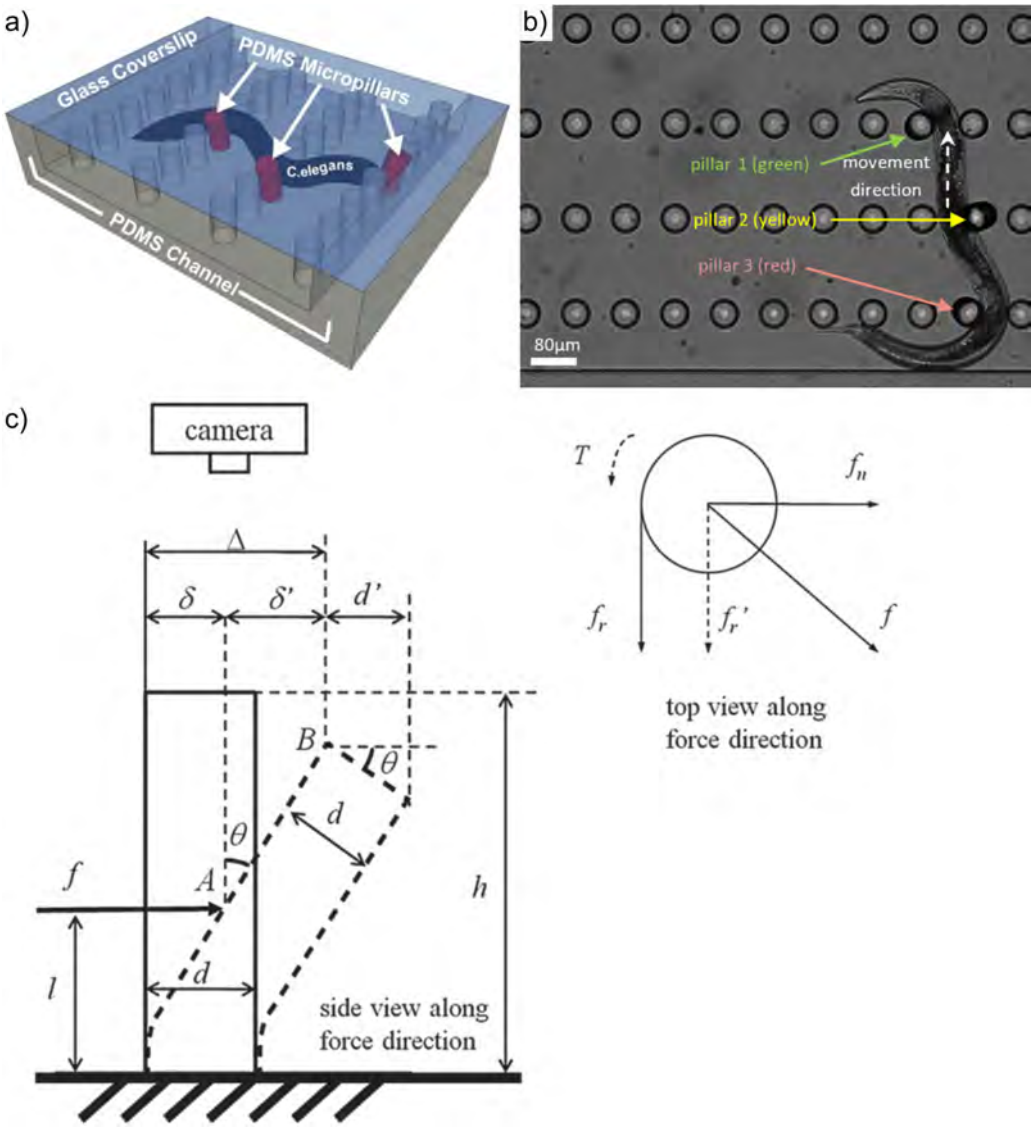


Figure 3.1: Micropillar matrix device for *C. elegans* force measurements. (a & b) Schematic and experimental result of a worm deflecting micropillars while moving in a channel. (c) Schematic illustrating the side- and top-down view of a sensor pillar deflected by an applied force (f) and associated parameters. Adapted with permission from [115].

various micropillar arrangements [115–117]. Circular pillars were chosen for this work as their shape allows for relatively simple analysis of mechanical bending in response to the application of an external force. To match the width of *C. elegans* nematodes and expected force magnitudes, the diameter and height of micropillars were set to 40 and 100 $\mu$m, respectively [118]. Each micropillar functioned as an independent force sensing unit dedicated to one individual *C. elegans*, and the deflections of micropillars were recorded using bright field microscopy. Locomotive forces were then deduced from the recorded deflection by use of an image processing algorithm implemented in MATLAB. Considering the isotropic properties in the radial direction for the pillar, the force was treated as a concentrated load at the contact point where worm and pillar touch, typically at half the diameter of the nematode. Both bending and shear contribute to the imposed force on a cantilevered beam, such as the pillar, at the contact point when the aspect ratio (height-to-diameter ratio) is less than 5. Therefore, the force could be calculated as follows:

$$f = \frac{\Delta}{(\frac{l^3}{3EI} + \frac{d^2(1+\gamma)l}{4EI}) + \frac{l^2}{2EI}(h-l)} \tag{3.1}$$

where $\Delta$ is the deflection of micropillar at the free end, which could be obtained by the image processing. $d, h, l$ are the micropillar diameter, height, and the height from contact point $A$ to the fixed end, respectively. $I$ is the moment of inertia, which can be given by $\frac{\pi d^4}{64}$, when pillar diameters are uniform along the height. $E$ and $\gamma$ are the calibrated Young's modulus and Poisson's ratio for PDMS. The first and second term in the denominator correspond to pure bending and shear, while the third one is the linear displacement $\delta'$ of the free end $B$ (see Fig. 3.1(c)). Using Equation 3.1, 1571 data points from 13 *C. elegans* samples were measured, resulting in a maximum force level of 61.9 $\mu$N [115]. Further work found that the frequency and speed of locomotion of *C. elegans* increased with the spacing of pillars, but also that nematodes maintained their natural sinusoidal movement in all of the devices [116].

Given the geometric similarities between nematodes and hyphae, this facile force sensing technology using cantilever-like micropillars was then adapted by our group to study protrusive force generation by fungi and oomycetes [22]. Initial work focused predominantly on demonstrating that hyphae of the oomycete *A. bisexualis* would be able to interact with and deflect circular PDMS micropillars. Because of the typical hyphal size of *A. bisexualis*, the micropillars had to be reduced in size to 15 $\mu$m in diameter and 30 $\mu$m in height. As shown in Fig. 3.2, the initial proof-of-concept device comprised a large array of these micropillars inside a microchamber. A mycelial plug

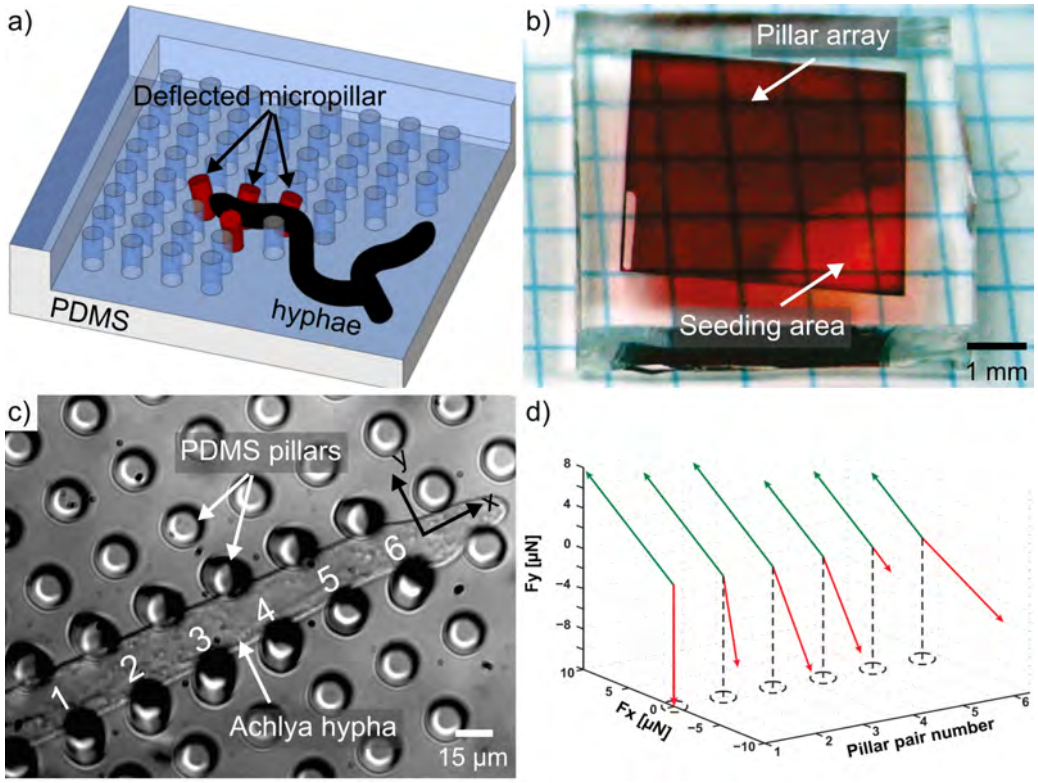


Figure 3.2: LOC platform with force-sensing micropillar array for oomycete hyphae. (a) Schematic of the device showing hyphae growing from a mycelium seeding area into a pillar array and pushing against PDMS pillars in the process. (b) Photograph of fabricated PDMS chip. Red-colored liquid was used to visualize the chip. (c) Light micrograph of an *A. bisexualis* hypha passing through the PDMS pillar array. (d) Plot of force magnitudes and directions along the length of the hyphae as function of pillar pair number. Green arrows correspond to top, red to bottom pillar row. Adapted with permission from [22].

from a *A. bisexualis* culture was then successfully transferred onto the PDMS chip filled with peptone-yeast-glucose (PYG) broth media and hyphae grew into the micropillar arrays. A maximum total force of 16 $\mu$N was recorded from pillar deflections, suggesting that the platform was capable of measuring the forces exerted by fungi and oomycetes. However, it took approximately 12 hours for hyphae to grow from the seeding area into the micropillar arrays, making the whole experiment time-consuming and intractable. It was also difficult to measure protrusive forces as hyphae passed through the space between the micropillars rather than hitting them head on. In fact, not a single hypha was observed to impact pillars with the tip in this platform.
As a result, a modified microfluidic device which contained micropillar arrays (diameter 10 $\mu$m, height 30 $\mu$m) at constrictions within 16 radial microchannels was developed with the aim to mechanically guide hyphal tips against the sensing pillars [23]. Using this setup, interactions between a hyphal tip and a PDMS micropillar were observed for the first time. As shown in Fig. 3.3, the force exerted by a single hyphal tip increased to a maximum of 7.5 $\mu$N during tip contact and reached 19 $\mu$N for bending force after the tip deflected past the pillar. Nevertheless, challenges in measuring the force generated by individual hyphae remained, mainly because hyphae continued to evade the pillars and several hyphae could grow into the same channel simultaneously. The latter limitations in particular necessitated the design of a new microfluidic platform, which specifically guided a single hypha of *A. bisexualis* towards a designated sensing pillar for deflection and protrusive force measurement. In parallel, a second version of the re-designed platform was used to demonstrate miniaturization for use with smaller hyphae, such as the fungus *N. crassa*. Both these efforts, together with related experimental improvements, are discussed in the remainder of this chapter.

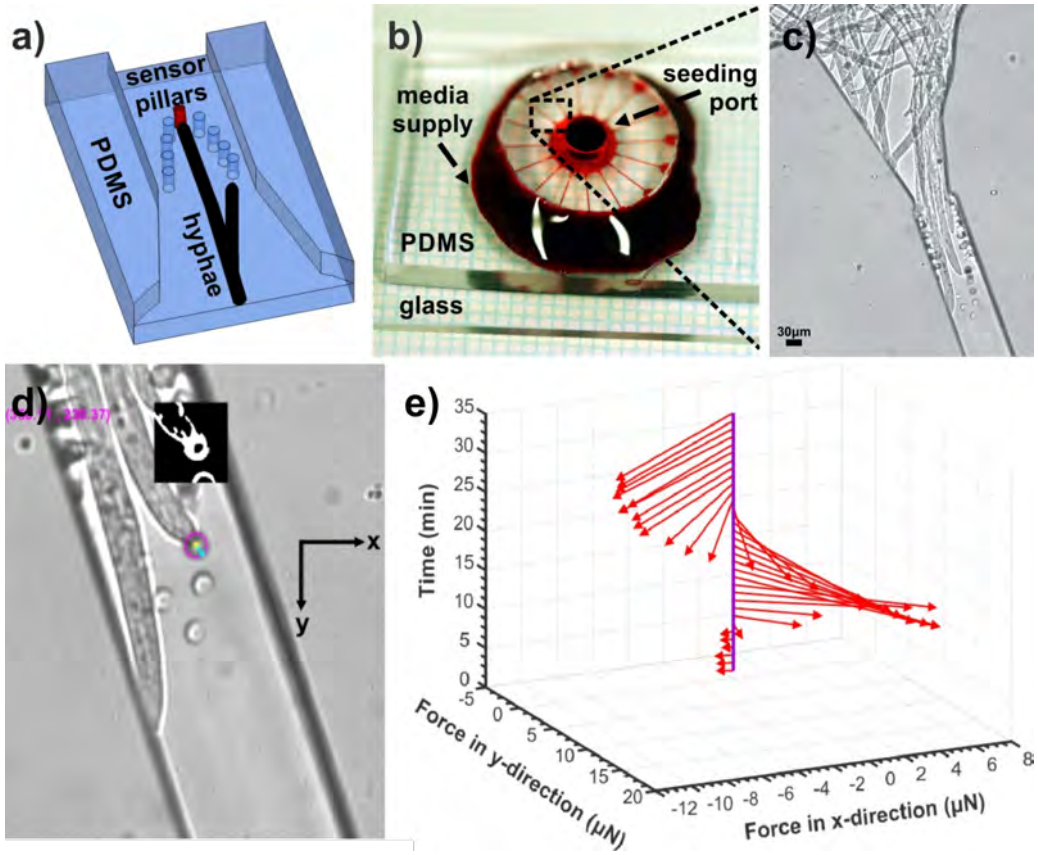


Figure 3.3: Modified platform with micropillar array in radial micro-channels. (a) Schematic of a channel showing a hypha growing inside it and impacting a sensor pillar. (b) Photograph of fabricated PDMS chip containing 16 radial microchannels and one mycelium seeding port. Red-colored liquid was used to visualize the chip. (c) Light micrograph of multiple *A. bisexualis* hyphae growing into one microchannel. (d) Enlarged micrograph of the micropillar top being tracked during deflection. (e) Plot of force exerted on the pillar by a hypha. Adapted with permission from [23].

## 3.2 Mycelial platform for oomycete *Achlya bisexualis*

### 3.2.1 Materials and methods

#### 3.2.1.1 Microfluidic platform design

The microfluidic platform was composed of ten parallel measurement channels, each with an integrated, freely bending single elastomeric micropillar as a force sensor. Measurement channels connected a seeding area for inoculation with a mycelial plug and two media inlets for media supply and independent chemical stimulation, as shown in Fig. 3.4. A mycelial plug was transferred and cultured in the seeding area, fungal hyphae then grow into the measurement channels and deflect the force-sensing micropillars. Compared to the previous radial microchannels, the parallel aligned measurement channels in the new design enabled better simultaneous microscopical observation and analysis of the growth of multiple hyphae, each in a separate channel. As the hyphal diameter of *A. bisexualis* typically ranges from 18 to 30 $\mu$m, the width and height of channel were set to 35 and 30 $\mu$m, respectively. This was done to allow only a single hypha to grow into each channel. As shown in Fig. 3.5, a vertical spacer 5 $\mu$m in height was retained in order to prevent the pillar top from touching the channel lid, allowing it to freely bend. Given that the mask writer ($\mu$PG101, Heidelberg Instruments) and the mask aligner (MA6, SUSS MicroTec AG) used for this work were, in combination, resolution limited to approximately 3 $\mu$m, two pillars sizes of 5 and 7 $\mu$m in diameter were trialed. While smaller pillars would be more sensitive, and thus able to resolve even smaller forces, these diameters were considered sufficient for *A. bisexualis* and a good trade-off in light of the fabrication technologies available. To prevent hyphae from avoiding the pillars, as observed in the previous work, these were placed as close to the channel walls as possible. Thus, the horizontal gap between channel wall and pillar was set to 3, 5, 7 or 10 $\mu$m for each size of pillar to determine the minimum gap achievable during fabrication.

#### 3.2.1.2 Fabrication of microfluidic chip

The microfluidic PDMS chip was fabricated by replica-molding off a two-layer resist master, where the second layer provided the vertical spacer between the top of the micropillar and the channel lid. Previous proof-of-concept LOC platforms shown in Fig. 3.3 had to be fabricated by replica-molding off a two-layer liquid SU-8 negative photoresist master and consecutive PDMS double-casting to achieve the resolution required for pillar definition. Photolithography was first utilized to produce pillars

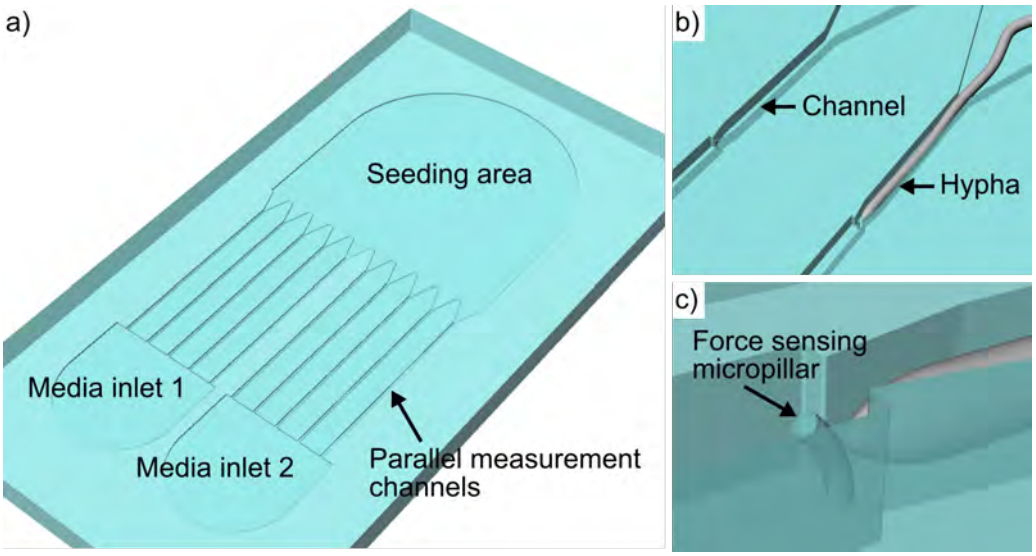


Figure 3.4: Concept design of the new lab-on-a-chip platform for the oomycete *A. bisexualis* developed as part of this thesis. (a) An entire chip showing the geometry of the device including ten parallel channels, one seeding area and two media inlets. (b) Detail view of the measurement channel with a hypha growing into it towards the pillar constriction. (c) Illustration of the force sensing process by deflection of a pillar pushed by an individual hypha.

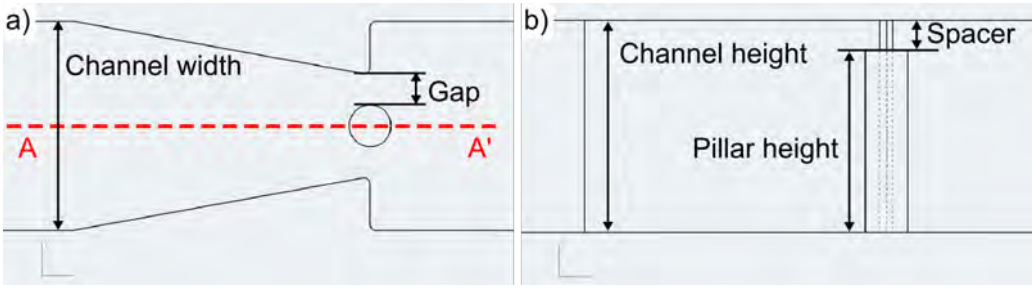


Figure 3.5: Detailed channel design showing (a) the top view of the pillar and horizontal gap to the channel wall and, (b) a cross-section through A-A' with the vertical gap defined by the spacer in the resist mold.

in spin-coated dual layer SU-8 on a silicon wafer as high-resolution optical transfer into negative resist favored the use of mostly opaque masks to form the master mold. However, due to reliability issues with the cast separation steps of the PDMS double-casting process, this meant that the micro-pillar diameter, aspect ratios, the horizontal gap and PDMS chip yield were limited.

To avoid PDMS double-casting processes and improve resolution, direct production of pillar cavities in dry-film SU-8 dual layers was also trialed, but the fabrication of SU-8 molds with negative microstructures (deep cavities) proved difficult due to the lack of exchange of fresh SU-8 developer in micro-cavities such as the ones defining the micro-pillars [119]. In the work presented here, the cavity problem was significantly compounded by the device design and the mask polarity required for a negative resist, such as dry-film or liquid SU-8. For this type of resist, the portion exposed to UV light becomes cross-linked and insoluble to the photoresist developer. Thus, as shown in Fig. 3.6(a), it remains on the substrate, while unexposed areas are dissolved by the developer [120]. If the photomask used for fabrication of pillar cavities contains large

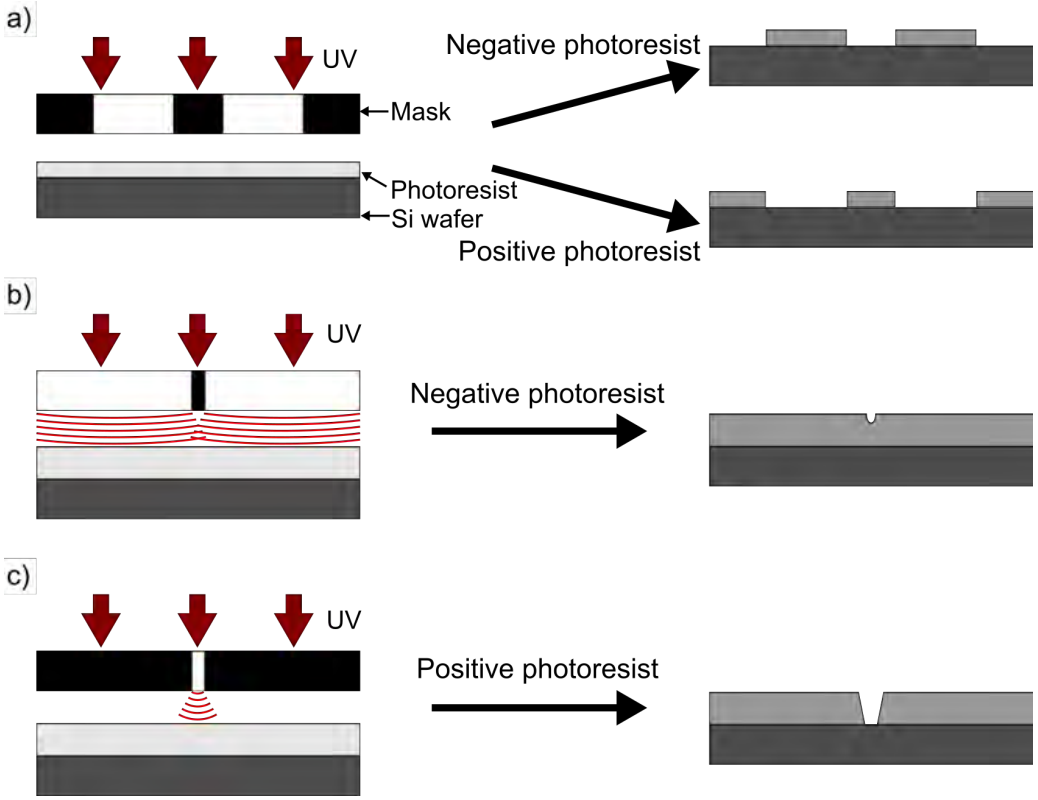


Figure 3.6: Schematic diagram illustrating the difference between negative and positive photoresists showing produced patterns using two types of photoresist (a) and in cases of small pillar cavity fabrication (b & c).

open/transparent areas (channels) and small opaque/dark dots (pillar cavities) in the middle, as illustrated by Fig. 3.6(b), diffraction and refraction effects of UV light lead to smaller and shallower holes, or even no holes being developed [121, 122]. This becomes a lithographically simpler problem if resist polarity can be swapped via the use of positive-tone resists. The chemical structure of positive photoresists changes when exposed to the UV light and becomes more soluble and thus easier to remove by the developer. Because of the inverse pattern required on the mask, wider and slightly tapered cavities can be obtained even though similar optical phenomena apply (see Fig. 3.6(c)). Taking into account the phenomenon that positive photoresists start to soften and round (reflow) at a higher temperature (approximately 100 - 130 °C), a combination of novel negative and positive photoresists was employed to fabricate an integrated mold retaining the 5 $\mu$m high spacer layer and high-aspect pillar cavity (5 - 10 $\mu$m in diameter, 25 $\mu$m in height) inside a channel constriction and thus overcome the pattern transfer problem.

Figure 3.7 illustrates the fabrication process for the microfluidic chip. In detail, mask files used to produce the two masks were designed by an integrated circuit (IC) physical design software (Tanner L-Edit, Mentor Graphics Corporation). The first layer mask contained the channel outlines, seeding area and inlets, while the second layer mask contained the same features with the addition of measurement pillars (Fig. 3.8(a & b)). Two 4 inch chrome-on-glass photomasks (Nanofilm, USA) were prepared using a tabletop micro pattern generator ($\mu$PG101, Heidelberg Instruments). The photomasks were then chrome wet-etched in the in-house-made etchant, containing 16.5 g ceric ammonium sulphate and 4.3 mL perchloric acid in 100 mL DI water, and rinsed with DI water, followed by development in resist developer (AZ 326MIF, M.M.R.C Pty Ltd.) for 45 s and rinsing with DI water. The photomasks were completed by removing the remaining photoresist covering the chrome pattern with acetone. A 4 inch prime grade single-side polish silicon wafer, 525 $\mu$m thickness, was dehydrated in a 185 °C oven for over 2 hours and cleaned by oxygen plasma (K1050X, Emitech) for 10 min at 100 W. Then a dry-film negative photoresist, ADEX05 (thickness 5 $\mu$m, DJ Microlaminates [123]), was laminated onto the pre-cleaned Si wafer at 65 °C and speed 1 setting using a hot-roll laminator (SKY335R6, Sky-Dsb Co. Ltd). After removing the carrier polyethylene terephthalate (PET), the ADEX05 was exposed using the first layer mask using the UV lithography system (MA-6, SUSS MicroTec AG) at an exposure dose of 170 mJ/cm² in vacuum contact mode with a short wavelength exclusion filter (PL-360). The ADEX05 was developed in propylene glycol monomethyl ether acetate (PGMEA) for 5 min, rinsed with isopropyl alcohol (IPA) and dried with Nitrogen ($N_2$), followed by a ramped post-exposure bake (100 °C/hours) of 5 min at 65 °C and 10 min at 95 °C

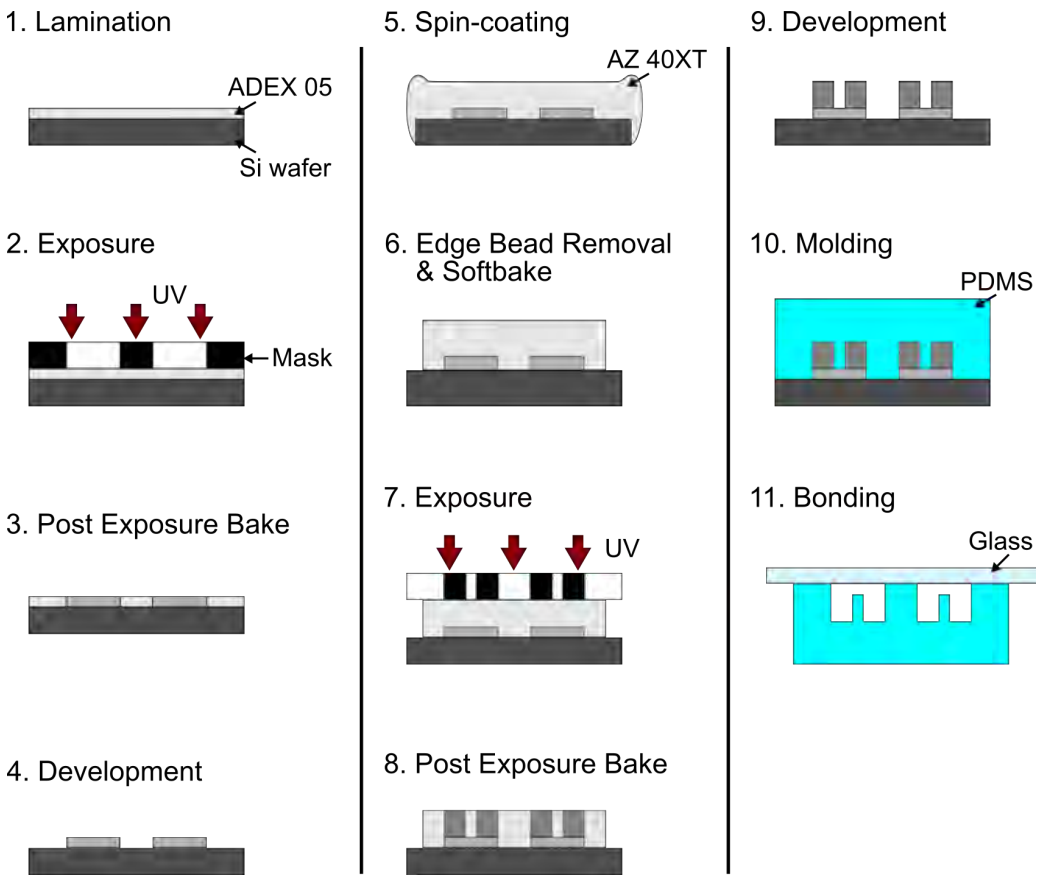


Figure 3.7: Optimized fabrication process of the microfluidic platform based on negative- and positive-tone resist technology. Steps 1-4: Fabrication of the first layer of dry-film negative photoresist using ADEX05. Steps 5-9: Fabrication of the second layer of positive photoresist using AZ 40XT. Steps 10, 11: PDMS molding of microfluidic platform.

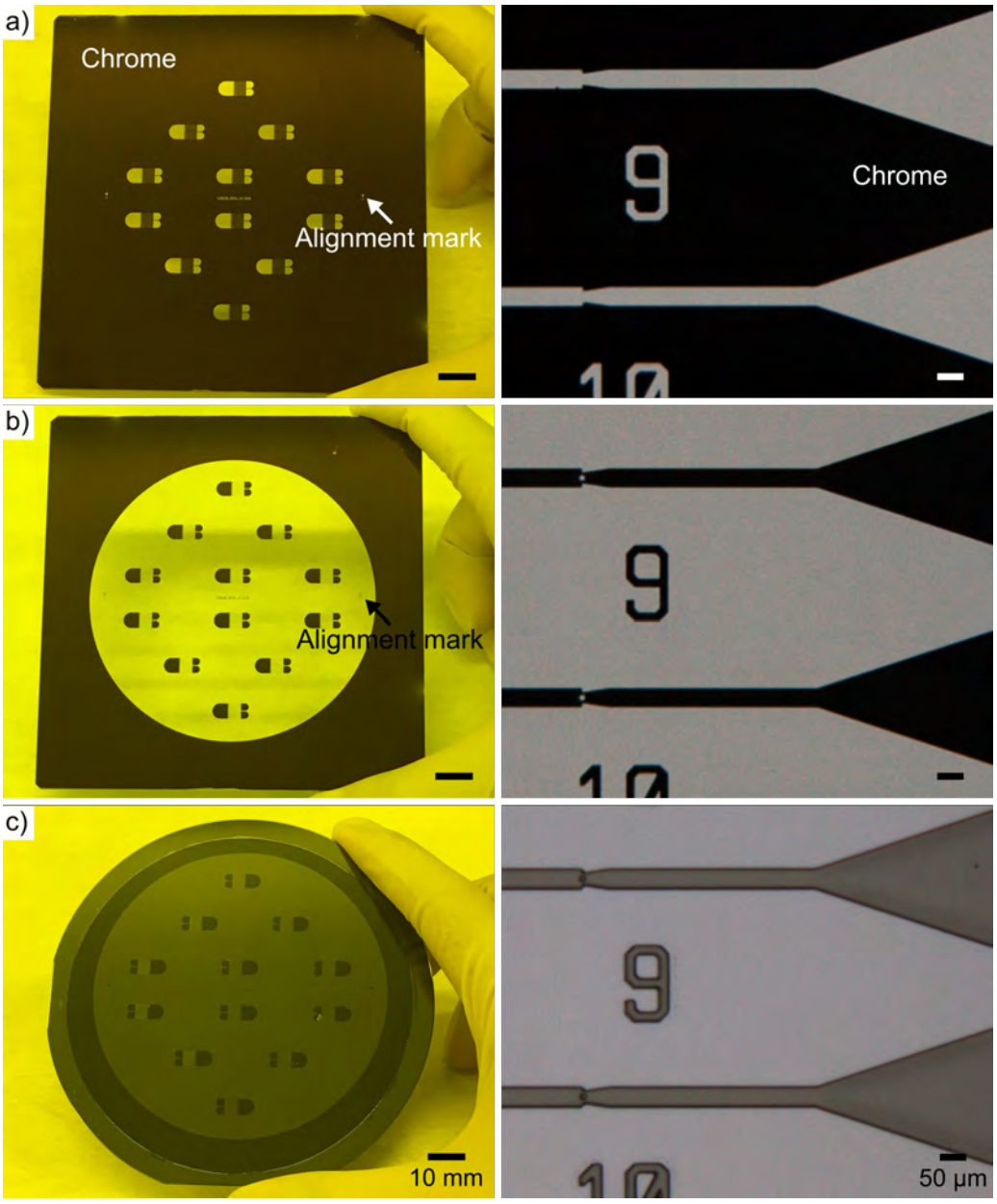


Figure 3.8: Fabricated photomasks and resist master mold. (a) Photograph of the first layer mask for a negative photoresist including entire photomask, detail of measurement channels and alignment mark. (b) Photograph of the second layer mask for a positive photoresist illustrating the inverted mask polarity. (c) Photograph of the resist master mold. Each mold contained 12 individual chips.

on a contact hotplate (HP30, Torrey Pines Scientific, Inc.). To avoid the formation of air bubbles during the second layer photoresist spin-coating, as shown in Appendix A.1, a 2-step process was utilized on a programmable spin-coater (WS-650, Laurell). The second layer of positive photoresist (AZ 40XT, M.M.R.C Pty Ltd. [124]) was spin-coated onto the first spacer layer as follows: Step 1: 20 s at 500 rpm, Step 2: 30 s at 2000 rpm, achieving a total thickness of $30.8 \pm 0.62$ $\mu$m. After edge-bead removal and a soft-bake for 3 min at 126 °C on a hotplate, the AZ 40XT was exposed using the second layer mask also using the MA-6. This was followed by a post-exposure bake at 105 °C for 80 s, and development of the master mold in resist developer AZ 326MIF for 3 min, rinsing with DI water and drying with $N_2$ (see Fig. 3.8(c)).
Notably, a special set of alignment marks used to align the second layer onto the first layer had to be designed to improve the alignment accuracy of the two photoresist layers. Appendix A.2 shows the previously used alignment mark, which contained a large square on the first layer and four small squares on the second layer overlapping at each corner of the large square. Due to the insufficient aligning position, it proved difficult to align two layers with the required precision with these marks, especially in the area of the pillar cavity. The new set of alignment marks was composed of a cross-pattern and simplified three-directional Moire-fringe patterns [125, 126]. The fringes on both layers were 12 $\mu$m wide, and the distance between fringes on the first layer was 12 $\mu$m, while that on the second layer was increased 2 $\mu$m from the middle to the edge to enable an alignment accuracy of $< 2$ $\mu$m (see Fig. 3.9).
According to the reaction principle of positive photoresists, the more exposure power of UV light that is applied to a AZ 40XT resist, the larger and deeper a cavity is able to be generated. Simultaneously, the channel width becomes narrower. Thus, the exposure latitude of the positive photoresists was characterized in combination with the subjacent negative resist by measuring the widths of channels and diameters of pillar cavities for various exposure doses. An exposure dose trial ranging from 200 to 350 mJ/cm², was conducted on the channel patterns with 5 and 7 $\mu$m diameter pillar cavities and 3, 5, 7 and 10 $\mu$m wall gaps, with the negative photoresist ADEX05 acting as the first channel layer. Detailed results of the fabricated resist molds, shown in Fig. 3.10, demonstrated that the gaps between channel walls and cavities became narrower when the exposure power increased, while the narrowest pillar-wall gap of 3 $\mu$m could not be resolved at exposure doses higher than 250 mJ/cm². Moreover, Figure 3.11 shows the plot of the dose trial results for the photoresist AZ 40XT. For both cavity 5 $\mu$m and 7 $\mu$m patterns, the diameter of cavities increased with the increase of exposure dose from $4.7 \pm 0.01$ to $7.3 \pm 0.14$ $\mu$m, and from $7.4 \pm 0.08$ to $9.4 \pm 0.08$ $\mu$m, respectively, while the width of the channel decreased from $34.2 \pm 0.10$ to

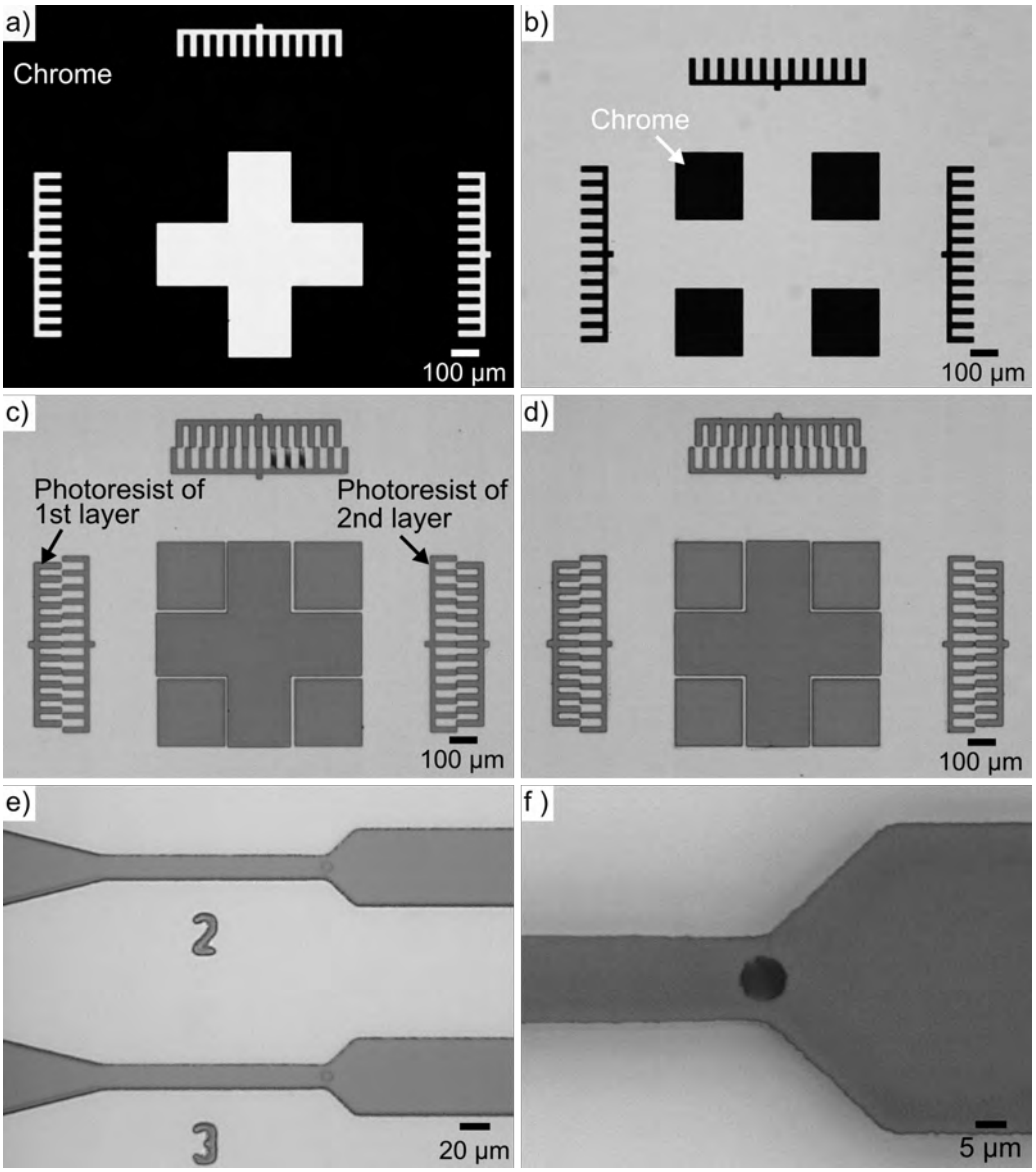


Figure 3.9: Light micrographs of the improved set of alignment marks. (a & b) Patterns on the first and second layer masks. (c & d) Fabricated alignment marks in resist on left and right side of the photoresist master showing the Moire patterns. (e & f) Images of the measurement channels on the same master with the two layers of photoresist well aligned.

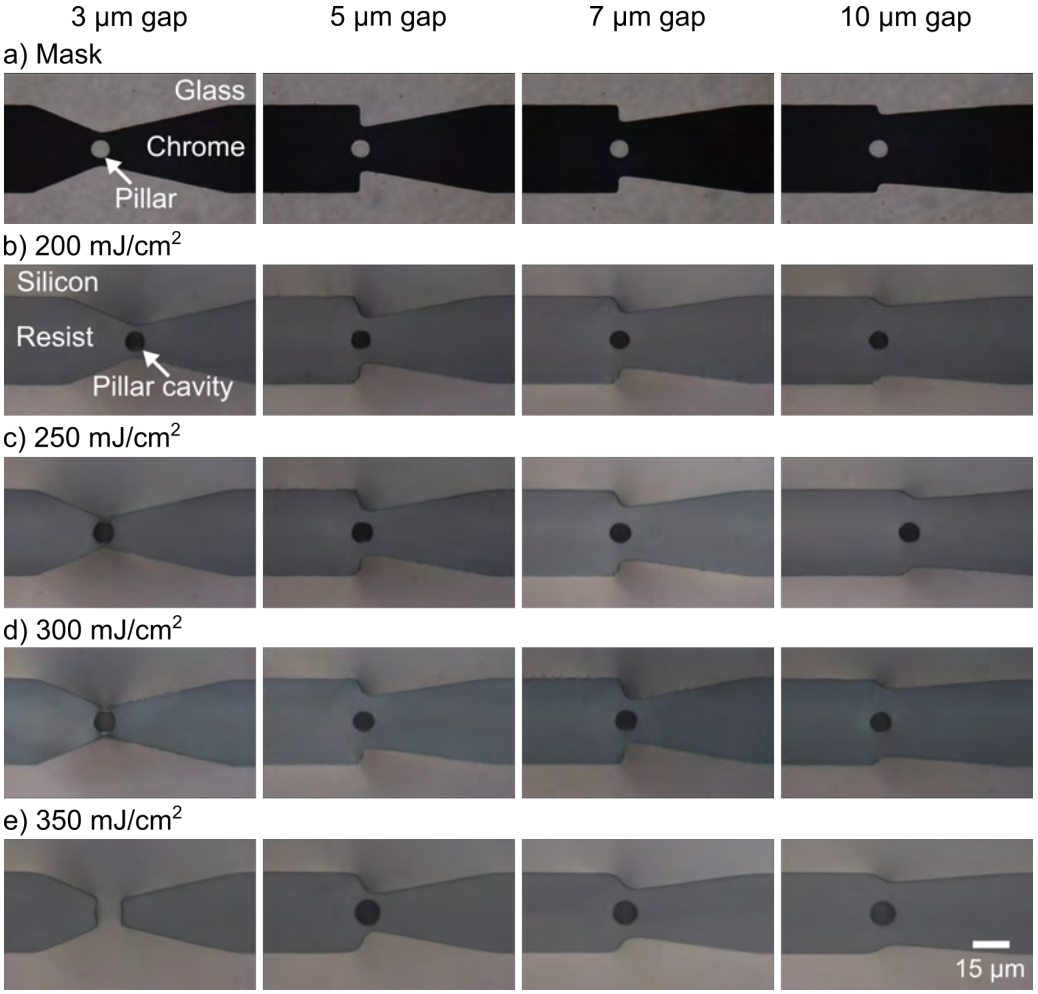


Figure 3.10: Fabrication results of the *A. bisexualis* chip with a 7 $\mu$m pillar, and 3, 5, 7 and 10 $\mu$m gaps. (a) Light micrographs of the mask patterns used. (b-e) Light micrographs of the resulting resist patterns for optical exposure powers from 200 to 350 mJ/cm² applied using the MA-6.

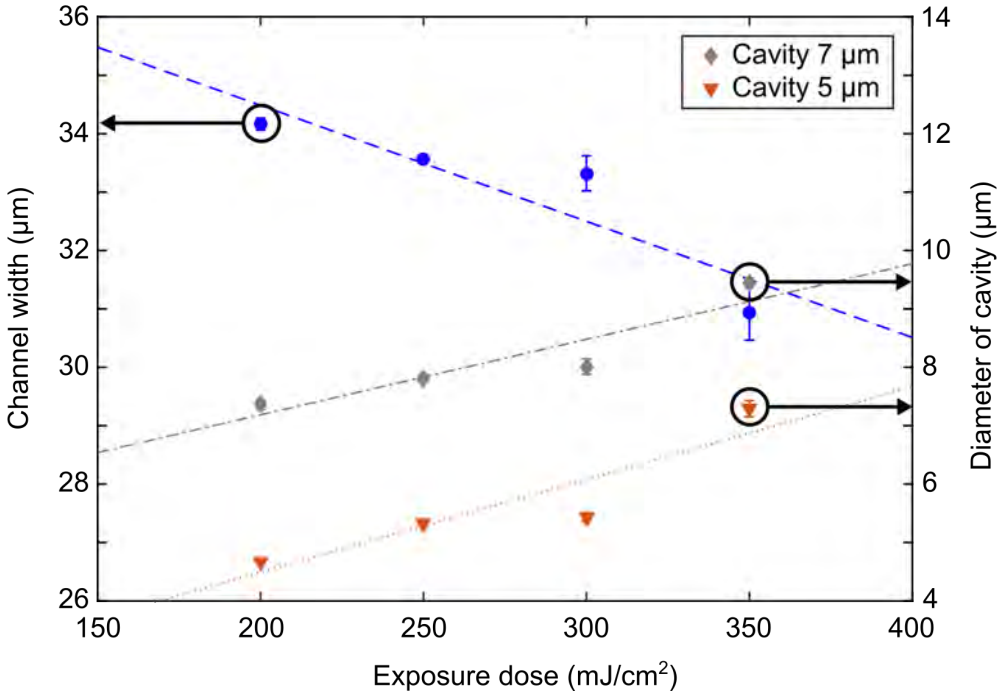


Figure 3.11: Plot of dose trial results for AZ 40XT under optical exposure powers ranging from 200 to 350 mJ/cm². The dots (blue) represent the width of the channel, and triangle (orange) and diamond (gray) are the diameters of the 5 and 7 $\mu$m cavities, respectively.

30.9 $\pm$ 0.47 $\mu$m. In comparison, the channels and pillar cavities on the mask were measured as 34.5 $\mu$m in width, 6.9 and 4.7 $\mu$m in diameter. The optimum exposure power for fabrication of successive *A. bisexualis* chips was thus set to 250 mJ/cm². PDMS chips were molded off the master using Sylgard 184 silicone elastomer (Dow Corning, Electropar Ltd., NZ). The base and curing agent were mixed thoroughly in a 10:1 w/w ratio and degassed in a desiccator for 30 min. Meanwhile, the master mold was treated by vapor-coating with Trichloro(1H,1H,2H,2H-perfluorooctyl)silane (TFOCS, Sigma-Aldrich, Inc.) in a desiccator for 30 min to facilitate mold release. Then, pre-mixed PDMS was poured onto the treated mold and degassed again until all bubbles had disappeared ($>$ 30 min). After a 2 hour bake at 80 °C on a hotplate, the PDMS chips were peeled off carefully and placed on a hotplate for an additional 4 hour bake at 80 °C to ensure the PDMS was completely cured and mechanical properties were stabilized [127]. Glass covers were prepared by drilling through-holes into a standard 75 $\times$ 25 mm glass microscope slide (VWR) using a 3 mm diameter diamond-coated hole drill (28.5030, Esslinger) and cleaned in a sequence of ethanol, methanol and IPA for 5 min each. Both fabricated PDMS chips and cleaned glass covers were treated with oxygen plasma (100 W, 30 s) using the same plasma-asher as for wafer cleaning. Assembly of a microfluidic chip was achieved by manually aligning and bonding PDMS chips with glass substrates and baking them for 2 hours at 80 °C on a hotplate. Assembled microfluidic chips were degassed for 2 hours in a vacuum chamber to improve filling with media [128], and sealed into food-grade vacuum bags using a vacuum sealer (Sunbeam FoodSaver) for storage. Figure 3.12 shows a fabricated *A. bisexualis* microfluidic chip with a single mycelium seeding area and two media inlets. These inlets could be supplied separately with nutrients and/or inhibitors allowing one to measure six samples in parallel. Externally, chips could either be connected with tubes through manually-cored side ports to actively provide media exchange, as demonstrated by the infusion of colored water in Fig. 3.12(a), or passively by coring a common inlet overlapping both. The side view of a cleaved measurement channel shown in Fig. 3.12(c) verified that the produced pillar was 7 $\mu$m in diameter and 24 $\mu$m in height with the spacer gap above it, thus achieving smaller and higher aspect ratios than that of previous work with 10 $\mu$m diameters and 24 $\mu$m heights [23].

#### 3.2.1.3 Application of dye to the PDMS chips

The decrease of micro-pillar diameter made it more difficult to visually track the movement of the micro-pillar top by automatic image processing. This was due to

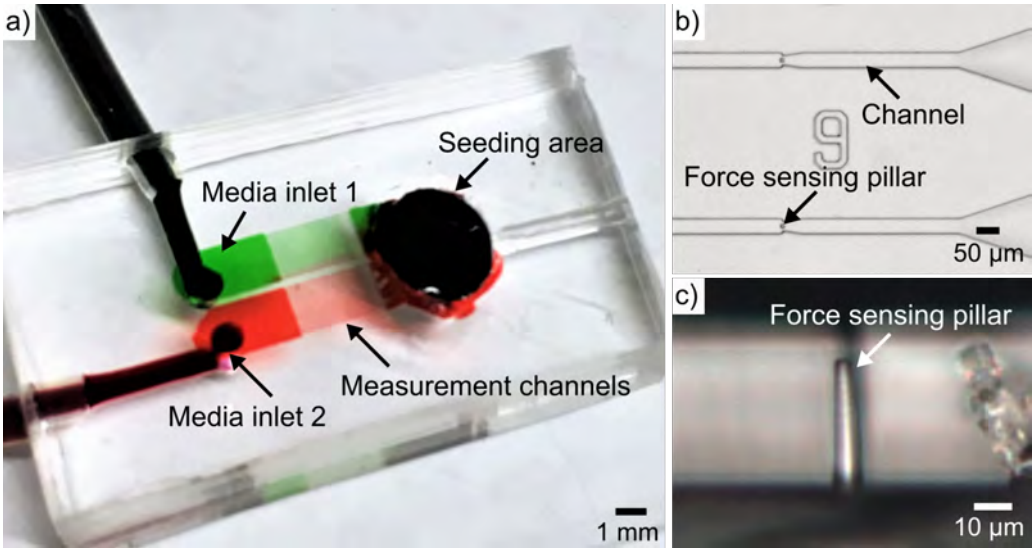


Figure 3.12: Fabricated PDMS chip for *A. bisexualis*. (a) Photograph of the entire chip with tubing attached. Colored liquid was used to visualize the channels. (b) Top-down optical micrograph of measurement channels on the chip. (c) Side-view optical micrograph of a PDMS measurement pillar in a channel. The image was obtained by mechanically cleaving a sample chip along a measurement channel.

the decreased contrast between the transparent hyphae and the equally transparent PDMS micro-pillars. To improve on this, a dyeing method to selectively color the force sensing pillars was investigated [129]. Silc Pig® silicone pigment (Smooth-On, Inc.) was used for PDMS dyeing. PDMS (10:1 w/w) was mixed with 3 % red pigment, the largest concentration recommended by the manufactures [130], relative to total PDMS weight and poured onto the patterned Si wafer, as shown in Fig. 3.13(a). After degassing in a vacuum desiccator for 30 min, excess colored PDMS was removed. Clean PDMS (10:1 w/w) was then poured on top of the previous layer and baked at 80 °C for 2 hours to form a continuous structure. After cooling down to room temperature, the PDMS was peeled off and bonded onto a glass slide. Consequently, PDMS devices with red colored pillars were obtained after another 2 hours bake at 80 °C.

Figure 3.13 shows the fabricated measurement channels with 7 $\mu$m pillars made of pigment-dyed PDMS. As illustrated by Fig. 3.13(b), the measurement channels were light pink, while the rest of the PDMS device was red. However, after being observed with a 50× microscope objective lens, no significant contrast difference between the pillar and channel could be seen when back illumination was used (see Fig. 3.13(c)). Side-illumination, achieved by placing a secondary light source transversely to the

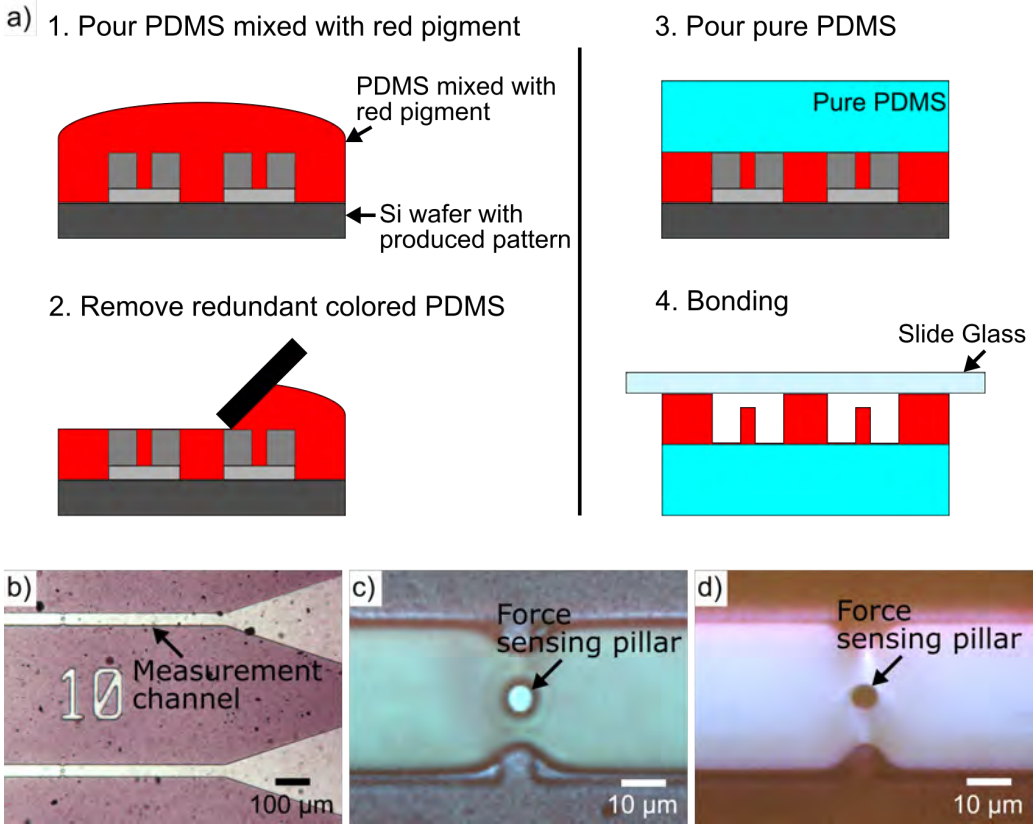


Figure 3.13: Fabricated device with pigment-colored PDMS. (a) Fabrication process used to mix PDMS with red pigment while retaining optical clarity for microscopy. Light micrographs of the resulting PDMS pattern under back illumination using (b) 10× and (c) 50× microscope objectives. Note: very little contrast improvement could be observed due to the small size of the pillars. (d) Light micrograph of the resulting PDMS pattern under side illumination using a 50× objective. While contrast is improved significantly, side-illumination is difficult to accomplish on a standard microscope.

chip, improved the contrast between the pillar and channel (see Fig. 3.13(d)). However, this would be difficult to implement in a conventional microscopy setup.

### 3.2.2 Experimental setup and platform use with *A. bisexualis*

For use with microorganisms, the fabricated microfluidic platform was promptly filled with sterilized PYG broth (containing [in% w/v] peptone [0.125], yeast extract [0.125] and glucose [0.3]) [71] once it was taken out from the sealed vacuum package. Prior to this, the oomycete *A. bisexualis* was cultured on PYG agar Petri dishes (containing [% w/v] peptone [0.125], yeast extract [0.125], glucose [0.3], and agar [2]) for 48 hours. An inoculation plug of *A. bisexualis* approximately 3 mm in diameter was cut from the culture's growing edge and transferred to the seeding area of the platform. The processes of chip filling and oomycete inoculation plug transport were implemented in a sterile laminar flow hood, while no sterilization of platforms was required. Alternatively, the platforms could be pre-cleaned through ethanol flushing, followed by media rinsing or UV exposure in flow hood if the need arose. Hyphae were then observed regularly while they grew from the seeding area into the measurement channels. As the hyphae grew close to the force sensing pillars, hyphal growth and pillar deflection by the tip of each hypha were recorded using an upright epi-fluorescence microscope (Nikon Eclipse 80i) and a digital camera (ORCA-Flash4.0 V2, Hamamatsu) controlled using image-capture software (HCImage Live, Hamamatsu). The force exerted by hyphae was calculated using a combination of image processing for tracking in ImageJ (V1.51u, FIJI) and subsequent force analysis in MATLAB (2016a, Mathworks) [131]. Image sequences were imported into ImageJ, analyzed using the TrackMate plugin [132] and exported in 2D coordinates/time (x, y, t) format representing the position of the pillar top circle as a function of time. Given a half-hyphal diameter contact height, both force magnitude and direction were calculated by a custom algorithm implementing Formula 3.1, combining pure bending and shear of the imposed force to a cantilever beam [23].

For high-resolution confocal imaging of *A. bisexualis* on the chips, PDMS devices were plasma-bonded, as described above, to fluorodishes (FD35-100, WPI Inc.) instead of glass microscope slides to reduce the glass thickness. Instead of glass drilling, inlet and outlet holes were punched through the PDMS using a 3 mm diameter hole punch before bonding. PYG broth on the chip was replaced with PYG containing tartrazine (trisodium 1-(4-sulfonatophenyl)-4-(4-sulfonatophenylazo)-5-pyrazolone-3-carboxylate)), which is a synthetic lemon-yellow dye that is commonly used as a food colouring (E102). The tartrazine was bought in form of yellow food colouring

(Hansells Food Group, Auckland, NZ) from a local supermarket. Solutions on the chips were changed using a perfusion method. This was done by first removing some of the PYG broth from the seeding area on the chip using a pipette after the mycelium had been left to settle and grow on the chip. Then the dye solution was added to the media supply port. Hyphae and pillars were imaged with a confocal microscope (Leica TCS SP5) using a 63x (NA 1.3) glycerol objective lens. Tartrazine was excited using an argon laser at 488 nm with 30 % intensity with an emission bandwidth of 502-605 nm. The fluorescence was detected concurrently with transmitted light images collected with bright field optics. Data was analyzed using the 5D Viewer plug-in of ImageJ. Recorded fluorescence data was inverted in post-processing to visualize the hyphae, pillar and channel.

An example of the measurement of protrusive force exerted by a single hypha of the oomycete *A. bisexualis* is shown in Figure 3.14. Prior to force sensing, hyphae were observed using lower magnification 5 or 10× objectives while they grew out from the seeding area into the measurement channels. Once hyphae grew close to a sensor pillar observation was switched to a higher magnification 20× objective and the microscope was focused on the top of the respective sensor pillar for improved pillar tracking. By narrowing the measurement channels on the new platform, hyphal growth was successfully restricted so that only a single hypha could grow along each channel and be guided to hit the sensor pillar. In the particular example shown in Fig. 3.14(b &

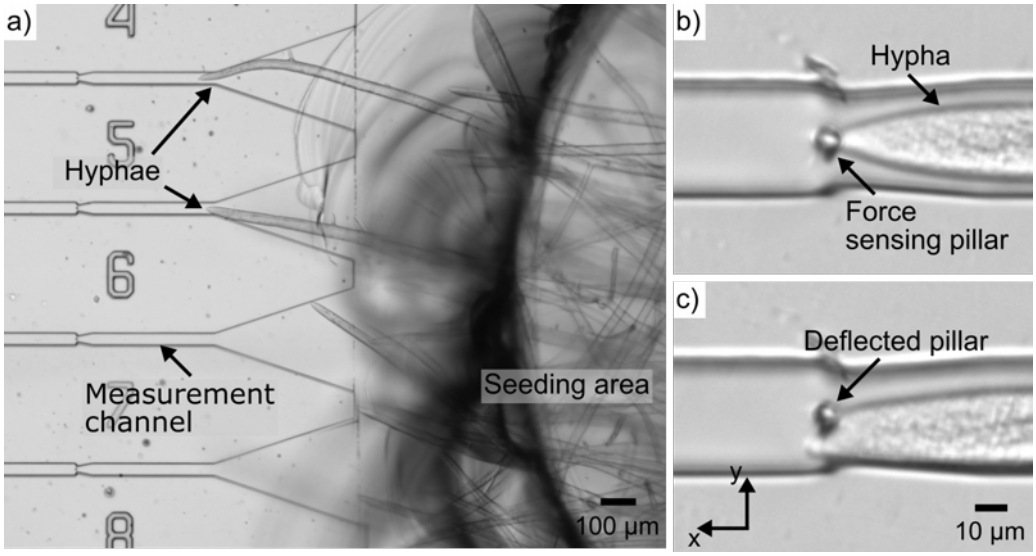


Figure 3.14: Force measurement on oomycete *A. bisexualis* (a) Light micrographs of *A. bisexualis* hyphae growing out of the mycelium seeding area into the measurement channels. (b) Light micrographs of a single hypha hitting the force sensing pillar and (c) passing the pillar after initial protrusive force application and pillar deflection.

c), the hypha was observed to contact the micropillar of 7 $\mu$m in diameter, directly hit it and ultimately squeeze past it. By tracking the pillar top, both force magnitude and direction could be recorded as a function of time. As shown in Fig. 3.15, the protrusive force exerted by the example hypha, which corresponds to Fx-component was measured to initially increase by 2.4 $\mu$N.

The contact area between the hyphal tips and force sensing micropillars could be estimated from the hyphal diameter using the formula $2\pi r^2$ [84]. For the example hypha, its diameter was measured as 4.4 $\mu$m. In doing so, the pressure exerted by example hypha was calculated to be 0.08 $\mu$N $\mu$m$^{-2}$, which was comparable with the value of $0.11 \pm 0.02$ $\mu$N $\mu$m$^{-2}$ obtained by Money et al. for *A. bisexualis* hyphae using strain gauges [84]. Using confocal imaging, we were further able to record the first ever three-dimensional time-lapse images of the hypha-pillar interactions on the chips. As illustrated by the sequence of images and corresponding cross-sections in Fig. 3.16, force application by the hypha was mainly in the x-y chip plane. Measurement noise made it difficult to determine whether minor changes in the cross-sectional plot in Fig. 3.16(c) corresponded to deflection in the z-direction or swelling of the hyphal tip during interaction with the pillar [133]. This led to the conclusion that the measured force and pressure values corresponded in full to those applied by the hypha. This platform has since been used in our group to further investigate the protrusive forces generated by *A. bisexualis* hyphae and the role of the cytoskeleton in these processes [134]. It proved that, compared to previous platforms with micropillar arrays in radial microchannels, the new platform enabled simultaneous observation of hyphal growth and force sensing in parallel channels, and successfully prevented multiple hyphae from growing in the same measurement channels.

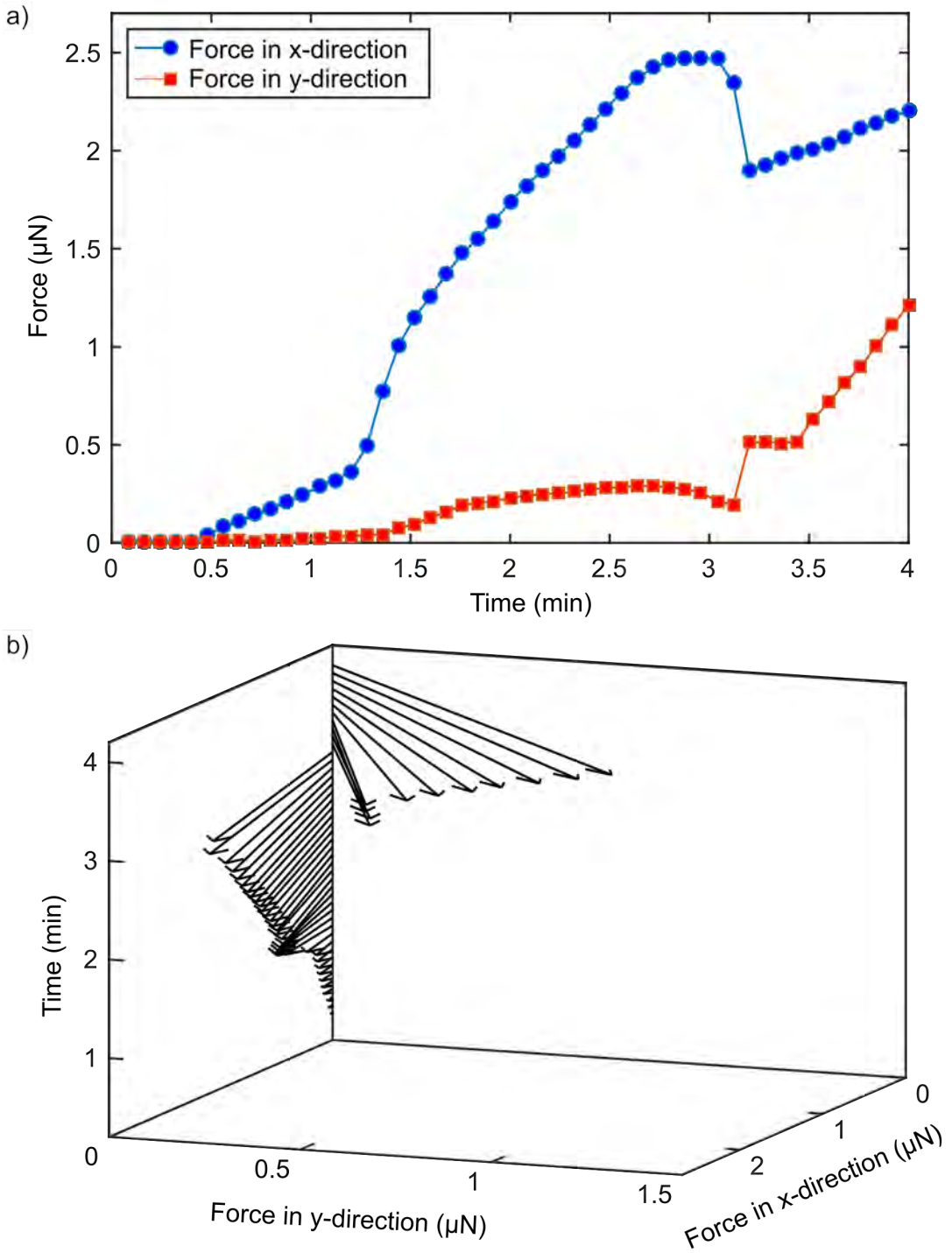


Figure 3.15: Plot of the *A. bisexualis* forces recorded during the experiment shown in Fig. 3.14. (a) Plot of the force components in the x- and y-direction as function of time, with x-direction corresponding to the growth axis of the hypha. (b) Plot of the same data as force vector over time. Note the ability of the measurement system to capture magnitude and force direction simultaneously.

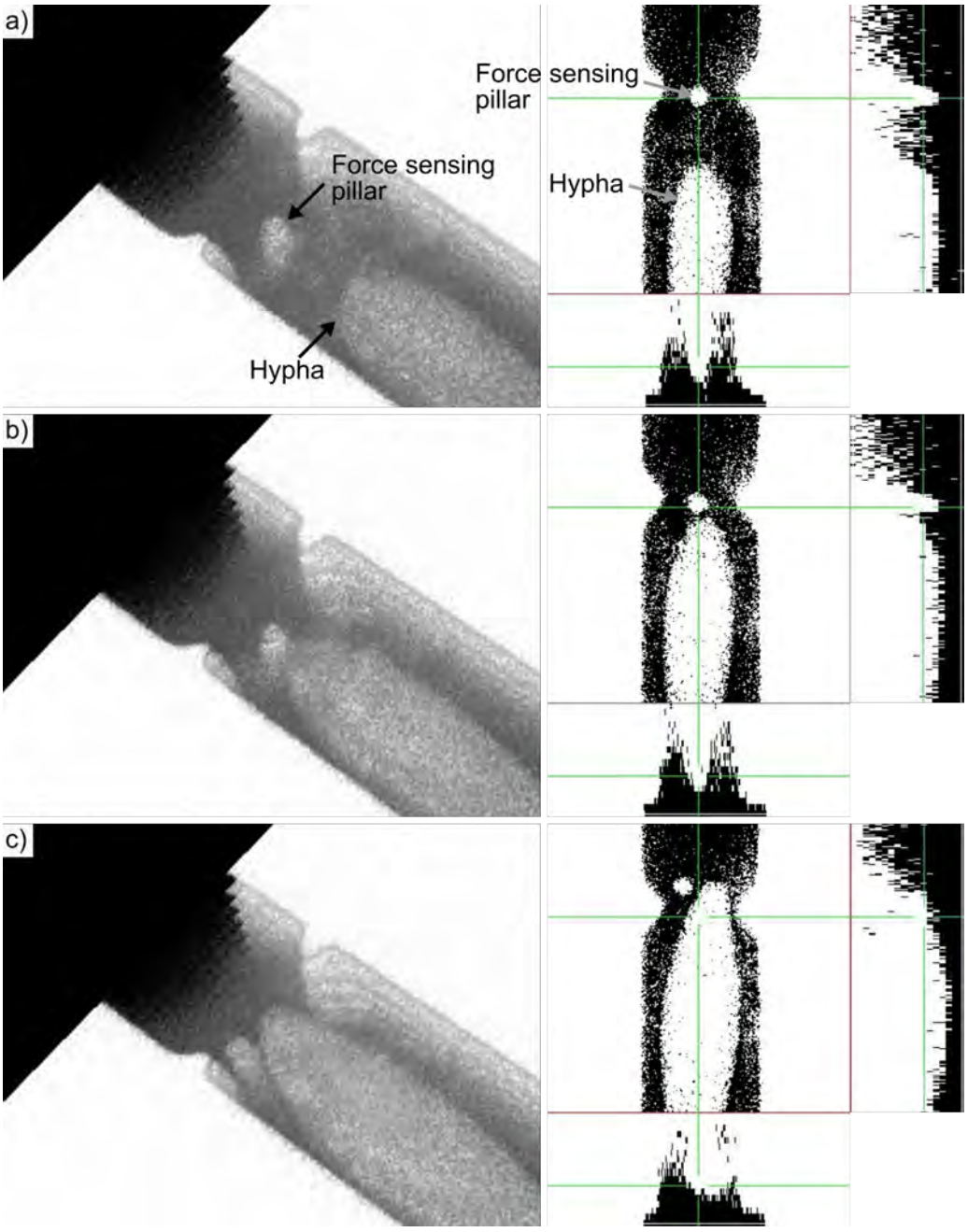


Figure 3.16: Confocal microscopy time-series of a single *A. bisexualis* hypha deflecting a sensor pillar on chip. (a) Hypha extended down a measurement channel filled with fluorescein sodium towards a force sensing pillar. The 3D rendering of the event is shown on the left (data inverted), top-view and cross-sections are shown on the right. (b) The hypha touched the pillar and (c) then proceeded to squeeze through the gap between the pillar and the channel wall, bending the pillar in the process. Cross-sections in (b) and (c) indicate no obvious up and down movement of the hypha during the interaction, thus validating the force measurement.

## 3.3 Miniaturized mycelial platform for the fungus *Neurospora crassa*

### 3.3.1 Materials and methods

#### 3.3.1.1 Microfluidic platform design

The overall design of the mycelial platform chips for *Neurospora crassa* was similar to that used for *A. bisexualis* and described in the previous sections. However, given that the hyphal diameter of *N. crassa* at 8 - 15 $\mu$m is much smaller than that of *A. bisexualis*, the channels of the chip had to be scaled-down to continue to individualize hyphae for force measurement. This meant that all related dimensions had to be adjusted as permitted by the available fabrication technologies. In particular, the width and height of the channels were both set to 15 $\mu$m. The vertical spacer layer and the horizontal gap between the pillar and channel wall were further reduced to 3 and 5 $\mu$m, respectively, so that the hyphae could not grow through the constriction without touching the force sensing pillar. As discussed in the previous section, the values for the latter coincided with the resolution limit of the fabrication processes available and thus required significant process optimization to effectively measure forces.

#### 3.3.1.2 Fabrication of the microfluidic chip

The overall fabrication process utilized the same principles as described in Section 3.2.1 to fabricate the microfluidic chips for *N. crassa*, in particular the replica-molding off a negative and positive-tone photoresist combined two-layer master. A 4 inch prime grade single-side polished silicon wafer of 525 $\mu$m thickness was dehydrated at 185 °C in an oven for over 2 hours and cleaned using oxygen plasma for 10 min at 100 W. For the first spacer layer, the negative-tone dry-film photoresist ADEX05 was replaced with liquid negative-tone AZ 15nXT (115 CPS, M.M.R.C Pty Ltd. [135]). This was done as ADEX05 with a nominal thickness of 5 $\mu$m is currently the thinnest negative-tone dry-film available, thus limiting the spacer layer thickness. AZ 15nXT on the other hand is a recently introduced negative-tone resist with excellent resolution, the thickness of which could be controlled via spin-coating. It was spin-coated onto the pre-treated Si wafer using a spin-coater (WS-650, Laurell) at 5000 rpm for 30 s. After 2 min of soft-baking at 110 °C on a hotplate, the AZ 15nXT was exposed using the first layer mask, shown in Fig. 3.17(a), with the MA-6 in vacuum contact mode. The resist was then baked for 1 min at 120 °C on a hotplate and developed in AZ

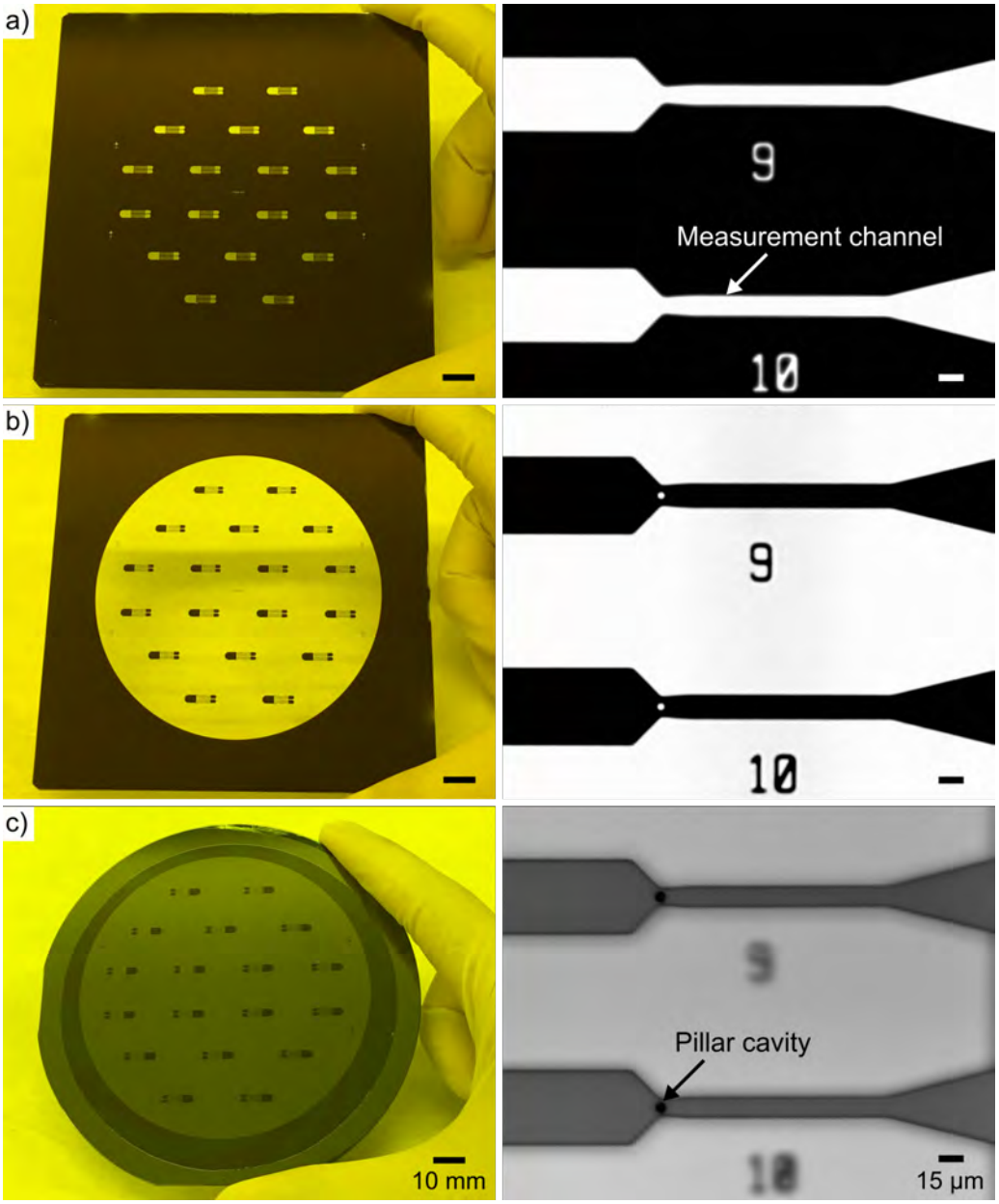


Figure 3.17: Fabricated photomasks and resist master mold for the *Neurospora crassa* platform. (a) Photographs of the first layer mask used for negative-tone photoresist. (b) Photographs of the second layer mask used for positive-tone photoresist. (c) Photographs of the resist master mold. Each mold contained 18 chips.

326MIF developer for 50 s, rinsed with IPA and dried by $N_2$. A 10 min hard-bake at 200 °C on a hotplate was performed after development to increase the structural stability of the resist for subsequent processes. The average thickness of AZ 15nXT layer was measured as 2.6 ± 0.01 $\mu$m at three points on the master wafer using a surface profiler (Dektak 150, Veeco). For the pillar layer, the novel positive-tone photoresist AZ 12XT (20PL, M.M.R.C Pty Ltd. [136]) was utilized instead of AZ 40XT, as the former has a lower viscosity and thus obtainable minimum thickness. Following application optimization, AZ 12XT was coated onto the first spacer layer using a 2-step spin-coating process with the same spin-coater. After edge-bead removal and soft-bake (3 min at 110 °C) on a hotplate, the resist was exposed using the inverted polarity second layer mask in the MA-6 (see Fig. 3.17(b)) at exposure doses discussed below. After post-exposure baking at 90 °C for 1 min, the master mold was completed by immersion in resist developer AZ 326MIF for 2 min, rinsed with IPA and dried by $N_2$ to give the resist structures shown in Fig. 3.17(c). The subsequent PDMS casting and bonding processes, and the microfluidic chip sealing were kept identical to those for *A. bisexualis* chips described in previous section. An example of a fabricated microfluidic chip for use with *N. crassa* and bonded to a fluorodish is shown in Fig. 3.18.

Since the photoresists AZ 15nXT and AZ 12XT were brand new at the time this work was performed, very little information existed in the public domain on their use and optimal processing parameters. In particular, no data existed on their application in multi-layer arrangements. Due to this, and comparable to the exposure dose

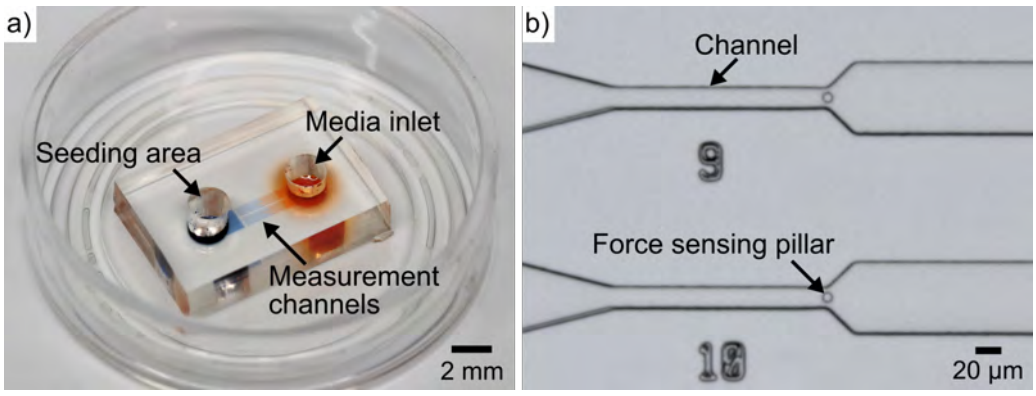


Figure 3.18: Fabricated mycelial platform chip for use with the fungus *N. crassa*. (a) Photograph of the entire chip bonded to a fluorodish. Colored liquid was used to visualize the channels. (b) Light micrograph of the PDMS chip showing two of the parallel measurement channels and force sensing pillars. Note: the hyphae grew from the left side to the right side of the channels in the image.

trial conducted for photoresist AZ 40XT, three different exposure doses (80, 90, 100 mJ/cm²) were trialed for AZ 15nXT resist spin-coated to a target thickness of 2.6 $\mu$m. Measuring channel width over multiple optical microscopy images, the results of the relationship between exposure dose and channel width were acquired. Figure 3.19 shows channel micrographs and the plot of the dose trial results for the photoresist AZ 15nXT. The narrow side before the pillar constriction connecting with seeding area was defined as Channel width 1 and the wide side after the pillar constriction connecting with media inlet was defined as Channel width 2 (see Fig. 3.19(a)). As expected for a negative-tone resist, both channel width 1 and 2 increased with increasing exposure dose from 53.9 $\pm$ 0.16 to 56.0 $\pm$ 0.14 $\mu$m and 14.0 $\pm$ 0.07 to 16.2 $\pm$ 0.26 $\mu$m, respectively, while in comparison the channel width 1 and 2 on the photomask were 55.0 and 15.0 $\mu$m, respectively. Therefore, an exposure dose of 90 mJ/cm² was chosen for subsequent fabrication of devices.

Appendix A.3 shows the relationship between the spin-coating speed of AZ 12XT with the pre-processed negative photoresist AZ 15nXT coated to a thickness of 2.6 $\mu$m as the first layer and the resulting total thickness of the measurement channels. In this arrangement the thickness of measurement channels decreased from 18.6 $\pm$ 0.26 to 10.2 $\pm$ 0.38 $\mu$m, while the speed of spin-coating increased from 1000 to 2000 rpm. As a result, the spin-coating speed of photoresist AZ 12XT was set as 1500 rpm for all further fabrication runs, achieving a total thickness of 13.7 $\pm$ 0.09 $\mu$m. An exposure dose trial with the positive photoresist AZ 12XT, ranging from 180 to 350 mJ/cm², was then carried out using channel patterns with both 5 and 7 $\mu$m diameter cavities. Figure 3.20(b & c) shows detailed images of the fabricated resist molds under increased exposure power taken with the microscope objective lens focused on the top and bottom of the resists. It was found that the AZ 12XT was not completely removed after development when exposed to the lower power UV light. At lower exposure doses of 180 and 220 mJ/cm² the widths of the channel outline also varied over the height of the resist, decreasing from top to bottom and indicating non-vertical side walls. Overall results of the dose trial for the photoresist AZ 12XT with 11 $\mu$m in thickness are plotted in Fig. 3.20(d). For both cavity patterns the diameter of cavities increased with increasing exposure dose from 5.4 $\pm$ 0.07 to 6.3 $\pm$ 0.07 $\mu$m for 5 $\mu$m cavities and from 7.9 $\pm$ 0.10 to 8.8 $\pm$ 0.05 $\mu$m for 7 $\mu$m cavities. Simultaneously, the width of the channel decreased from 13.3 $\pm$ 0.21 to 12.2 $\pm$ 0.07 $\mu$m. For comparison, the measured results on the mask were 14.7 $\mu$m in width, and 6.9 and 4.3 $\mu$m in diameter for the channel and cavities. The optimum exposure power for AZ 12XT for the *N. crassa* chips was thus set to 260 mJ/cm².

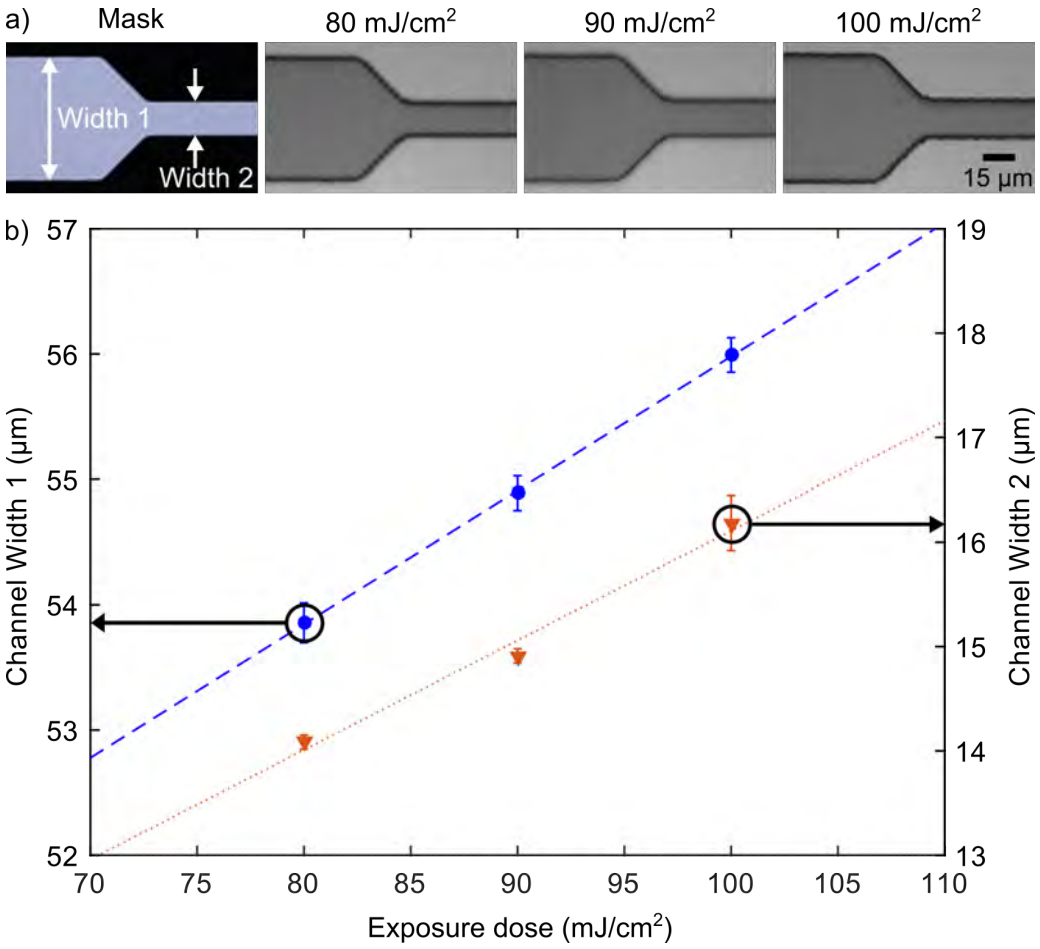


Figure 3.19: Dose trial results for the negative photoresist AZ 15nXT (115CPS) used for the first layer of the *N. crassa* chip with a thickness of 2.6 $\mu$m. (a) Light micrographs of the mask and resulting resist pattern in AZ 15nXT at exposure doses of from left to right 80, 90, 100 mJ/cm². (b) Plot of the channel width before (Channel width 1) and after (Channel width 2) the pillar constriction as a function of exposure power. The dots (blue) represent channel width 1, and triangle (orange) is channel width 2.

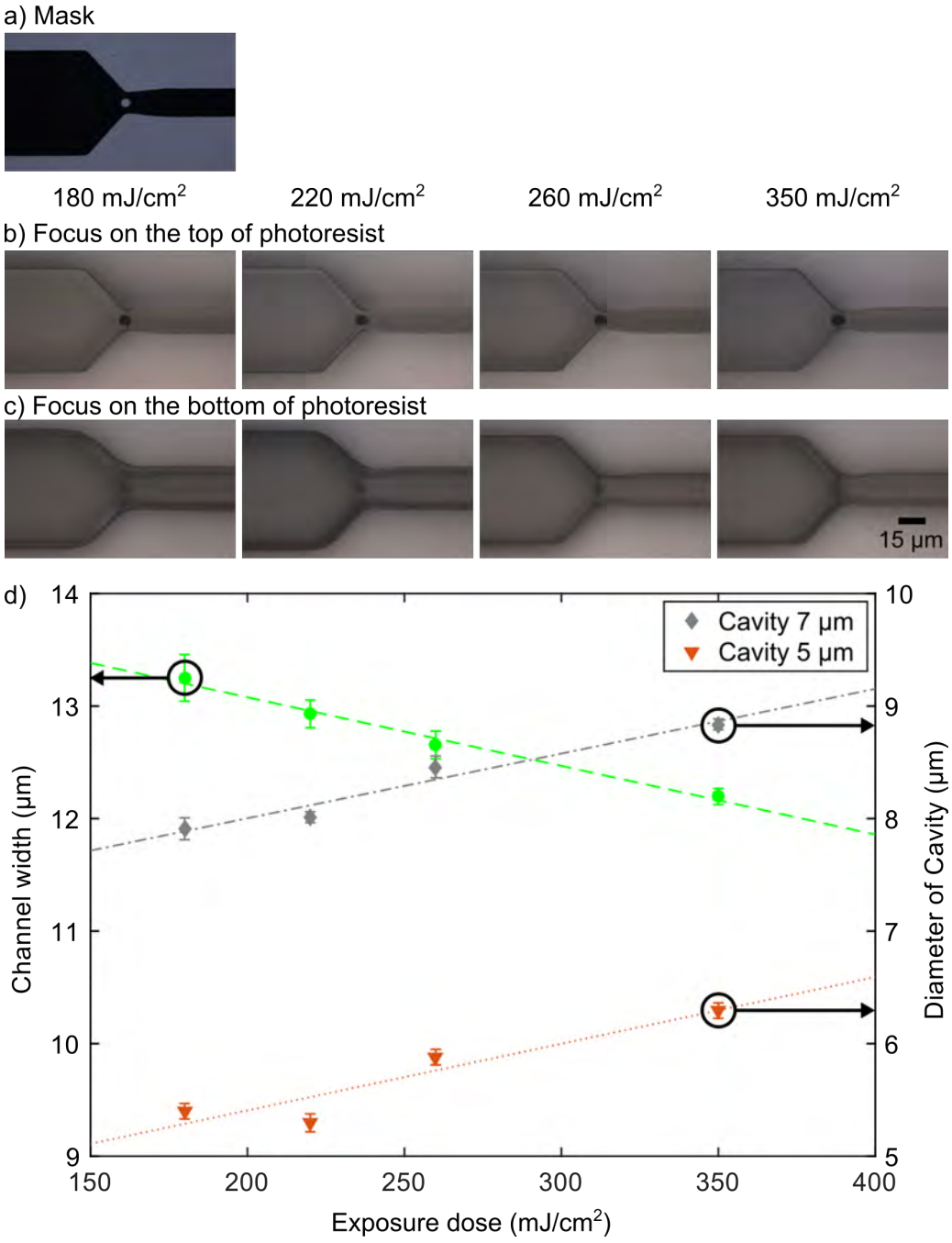


Figure 3.20: Dose trial results of the positive photoresist AZ 12XT for the *N. crassa* chips. (a) Light micrograph of the mask pattern. (b & c) Light micrographs of the resulting resist patterns using exposure dose from 180 to 350 mJ/cm². The microscope was focused on either the top or bottom of the resists. (d) Plot of dose trial results for the positive photoresist AZ 12XT. The dots (green) represent channel width, and diamond (gray) and triangle (orange) are cavities of 7 and 5 $\mu$m diameter, respectively.

### 3.3.2 Experimental setup and platform use with *N. crassa*

For use the fabricated microfluidic platform was promptly filled with sterilized Vogel's broth (containing [in % w/v] sucrose [1.5] and 2 mL of Vogels 50X salt solution) [134] once taken out from the sealed package. The fungus *N. crassa* was cultured on Vogel's agar media (containing [in % w/v] sucrose [1.5], agar [1.5] and 2 mL of Vogels 50X salt solution) for 24 hours at 26 °C. An inoculation plug of *N. crassa* (2.5 mm in diameter) was cut from the culture's growing edge and transferred to the mycelium seeding area of the platform. Hyphae were then observed regularly using microscopy during growth from the seeding area into the measurement channels. When the hyphae grew close to the force sensing pillars, pillar deflection by the tip of each hypha was recorded using the optical microscope and digital camera. As described previously, the force was calculated using a combination of image processing for tracking in ImageJ and force conversion in MATLAB.

Figure 3.21 shows an example of a force measurement on a single hypha of the fungus *N. crassa*, which was observed to grow out from the seeding area into a measurement channel and contact the force sensing micropillar. Force values recorded at each time-point were plotted in x- and y-directions, and as total force (see Fig. 3.22). For the example hypha shown, the Fx-component, which corresponds to the protrusive component, increased and reached a maximum of 8 $\mu$N. From the force vector plot

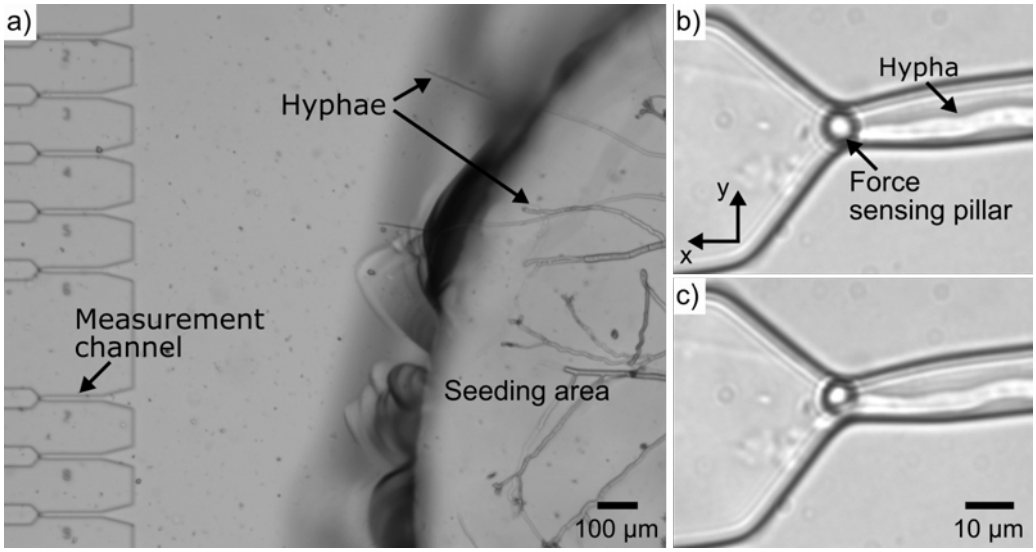


Figure 3.21: An example of a protrusive force measurement experiment on the fungus *N. crassa*. (a) Light micrograph of *N. crassa* hypha growing from the mycelium seeding area towards the parallel measurement channels. (b) Light micrograph of a single hypha impacting a force sensing pillar and (c) squeezing past after deflection.

in Fig. 3.22(b), it can further be observed how the direction of the applied force changed while the hypha interacted with the pillar, from initial tip contact to the hypha squeezing past the pillar. More experiments using the miniaturized platforms have been performed by other members of our group to evaluate the on-chip hyphal growth and forces generated by *N. crassa* [24, 134]. The results from 21 independent experiments showed *N. crassa* hyphae grew slower on the chips than on Petri dishes and 78 single hyphae impacted the force sensing micropillars. Additionally, because of their similar hyphal sizes to the fungus *N. crassa*, the pathogenic oomycete *Phytophthora* species, such as *Phytophthora nicotianae*, *Phytophthora cinnamomi* and *Phytophthora sojae*, have also been successfully studied on the miniaturized mycelial platform [137]. The growth rate and two types of forces, squeezing and tip deflection force, of 64 example hyphae were measured and quantified. In summary, through reducing all related dimensions of the mycelial platforms for the oomycete *A. bisexualis*, including the width and height of the measurement channels and force sensing micropillar diameter, the miniaturized platforms were demonstrated to be able to guide single fungal hyphae into the measurement channels and measure the forces exerted by these smaller sized hyphae.

## 3.4 Conclusion

This chapter has described the re-development and optimization of a lab-on-a-chip platform for use with mycelial samples of fungi and oomycetes. It combines single elastomeric force sensing micropillars in channel constrictions with organism maintenance structures, which enabled the first repeatable measurements of protrusive forces exerted by individual fungal hyphae. A combination of novel negative- and positive-tone photoresists was introduced to build an integrated mold with high-aspect ratio pillar cavities inside channel constrictions, and a vertical gap between the top of the micropillars and the channel lid for free bending. The fabrication process changes required to adapt the microfluidic devices from wider oomycete hyphae to thinner fungal hyphae were described. These included optimization of exposure dose for the novel positive photoresists, AZ 40XT and AZ 12XT, and negative photoresist AZ 15nXT processes, which are likely to be useful for other force-sensing and MEMS applications. Resulting from this, single free-bending micropillars of 7 $\mu$m diameter and 24 $\mu$m height were successfully fabricated in channel constrictions for the study of wider oomycete hyphae, while 5 $\mu$m diameter and 11 $\mu$m high micropillars were produced for the study of thinner fungal hyphae.

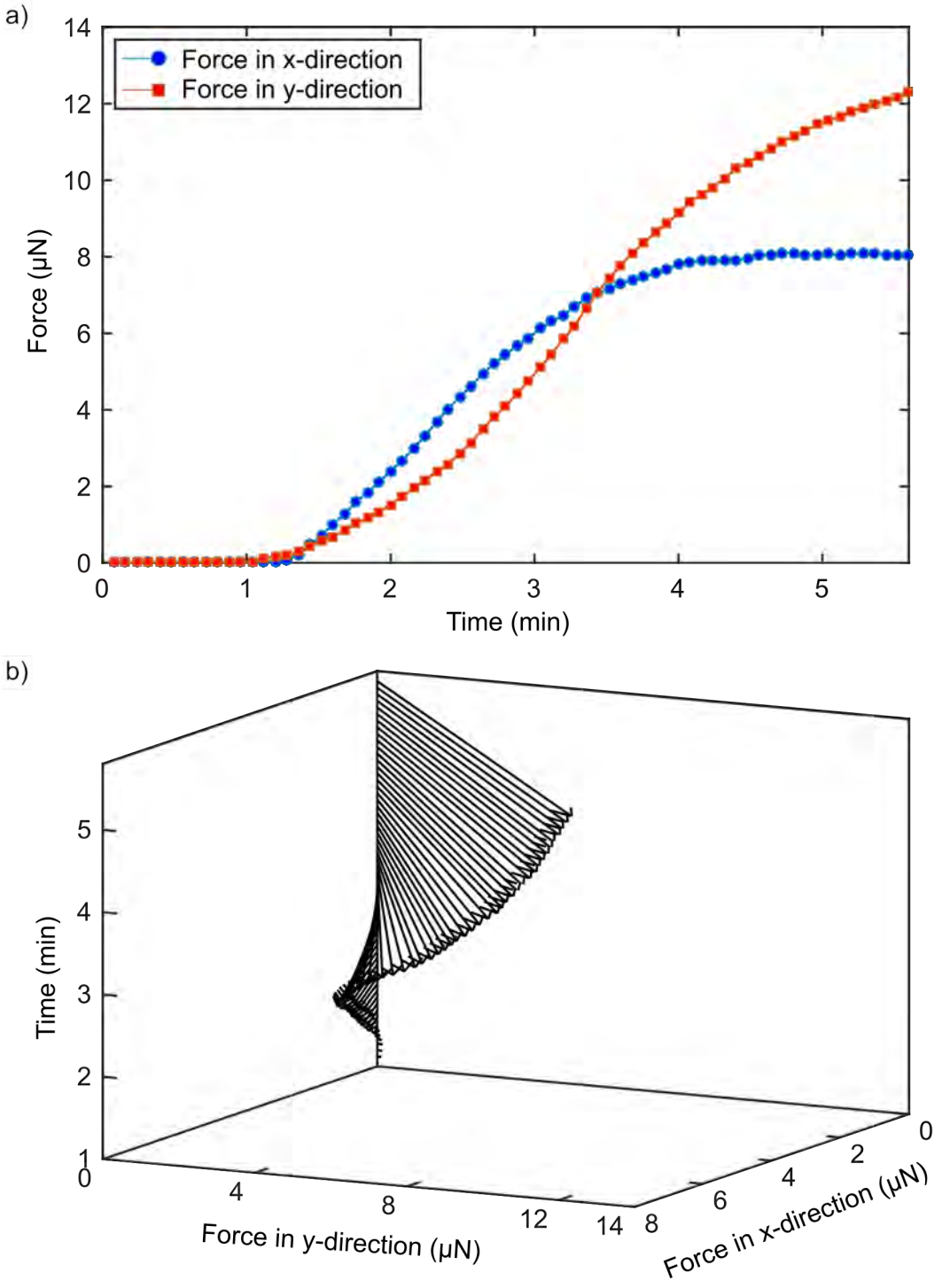


Figure 3.22: Results of the force measurement experiment on the fungus *N. crassa* shown in Fig. 3.21. (a) Plot of the force components in the x- and y-direction as a function of time. (b) Plot of the total force vector as function of time.

Finally, the applicability of the devices was demonstrated via the on-chip culture of the oomycete *A. bisexualis* and the fungus *N. crassa*. Single hyphae of both *A. bisexualis* and *N. crassa* were guided into the measurement channels for deflection of the force sensing pillars. The forces exerted by individual hyphae of these organisms were measured, and both force magnitude and direction were recorded as function of time. Both platforms have since been utilized to characterize the protrusive forces exhibited by single hyphae and the relationship between hyphal diameter and force magnitude in our lab [24, 133]. Additionally, the miniaturized mycelial platform is currently being used to study protrusive forces and cytoskeletal processes in oomycetes *Phytophthora infestans* and *Phytophthora palmivora* expressing LifeAct-eGFP in collaboration with Wageningen University, since their hyphal sizes are similar to fungus *N. crassa*. The platform will help to extend the understanding of mechanisms that underlie invasive growth and pathogenicity of these microorganisms.

# Chapter 4

# Monolithic Platform for Single Zoospore Capture, Germination and Single Germling Force Sensing

The following chapter describes the development of a microfluidic platform integrating zoospore capture with force sensing to enable high-throughput screening of the effect of compounds on hyphal parameters, such as growth rate and protrusive force generation of germling hyphae that germinate from the zoospores. The chapter begins by introducing existing platforms capable of single zoospore compartmentalization and their key components, hydrodynamic traps and microvalves. Following this, integration of zoospore traps and normally-open sieve microvalves with the force sensing pillars is demonstrated. The chapter concludes by showing the use of the devices for trapping and maintenance of individual zoospores of *A. bisexualis*, as well as the measurement of forces generated by germ tubes growing from these zoospores.

## 4.1 Background

Recent years have seen increasing efforts to screen naturally bioactive compounds and develop new biocontrol strategies as an alternative to agrochemicals [138]. Common to all these activities is the need to screen a large number of potential candidates for their impact on fungal and oomycete growth, as well as penetrative force generation at various stages in their respective life cycles. One such crucial stage is the germination of hyphae from either zoospores or conidia, leading to penetration into and infection of parts of a plant or animal [21]. In order to investigate the effect of cell-to-cell

variability and heterogeneity on hyphal germination/growth and protrusive forces of organisms, in-channel high-aspect ratio sensing pillars for protrusive force measurements on hyphal organisms [24, 133] had to be combined with zoospore trapping, on-chip germination and maintenance. Therefore, the design of modified platform needed to meet four criteria: (i) single zoospores or conidia needed to be able to be trapped from cell suspensions and reversibly immobilized at the entrances of parallel microchannels, (ii) traps needed to allow germinating germ tubes to grow into the individual channels for parallelized screening, (iii) the device needed to continuously provide nutrients to trapped cells for maintenance and analysis over long periods of time, (iv) the platform needed to enable the interaction of the resulting germ tubes with free-bending micropillars for protrusive force sensing. In the following section the components required to achieve this, and existing, comparable platforms, are briefly reviewed.

### 4.1.1 Hydrodynamic single cell trapping

Hydrodynamic trapping is the most commonly used technique to reversibly trap single cells at designated positions from a population of cells in microfluidic systems. The technique has fundamental advantages compared with optical, electrical or magnetic methods, including being simple to implement, enabling high throughput and being easy to integrate with other analysis functionalities [139].

Trapping arrays of U-shaped structures with 2 $\mu$m high gaps were proposed by Di Carlo et al. [140, 141] to culture and observe *HeLa* (human cervical carcinoma) cells. The gap provided an opening to a fraction of fluid carrying cells to enter each trap. Once a cell had been located within the trap this partial flow would be blocked by the cell and other cells would be carried around the occupied trap. Cell loading processes were able to be conducted in less than 30 s. In average, 85 % of *HeLa* cells could be maintained within the primary trapping site after 24 hours, and the rates of cell adhesion, division and death were comparable to control experiments.

Modified U-shaped structures with added narrow gaps were reported by the Cooper group, enabling trapping of cells in lower shear stress zones for time-lapse studies on hematopoietic cells and leukaemia [142, 143]. Computer simulations showed that the average shear stresses experienced by trapped cells were much lower than outside the trapping structures, achieving an over 90 % cell viability of histiocytic leukaemia cells after 24 hours of on-chip culturing.

More recently, U-shaped trapping arrays have been adapted for a range of different

applications. For instance, an array of each traps containing front and back side capture cups and support pillars on either side of the cups for cell pairing and fusion was presented by Skelley et al. [144]. It was demonstrated that the device could immobilize and properly pair thousands of cells at once, including several types of cells (*i.e.* fibroblasts) at a 70 % pairing efficiency. Platforms incorporating a U-shaped trap into the microchambers were designed for week-long clonal expansions of single cells [145, 146]. Single cells including fibroblasts, myoblasts and leukaemia cells were able to be captured by the traps and subsequently cultured in the large-sized microchambers for weeks.

To improve the efficiency of single cell capture, an approach based on different fluidic resistances in microchannels was firstly reported by Tan et al. [147], named as the $\mu$-Fluidic Trap. The platform consists of square-wave shaped loop channels superimposed onto a straight channel with constricted regions just before intersections acting as traps. It was designed so that the straight channel had a lower flow resistance than the loop channel, resulting in a particle carried into the trap by the main flow along the straight channel. Because the flow resistance of the straight channel drastically increased after trapping of a particle, the subsequent particles then flowed along the loop channel, passing by the filled trap to the next empty one. This concept was modified for the capture of mammalian cells [148], and even highly motile cells [149], by varying the dimensions of the microchannels. The trapping efficiencies for single lymphoma cells were demonstrated to be improved up to 97 %, with a high cell viability (over 90 %) and a minimization of cell loss. Furthermore, Frimat et al. proposed an adapted $\mu$-Fluidic Trap microfluidic platform for both homotypic and heterotypic single cell pairing and co-culture [150]. In this case, the traps in the straight channel were mirrored and interfaced by the sub-cellular-sized aperture. The second type cells were sequentially arrayed using reversal of the flow, obtaining a high cell pairing of 70 %. More recently, Chen et al. reported a single-cell migration platform integrated $\mu$-Fluidic Trap with narrow migration channel [151]. Using this platform, the chemotactic behavior of individual cancer cells could be specifically traced and delineated by positioning single cells at the entrance of each migration channel.

Although extensive hydrodynamic approaches to trap single mammalian cells have been developed for studies on comprehensive cellular heterogeneity, their application to tip-growing cells germinating from spores remains limited [86]. One particular challenge for the design of platforms for tip-growing cells is that a spherical/oval spore needs to be trapped so that the resulting germ tube can elongate and be exposed to a variety of analysis. Agudelo et al. developed an experimental platform,

named TipChip, enabling efficient and high-throughput large-scale phenotyping of pollen tubes [107, 152]. The device allowed suspended pollen grains to be transported through a distribution chamber, after which they were positioned at the entrances of the microchannels. These channels guided pollen tubes growing from the grains along and exposed elongating tubes to a variety of mechanical obstacles and constraints. After pollen grains were trapped, the culture medium could be set to continuously flow in to maintain a nutrient-rich environment, while keeping grains trapped at the entrances of the microchannels by fluid pressure. The device was later modified to implement an on-chip bending test for the investigation of biomechanical properties of pollen tubes [153]. To achieve this, the growing pollen tubes were guided through a short microchannel and subsequently exposed to a bending force by the fluid flow orientated perpendicular to the tubes. Ghanbari et al. further improved the TipChip platform to achieve the trapping of exactly one and not more pollen grains at the entrance of each microchannel [108]. Improvements also guaranteed identical fluid flow conditions in all microchannels for more comparable pollen tube growth.

Apart from the many advantages, one major intrinsic limitation of flow-assisted cell trapping is that the trapped cells have to be constantly exposed to the fluid flow for immobilization. While this helps with nutrient supply, shear stresses applied to the cells pose the risk that trapped cells are mechanically compressed, which may alter biological responses such as cell growth and viability [154, 155]. On the other hand, if the applied fluid pressure is kept low to avoid shear stress related experimental artefacts, cells may escape during long-term culture, resulting in a relatively poor position accuracy or ultimately cell loss. For the work presented in this thesis, trapped single zoospores or conidia needed to be physically confined so that their individual germinating germlings could be guided to grow in the direction towards force sensing micropillars, while not affecting neighbouring ones. Therefore, it was required that a microfluidic trapping system could be integrated with a long-term culture method and sequentially compartmentalized for single zoospores/conidia growth analysis and protrusive force measurement of germ tubes. Microvalves are the natural choice for enabling such active compartmentalization and will be introduced in the next section.

### 4.1.2 Microvalves for on-chip cell culture

Passive compartmentalization approaches such as microfluidic droplets or microwells, elaborated in Section 2.4, allow for high throughput, controllable sample/reagent volumes, long culture periods and simple fabrication for encapsulation of single cells.

However, they are not easily integrated with the force sensing module used in this thesis, where hyphae grow along microchannels and contact with the free-bending measurement micropillars inside these channels. Thus, an alternative method for active compartmentalization after trapping was sought. Microvalves, which allow one to control routing, timing, and separation of fluids with fast response [156, 157], were thus investigated. Among various actuated sources of microvalves (*i.e.* electrokinetic, pneumatic, phase change [158]), pneumatic microvalves are preferentially used in microfluidic devices because of the ease of integration with standard soft lithography processes and simple system setup.

These types of valves were first reported by the Quake group and initial valves were formed by a crossed-channel architecture using a multilayer soft lithography technique [159]. When the pressure was applied to the upper channel (control channel), the membrane of polymer between two channels deflected downward, resulting in the closure of the lower channel (flow channel). Due to the valves closing after actuation, these valves are commonly referred to "Normally-open" membrane valves. To guarantee reliable and complete valve closure, a round cross-section is required for the flow channel. If operated into a flow channel of rectangular cross-section, incomplete deflection of the membrane into the channel corners causes fluid leakage, leading to this arrangement being termed "sieve-valve" [159]. Despite of or because of this leakage, sieve valves are typically only used to control the movement of larger particles in solution, which cannot bypass the constriction and are thus "sieved" [160]. Using pneumatic valves, large-scale integration and complex fluid manipulations with a minimal number of inputs by plumbing networks were demonstrated [161, 162]. More recently, the Quake valve was modified to reduce the actuation pressures required and increase the aspect-ratio of fluidic channel geometry (height:width, from 1:10 to 1:2) by switching the vertical position of the flow and control channels [163, 164]. As opposed to the previous version of the valve, in this version the membrane pushes up to seal off the flow channel and is thus called a "push-up" valve. Also, unlike in the previous version, where the thickness of membrane varied from the edge of the channel to the middle, the membrane of the modified valve was uniform and featureless, which made the complete closure independent from the depth of the fluid channel. Because of its ease of integration with both particles (cells) and liquid (reagents), the "push-up" membrane valve has been widely used for protein separation [165], batch culture of bacteria [166], migration of human T cells [167], colony expansion of hematopoietic stem cells [168], and whole genome amplification of cancer cells [169].

With increasing attention on single cells analysis, the normally-open membrane valves have further been adapted to help isolate single cells for subsequent analysis [170, 171].

Xu et al. demonstrated a microfluidic device for single cell targeted gene mutation analysis [171]. Cells in normal saline buffer were injected into a microchannel, and microvalves were closed to separate single cells from subsequent cells, followed by the single cell moving through the valves. However, due to limitations on cell density in the suspension and flow rate of cell introduction, this approach to isolate/trap single cells has proven time-consuming and of limited throughput. To address these issues, microfluidic platforms combing normally-open valves with hydrodynamic single cell trapping techniques were developed [172–175]. Chen et al. reported an integrated system to rapidly measure gene expression in individual cells for genetic stability assessment [173]. Single cells were trapped in a U-shaped sieve structure in each capture chamber, then pushed out of the traps and addressed to one of the reaction chambers by guidance of a series of microvalves. The device was used with cancer cells and immortalized cells, achieving 95 % occupancy of single cells in 1 min at a cell loading concentration of $5 \times 10^5$ cells/ml. Another successful case is the commercial product C1 system (Fluidigm Corporation.), which provides the first automated solution for single-cell genomics, including fluidic isolation of cells, staining, microscopy, lysis and qPCR preparation [176].

### 4.1.3 Microfluidic platform for single tip-growing cell analysis

The second component required for single zoospores/conidia trapping and germ tube protrusive force measurement is the tip-growth analysis part. Recently, several studies have reported parallelized manipulation and analysis of single tip-growing cells by applying single cell trapping and microvalving methods [109, 177]. The integrated microfluidic platform developed by Geng et al., as mentioned in previous Section 2.4, allowed single conidia to be trapped, from which individual germlings grew in separated channels for comparative germ tube growth and dynamics analysis [109]. A single normally-open microvalve located on a serpentine cell loading channel with rounded cross-section was utilized to compartmentalize conidia after hydrodynamic trapping. Germ tubes resulting from each conidia were prevented by this valve from extending into the cell loading channel, while compartmentalization allowed each to be exposed to equivalent environments. Although the device achieved a trapping efficiency of up to 70 %, it suffered from the accumulation of multiple cells in single trapping sites. More recently, Hu et al. presented a device for the characterization of mechanical properties of tip-growing cells in the form of pollen tubes [177]. In this case, the pneumatic membrane valves were not only used to fix pollen tubes inside the

chip, but also to exert a controlled uniform external pressure on the tubes acting as a form of soft indentation probe. The soft compression using the membrane produced a distributed force along a large area, allowing for the detection of averaged mechanical properties. The experimental results indicated that the compressibility and stretch ratio increased considerably with increasing initial diameter of pollen tubes.

Despite the number of existing platforms for tip-growing cell studies, reports that comprehensively integrate trapping with characterization and sensing methods for invasive growth forces on single tip-growing cell levels remain limited. The PDMS microchamber array, which has been described in Section 2.4, was developed as a force sensor for single cells of rod-shaped fission yeast by analysis of the growth of cells and deformation of the chamber [112]. However, similar to other microwell devices, placement of single cells into each microchamber was time-consuming and difficult to reliably replicate, as cells were pushed into the chambers by slightly pressing a glass coverslip onto them. Similarly, the adapted TipChip device was developed for penetrative forces exerted by pollen tubes, via measuring the deformation of the sidewalls of moderate-sized gaps when tubes passed through the narrower gaps [113]. Nevertheless, while cells were exposed to continuous flow during the measurement, the elongating tubes may be pushed backwards by the force of hitting the sidewalls of the narrow gaps, which may affect the results of the force measurements. Finally, in terms of the lab-on-a-chip device combined with capacitive force sensor [114], because the pollen grains were randomly loaded in the reservoir, the tubes grew in a disorderly manner into the microchannel, potentially cross-contaminating measurements.

To overcome some of the limitations of the existing platforms described above, a new platform combining force sensing micropillars with single zoospore trapping, on-chip germination and organism maintenance was designed as part of this thesis. As described below, the platform monolithically integrates hydrodynamic trapping with microvalve-based compartmentalization and micropillar-based force sensors. Immobilization and on-chip culture of cells were realized using the techniques of hydrodynamic single cells trapping and normally-open membrane valves. In the remainder of this chapter the design and fabrication processes of a three-layer PDMS device are described, as is the characterization of the normally-open microvalves. Finally, the applicability of the platform is demonstrated by the introduction and capture of individual zoospores of the oomycete *A. bisexualis*. Zoospores are cultured on the device and the microNewton forces exerted by germ tubes measured by tracking the deflection of elastomeric micropillars. The platform allows for high-throughput compartmentalization of individual zoospores or conidia into separate force measurement channels for parallelized screening, taking into account cellular heterogeneity, nuclear

distribution and dynamics at the individual hyphal level in response to exposure to various biocontrol strategies.

## 4.2 Materials and methods

### 4.2.1 Microfluidic platform design

The microfluidic platform was devised to consist of two PDMS layers, a gas control and a fluidic layer, separated by a PDMS membrane of 15 $\mu$m thickness, as shown in Fig. 4.1. The gas layer on the top contains a 200 $\mu$m wide and 50 $\mu$m high microchannel connecting with a gas inlet, which allows for on-off control of the microvalve via pressurization. The fluidic layer on the bottom is composed of parallel measurement channels, integrated with a zoospore trap-site close to the entrance and a freely bending elastomeric micropillar as a force sensor in each channel. Measurement channels connect with a zoospore loading channel on one side and a media supply channel on the other side, both 30 $\mu$m in height. The width and height of measurement channels were set to 35 and 30 $\mu$m, respectively.

Figure 4.2 shows the principle design of the device and membrane microvalve operation. A series of zoospores are introduced from the zoospore inlet, flow along the loading channel and are captured in the trap sites one after another when the zoospore and media outlets are open. After all the trap sites are occupied, the zoospore inlet is closed and gas is injected into the gas layer to shut off the sieve microvalve located on the right above the zoospore loading channel, preventing trapped zoospores from escaping. Zoospores are cultured through germination until germ tubes appear. The germ tubes germinated from trapped zoospores then grow through the measurement channels and deflect the force sensing pillars, while media continues to be supplied from the media inlet.

Two types of constriction structures were designed for the trap-site to investigate the capability of single zoospore capture (see Fig. 4.3). Because the diameter of *A. bisexualis* zoospores ranges from 10 to 15 $\mu$m, the constriction width, where the channel width is reduced, was set to 8 $\mu$m. Constriction type A has constrictions in both the horizontal and vertical directions (8 $\mu$m in width and 5 $\mu$m in height), while type B is a horizontal-only constriction (30 $\mu$m in height, which is the same as the other region of the measurement channel). The width of zoospore loading channel was varied between 60, 120 and 180 $\mu$m to optimize the closing function of membrane valve.

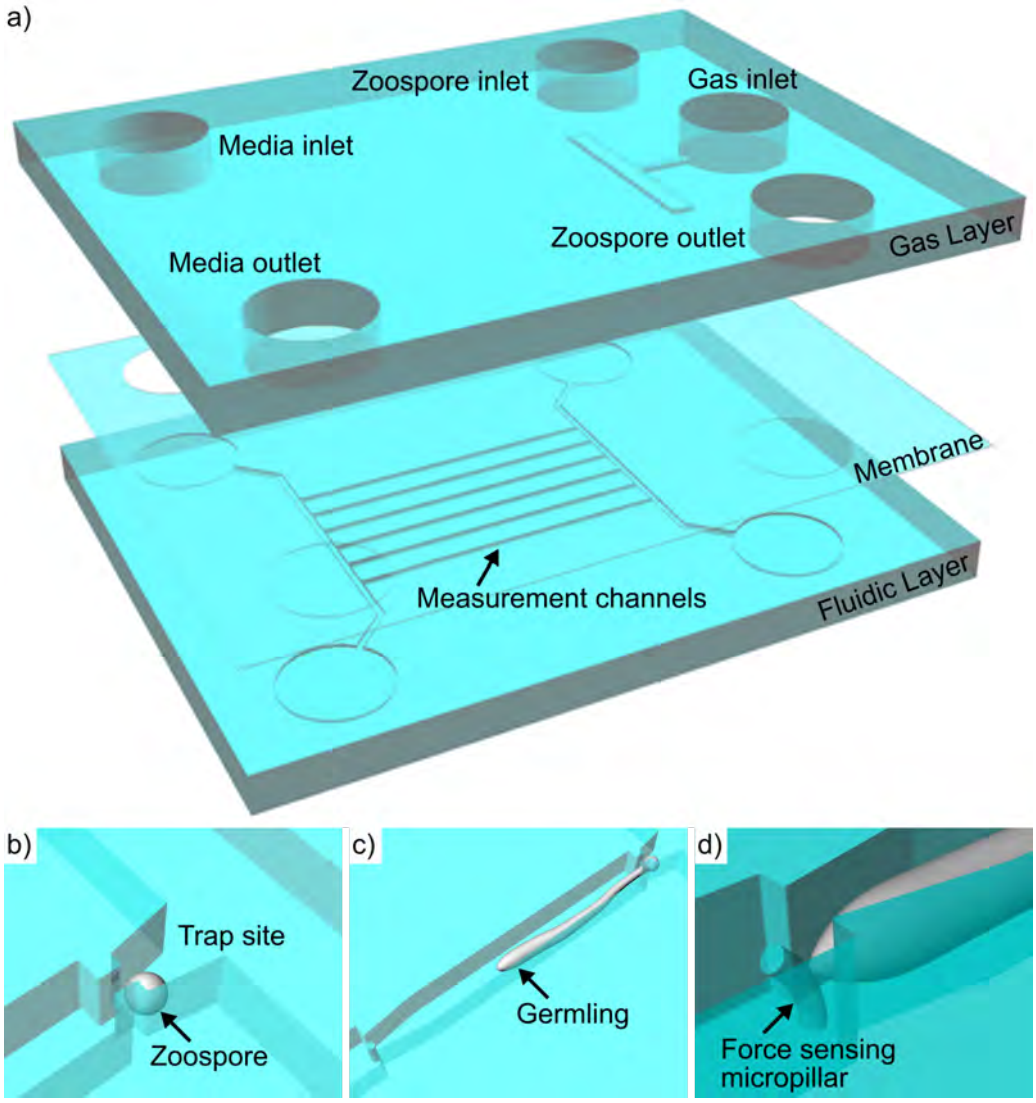


Figure 4.1: Concept design of modified microfluidic platform for zoospore capture, germination and germ tube force sensing. (a) Entire chip showing the geometry of device including two PDMS layers and a PDMS membrane. (b) Detailed view of the measurement channel in the fluidic layer while a zoospore flows into and is captured by the trap site. (c) Detailed view showing a germling developing from a zoospore growing in the measurement channel. (d) Detailed view showing the germ tube hitting the force sensing micropillar which causes the pillar to bend, enabling determination of the applied force.

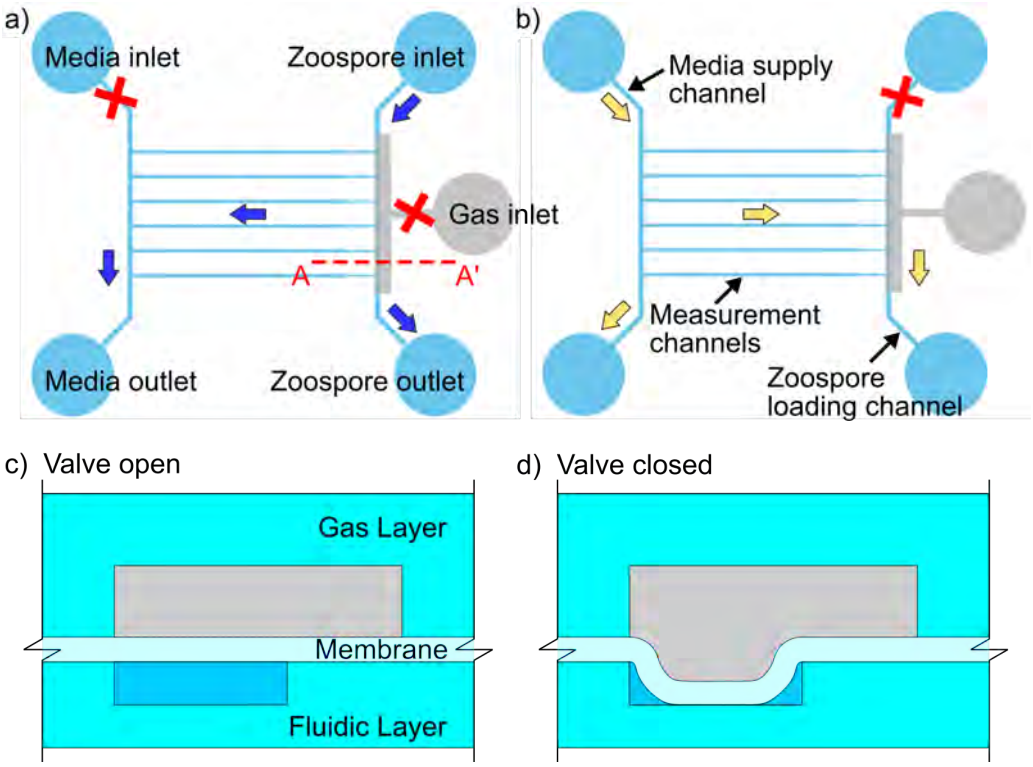


Figure 4.2: Schematic diagram of the fluidic microchannels and the membrane microvalve showing the operating principle of the device. (a) Microchannel design of the gas layer (gray) and the fluidic layer (blue). The gas inlet and media inlet are closed while zoospores are introduced. (b) After trapping of zoospores the microvalve is closed by pumping air into the gas layer and the media is supplied from the media inlet while the zoospore inlet is closed. (c) and (d) Cross-section through A-A' during zoospore introduction (microvalve is open) and zoospore maintenance (microvalve is closed).

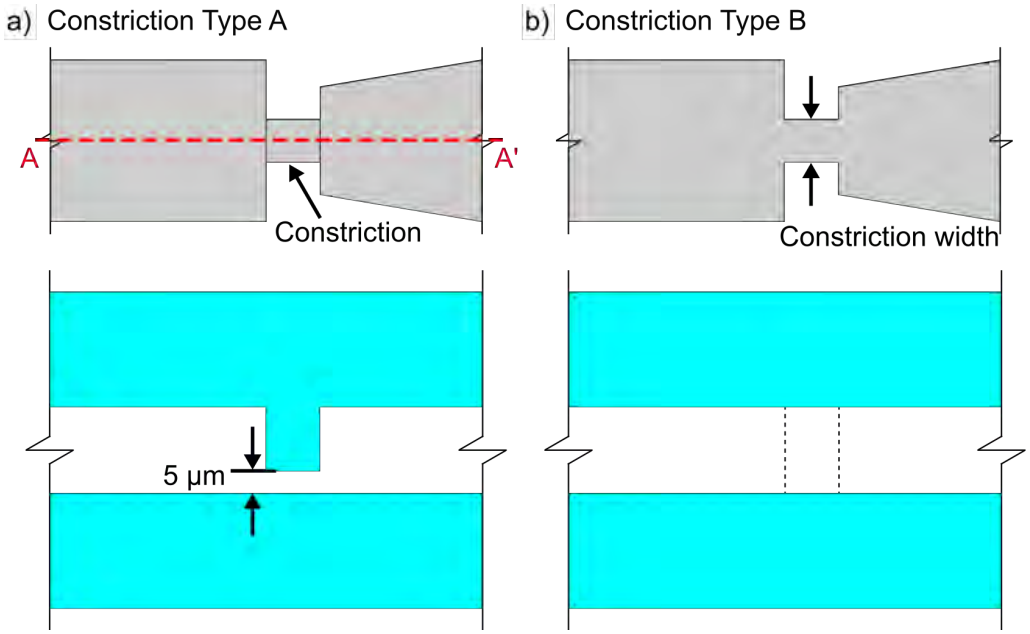


Figure 4.3: Schematic diagram of the two types of constriction structures A and B in the measurement channels and their A-A' cross-sections. (a) Type A, both horizontal and vertical constriction (8 $\mu$m in width and 5 $\mu$m in height). (b) Type B, horizontal constriction only (8 $\mu$m in width and 30 $\mu$m in height).

### 4.2.2 Fabrication of microfluidic chip

The PDMS chips containing either the gas or fluidic layer were fabricated by replica-molding of photoresist masters and bonded via a thin PDMS membrane. We utilized the same fabrication processes protocol, as described in Section 3.2.1, to produce a two-layer photoresist master for the fluidic layer by combining negative (ADEX05) and positive (AZ 40XT) photoresist. In brief, two photomasks were designed for the two-layer photoresist master using Tanner L-Edit software (Mentor Graphics), and manufactured using a micro pattern generator ($\mu$PG101, Heidelberg). The first-layer mask for the negative photoresist contained the outline of channels and constriction structures inside channels (see Appendix B.1), while the second-layer mask for the positive photoresist had additional features of micropillar cavities and vertical obstacle for constriction type A. Next, a 4" silicon wafer was coated with 5 $\mu$m thick negative photoresist ADEX 05 by lamination at 65 °C, followed by dehydration and pre-cleaning of the wafer. The photoresist was exposed at a power of 170 mJ/cm² using the first-layer photomask and short wavelength filter, and post-baked by ramping up at 100 °C/hour to 65 °C (5 min) and 95 °C (10 min) on a programmable hotplate. The wafer with the first-layer pattern was developed in cyclohexanone for 5 min, rinsed with IPA and dried by $N_2$. Then, the positive photoresist AZ 40XT was spun on the

wafer at 500 rpm for 20 s and 2000 rpm for an additional 30 s, edge-bead removed, and soft-baked at 126 °C for 3 min, achieving a thickness of 25 $\mu$m for the second layer. After exposure at 250 mJ/cm² using the second-layer mask, the wafer was heated to 105 °C for 80 s on a hotplate. The two-layer master for the fluidic layer, as shown in Fig. 4.4, was completed by 3 min development with developer AZ 326MIF, rinsed with IPA and dried with $N_2$. Figure 4.5 shows detailed views of the fabricated photomasks for the two layers, as well as the photoresist master with constriction type B. Since the channels only shrink in the horizontal direction for constriction type B, the constriction feature in the second-layer in the photomask was the same as that of the first-layer.

For the gas layer master, standard photolithography processing was used, as shown in Figure 4.6 step 1-4. A 4" chrome-on-glass photomask containing the gas layer pattern was prepared using the $\mu$PG101. A 4" silicon wafer was dehydrated in a 185 °C oven for over 2 hours and cleaned by oxygen plasma for 10 min at 100 W. Then, a dry film negative photoresist, ADEX 50 (thickness 50 $\mu$m, DJ DevCorp), was laminated onto the pre-cleaned Si wafer at 65 °C. This was exposed using the gas layer mask in the UV lithography system at an exposure dose of 325 mJ/cm² in low-vacuum contact mode with the short-wavelength exclusion filter. Following this, the wafer was developed in cyclohexanone for 20 min, rinsed with IPA and dried by $N_2$. Finally, it was post-exposure baked by ramping (100 °C/hour) to 65 °C (5 min) and 10 min at 95 °C on a programmable hotplate. The master mold of the gas layer was completed via a hard-bake at 150 °C for 1 hour, as shown in Appendix B.1.

Both PDMS chips of the gas and fluidic layer were molded into Sylgard 184 silicone elastomer (10:1 w/w). The two master molds were treated by vapour-coating with TFOCS in a desiccator for 30 min to facilitate mold release. Pre-mixed and degassed PDMS was then poured onto the treated molds and degassed for an additional 30 mins until all bubbles had disappeared. After a 2 hour bake at 80 °C on a hotplate, the PDMS chips were peeled off carefully. Meanwhile, a 4" silicon wafer was dehydrated at 185 °C in an oven for over 2 hours, cleaned by acetone, IPA and then treated by vapor-coating with TFOCS in a desiccator for 30 min. Pre-mixed (10:1 w/w) and degassed PDMS was spin-coated onto the pre-treated Si wafer by a spin-coater (WS-650, Laurell) at 3000 rpm for 30 s, achieving an average thickness of 17 $\mu$m. The PDMS membrane was cured via a 2 hour bake at 80 °C.

The two PDMS chips and thin membrane were assembled by oxygen plasma bonding (Tergeo, PIE Scientific). The gas inlet port was punched into the gas layer using a 1.0 mm diameter biopsy punch. Both the gas layer and membrane still on the silicon wafer were plasma treated (5 sccm $O_2$, 15 W, 1 min), bonded together, and baked

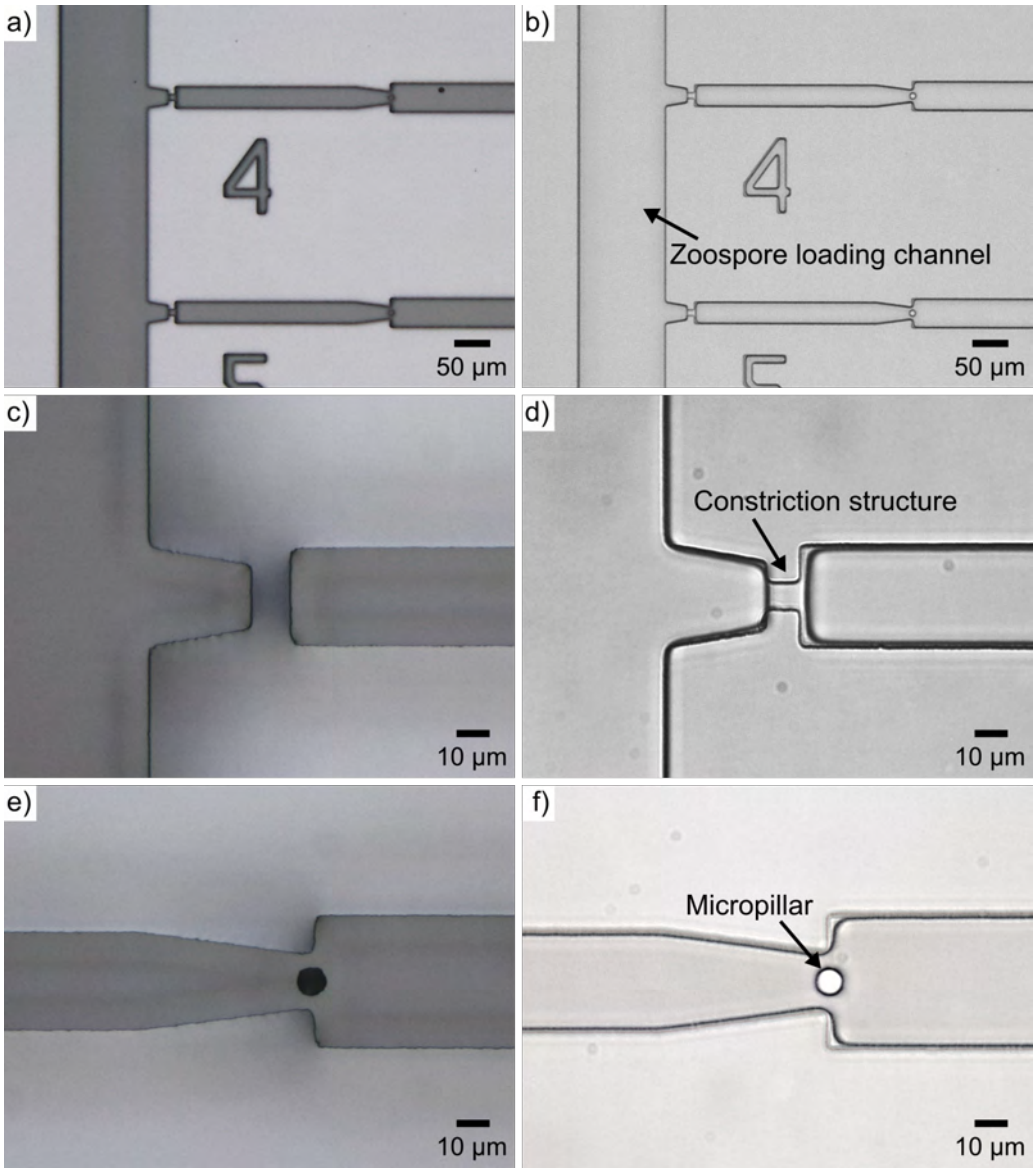


Figure 4.4: Light micrographs of fabricated photoresist master mold and PDMS chip for the fluidic layer with constriction type A. (a) Master mold of the fluidic layer including 120 $\mu$m wide zoospore loading channel and measurement channels patterned by negative photoresist ADEX 05 as first layer and positive photoresist AZ 40XT as second layer. (c & e) Detailed view of the constriction structure and micropillar cavity of the dual-layer photoresist master. (b, d and f) PDMS chip of the fluidic layer, detailed constriction structure and force measurement micropillar.

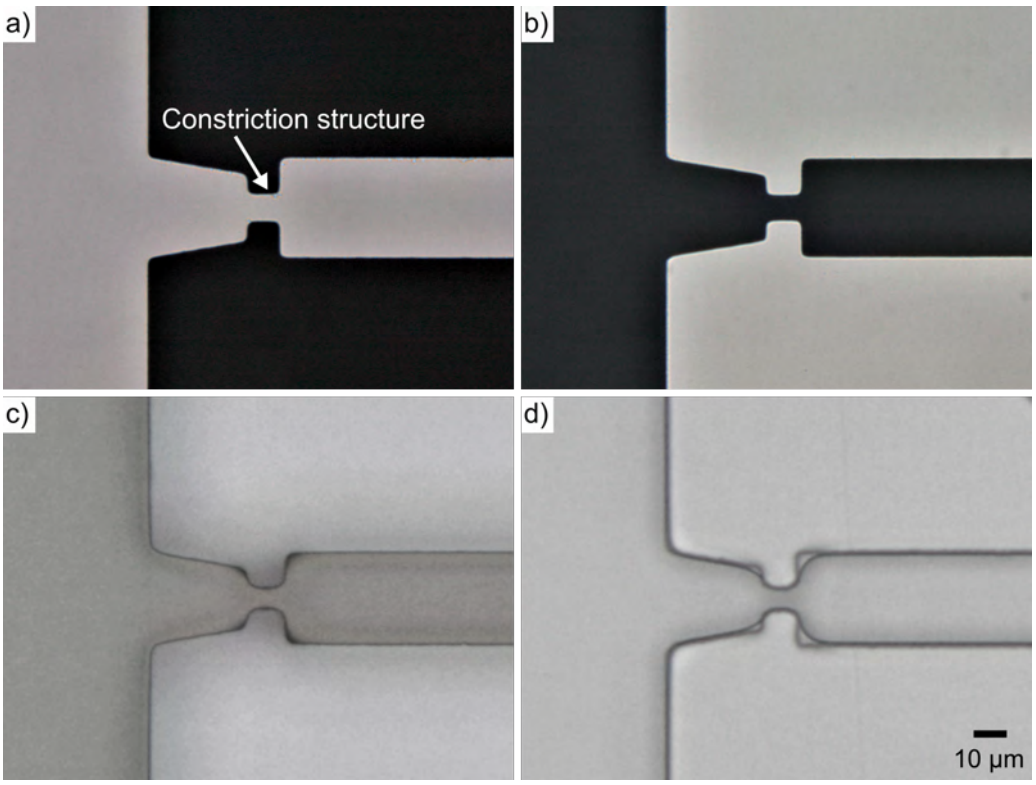


Figure 4.5: Light micrographs of fabricated photomasks, photoresist master mold and PDMS chip of constriction type B. (a & b) Detailed view of photomasks of first and second layers of the constriction structure. (c) and (d) Detailed view of photoresist master mold and PDMS chip of the vertical-only constriction structure.

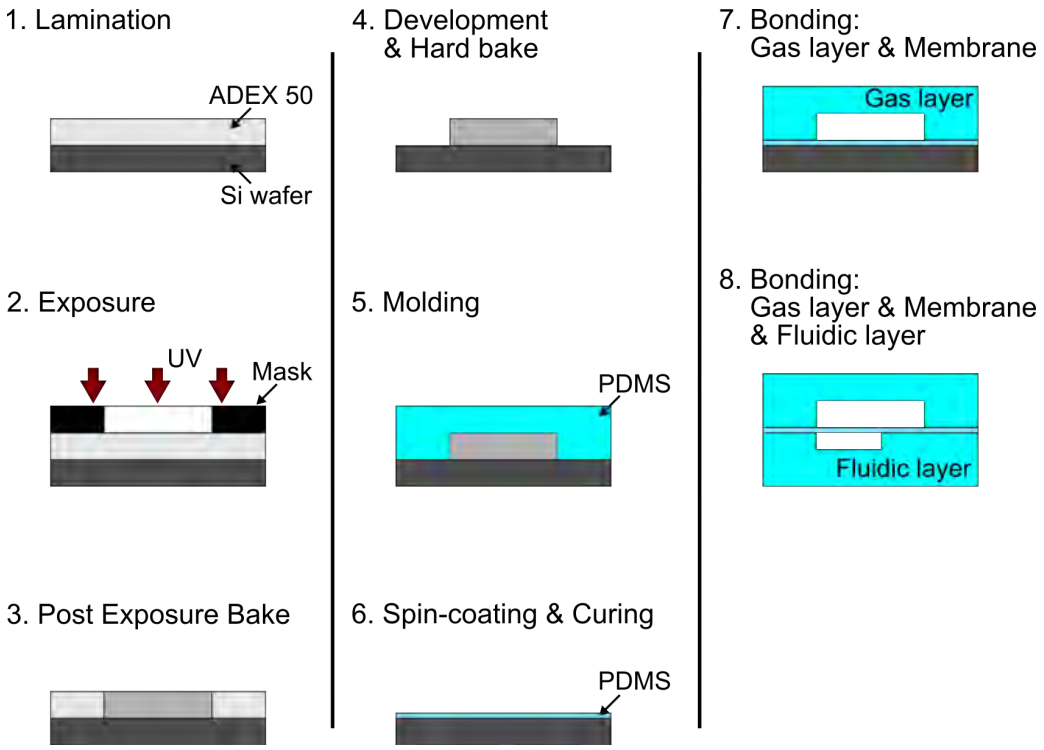


Figure 4.6: Fabrication processes of the gas layer photoresist master using standard photolithographic methods (Steps 1-4). Steps 5 and 6, PDMS casting of two chips and spin-coating of the thin PDMS membrane. Steps 7 and 8, device assembly. The gas layer chip was first bonded onto the PDMS membrane, and carefully peeled off from the silicon wafer together with the attached thin membrane. Finally, the fluidic layer chip was manually aligned and bonded to the PDMS membrane with the gas layer attached on the opposite side.

for 2 hours at 80 °C. Then, the gas layer bonded with membrane was peeled off carefully from the silicon wafer. Similarly, after punching of the zoospore and media inlet/outlet ports on the gas layer, the fluidic layer and membrane with gas layer were plasma treated (5 sccm $O_2$, 15 W, 1 min), manually aligned and bonded together. The LOC device was completed after a 2 hour bake at 80 °C on a hotplate. Notably, all PDMS alignment steps during the device assembly were performed using a customized alignment stage built specifically for PDMS chips [178]. This stage included back illumination, a XY-stage with rotation (THORLABS,Inc.) as bottom layer holder, a glass holder for the top layer and a digital microscope (Dino-lite, AnMo Electronics Corporation) connected to a PC and as shown in Fig. 4.7. For alignment the gas layer bonded to the thin membrane was placed on glass and slid into the top layer holder. By adjusting the position of the fluidic layer on the bottom layer holder the two chips were aligned under the microscope and then brought into contact. The bonding process was then completed via baking. Figures 4.7 (c-e) show two chips being aligned using the alignment marks under the illumination from top, back and both. As can be seen, the light from bottom provided better contrast for PDMS alignment, and the alignment error could be reduced to within $\pm 10$ $\mu$m this way. As a last fabrication step, assembled devices were degassed for 1 hour in a vacuum chamber to improve filling with media and sealed into food-grade vacuum bags using a vacuum sealer for storage. As shown in Figure 4.8, using the above protocol high-aspect ratio, in-channel force sensing micropillars were successfully integrated with hydrodynamic traps on a monolithic PDMS valving platform. The three-layer prototype device contained six parallel measurement channels, each made of a trap and sensor pillar, while a single large valve closes off the zoospore inlet channel and thus all the measurement channels. In the next section the procedure to induce *A. bisexualis* zoospores for introduction to the platform will be described.

### 4.2.3 *Achlya bisexualis* zoospore induction procedure

*A. bisexualis* zoospores were produced through a starvation cycle [179]. A nappy liner (Asaleo Care Limited) was cut slightly smaller than the diameter of a Petri dish, boiled 3 times for 10 min each in distilled water, and autoclaved. It was then placed carefully on PYG agar in a Petri dish (containing [in% w/v] peptone [0.125], yeast extract [0.125], glucose [0.3], and agar [2]). Six inoculum plugs from a fresh culture growing edge of *A. bisexualis* were cut on a 45° angle to reduce the amount of media transferred across. The inoculation plugs were evenly spread around the plate on the nappy liner, as shown in Fig. 4.9(a). After incubation at 26 °C for 24 hours, the nappy liner with the

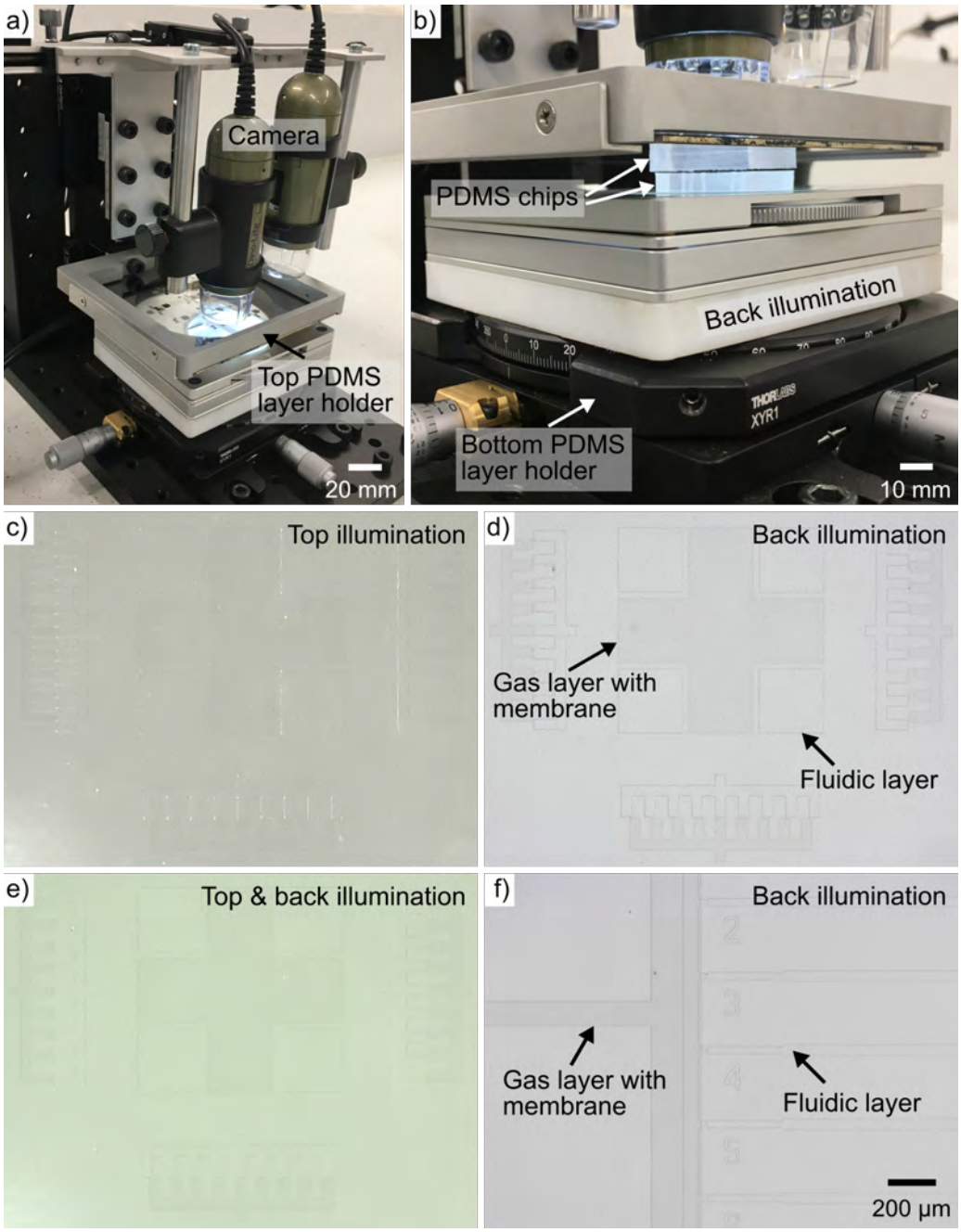


Figure 4.7: (a) and (b) Photographs of the customized stage for PDMS chip alignment during device assembly, including a back illumination light source, a XY-stage with rotation as bottom layer holder, a glass holder for top layer and a digital microscope. (c-e) Light micrographs of the alignment mark of two PDMS chips after alignment under top, back and top & back illumination. (f) Light micrograph of aligned gas layer and fluidic layer in the microvalve area under back illumination.

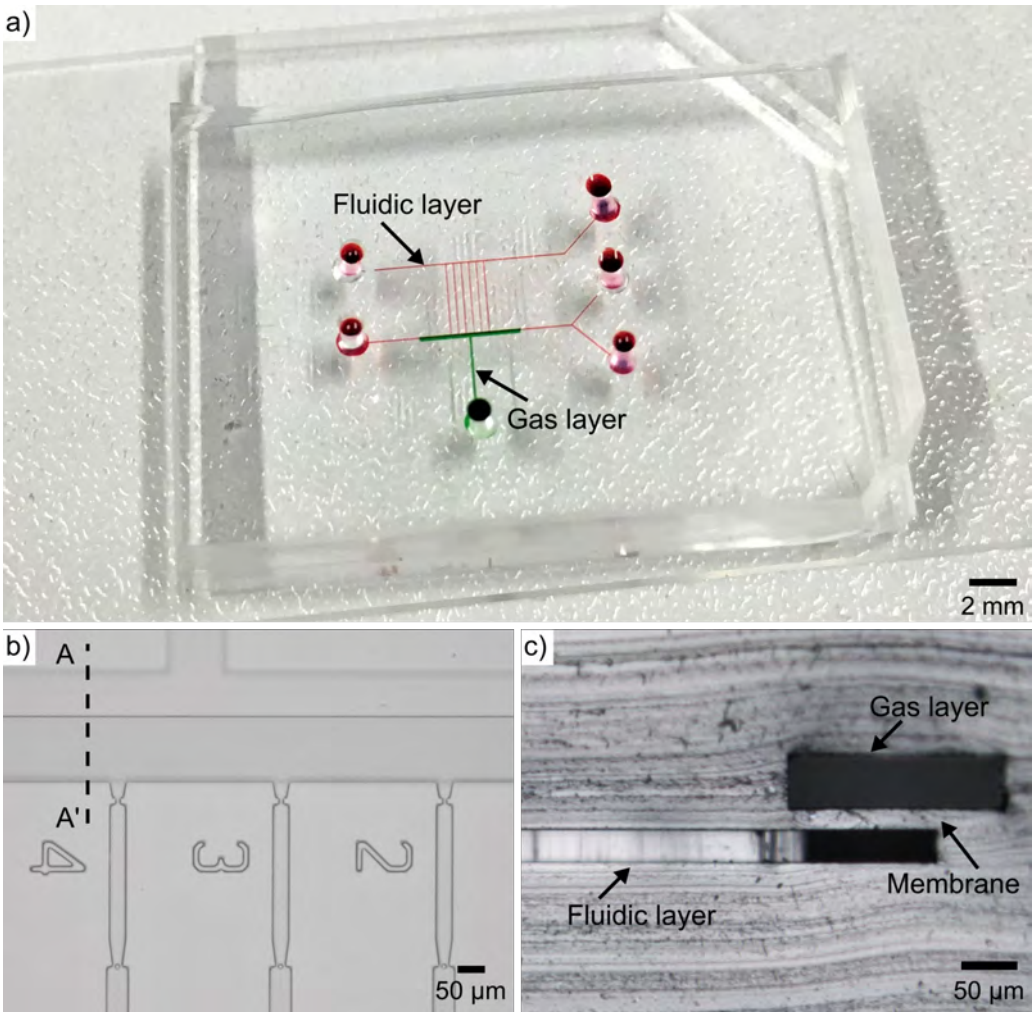


Figure 4.8: Fabricated PDMS platform. (a) Photograph of the monolithic PDMS platform on a glass microscope slide filled with colored liquid (red coloring for the fluidic layer, green for the gas layer). (b) Light micrograph of assembled platform containing six parallel measurement channels with a trap and force sensing micropillar, and a single large membrane valve above the zoospore loading channel. (c) Light micrograph of cross-section through A-A' showing the three layer structure of the platform.

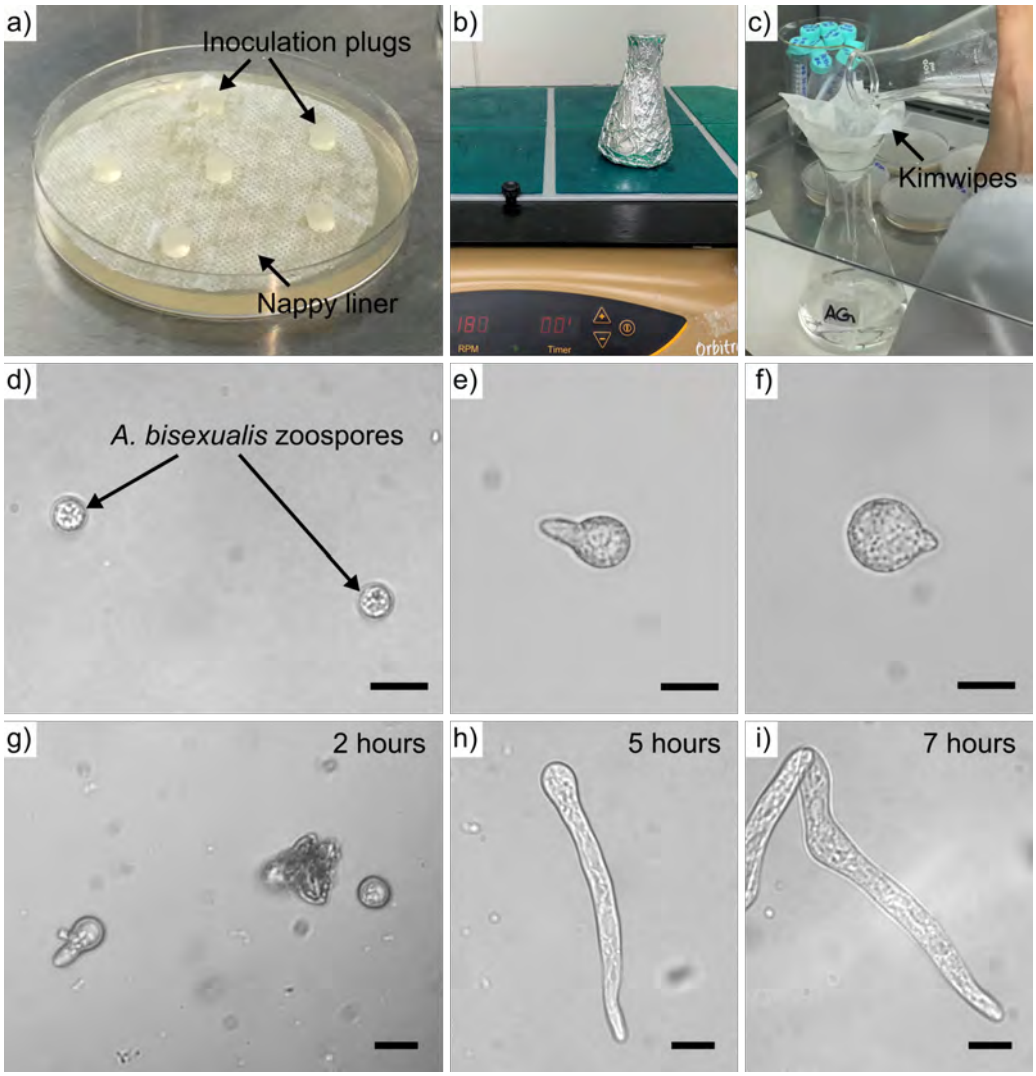


Figure 4.9: *A. bisexualis* zoospore induction. (a) Photograph showing six inoculation plugs placed on the PYG agar Petri dish with nappy liner. (b) Photograph of the flask, containing the nappy liner with the growing colony, on an orbital shaker. (c) Photograph showing zoospores being collected in the flask. (d) Light micrograph of produced *A. bisexualis* zoospores on a microscope slide. (e & f) Light micrographs of germinating zoospores after 2 hours of being cultured in PYG broth at 26 °C. (g-i) Light micrographs showing the zoospores germinating and growing in the seeding area of the previous PDMS platform filled with PYG broth after 2, 5, 7 hours, respectively. The scale bars are 20 $\mu$m.

colony growing on it was peeled off from the PYG agar, and placed aseptically into a 250 mL flask containing 100 mL autoclaved PYG broth (containing [in% w/v] peptone [0.125], yeast extract [0.125] and glucose [0.3]). Following gentle swirling on an orbital shaker at 150 rpm for 24 hours at 26 °C in the dark, the PYG broth in the flask was exchanged with mineral salt solution (containing 5 mM $KNO_3$, 10 mM $Ca(NO_3)_2$, 4 mM $MgSO_4$, 20 mM $FeSO_4$ and 20 mM di-sodium Ethylenediaminetetraacetic acid (EDTA)) five times in the first hour. Between each change the flask was returned to the orbital shaker at 26 °C and shaken at 150 rpm. The sixth solution exchange was implemented after 1 hour of swirling on the orbital shaker at 150 rpm, 26 °C, after which the flask was again replaced on the orbital shaker and left overnight. The next day the contents in the flask were poured through two layers of sterile Kimwipes into a sterile flask and vortexed for 10 s to collect the fully developed zoosporangia and encyst the zoospores in solution. After distributing the zoospore solution into several centrifuge tubes, these were centrifuged at 800 rpm for 10 min at 20 °C, and the supernatant of the solution was carefully removed. The zoospores in the bottom of the tubes were re-suspended in the mineral salts solution, and stored at 4 °C until use. The germination of zoospores was observed after mixing of the produced zoospore solution with PYG broth (1:1 v/v) and incubation at 26 °C for 2 hours. As they germinated (Fig. 4.9(d)), zoospores grew larger and started putting out a germling after 2 hours of culture (Fig. 4.9(e) and (f)). In order to also demonstrate the germination of *A. bisexualis* zoospores on the PDMS device, a series of zoospores in PYG broth media (1:1 v/v) were introduced into the seeding area of the previous microfluidic force sensing platform, as shown in Figure 3.12. After 2 hours of culture on the platform, a number of zoospores were observed starting to germinate. These germlings grew robustly and branched after 7 hours, as shown in Fig. 4.9 (g-i), indicating good compatibility with the PDMS material.

### 4.2.4 Experimental setup

The system for single zoospore capture, maintenance and germ tube force sensing was operated using the setup depicted in Figure 4.10. A 1 mL syringe with zoospore sample, actuated by a syringe pump (NE-300, New Era Pump Systems), was connected to the zoospore inlet using a Teflon tube (ETFE 1/16", Upchurch Scientific), a short Tygon tubing adapter (Cole-Parmer) and metal needle (blunt end, 90 degree bent tip, 18 gauge) for sample introduction. A pressure controller (OB1 Mk3+, Elveflow) combined with a compressor silent air system (SAS-062, Dürr Technik GmbH & Co. KG) was utilized to drive the membrane microvalve by applying positive pressure. The

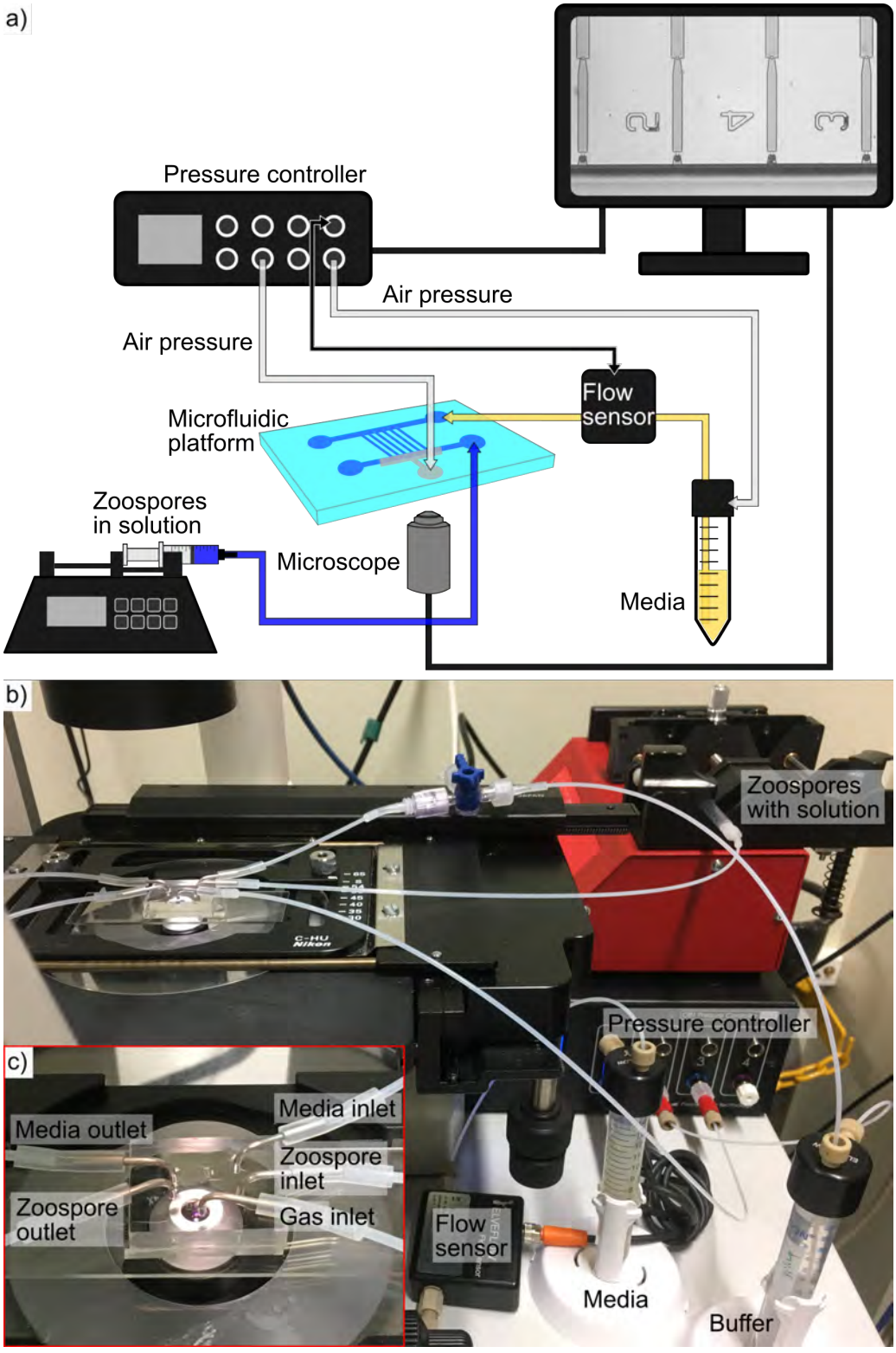


Figure 4.10: Experimental setup for the zoospore capture and maintenance device. (a) Schematic diagram of the flow system. (b) Photograph of the entire experimental setup including flow control and microfluidic device mounted on the inverted microscope. (c) Detailed view of the platform on the microscope stage with inlets/outlets and valve control connected.

same controller was also used to supply media by connecting to a 5 mL reservoir with media, a microfluidic flow sensor (Elveflow), the bent tip needle and the media inlet to a second channel. Both, the positive pressure for microvalve and flow rate of media were regulated using the supplied software interface (ESI, Elveflow). The capture of single zoospores, growth of germlings from zoospores in the measurement channels and micropillar deflection by the tip of each germ tube were recorded using an inverted microscope (ECLIPSE TS 100, Nikon) and a digital camera (xiQ MQ013MG-E2, Ximea) connected to a PC running digital acquisition software (CAMTool, Ximea).

## 4.3 Experimental results and discussion

This section summarizes and discusses the experimental results obtained with the integrated monolithic platform for single zoospore capture, germination and single germ tube force sensing. First, sieve valve membrane operation and optimization of the zoospore loading channel are discussed. This is followed by results relating to zoospore capture and maintenance. Finally, the first force measurements on single germlings originating from individual zoospores are demonstrated on the platform.

### 4.3.1 Optimization of zoospore loading channel and membrane valve driving test

Device fabrication was complicated by the fact that pillar integration requires channels with a rectangular cross-section [24], while normally-open valves require rounded channel profiles [159]. The positive resist layer required to integrate the pillars currently precludes the use of resist reflow to form rounded structures for complete valve closure, as this would also distort the pillar cavity shape. Figure 4.11 shows one example of the photoresist mold with positive photoresist AZ 12XT patterned. The cavities in the channels were destroyed during the reflow process at 130 °C for 1 min, while other parts of channels formed rounded corners. As such, the target of the current design using sieve membrane microvalves was foremost to retain zoospores in the trap-sites of measurement channels to guide the growth of germ tubes towards the measurement pillars.

Based on this, the width of the zoospore loading channel had to first be optimized, as a wider channel allows the PDMS membrane to bend more markedly, resulting in a better sealing effect of the sieve microvalve, and a reduced chance of zoospores escaping the traps. A zoospore loading channel that is too wide reduces the zoospores

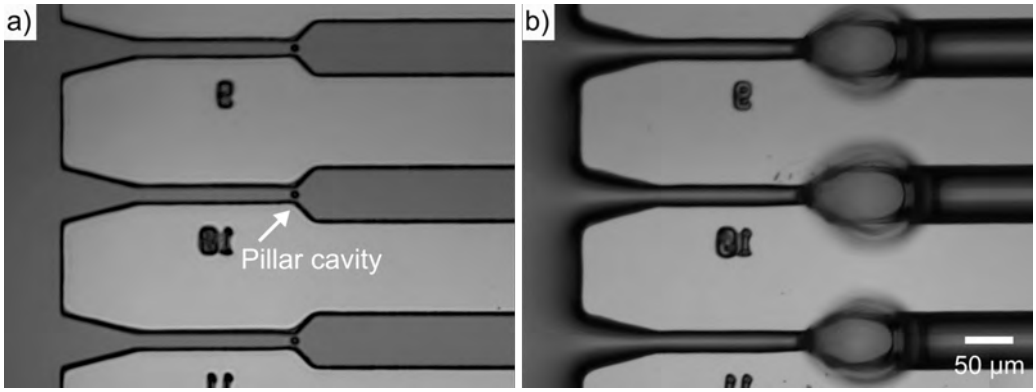


Figure 4.11: Light micrographs showing the channel patterns of positive photoresist AZ 12XT integrated with micropillar cavities before (a) and after (b) the reflow process at 130 °C for 1 min.

trapping rate since more zoospores flow further from the measurement channels and are thus not able to be captured. To investigate this, devices were fabricated with a zoospore loading channel width of either 60, 120, 190 $\mu$m and used to evaluate cell capture and retention efficiencies. Furthermore, device assembly led to a typical alignment error of a few micrometers between the two PDMS parts, inevitably in some platforms the microvalve chambers were well-aligned to the zoospore loading channel, while in others the microvalve chambers were partially overlapped. To take account of this, both well-aligned and overlapped platforms with each loading channel width were tested.

Prior to this, the deflection of the thin membrane was evaluated for various pressures up to 2.0 bar, which was the maximum positive pressure available on the particular OB1 flow controller. This test was performed while the fluidic layer of the platform was filled with DI water and the results showed that obvious membrane deformation (dark region at the edge of the microvalve chamber) could be observed when the pressure was higher than 1.0 bar for 120 and 190 $\mu$m wide zoospore loading channels, and 2.0 bar for the 60 $\mu$m wide channel (see Fig. 4.12 (a-c)). The dark region became noticeably wider and darker with the increase of applied positive pressure. Polystyrene microspheres (20 $\mu$m in diameter) suspended in DI water were injected into the fluidic layer from the zoospore inlet after the microvalve was closed (pressure = 2.0 bar). Since the PDMS membrane did not completely seal the zoospore loading channel, the water continuously flowed along the bottom two corners of the rectangular channel (dark area in the figures). Microspheres were stopped by the deformed membrane at the edge of the microvalve, which further confirmed sufficient deflection of PDMS membrane.

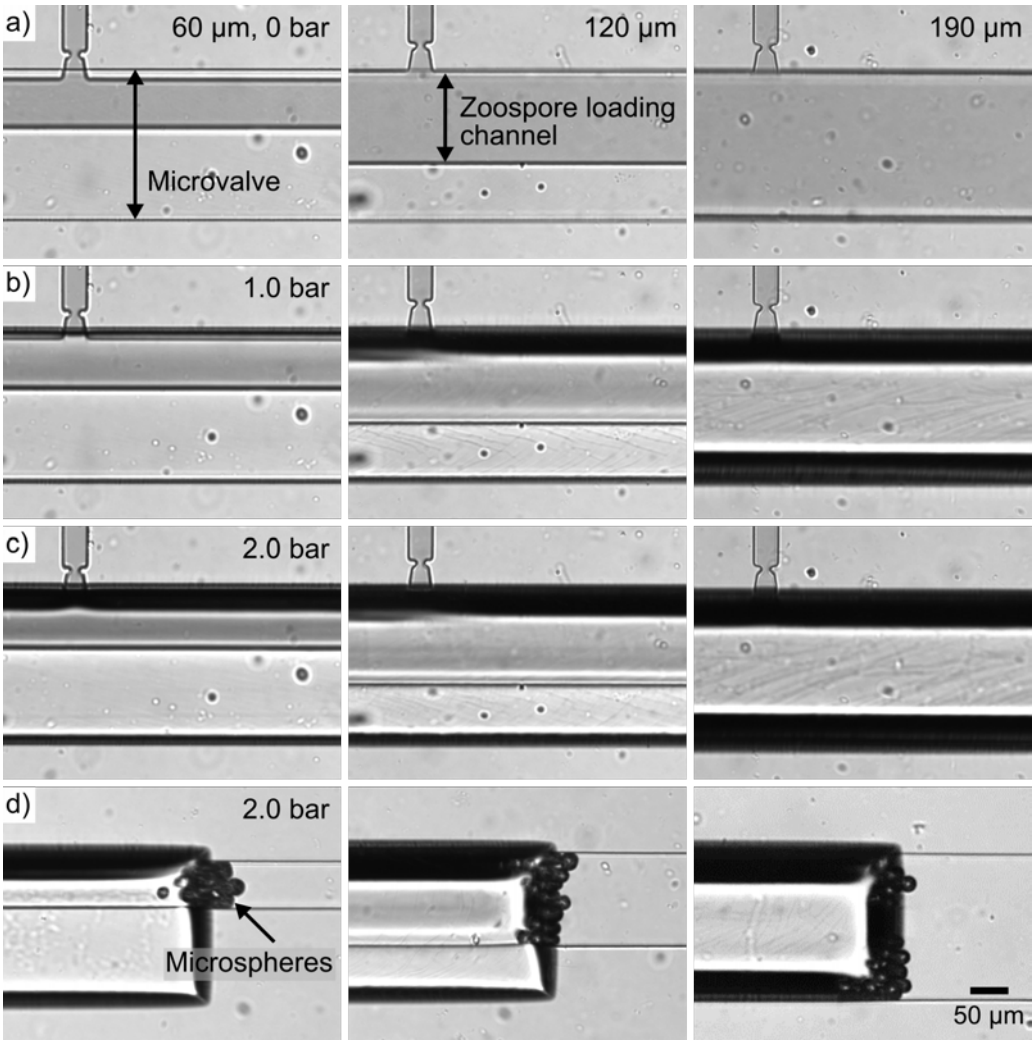


Figure 4.12: Membrane microvalve driving test under various pressures and zoospore loading channel widths. (a-c) Light micrographs of normally-open microvalves at applied pressures of 0, 1.0, 2.0 bar, respectively. (d) Light micrographs showing 20 $\mu$m diameter microspheres being stopped by the deflected PDMS membrane while the applied pressure was 2.0 bar. Each column represents a different width of zoospore loading channel, from left to right: 60, 120 and 190 $\mu$m.

To optimize the width of the loading channel for cell retention, the same 20 $\mu$m diameter polystyrene microspheres were suspended in DI water and injected into the fluidic layer from the zoospore inlet at a flow rate of 20 $\mu$L/min using the syringe pump. After capture of the microspheres in the trap-sites of the measurement channels, the membrane microvalve was closed by applying the previously determined positive pressure (2.0 bar) to the gas layer of the platform. DI water was then pumped into the fluidic layer from the media inlet at a flow rate of 5 $\mu$L/min using the pressure controller, while sample flow from zoospore inlet was stopped. The results for the 60 $\mu$m wide zoospore loading channel were shown in Appendix B.2. While a single microsphere was successfully captured in a trap-site of a measurement channel, the same microsphere could be dislodged back into the corner of the zoospore loading channel even after the membrane valve was closed. The DI water injected from the media inlet clearly provided enough pressure, suggesting that the PDMS membrane was not deflected enough to retain the microsphere inside the trap-site. This was the case whether microvalve chamber and zoospore loading channel were perfectly aligned or not.

In comparison, closed membrane microvalves successfully prevented all trapped microspheres from escaping when 120 or 190 $\mu$m wide zoospore loading channels were used, as shown in Figure 4.13 and Appendix B.2. This indicated that, even though the membrane valve on the current platform could not completely block the zoospore loading channel, it should possess the capability to keep zoospores trapped. At the same time, the error of alignment during the chip bonding appeared to have no distinct effect on the microvalve closure and particle/cells immobilization. Given that, the further away from the trap sites the zoospores flow through the loading channel, the lower the probability for zoospores to be trapped, platforms with 120 $\mu$m wide zoospore loading channels were used in the subsequent experiments.

Finally, red food coloring was mixed in with the polystyrene microsphere solution to achieve better visualization of the entire trapping operation. Figure 4.14 shows an example of a single microsphere flowing into a measurement channel, blocking the constriction of the trap site, and thus diverting successive microsphere to the next trap. After becoming trapped, the microspheres were successfully retained in the trap site by closure of the membrane valve. DI water, perfused from the media inlet to simulate convection-based media supply, faded the red color in the channel, but did not dislodge the microspheres from the trap sites. Following this successful trapping demonstration, microspheres were replaced with live zoospores, as described in the next section.

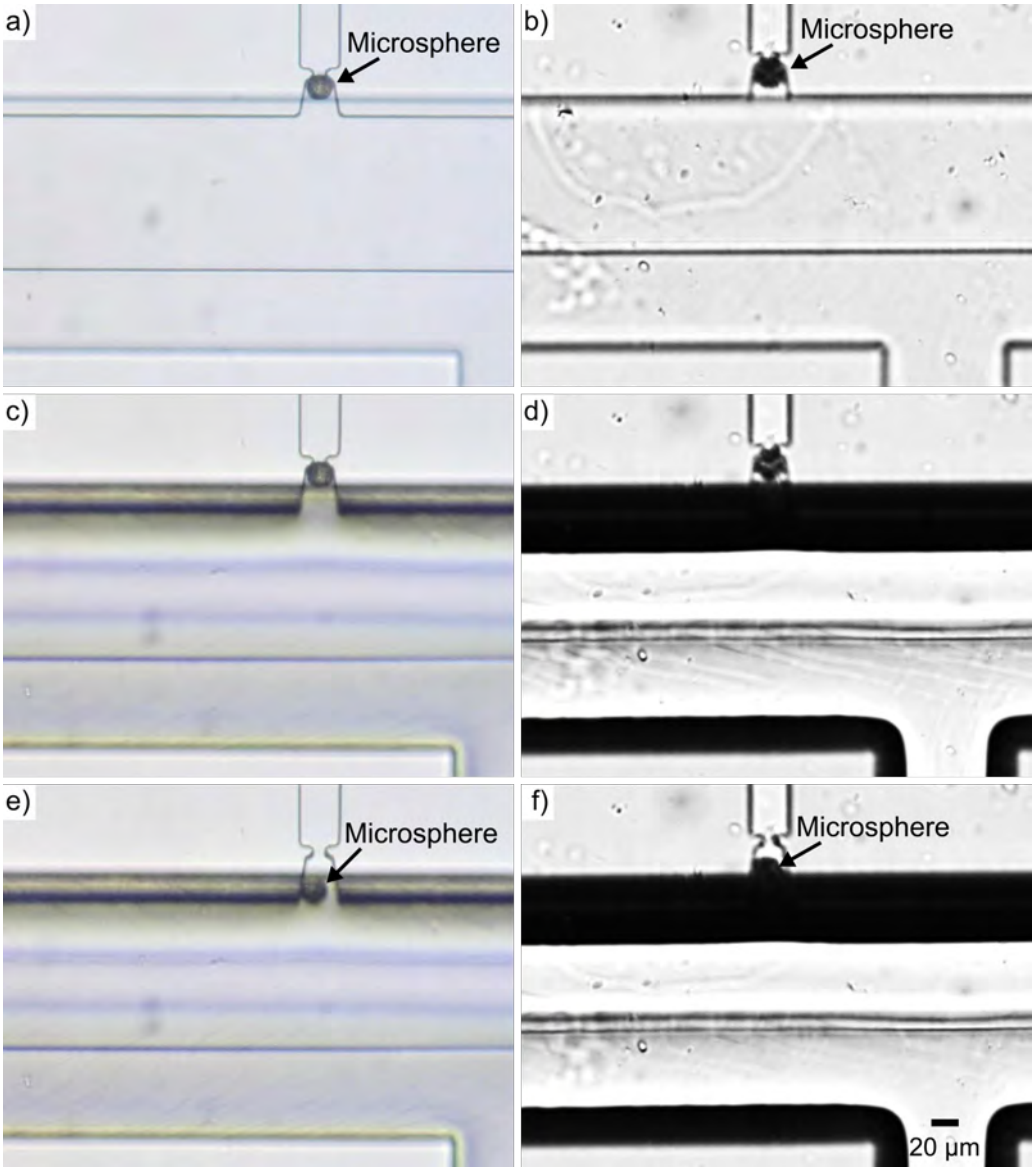


Figure 4.13: Microsphere capture and retention tests on the platform with a 120 $\mu$m wide zoospore loading channel. (a), (c) and (d) Light micrographs showing a single microsphere being captured in the trap-site of one measurement channel, the membrane microvalve being closed at a pressure of 2.0 bar, and the microsphere flowing back against the membrane valve after the DI water was pumped from media inlet. Note, in this example the microvalve chamber was overlapping the zoospore loading channel due to an alignment error. (b), (d) and (f) Light micrographs showing the same result on a device where the microvalve chamber was more precisely aligned to zoospore loading channel.

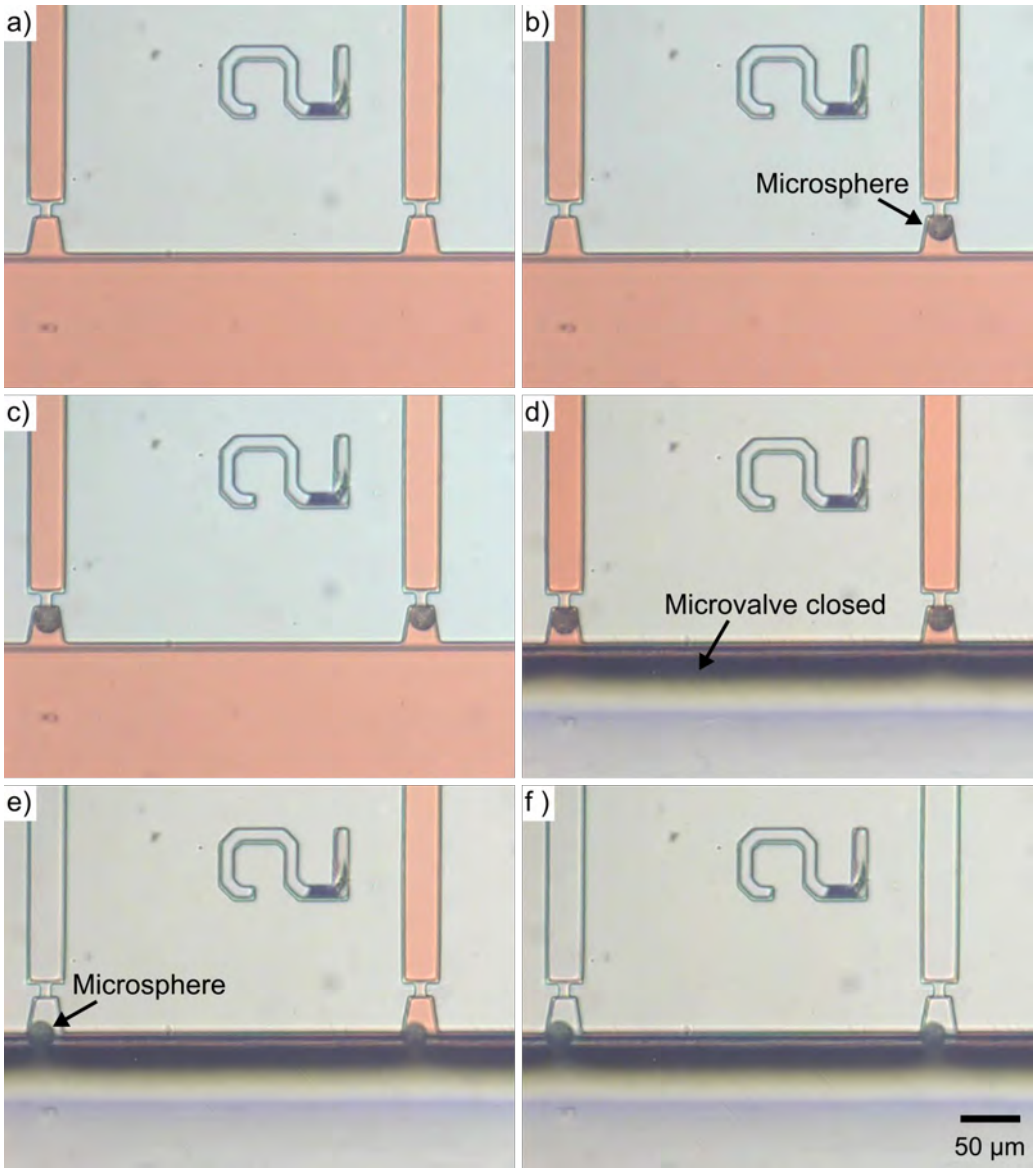


Figure 4.14: Simulation of experimental device operation using polystyrene microspheres suspended in water with red food coloring. (a-c) Light micrographs showing a single microsphere flowing into a measurement channel, being trapped by the constriction structure, and the subsequent microsphere captured in next trap site. (d-f) Light micrographs showing the closure of the membrane valve and how DI water injected from the media inlet faded the red color in the measurement channels. Microspheres were successfully retained by the microvalve during the complete procedure.

### 4.3.2 Zoospore capture and maintenance

The same processes as used with microspheres were applied to *A. bisexualis* zoospores, which ranged from 10 to 15 $\mu$m in diameter and were suspended in mineral salts solution. The fluidic layer of PDMS platform was first filled with the PYG broth immediately after each device was taken from its vacuum package. The zoospore solution was then introduced from the zoospore inlet via syringe pump at a flow rate of 20 $\mu$L/min and zoospores were hydrodynamically captured in the trap sites. Following this, the membrane valve was shut off with an applied pressure of 2.0 bar, while PYG broth continued to be supplied from the other side of the measurement channels via the media inlet at a flow rate of 5 $\mu$L/min. During the zoospore maintenance stage, both microvalve closure and media supply were driven by the pressure controller OB1. The growth of germlings germinating from zoospores compartmentalized into separate channels was observed using the inverted microscope.

As described in Section 4.2.1, two types of constrictions, type A and type B were tested following the above operation. Figure 4.15 shows an example of the trapping and successful retention of a zoospore during a media exchange cycle on the platform with constriction type A. Since the measurement channel was constricted in both dimensions in this type, it was blocked by the trapped zoospore, resulting in no subsequent zoospores entering this measurement channel. However, for the constriction type B, rather than fully blocking fluid flow, the flow rate around the zoospore in the constriction structure significantly increased. As a result, it could be observed that smaller captured zoospores were eventually squeezed and pushed through the trap sites (see Appendix B.3). To address this issue, zoospores were later pre-cultured in centrifuge tubes before introducing them to the platform, as this allowed zoospores to grow larger. The zoospore solution was mixed with PYG broth (1:1 v/v), and cultured in a 26 °C incubator for 2 hours. Figure 4.16 shows a pre-germinated zoospore flowing into the measurement channel and its capture by the constriction structure and retention during the media exchange.

Following trapping, the growth of germlings germinating from zoospores into separate measurement channels was observed on the platforms with each of two types of constrictions. Figure 4.17 shows an example of a trapped zoospore germinating, and the resulting germling growing through the constriction and along the measurement channel. Similarly, the germlings from pre-cultured zoospores were observed to grow along the measurement channel during the supplementation of culture media (see Fig. 4.18). In general, as shown in Figure 4.19, the growth success ratio (7/10) of the zoospores captured by horizontal constriction, Type B was much higher than that

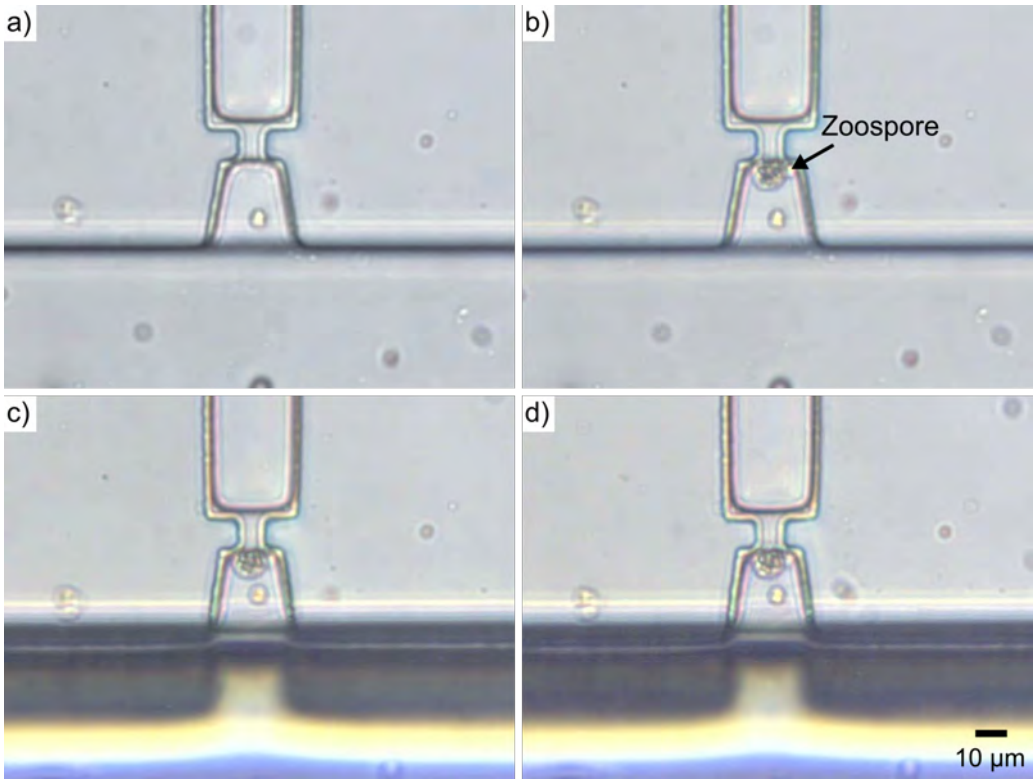


Figure 4.15: Single zoospore trapping and immobilization test on the platform with constriction type A (constriction in both vertical and horizontal directions, 8 $\times$ 5 $\mu$m width $\times$ height). Light micrographs showing the empty constriction (a), a zoospore being captured by the constriction structure (b) and successfully retained during the media exchange cycle (c & d).

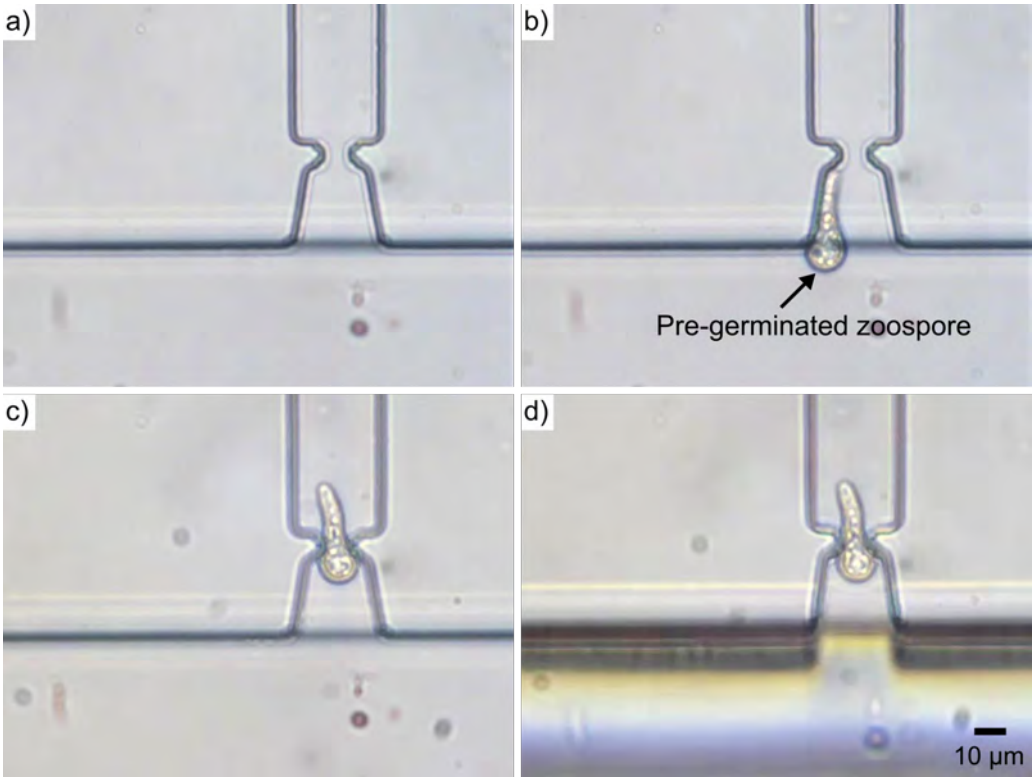


Figure 4.16: Trapping and immobilization test of pre-cultured zoospores on the platform with constriction type B. Light micrographs showing the empty trap site (a), a pre-germinated zoospore being captured by the constriction structure (b & c) and successfully retained during the media exchange cycle with the sieve microvalve closed (d).

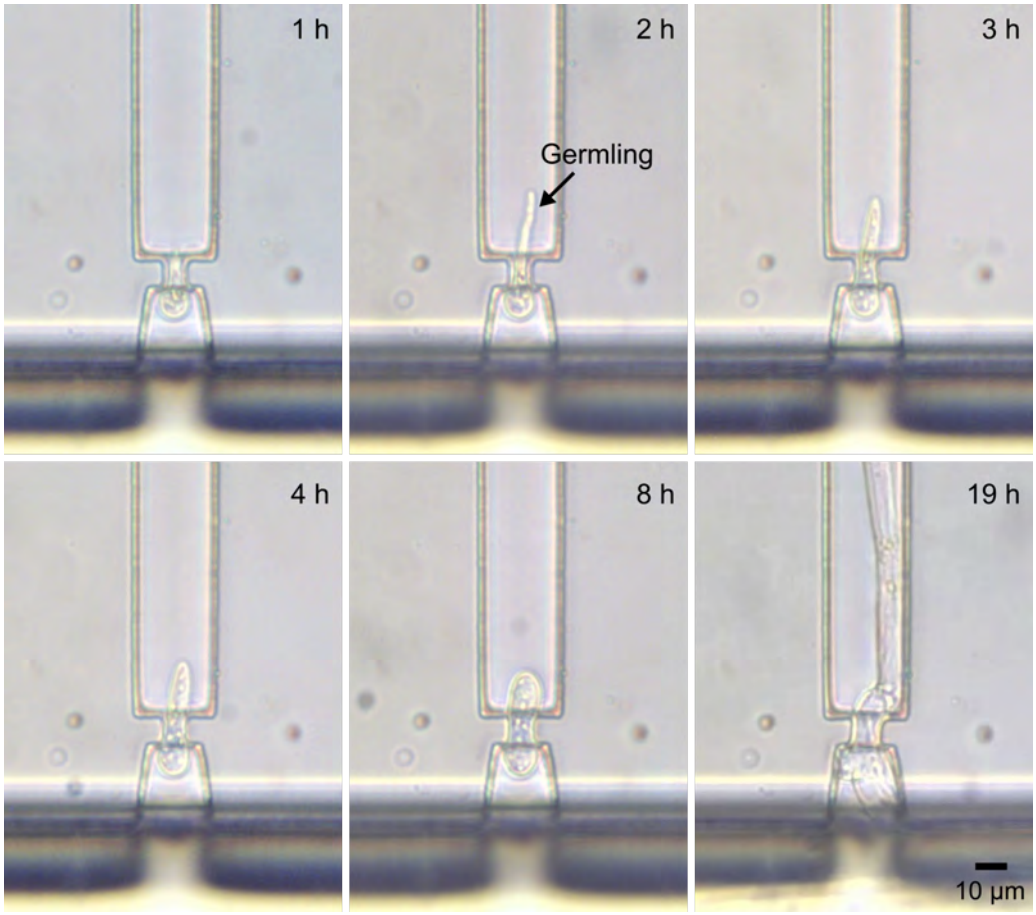


Figure 4.17: A time sequence of light micrographs showing germ tube growth from an individual zoospore through a combined horizontal and vertical constriction (Type A, $8 \times 5$ $\mu$m width $\times$ height) along the measurement channel at 1, 2, 3, 4, 8 and 19 hours after trapping and culturing on the platform.

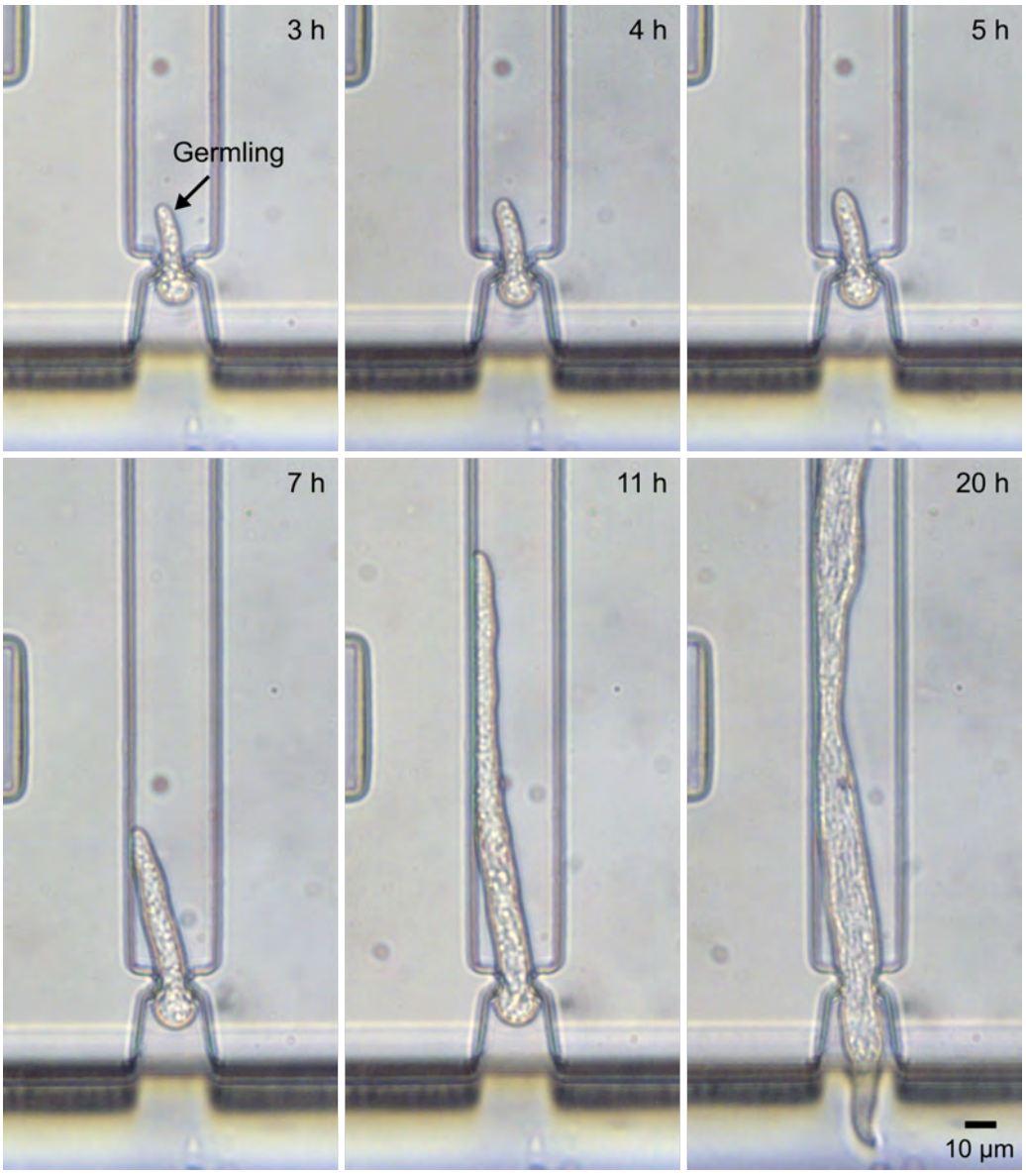


Figure 4.18: A time sequence of light micrographs showing germ tubes growth from an individual zoospore along the measurement channel of the platform with horizontal-only constrictions (Type B, 8 $\times$ 30 $\mu$m width $\times$ height) at 3, 4, 5, 7, 11 and 20 hours after trapping and culturing on the platform.

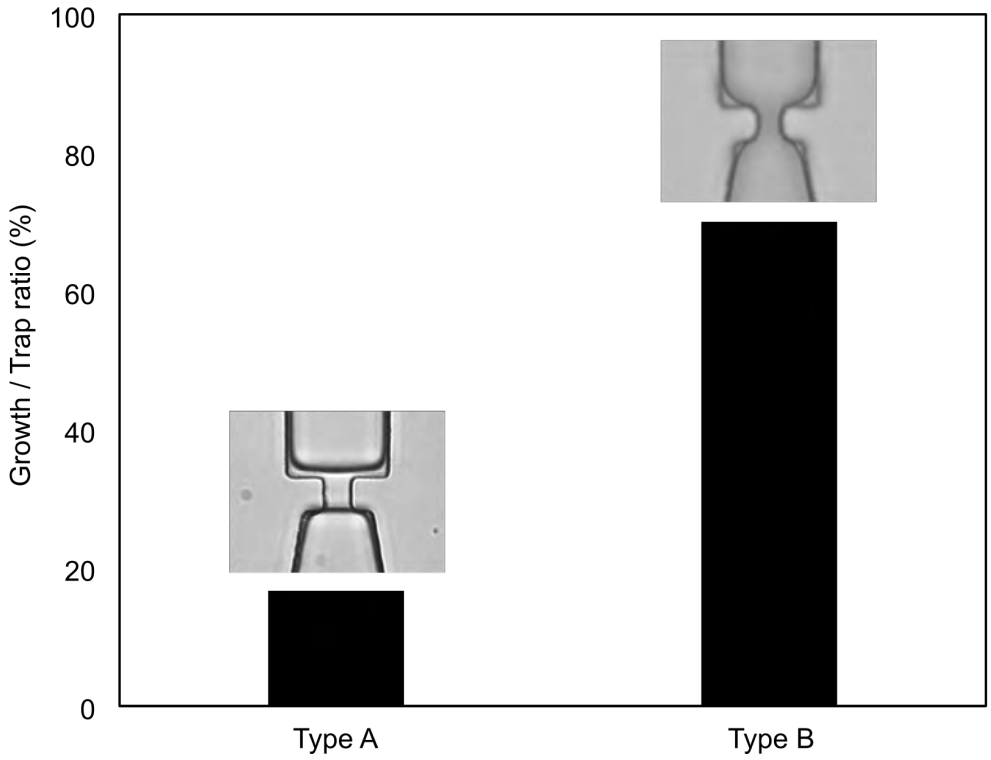


Figure 4.19: Bar chart of growth success-ratio for trapped zoospores with constriction Type A and B. The growth success ratio (7/10) of the zoospores captured by horizontal constriction Type B, was much higher than that trapped by both horizontal and vertical constriction Type A (2/12). Insets show a top-down view of the two different trap site geometries in PDMS.

trapped by both horizontal and vertical constriction, Type A (2/12). Although this observation was based on a limited sample number, it indicated the possibility of a yet to be determined mechanosensory response by the zoospores. Mechanosensory mechanisms are widespread in fungal and oomycete species [180]. As mentioned previously, only a very limited number of studies have been conducted in which zoospores or conidia were hydrodynamically trapped, such as described here. The only other study so far, by Geng et al. [109], which used a combined horizontal and vertical trap design to trap and compartmentalize conidia, did not discuss conidia germination success rates. Interestingly though, in oomycete zoospores, low levels of encystment and germination have been predicted to be associated with zoospores becoming mechanically trapped within root hairs [181]. As such, this observation may warrant further investigation in the future.

For the current design of the platform, an inherent shortcoming is that fluid, in particular nutrients provided to the trapped cell via the media inlet, can flow through the only partially-sealed edges of the zoospore loading channel. While this is an unavoidable limitation brought about by the incomplete seal formed by the sieve membrane valve, it can lead to zoospores putting out germ tubes into this space which should ideally be closed off. As previously demonstrated via maze-like structures, fungi explore geometrical structures both in response to nutrient gradients [182] and nutrient-independent based on search algorithms, which are thought to maximize survival and biomass homogeneity in microconfined networks [94]. A similar behavior was observed for the zoospores and their resulting germ tubes on the sieve valve platform. Figure 4.20 (a) shows an extreme example of a trapped zoospore putting out a germ tube backwards, which then grew against the deformed PDMS membrane and into the zoospore loading channel, most likely using the mechanisms described above.

Furthermore, after extended culture hyphae could be observed entering neighbouring measurement channels via the zoospore loading channel. For example, a germ tube, originally put out by the zoospore in channel No.4, branched in the zoospore loading channel and grew into the adjacent channel No.5 (see Fig. 4.20 (b)). Although the hypha did not affect the force sensing of the germ tube growing towards the micropillars in the measurement channel in this case, the cross-growth may have the undesired effects on the value of measured forces due to the multiple branching of the measured hypha itself or via direct physical contact between unrelated hyphae. No distinct patterns for hyphal extension and branching were observed, and no further analysis regarding space searching exhibited by hyphae was undertaken, as this design was discarded in favour of normally-closed valves.

In addition to cross-growth, long-term culture also increased the risk of other con-

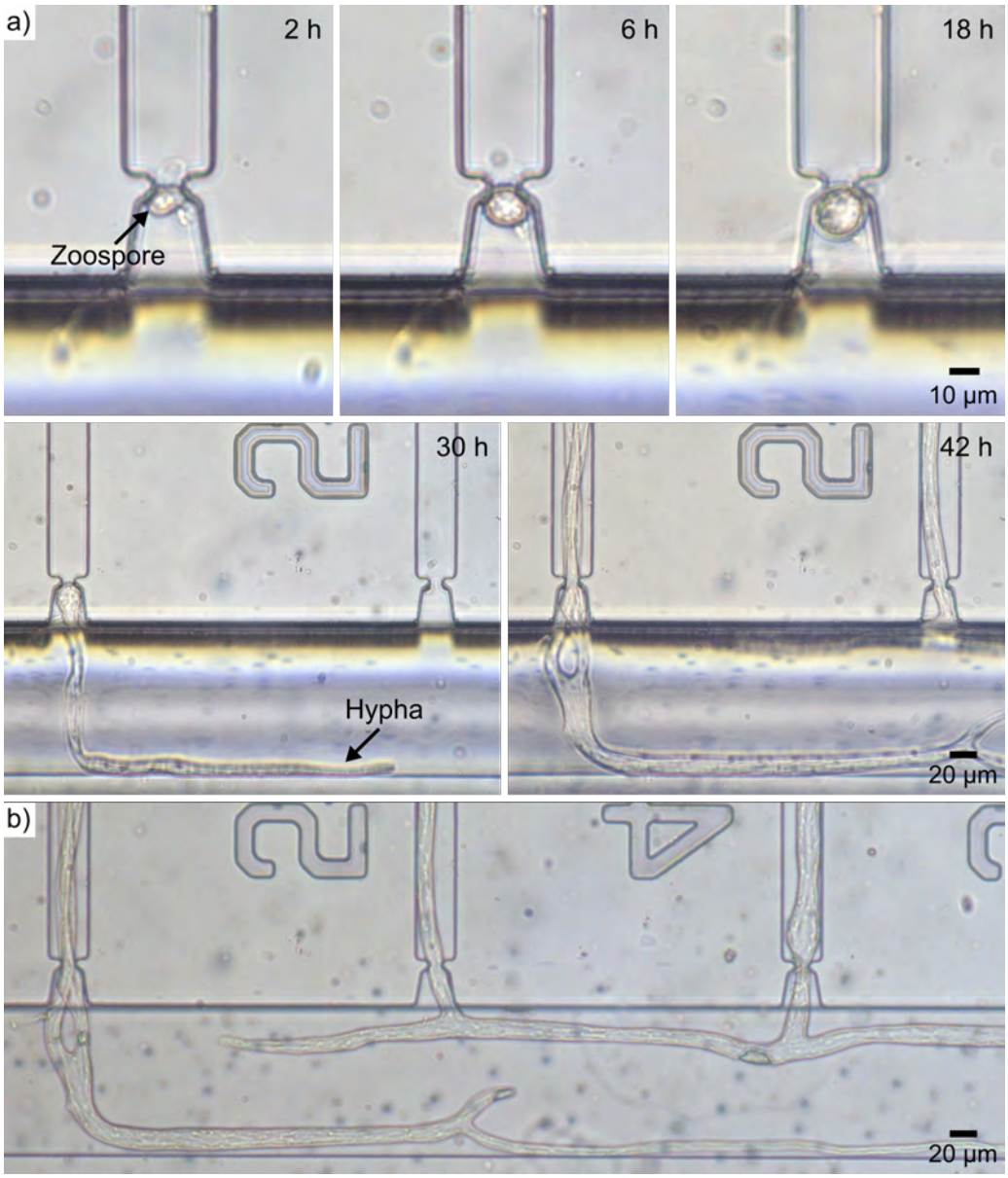


Figure 4.20: Light micrographs of germling growth backwards towards the membrane valve. (a) A germ tube germinating from a trapped zoospore grew against the deformed PDMS membrane and underneath it into the zoospore loading channel over a period of 42 hours of culture on the platform. (b) The hyphae originating from channel No.4 could be observed to grow into the zoospore loading channel, branch and grow into the neighbouring measurement channel (No.5) during 42 hours of on chip culture. Note, the membrane valve was opened for better visualization.

tamination occurring in the platform. Figure 4.21 shows two severe cases of a hypha contaminated with bacteria and other undefined organisms growing in the platform. In order to reduce the occurrence of this sort of contamination, chip and materials handling processes were improved over time. For example, all tubing, fittings and sample/media containers were autoclaved before experiments, and set up in a sterile laminar flow hood. As the flow control system could not be sterilized, possible contamination by it and the non-sterile gas source was reduced by adding filters (Kinesis Ltd.) with 0.22 $\mu$m diameter pores onto each pressure channel of the OB1 before the gas inlet and media reservoirs (see Appendix B.4).

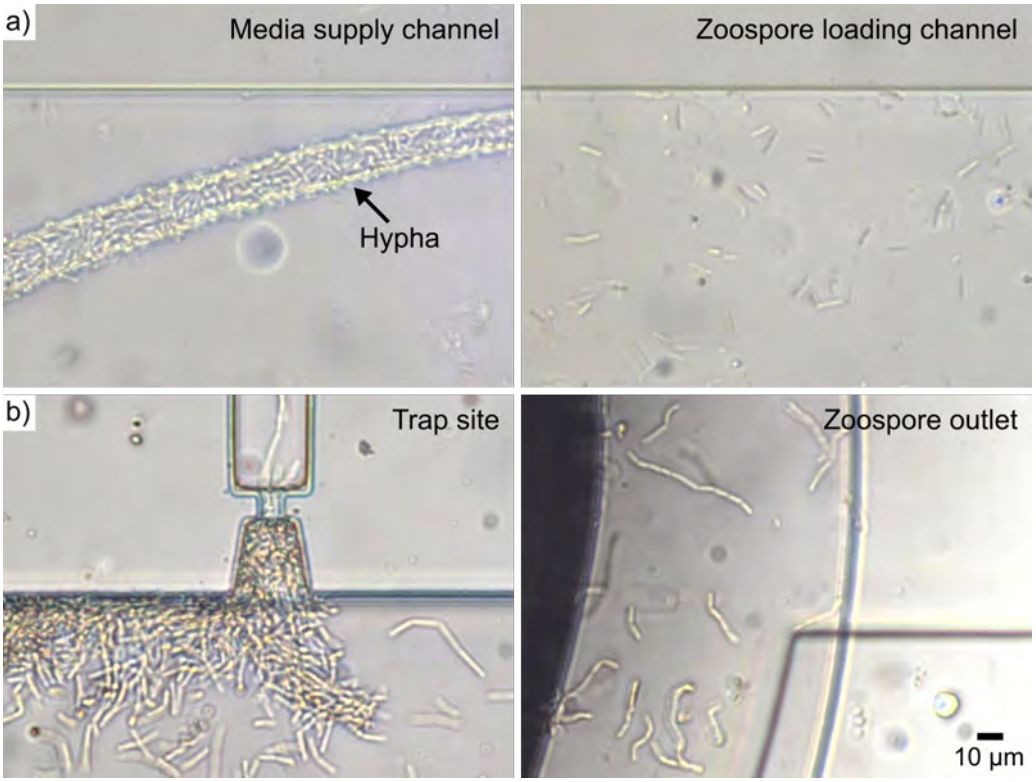


Figure 4.21: The problem of contamination during long-term culture on the platform. (a) Light micrographs of a hypha covered with bacteria in the channel, and bacteria in the zoospore loading channel after 19 hours of culture on the platform. (b) Light micrographs of a platform contaminated with unknown organisms in the area of a trap site and zoopore outlet after 17 hours of culture.

### 4.3.3 Force measurement on single germ tube

Using the media exchange described above, trapped zoospores could be maintained on the platform until germlings had germinated and extended to the force sensing pillars in their respective measurement channels. In general, it took germ tubes upwards of 20 h of culture to reach the measurement section of the culture channel. Considering that the distance from zoospore trap site to the micropillar was 310 $\mu$m, the growth rates of resulting germlings towards micropillar ranged from 0.26 to 0.4 $\mu$m/min (sample number, n = 9). These were much lower than the growth rates of hyphae from mycelium on the previous mycelial platform (average = 6 $\pm$ 1.6 $\mu$m/min) [133]. However, this value was consistent with the growth rate of *N. crassa* germlings ($\sim$20 $\mu$m/h) observed on the LOC chips by Geng et al. [109]. Interpretation of all events was further impacted by whether the respective zoospore also sent out a germ tube backwards into the sieve valve structure, something a majority of zoospores were observed to do. Due to a large variability in responses during germination in the traps, not enough data could be collected to determine whether growth rates of germlings or forces exerted by zoospores producing only a single germ tube versus two bi-directional germ tubes may differ. At the impact point, the movement of the top of the micropillar was recorded using the inverted microscope and digital camera. The mechanical model and computational image processing techniques described in Section 3.1 were then used to derive the forces exerted by germ tubes on the micropillars.

Figure 4.22 illustrates that both magnitude and direction of the force exerted by a single germ tube originating from single zoospores could be recorded as function of time. For the germ tube shown in Fig. 4.22(a), the force in x-direction increased to 0.8 $\mu$N, while the force in y-direction fluctuated around 0.1 $\mu$N. These force values from the example germ tube were much lower than those measured by hyphae from mycelium in previous mycelial platforms, which is supported by the results obtained by Wright et al. who found that the force generated by a germ tube is less than that of a leading hypha from mycelium [80]. As further illustrated by the plot of force versus time in Fig. 4.22(b), this significant increase in force perpendicular to the growth direction of this particular germ tube indicates a squeezing type event, where the germ tube is deflected into the gap between the micropillar and channel wall and exerts force with the tube wall while traversing the gap. Compared with the microchannel array developed by Geng et al. [109], not only germling growth and morphology from zoospores/conidia could be observed, but also the protrusive forces exerted by resulting germ tubes. By simply changing the position of the force sensing micropillars or adding multiple pillars spaced along the measurement channels, the

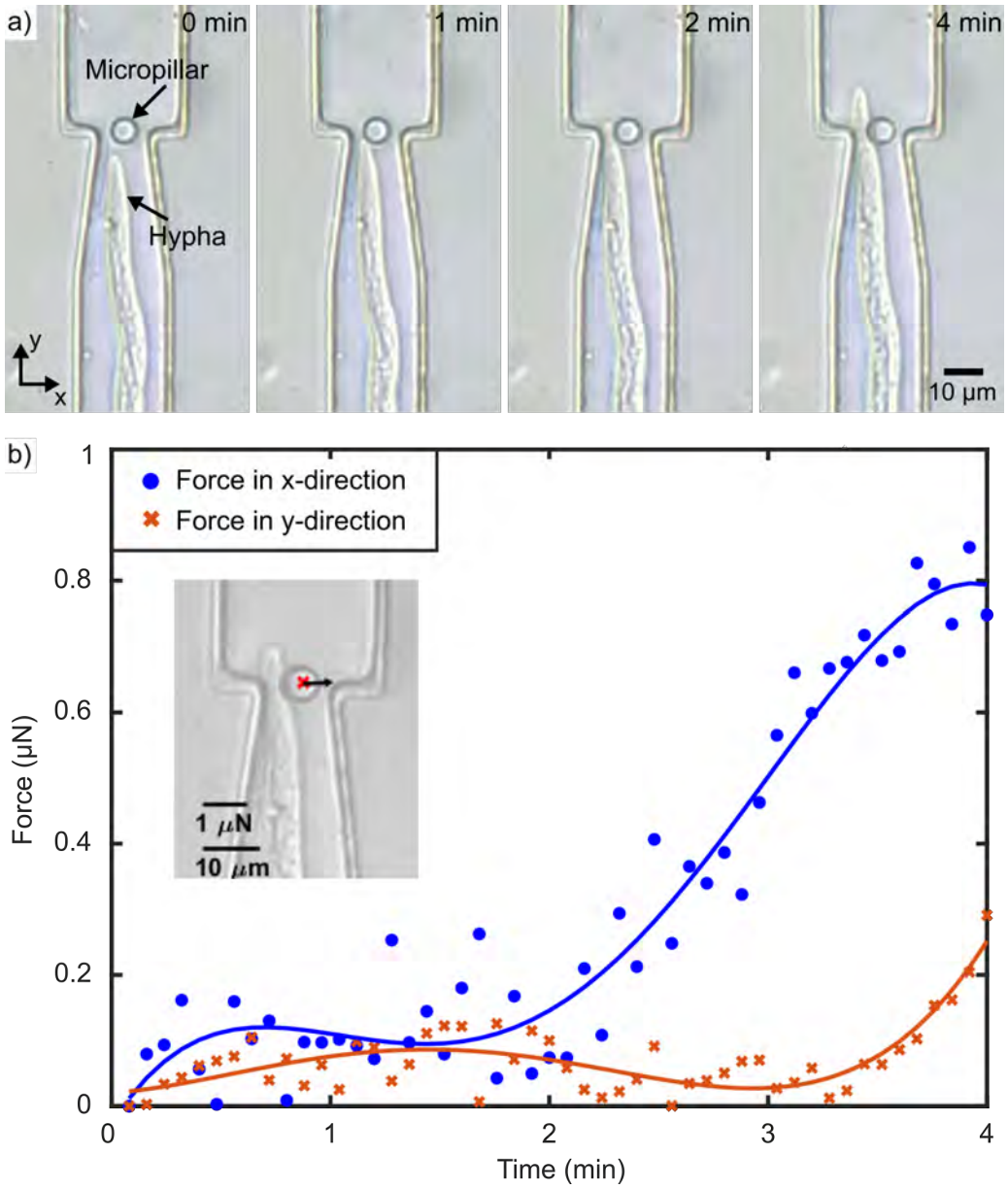


Figure 4.22: Force sensing on a germ tube of *A. bisexualis* growing from an individual zoospore. (a) Time sequence of micrographs showing the hypha growing towards a force sensing micropillar, hitting and deflecting it, and growing past it. (b) Plot of the force exerted by the germ tube on the sensing pillar in both x- and y-directions as function of time. Force in x-direction can be seen to increase throughout the interaction, indicating a squeezing type event. The inset shows an example of the force vector overlay generated by the combined ImageJ and Matlab image analysis. Both, magnitude and force direction can be determined and visualized.

forces generated by germ tubes at different stages could also be measured. Moreover, the micropillars can be easily placed in each measurement channel for large scale parallelized screening, while a capacitive force sensor, with a relative large obstacle placed at the end of microchannels, could only measure one hypha at a time, before having to move to the next hypha [114].
While the above demonstrated that the platform could facilitate the first successful protrusive force measurements on germ tubes originating from individual zoospores, overall observations led to the conclusion that, to collect statistically-relevant sample numbers, rather than repeating experiments on the current platform, a different way to sieve valves would have to be found to improve compartmentalization and reduce backwards growth.

## 4.4 Conclusion

In this chapter an improved LOC device, which integrated the existing force sensing technique of freely bending micropillars with a single zoospores trapping system was demonstrated. The device was designed to help investigate cell-to-cell variability and heterogeneity on zoospore/conidia germination, germling growth and protrusive forces of organisms. Due to the fabrication requirements for the force sensing mechanism, normally-open sieve valves were implemented for compartmentalization. Successful hydrodynamic capture of single particles in the trap sites via the constriction structures in the parallel measurement channels was demonstrated. Optimization results of the loading channel indicated a width of 120 $\mu$m and applied pressure to the gas layer of 2.0 bar to aid membrane valve immobilization of trapped particles during media exchange. A protocol to induce *A. bisexualis* zoospores was implemented, and loading and retention of captured zoospores in the trap site was shown. Sieve valves were used to compartmentalize live zoospores and germinate germ tubes for growth into the individual measurement channels. Trapping and germination efficacy tests indicated that the combined horizontal and vertical type A trap had greater ability of single zoospores capture, while the vertical–only type B trap could only trap pre-germinated zoospores due to their larger size. In addition, traps of type B regularly exhibited multi-zoospore accumulation in the same trap site as a result of incomplete blocking of the vertical-only trap by individual zoospores, which let to subsequent zoospores entering the trap site. However, the growth success ratio of zoospores trapped by type B (7/10) was much higher than in type A (2/12). Long-term culture of germlings was facilitated by injection of fresh media into the fluidic layer from the other side of the measurement

channels. Growth of germ tubes was observed to occur in both directions, towards the measurement pillars, but also into the sieve valves. The latter was attributed to the incomplete seal provided by the sieve valve geometry and illustrated interesting space-finding attributes of the organisms. Nonetheless, the devices enabled germ tube growth and forces exerted by single germling originating from individual trapped zoospores to be recorded for the first time. Recorded force magnitudes were smaller than for established hyphae used on the previous mycelial platform, a difference which will be further discussed in the following chapter. In summary, the platform introduced in this chapter enabled the first concurrent study of cell-to-cell variability in germ tube growth and protrusive force generation, and provides a new tool to help understand protrusive growth at the single cell level. Issues identified with this platform included the backwards growth of germ tubes and accumulation of zoospores in the trap sites of constriction type B. Both these issues will be addressed in the next chapter.

# Chapter 5

# Integration of Normally-Closed Microvalves

The following chapter describes the integration of normally-closed microvalves into the force sensing platform to overcome the valving limitations and resulting hyphal contamination discussed in Chapter 4. The chapter begins by introducing the platform design and working mechanism. This is followed by the presentation of novel fabrication protocol and the resulting devices. The chapter concludes by demonstrating the operation of the platform using polystyrene microspheres.

## 5.1 Introduction

As discussed in the previous chapter, normally-open membrane valves have been widely used in many microfluidic applications because of their simplicity and ease of device assembly. They are well-suited for hydrodynamic trapping devices as they require no external input in the open state and do not disturb partial flow into the traps. However, application of these devices to rectangular cross-section fluidic channels leads to incomplete sealing of the channel corners, giving rise to sieve valves as described in the previous chapter. In the case of this thesis, the incomplete sealing led to the unintended growth of secondary germ tube from the trapped zoospores into the valve and loading channel, and thus cross-contamination between measurement channels. For applications requiring complete sealing of rectangular channel cross-sections with normally-open valves, *in-situ* fabrication of valve seats via photopolymerization has been proposed [183]. While this improves sealing for such geometries, it was not initially considered for this work as it requires highly customized fabrication setups

to control localized polymerisation, significantly increasing fabrication complexity beyond standard photolithography.

The experimental results obtained with *A. bisexualis* zoospores, as discussed in the previous chapter, demonstrated that the sieve microvalves were capable of preventing captured zoospores from escaping out of the trap-site during application of media. However, the incomplete closing led to unintended hyphal growth during long-term culture. Even though the remaining space between deformed PDMS membrane and the corner of zoospore loading channel was very small when valves were closed, the germlings were able to sense the space and media flow inside, resulting in germ tubes growing against the membrane and branching into other measurement channels. As mentioned, reflowing and rounding the channel shape using positive photoresist is one of the most common methods to solve this problem [164]. The patterned photoresist of the fluidic layer mold is heated past its glass transition temperature after development and thus reflows. This forms a rounded cross-section, with the shape determined by surface tension. Because there are no 90°corners in the channels, the resulting microvalves are capable of complete closure. While initially considered, the reflow process could not be used for this work, mainly due to the high aspect-ratio (height/diameter) photoresist cavities required in each measurement channel for the force sensing micropillars. As such, an alternative had to be found to the normally-open and sieve valves initially integrated into the platform.

The other type of the pneumatic membrane valve is the 'normally-closed' PDMS microvalve, which is in a closed state when no pressure is applied [156, 184, 185]. Normally-closed valves not only address the above limitation of complete closure, but also retain some of the ease of fabrication, eliminating the need for photoresist reflow or in-channel photopolymerization. The principle of normally-closed microvalves is that a fluidic channel is interrupted by a valve seat sealed with a membrane in the rest state. The flow route is opened when negative pressure is applied to the control channel and the membrane is pulled into the overlying air chamber.

Hosokawa and Maeda first reported an entire PDMS normally-closed microvalve, which had a PDMS membrane sandwiched between two PDMS microchannel chips (fluidic and pneumatic chip) [184]. The valve was opened when the pressure difference across the membrane was higher than 10-20 kPa, and remained closed when the pressure difference was lower than this threshold value. However, because the fluidic chip was reversibly bonded to the PDMS membrane with the pneumatic chip, the microvalve could not resist against positive internal pressures higher than 10 kPa. Since the normally-closed microvalves are capable of transportation of different fluids without contamination and precise control of small fluid volumes, they have been

utilized for a wide range of applications in clinical diagnosis on detection of disease markers [186–189], cell analyses including bacteria [190, 191] and cancer cells [192], drug development [193], and chemical analysis [194, 195]. Moreover, these membrane valves have been further developed to perform some specific functions including cell seeding [196] and separation [197, 198], fluid mixing [199, 200], and droplet formation [201]. For instance, a chemical gradient microdevice with embedded normally-closed valves, which facilitated steady-state gradient in flow-free microchambers, was proposed by Mosadegh et al. [196]. The microvalves enabled fast and uniform seeding of cells by tilting the device inducing a gravity-driven flow and immobilization of cells while the microvalves were closed. The gradient was generated by passive diffusion of molecules, avoiding cells being directly exposed to constant fluid flow which was conducive to studies on non-adherent or shear stress sensitive cells. Li et al. [199] adapted the normally-closed valves to store and mix sub-nanoliter volumes of solutions at various mixing ratios. The final concentrations after mixing were verified to be very close to predicted values from the chamber design, profited from precise chamber volumes only defined by photolithography. Because no extra energy source was required to shut off normally-closed valves and keep them in closed state, the loaded device was highly portable, and allowed fluid to be stored for at least 7 days. Another distinctive application for normally-closed valves has been the generation of uniform emulsion droplets with various sizes [201]. The microvalve acted as a nano-channel to regulate the flow rate by changing the deflection of PDMS membrane, resulting in precise size control of the emulsion droplets. Sizes of generated droplets ranging from 5.5 to 55 $\mu$m were achieved without fabricating an extremely small channel or changing the velocities of sheath flows which may cause unstable flow and non-uniform droplets. While a number of devices integrated with normally-closed valves for handling cells and drugs in large scale have been proposed, fewer studies have used these valves for single cell analysis applications.

In general, normally-closed valves come with an inherent risk of permanent bonding between the PDMS membrane and valve seat during device assembly. As this would result in the valve remaining permanently closed, extra care has to be taken during device manufacturing. The initial practice used was to reversibly bond devices containing normally-closed valves by simply bringing the surfaces of a thin membrane and fluidic chip into contact [184, 199] or by clamping the whole device using two polymethyl methacrylate (PMMA) sheets [193]. As mentioned above, this method has limitations when positive pressure is applied, which may restrict the applications of the device. One strategy to circumvent the bonding issue is to add a localized passivation layer on the valve seat, such as mixtures of salt (NaCl) and polyvinylalcohol (PVA)

solution [202] or metal patches [197]. However, this selective deposition of sacrificial barriers and removal after bonding significantly increased the complexity of device manufacturing. Another alternative approach has been to micro-contact print PDMS oligomers to counteract plasma oxidation in selective regions [203]. In this technique the region of surface that contacted with the PDMS stamp received a thin layer of oxidized oligomers rendering it more hydrophobic. Although this technique has proven effective for large-scale integration of normally-closed valves, it presents a reasonable challenge for the alignment during stamping when the valves are relatively small.
In this chapter, the integration of normally-closed microvalves into the platform for individual zoospore trapping and germinated germ tube force measurement is demonstrated. This addressed the issue of germ tubes growing backwards to the zoospore loading channel by improving the seal with the normally-closed valves at the entrance of measurement channels. Furthermore, the independent control of microvalves was added to limit the number of zoospores collected in each trap site, a measure which increased the throughput of force sensing on single germ tubes in each platform. In the process, the size of the normally-closed valves was optimized for use on the platform, complete closure and independent control of microvalves were verified using microspheres, and the flow characteristics in various conditions of microvalve operation were characterized.

## 5.2 Materials and methods

### 5.2.1 Platform design and working mechanism

The platform consisted of a gas layer and a fluidic layer, separated by a PDMS membrane, which is similar to the membrane microvalve platform described in chapter 4. Instead of a large single valve chamber, the gas layer for normally-closed valves contained six 100 $\mu$m high air chambers forming the pneumatic membrane valves for each measurement channel. Depending on the device version, these air chambers could either be controlled simultaneously, via a single gas inlet, or individually, via six separate gas inlets. Apart from the zoospore trapping constriction structure and the force sensing micropillar, a valve seat was also added on the fluidic layer in the entrance of the parallel measurement channels for membrane valve closure. Based on the results shown in the previous chapter, horizontal-only constrictions were used in this design. Measurement channels were connected with a zoospore loading channel on one side and a media supply channel on the other side, both 60 $\mu$m in width and 30 $\mu$m in height.

A schematic illustration of the platform for zoospore capture and maintenance incorporating normally-closed valves is shown in Figures 5.1(a & b). A series of zoospores were introduced from the zoospore inlet and hydrodynamically trapped by the constriction structures. The membrane valve was then closed and the media was continuously supplied from the media inlet. However, as opposed to the driving principle of previ-

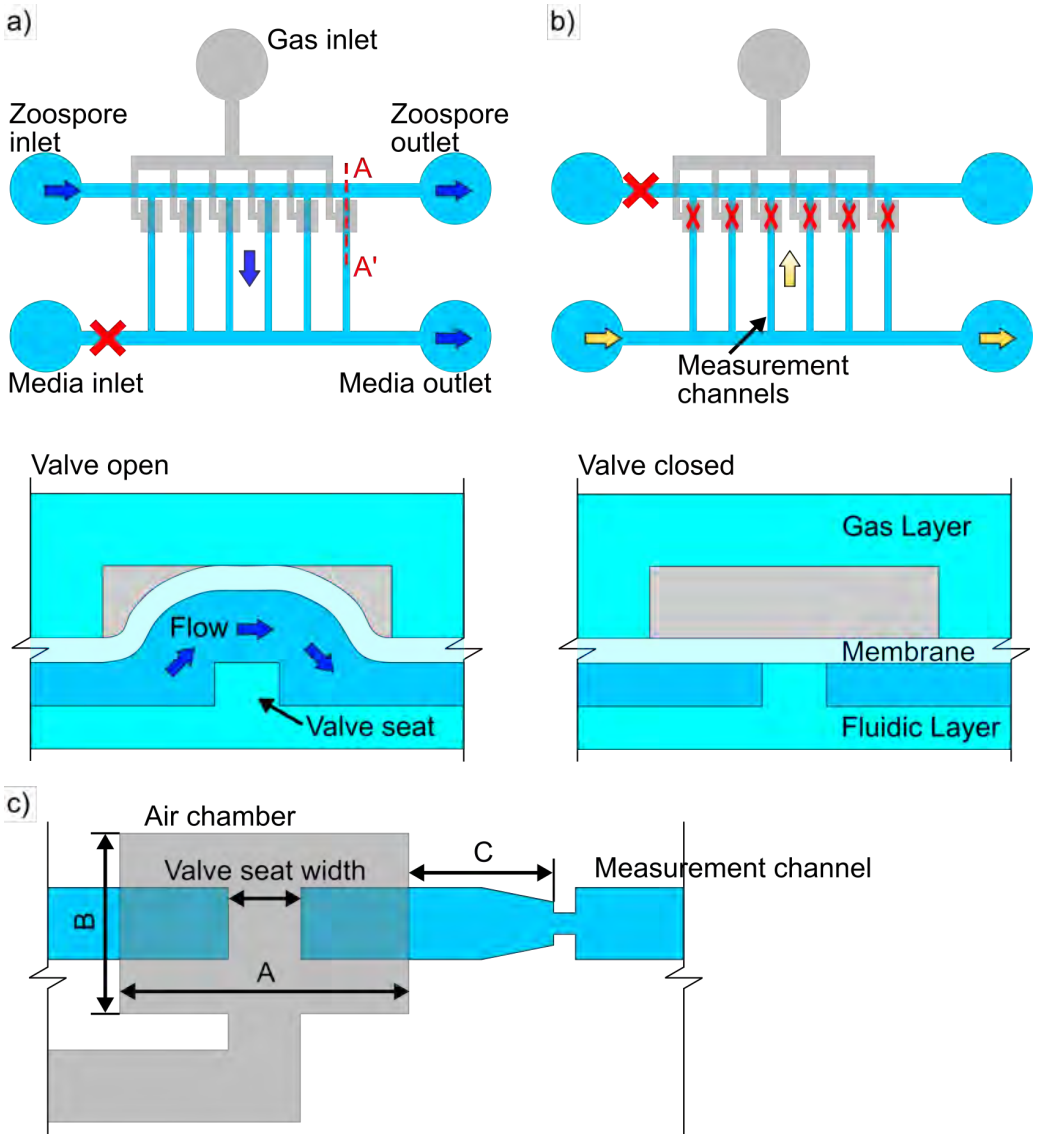


Figure 5.1: Schematic diagram of the monolithic platform for zoospore capture and culture integrated with normally-closed pneumatic microvalves. Channel design of the gas layer (gray), fluidic layer (blue), and cross-sections through A-A' showing the working principle of a microvalve while introducing (a) and culturing the zoospores (b). (c) Design of the membrane microvalves located in the entrance of each measurement channel with parameters shown as defined.

ous normally-open membrane valve, the normally-closed microvalves now performed opening and complete closure by applying a vacuum and injecting compressed air into the air chambers, respectively.
The width and height of measurement channels, the diameter and height of micropillars, and the width of constrictions and valve seats were set to 25, 30, 5, 25, 10 and 20 $\mu$m, respectively. In particular, the width of valve seat was set to 20 $\mu$m in order to prevent microspheres from sticking onto the top of the valve seat. In addition, the wider seat also provided more reliable sealing when the microvalve was closed. During testing, a series of size combinations of microvalve air chambers, including air chamber length (A), width (B), and distance from the constriction structure (C) were designed to optimize the microvalves for this particular application (see Fig. 5.1(c) and Table 5.1).

Table 5.1: Air chamber sizes of normally-closed membrane valves included for testing.

| Air chamber length, A ($\mu$m) | Air chamber width, B ($\mu$m) | Distance from constriction, C ($\mu$m) |
|---|---|---|
| 60, 100 | 100 | 20 |
| 140, 180, 220 | 120 | 30 |
| 140, 180, 220 | Same as for A | 30 |

### 5.2.2 Fabrication of entire PDMS platform

Both gas and fluidic layers of the platform were fabricated by PDMS casting from photoresist masters. For the gas layer photoresist master, standard photolithography processing was utilized. A 4 inch chrome-on-glass photomask with the gas layer pattern was firstly prepared using the pattern generator $\mu$PG101. A 4 inch silicon wafer was pre-cleaned by dehydration for 2 hours in a 185 °C oven and oxygen plasma (100 W, 10 min). It was then coated with negative dry-film photoresist, SUEX 100 (thickness 100 $\mu$m, DJ Microlaminates [204]), and soft-baked for 15 min on a 65 °C hotplate. The photoresist was exposed with an exposure dose of 900 mJ/cm² in low vacuum contact mode with a short wavelength filter (PL-360, Chroma), and post-exposure baked using a ramped process of 65 °C for 5 min and 95 °C for 10 min. The master mold of the gas layer was completed by development in PGMEA, rinsing with IPA and drying by $N_2$, followed by a hard-bake at 150 °C for 1 hour.
The two-layer photoresist master of the fluidic layer was fabricated according to the

protocol described in Section 3.2.1. Briefly, a dry-film negative photoresist ADEX05 was laminated on a pre-cleaned 4 inch silicon wafer and exposed using the first layer photomask at an exposure dose of 170 mJ/cm² in low vacuum contact mode with the short wavelength filter. After a ramped post-exposure bake, the wafer was developed in cyclohexanone for 5 min, rinsed with IPA and dried using $N_2$. Then, a positive photoresist (AZ 40XT) was spin-coated onto the first layer at a speed of 2000 rpm, edge-bead removed and soft-baked for 3 min at 126 °C. The wafer was exposed again with the second layer photomask at an exposure dose of 250 mJ/cm² and post-exposure baked at 105 °C for 80 s. The master mold for the fluidic layer was completed by development in AZ 326MIF for 3 min, rinsing with DI water, and drying with $N_2$.
The photoresist masters of the gas and fluidic layers were treated with TFOCS in a desiccator for 30 min before PDMS casting. Pre-mixed PDMS (10:1 w/w) was poured onto the molds, degassed, and baked at 80 °C for 2 hours. The PDMS chips were carefully peeled off from the masters. Meanwhile, the elastic membrane was produced on another silicon wafer. In brief, a pre-cleaned wafer was treated by vapour-coating with TFOCS in a desiccator for 30 min. Pre-mixed and degassed PDMS (10:1 w/w) was then spin-coated onto the wafer at 3000 rpm for 30 s by the spin-coater (WS-650, Laurell), and cured by baking on a hotplate for 2 hours at 80 °C.
The photomask, photoresist master and PDMS chip for the gas layer with various air chamber sizes, and two photomasks for the fluidic layer are shown in Appendix C.1. The photomask for the first negative photoresist layer contained the measurement channel outlines and valve seats, while the second layer photomask for positive photoresist contained the opposite chrome patterns of the first layer with the addition of the force sensing micropillar. The completed two-layer photoresist master, made of negative (ADEX05) and positive (AZ 40XT) photoresist using the masks mentioned above, and the corresponding fabricated PDMS fluidic chip are shown in Fig. 5.2. As shown in Fig. 5.2(g), micropillars were measured as 23 $\mu$m in height using a 3D profilometer (Profilm3D, Filmetrics), while the measurement channels were on average 29 $\mu$m deep.
The gas layer and PDMS membrane were bonded by oxygen plasma as described in Section 4.2.2. After manually punching the gas inlet port using a 1 mm diameter biopsy punch, the gas layer was bonded to the PDMS membrane, still attached to the silicon wafer, by oxygen plasma (100 W, 30 s) and heated for 2 hours at 80 °C. Following this, the bonded structure including the PDMS membrane was carefully peeled off from the wafer and the zoospore and media inlets/outlets ports manually punched using the same sized biopsy punch. Finally, the fluidic layer and membrane with gas layer were both plasma-treated again ($O_2$, 100 W, 30 s), visually aligned and

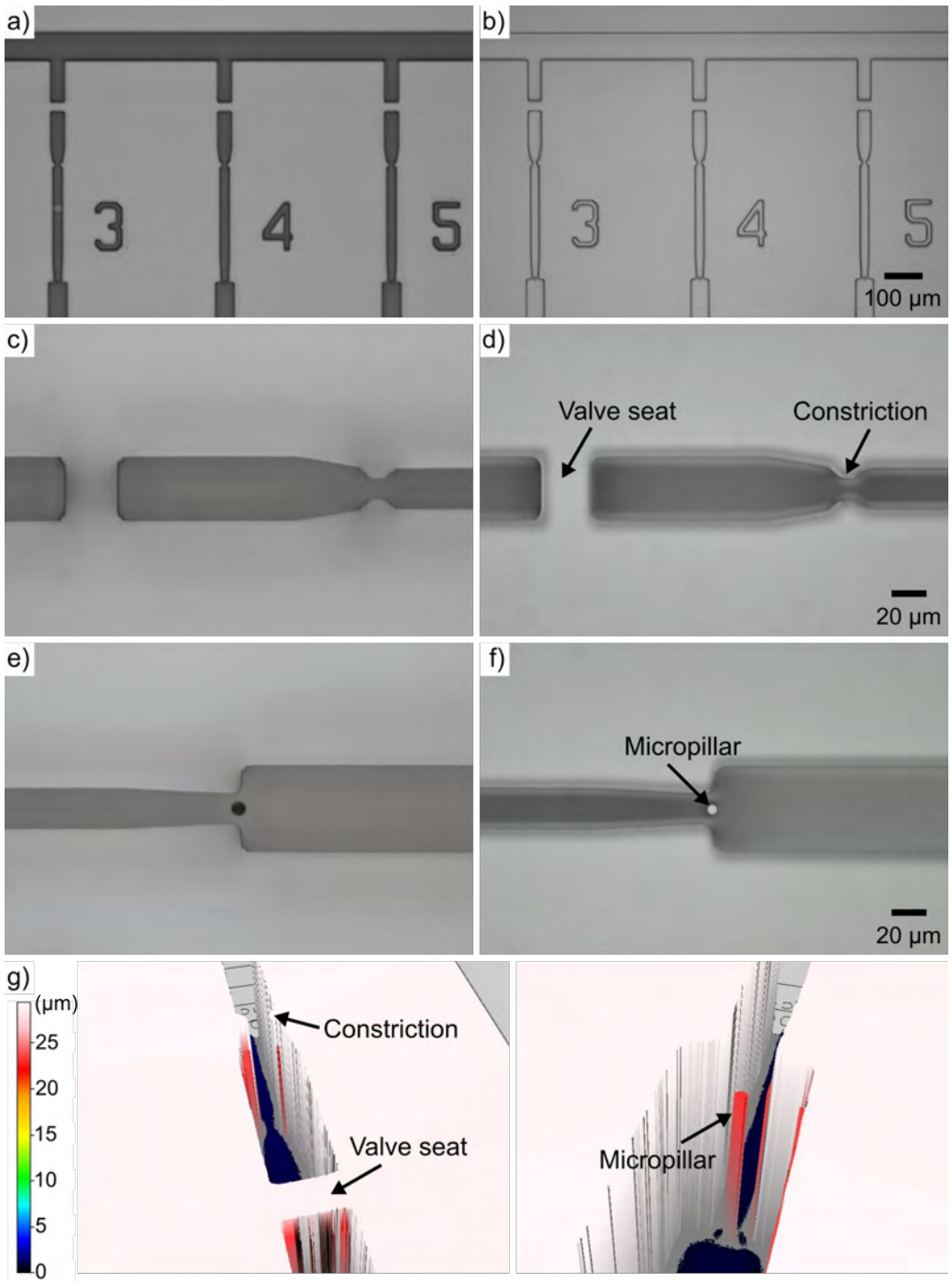


Figure 5.2: Light micrographs of fabricated photoresist master and PDMS chip for the fluidic layer. (a),(c) and (e) The master wafer and detailed view of the valve seat, constriction structure and micropillar cavity. (b),(d) and (f) The PDMS fluidic chip and corresponding details. (g) Height measurement of the PDMS chip using 3D profilometry, showing the valve seat, trap constriction and force measurement micropillar. As indicated, the top of the monolithically integrated micropillar terminates 5 $\mu$m below the channel height.

bonded together.

As mentioned in the previous Section 5.1, various methods have been developed to prevent the PDMS membrane from permanently attaching to the valve seat. Most of these require additional treatments of chip surfaces or optimization of plasma bonding conditions [200]. In order to not further complicate the fabrication processes, vacuum pressure was instead applied to the sealed gas layer during the alignment, bonding and baking processes [205, 206]. This vacuum was held throughout the whole process and prevented the valve membranes from contacting their respective valve seats while the surfaces of both layers were oxygen-activated. To achieve this, firstly a vacuum test of bonded gas layer and PDMS membrane was implemented before bringing them in contact with the fluidic chip. The gas inlet port was connected to blunt end 90 degree bent tip needles (18 gauge), Teflon tube and then a vacuum pump (Anest Iwata Sparmax Co., Ltd.).

Initially, a vacuum weakening (decreased light reflection of membrane) was observed in the microvalve air chambers and connecting channel after vacuum pressure was applied for 3 seconds, as shown in Fig. 5.3(c & d), along with the gas inlet port becoming blocked by the deflected PDMS membrane. This was solved by adding two micropillars (100 $\mu$m in diameter and 100 $\mu$m in height) in the gas inlet port to support the membrane during vacuum application where the port merged into the connecting channel (see Fig. 5.3(e & f)). Moreover, a wide range (from 0 to 0.8 bar) of vacuum pressures were tested to obtain the minimum pressure required to pull the membrane up and form an arch over the valve seat (see Fig. 5.4). The light reflection from the arched membrane initially increased along with increasing vacuum pressure, but changed little beyond -0.6 bar. This indicated that -0.6 bar was the minimum pressure required to fully open the valve.

After initial pressure testing, a customized PDMS aligner, described in Section 4.2.2, was utilized to assemble the gas and fluidic layers. Both the fluidic layer and membrane with the gas layer were first plasma-treated ($O_2$, 100 W, 30 s) before alignment. Then the gas layer with membrane was attached the top holder and connected to a blunt end 90 degree bent needle tip (18 gauge), Teflon tube and the vacuum pump, as shown in Fig. 5.5. It was aligned and brought into contact with the fluidic layer sitting on the XY stage under the microscope while the vacuum was continuously applied to the gas layer. The two layers were irreversibly bonded after being baked for 2 hours at 80 °C with the vacuum on. Figure 5.6 (a & b) show the results of the driving tests of the normally-closed valves, indicating that the PDMS membrane could successfully be pulled up towards the air chamber immediately after bond baking. However, after releasing the membrane 17 hours after bonding, it was found to repeatedly and perma-

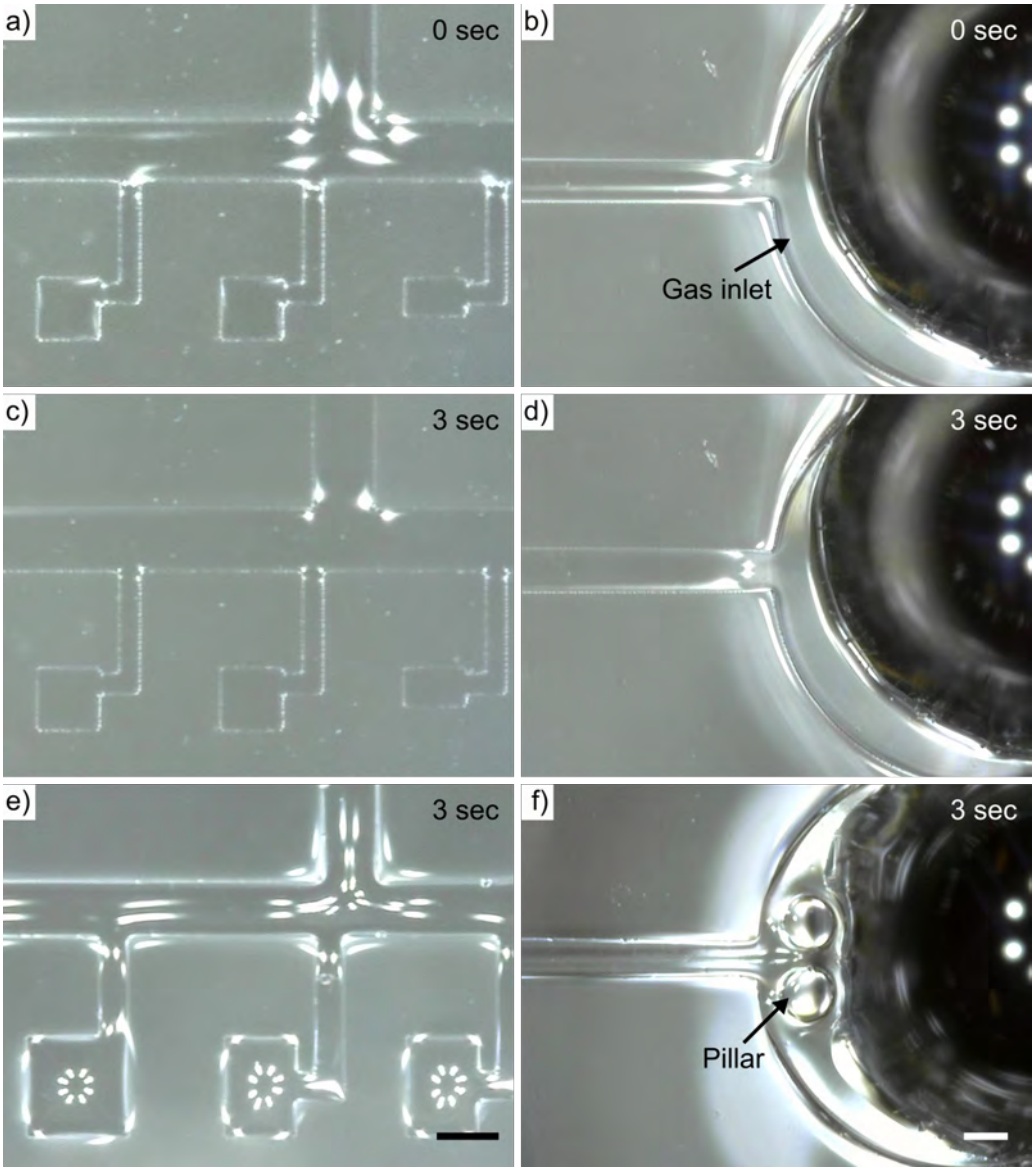


Figure 5.3: Light micrographs showing the vacuum problem of gas layer bonded with PDMS membrane under the vacuum pressure of 0.8 bar. (a & c) Air chambers and their connection channel lost the vacuum after vacuum pressure was applied for 3 seconds. (b & d) The gas inlet port was blocked after vacuum was applied for 3 seconds. (e & f) Air chambers and improved gas inlet port after vacuum pressure was applied for 3 seconds. Scale bar is 50 $\mu$m.

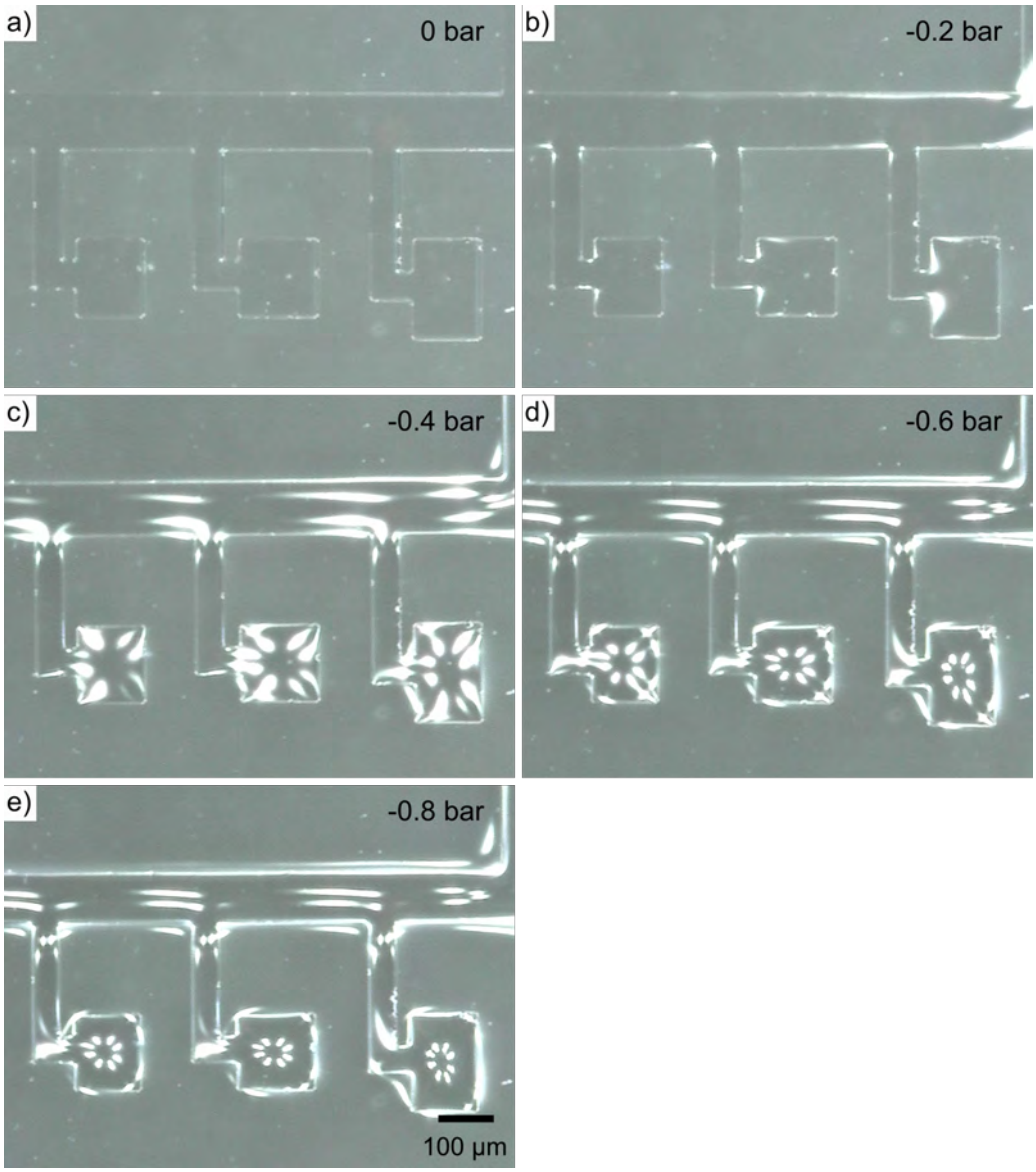


Figure 5.4: Light micrographs of the gas layer attached with membrane while vacuum pressure was applied by a vacuum pump. The image sequence shows pressures of 0, -0.2, -0.4, -0.6, -0.8 bars (a - e) with increasing light reflection indicting larger deflection into the valve chamber in the gas layer. Note: the fluid layer was not attached for this experiment.

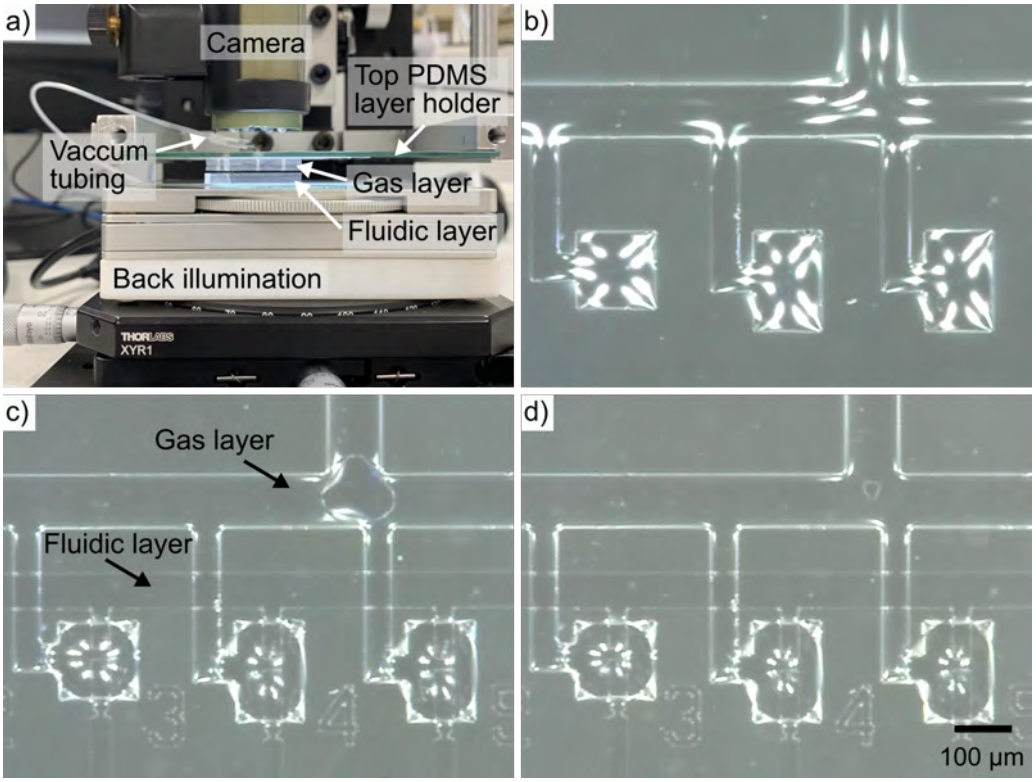


Figure 5.5: Alignment and bonding processes of the fluidic layer and gas layer attached with membrane. (a) Photograph of the customized PDMS aligner and setup. (b & c) Light micrographs of the gas layer before and after bonding onto the fluidic layer. (d) Light micrographs of the bonded chip after 2 hour bake. Note: Light reflection indicates that vacuum was continuously applied during the process, keeping the membrane lifted off the valve seat.

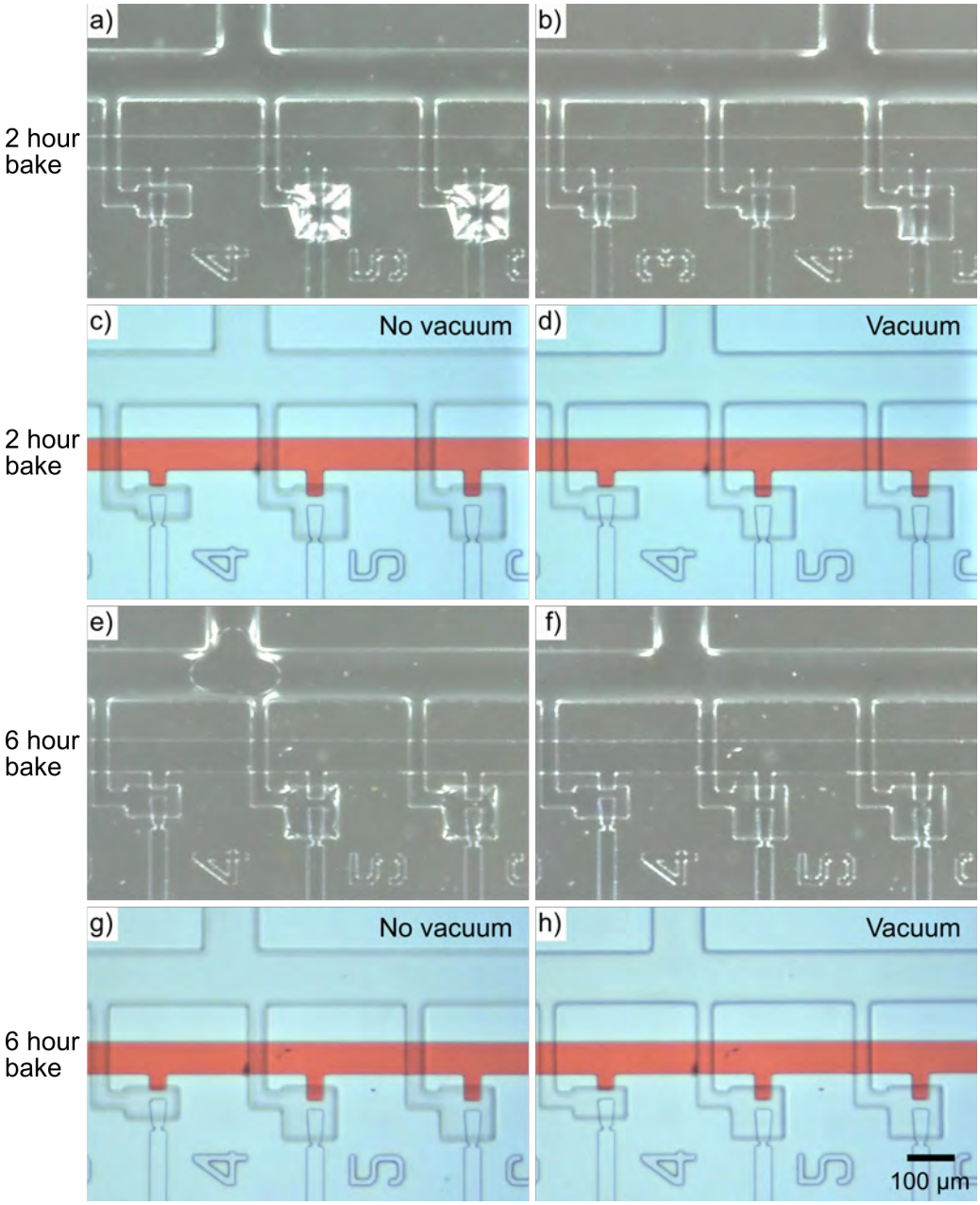


Figure 5.6: Light micrographs showing the microvalve driving test of the assembled platform under negative pressure of -0.6 bar. (a & b) Applied vacuum to the gas layer 0 and 17 hours after the bonding bake at 80 °C for 2 hours. (c & d) Before and after applying vacuum to the microvalves 17 hours after the bonding bake. Red food colouring was injected from the zoospore inlet to better visualize the flow in the measurement channels. No flow into the measurement channels could be observed even after applying -0.6 bar of opening pressure to the valves. (e & f) Application of vacuum to the gas layer 0 and 17 hours after increasing the bonding bake at 80 °C to 6 hours. (g & h) Obstruction of flow into the measurement channels before and after applying a vacuum to the microvalves that were long-term baked. In both the 2 hour and 6 hour bake cases, no valve opening could be observed, indicating accidental bonding of the membrane to the valve seat.

nently attach to the valve seats. Red food colouring was injected from zoospore inlet to better visualize flow before and after the microvalves were opened. This demonstrated that no flow entered the measurement channels even while the vacuum was applied, most likely because the surface effects of plasma oxidation still remained well beyond the 2 hour bake. As a result, the bake time after bonding was increased up to 6 hours to try to reduce the induced hydrophilicity of the PDMS membrane and fluidic chip surfaces. However, the same result of the membrane bonding with the valve seats after 17 hours was observed. This was again despite the membrane being able to be pulled upward into the air chamber by the negative pressure immediately after baking (see Fig. 5.6(e - h)). Therefore, the assembly process was further modified and methanol or DI water were injected into the fluidic layer through the zoospore inlet before stopping the vacuum application. This was done to prevent the PDMS membrane from contacting with the valve seats [207]. After keeping each liquid in the platform overnight, the microvalves of both platforms were verified to open properly while the vacuum was applied (see Fig. 5.7). Compared with the platform filled with methanol, fewer remnants were observed in the measurement channels of the one with DI water overnight (see Fig. 5.7(b & f)). Thus, DI water was used to fill the platform during the following chip assembly.

While successful, this approach presented a new issue in that the force sensing micropillars in the measurement channels could collapse towards the side walls of the channels after the fluidic chip dried out (see Appendix C.2). Given the randomness of the collapsing direction, surface tension effects during the drying process were considered to be the most likely cause for this [208]. To overcome this final issue, the platform was stored with DI water filling in the fluidic layer until further experiments were to be performed. Figure 5.8 shows the final assembled PDMS platform mounted on a slide glass. Blue and red epoxy dyes (Sudan dye, Sigma-Aldrich) were loaded into the platform and cured, following the procedures described by Soffe et al. [209], to visualize the fluidic and gas layers, respectively.

After a reliable manufacturing and layer assembly process had been established, the design of the gas layer had to be optimized to achieve individual control of the membrane valves for each measurement channel and thus avoid the capture of multiple zoospores in the same trap-site. Rather than converging at a single inlet, the air chamber of each valve was connected via a separated gas port (see Appendix C.3). Accordingly, the setup of the PDMS layer alignment and bonding process was adapted, including enlarging the space for connecting the vacuum tubing on the glass top layer holder and addition of a manifold (see Fig. 5.9). The manifold (P-191, IDEX Health Science) enabled 9 separate gas ports to be connected to the vacuum, and thus valve membranes

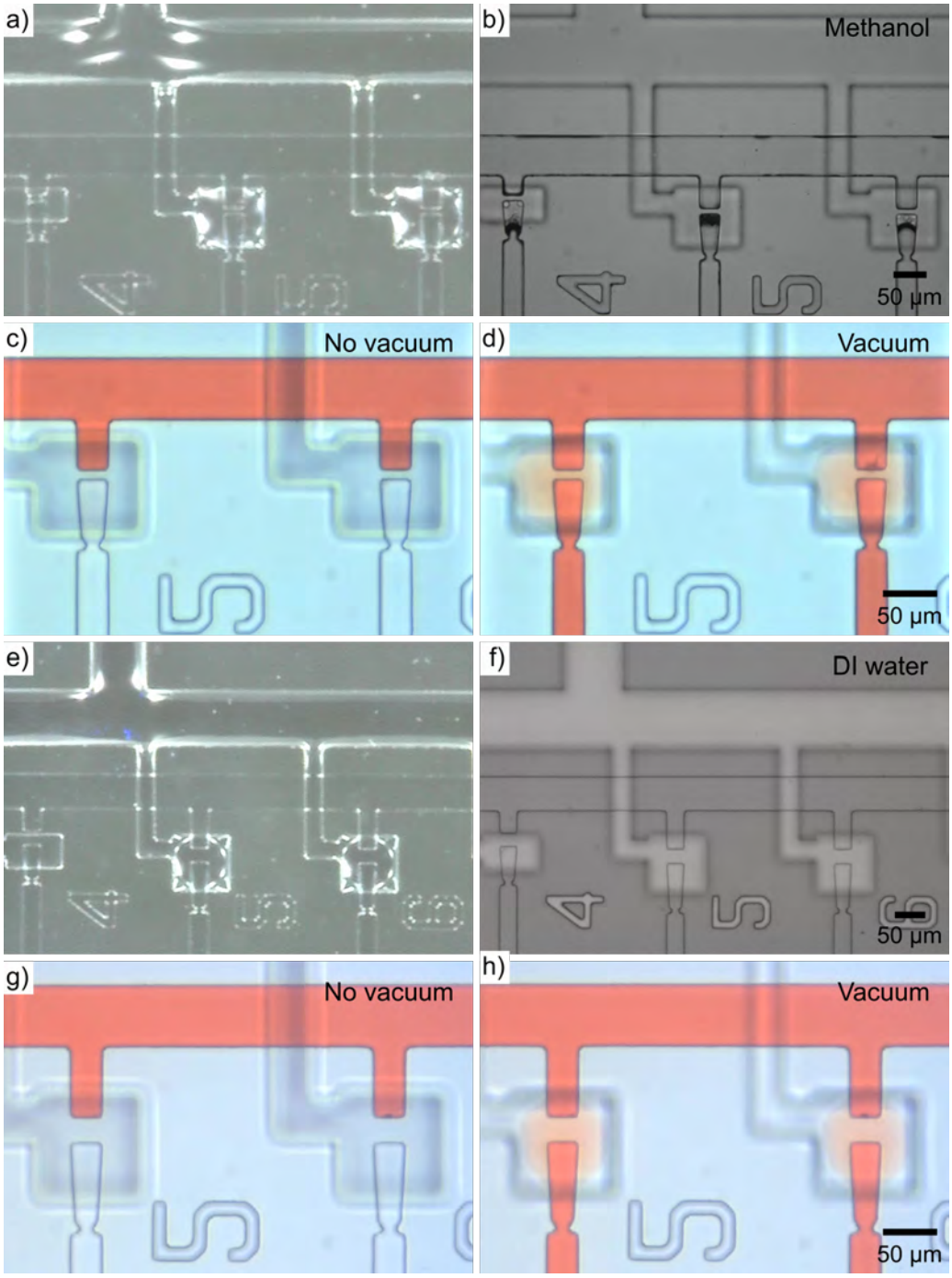


Figure 5.7: Light micrographs showing the microvalve driving test of the assembled platform filling with methanol or DI water. (a) A vacuum was applied to the gas layer after the bonding bake at 80 °C for 2 hours. (b) The fluidic layer was filled with methanol and kept overnight. (c & d) Prior to and after application of a vacuum to the microvalves. Red food colouring was injected from the zoospore inlet to better visualize the flow in the measurement channels. (e - h) The same processes as in (a - d) but the fluidic layer was filled with DI water. In both methanol and DI water cases, the microvalves of both platforms were shown to open properly.

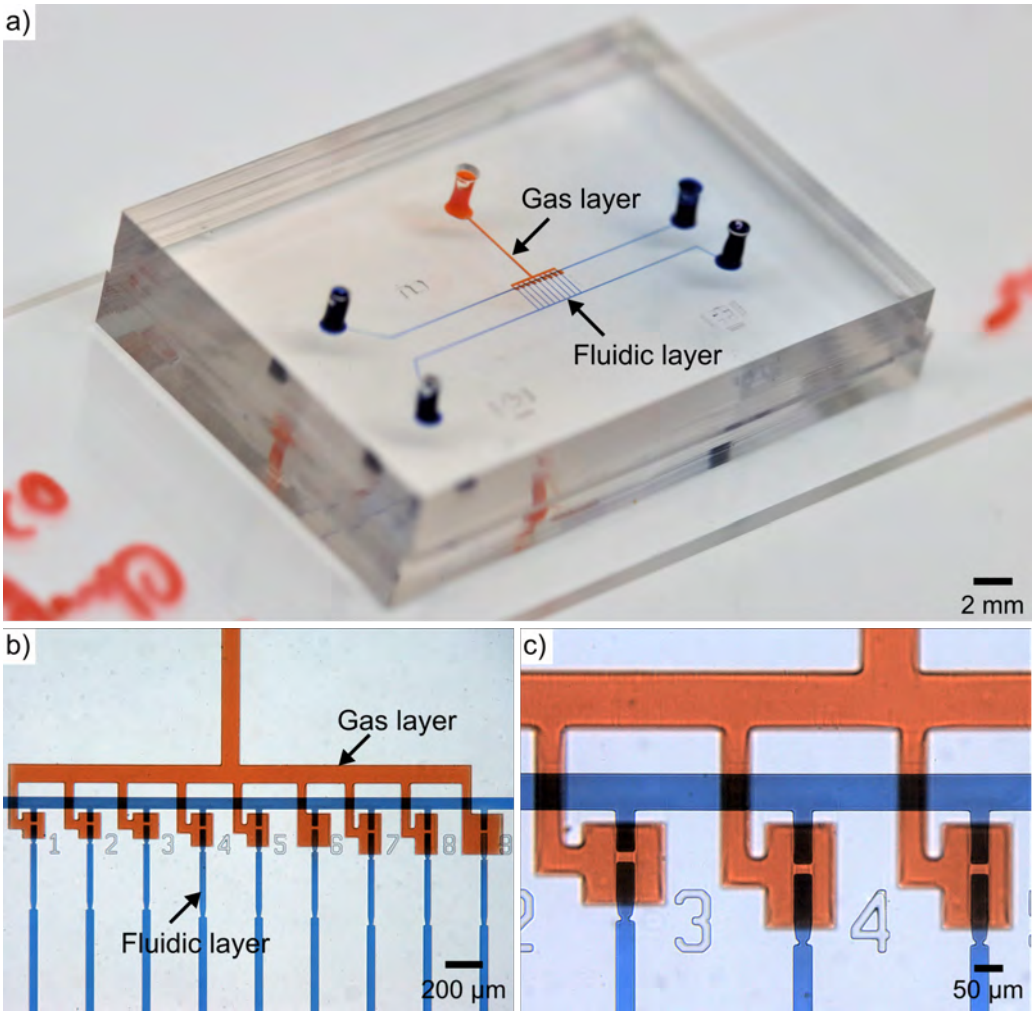


Figure 5.8: An assembled platform containing the two active layers separated by the PDMS membrane. (a) Photograph of whole platform sitting on a slide glass and filled with blue (fluidic layer) and red (gas layer) dye. (b & c) Light micrographs showing details of the platform with various air chamber sizes.

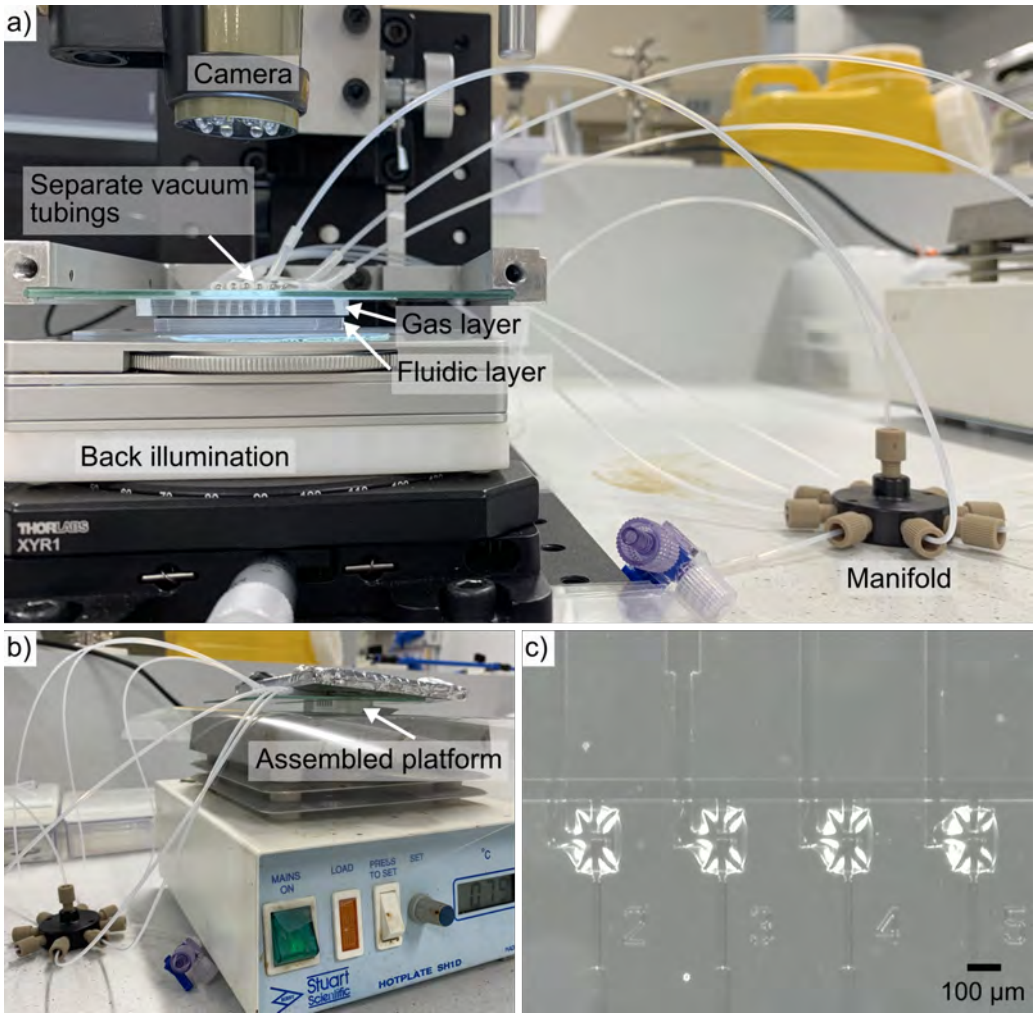


Figure 5.9: Alignment and bonding processes for the PDMS membrane attached to the gas layer and the fluidic layer. (a & b) Photographs of the adapted setup for the separated gas inlets while aligning, bonding two PDMS layers, and baking the assembled platform on a hotplate. (c) Light micrograph of the bonded PDMS chips under vacuum.

retracted at the same time during assembly. Figure 5.10 shows the final assembled PDMS platform incorporating six measurement channels, each with individual valve control, sitting on a slide glass. Different epoxy dye colours were used to visualize separated air chambers and their respective gas inlets, while blue colour illustrates the fluidic channels including each measurement channel. The following section will present results of the valve size optimization, individual valve operation for trapping and fluid flow characterization of the platform.

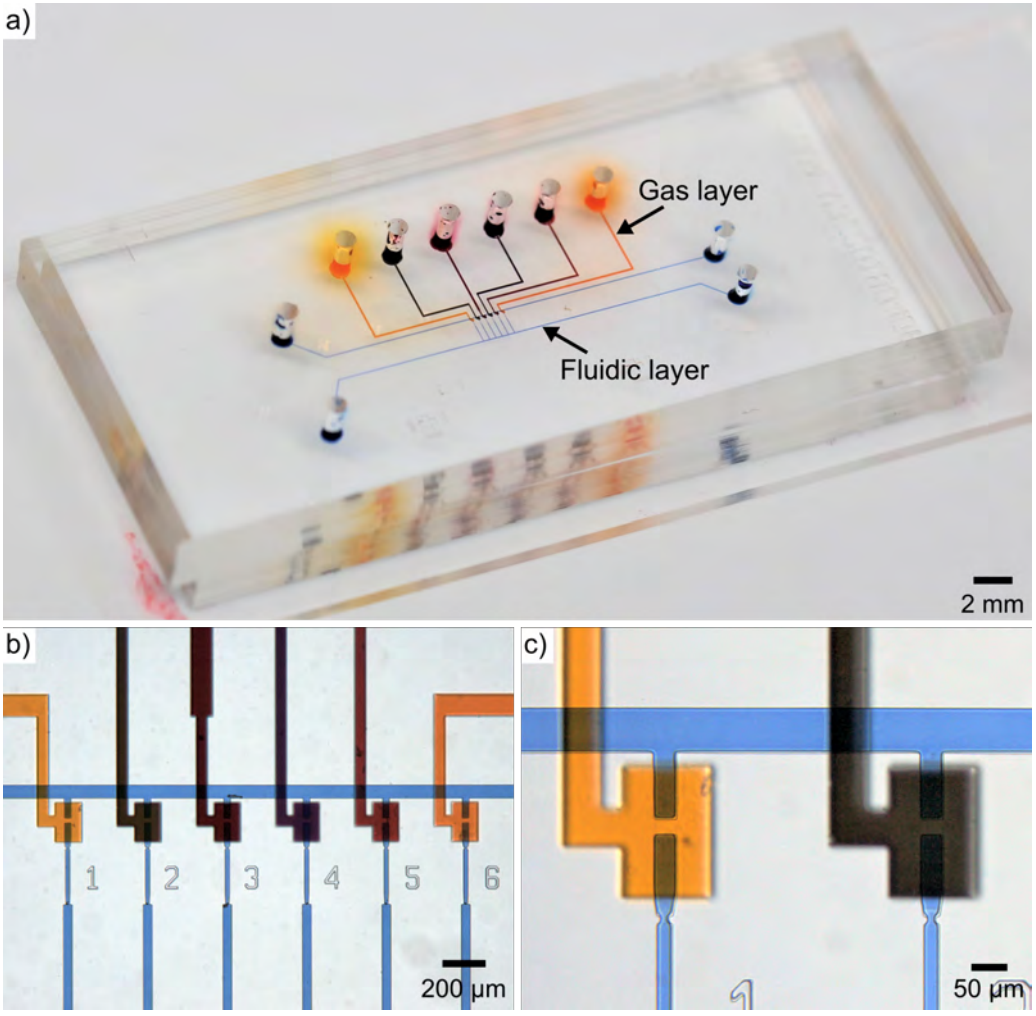


Figure 5.10: An assembled PDMS platform with separate gas inlets for each of the six valves. (a) Photograph of whole platform sitting on a slide glass and filled with different colour epoxy dyes for individual valve air chambers and blue for the liquid channels. (b & c) Light micrographs of detailed views of the six measurement channels and individually-addressed compartmentalization valves.

## 5.3 Experimental results and discussion

### 5.3.1 Optimization of the air chamber of normally-closed microvalves

Since current normally-closed microvalves are typically utilized for either transportation of chemicals or, at the other extreme, clusters of cells, their sizes are either too big for single zoospore trapping, or the opening space for fluid flow is too small for zoospores to pass the valve seats. As a result, air chamber sizes of the microvalves had to be optimized for the handling of single zoospores, which in the case of *A. bisexualis* commonly range from 8.5 to 10 $\mu$m diameter [210]. Red food colouring solution and polystyrene microspheres (UVPMS-BG-1.00, 10 - 20 $\mu$m in diameter, Cospheric LLC) suspended in DI water were used to optimize the air chambers of the normally-closed membrane valves. Platforms with various sized air chambers, described in Table 5.1, were tested with those to determine whether the valve could be opened by negative pressure, fully closed by positive pressure, and whether the opening space of the fluidic channel was large enough for zoospores to pass through. The experimental setup for the valve driving testing was similar to that mentioned in Section 4.2.4. The zoospore inlet was connected to a 1 mL syringe driven by the syringe pump to introduce the samples into the platform. The pressure controller OB1 MK3+ was utilized not only to provide vacuum and positive pressure to drive the membrane valves via the joint gas port configuration, but also to supply the media at a continuous and constant flow rate from media inlet.

Firstly, the microvalves were shut by applying positive pressure (1.0 bar, maximum pressure for the available OB1) from the gas inlet. The red colouring or DI water with microspheres were then pumped into the fluidic layer of the platform from the zoospore inlet at a flow rate of 10 $\mu$L/min and the behaviour of microvalves of different air chamber sizes was observed while vacuum (-1.0 bar, maximum negative pressure for this OB1) pressure was applied. No light reflection of the PDMS membrane in the air chamber was observed, while the chamber length (A) was 60 $\mu$m (see Fig. 5.11(a)), which indicated that this air chamber was too narrow for the PDMS membrane to deform. Figures 5.11(b & c) illustrate however that the microvalves with A = 100 $\mu$m could successfully be opened after applying vacuum to the air chambers. This was verified via the red food colouring now being able to flow through the valves into the previously closed-off measurement channels. However, in this configuration the flow path between PDMS membrane and top of the valve seat was too small for microspheres to pass through, as shown by microspheres being stopped by the valve

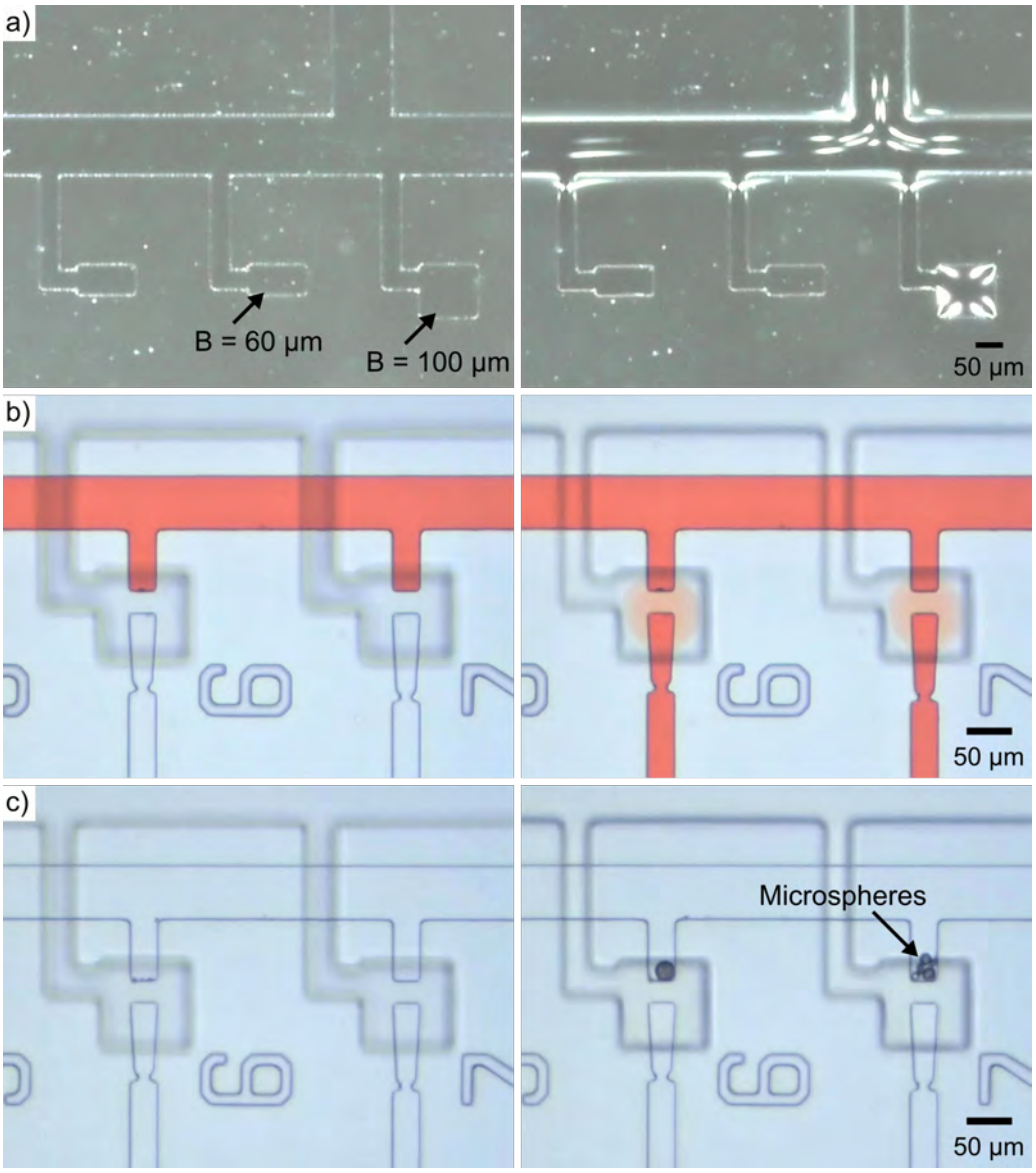


Figure 5.11: Membrane valve driving test A. (a) Light micrographs of the gas layer bonded with PDMS membrane not under a vacuum or under vacuum of -1.0 bar, while the air chamber lengths were 60 and 100 $\mu$m. (b) Light micrographs of the platform with 100 $\mu$m long air chamber, before (left) and after (right) applying vacuum to the gas layer (-1.0 bar). The red colouring was injected from the zoospore inlet before the test. (c) Light micrographs showing microspheres being stopped before the valve seat on the 100 $\mu$m air chamber platform while the microvalves were open.

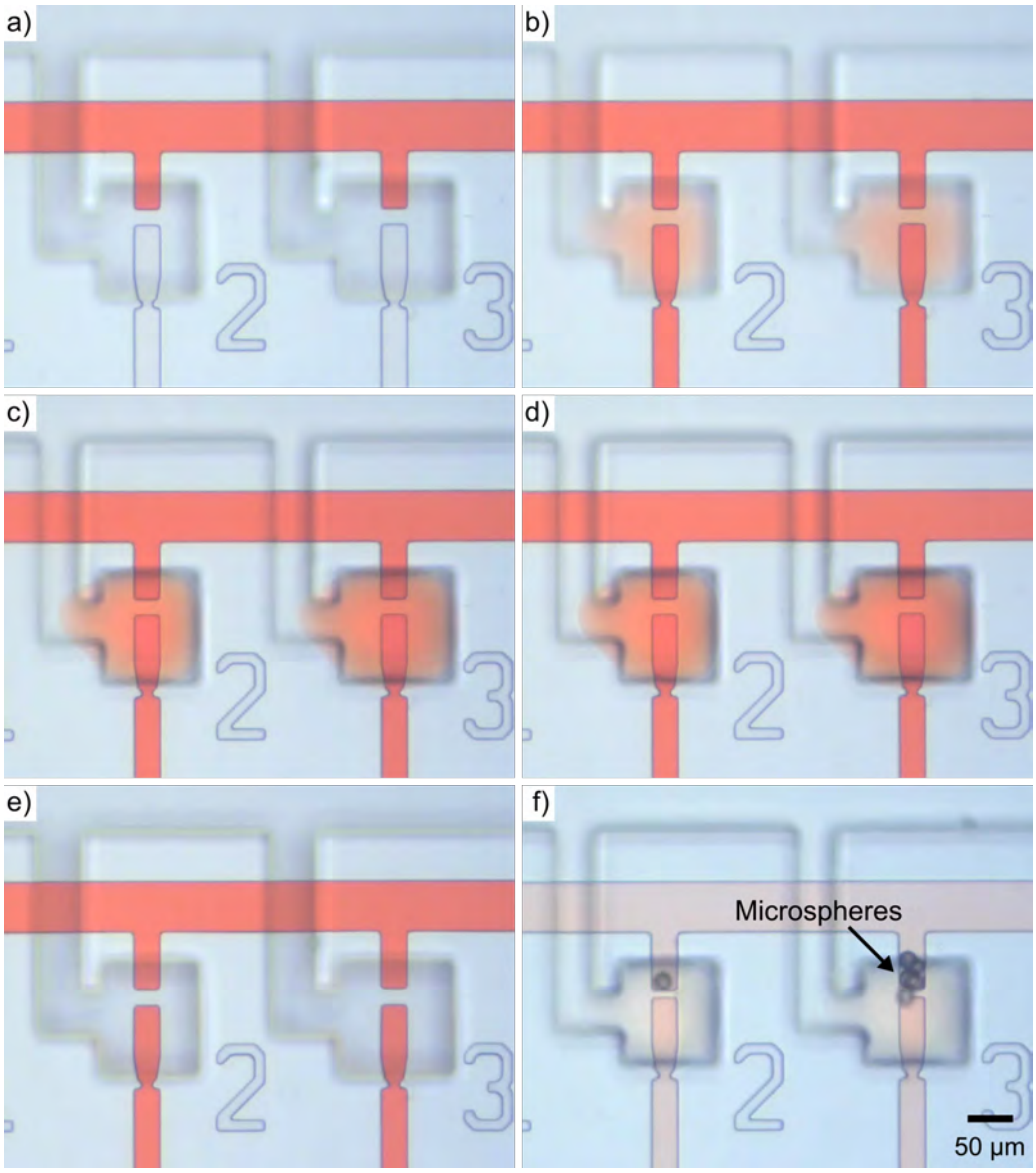


Figure 5.12: Membrane valve driving test B, in which the sizes of air chambers were 140 $\mu$m in length, 120 (channel No. 2) and 140 $\mu$m (channel No. 3) in width. (a-d) Light micrographs of microvalves under positive pressure of 1.0 bar, and negative pressure of -0.1, -0.5, -1.0 bar, respectively, while pumping the red coloured solution from the zoospore inlet. (e) Light micrograph of the microvalve completely closed under positive pressure of 1.0 bar. (f) Light micrograph showing the introduction of microsphere solution under negative pressure of -1.0 bar. Microspheres became stuck before the valve seats due to the insufficient valve membrane deflection.

seats. Similar results were obtained while the air chamber sizes were set at 140 $\mu$m in length, 120 and 140 $\mu$m in width, channel No.2 and No.3 in Fig. 5.12, respectively. In the latter design, the opening area (area filled with red food colouring below the air chamber) of the microvalves was observably larger. Moreover, the red colour became visibly darker while applied negative pressure increased from -0.1 to -1.0 bar, suggesting that the gap between the membrane and the top of valve seat became larger with the increase of applied negative pressure.

Figure 5.13 shows an example of microspheres successfully flowing over the valve seats and being captured by the constriction structure for air chambers that were 180 $\mu$m long. Occasionally, microspheres got stuck in the space between the PDMS membrane and the fluidic layer, rather than flowing along the channel into the trap site (see Fig. 5.13(f), channel No.6, for which chamber width was 180 $\mu$m). This indicated that a wider air chamber, while improving flow-through, also raised the risk that microspheres would become stuck in the valve structure instead of entering the measurement channel. This trend continued when even bigger air chamber microvalves were tested (see Fig. 5.14). Microspheres were able to flow through the microvalves, but the number of microspheres flowing into the measurement channels was less than for other channels, probably due to the lower flow rate for the bigger air chambers. Therefore, the air chamber design with a length of 180 $\mu$m and a width of 120 $\mu$m was utilized in all further experiments.

Finally, microvalve closure tests were conducted by injecting blue food colouring from the zoospore inlet or media inlet, respectively, while a positive pressure of 1.0 bar was applied. For this the microvalves were firstly opened and red food colouring was filled into the whole platform (see Fig. 5.15 (a)). Then the microvalves were completely closed using a positive pressure of 1.0 bar and the blue food colouring was pumped in from the zoospore inlet (see Figs. 5.15 (b - d)). No leakage of the microvalves was observed. This was confirmed by the zoospore loading channel turning blue, while the rest part of the platform remained red and the valve seat clear of colour. Furthermore, the blue colouring entered the measurement channels from the bottom channel by diffusion only, while it was injected from the media inlet (see Figs. 5.15 (e - f)). Using this process, each measurement channel could be turned from red to blue synchronously and completely within around 1 hour, with the perfused media supply channel acting as an infinite diffusion source for each channel. While food colouring was used for this experiment, the dynamics indicate that measurement channels should be able to be equilibrated by diffusion with fresh media within a similar time-scale.

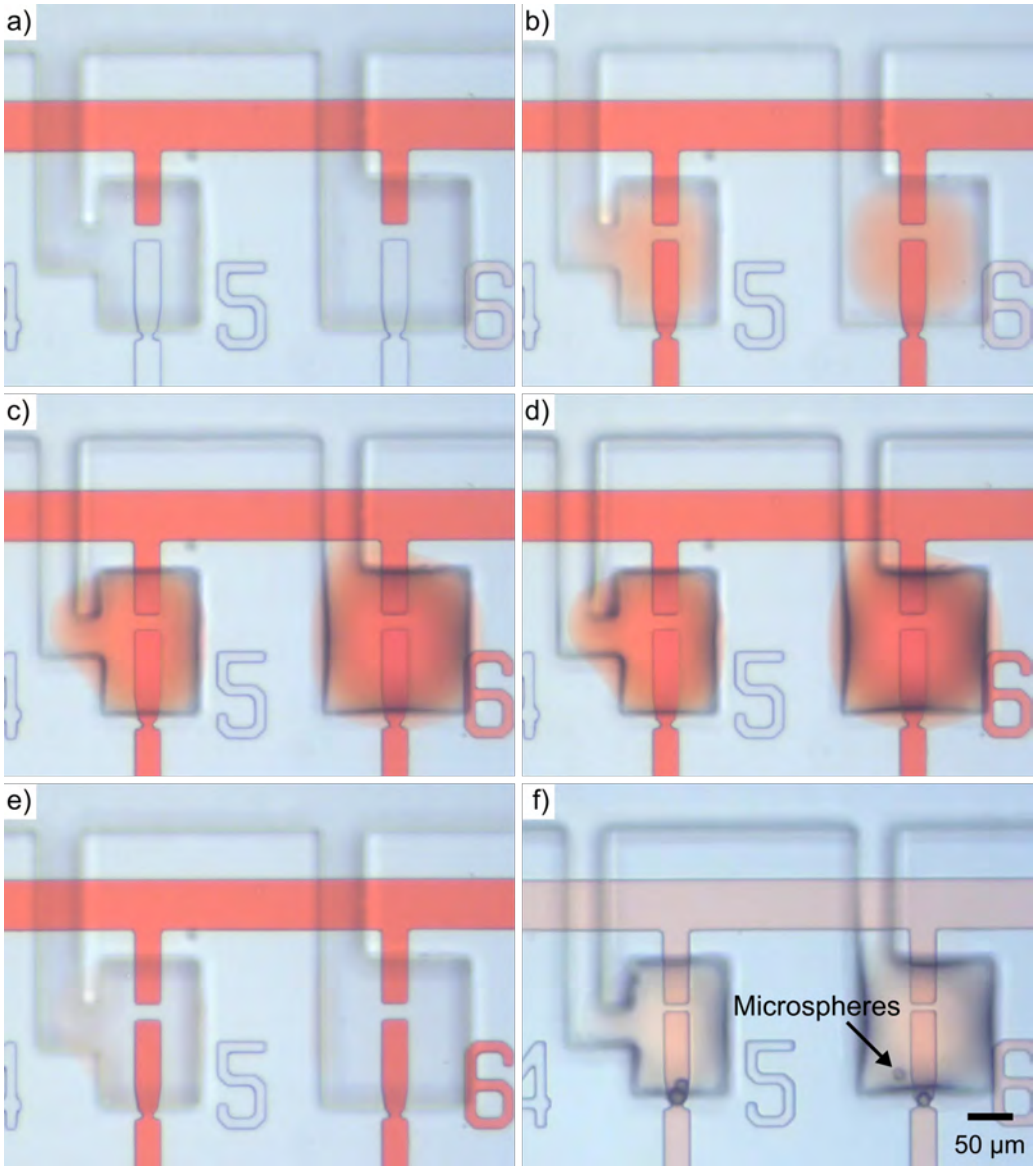


Figure 5.13: Membrane valve driving test C, which the sizes of air chambers were 180 $\mu$m in length, and 120 (channel No. 5) and 180 $\mu$m (channel No. 6) in width. (a-d) Light micrographs of microvalves under positive pressure of 1.0 bar, and negative pressure of -0.1, -0.5, -1.0 bar, respectively, while pumping the red coloured solution from the zoospore inlet. (e) Light micrograph of the microvalve completely closed under positive pressure of 1.0 bar. (f) Light micrograph showing the introduction of microsphere solution under negative pressure of -1.0 bar. Microspheres successfully flowed over the valve seat and became trapped by the constrictions.

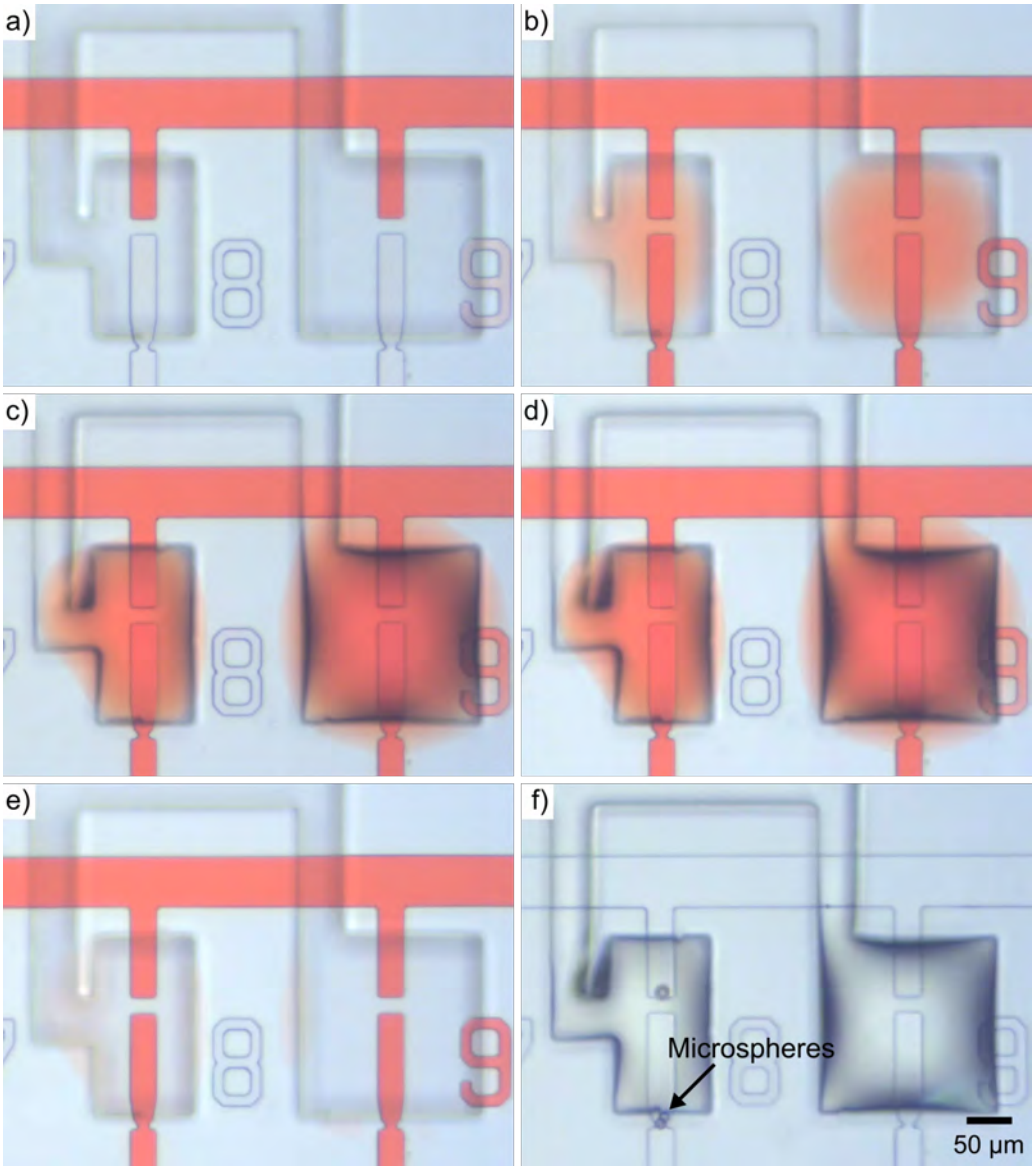


Figure 5.14: Membrane valve driving test D, which the sizes of air chambers were 220 $\mu$m in length, and 120 (channel No. 8) and 220 $\mu$m (channel No. 9) in width. (a-d) Light micrographs of microvalves under positive pressure of 1.0 bar, and negative pressure of -0.1, -0.5, -1.0 bar, respectively, while pumping the red coloured solution from zoospore inlet. (e) Light micrograph of the microvalve completely closed under positive pressure of 1.0 bar. (f) Light micrograph showing the introduction of microsphere solution under negative pressure of -1.0 bar. Microspheres successfully flowed over the valve seat and became trapped by the constrictions.

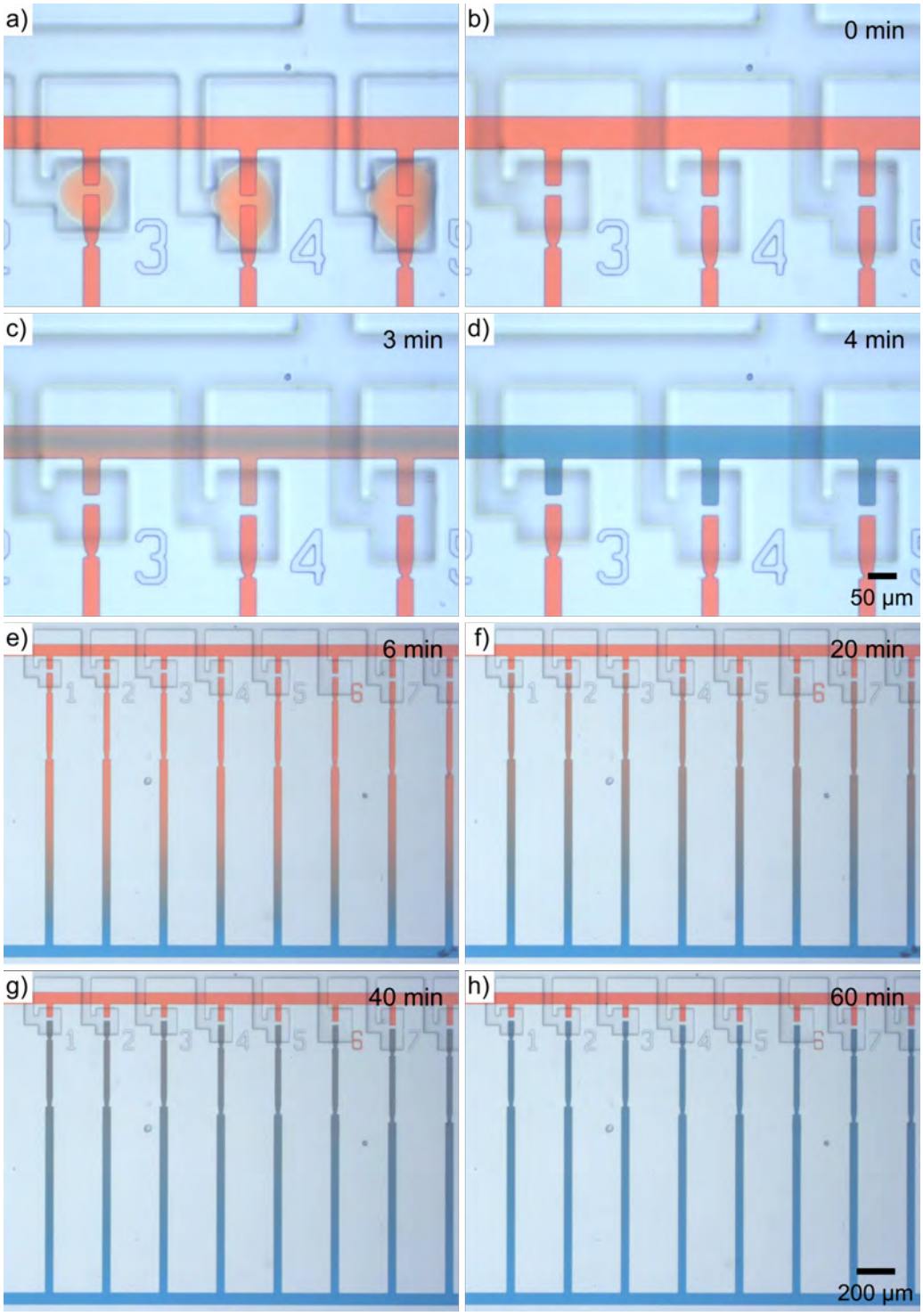


Figure 5.15: Membrane valve closure test. (a - d) Light micrographs showing microvalves open, completely closed, and blue colouring injected from zoospore inlet to demonstrate compartmentalization. (e - h) Light micrographs showing the blue food colouring diffusing into the measurement channels and replacing the red colour, while blue was pumped through the media channel with microvalves completely closed.

### 5.3.2 Adapted experimental setup and verification of experimental procedure using independently controlled microvalves

Individual control of normally-closed microvalves was achieved using the setup depicted in Figure 5.16. A flow switch matrix (MUX QUAKE VALVE, Elveflow) was introduced between the pressure controller OB1 and gas inlet ports to operate individual microvalves in three states, including fully open (negative pressure = -1.0 bar),

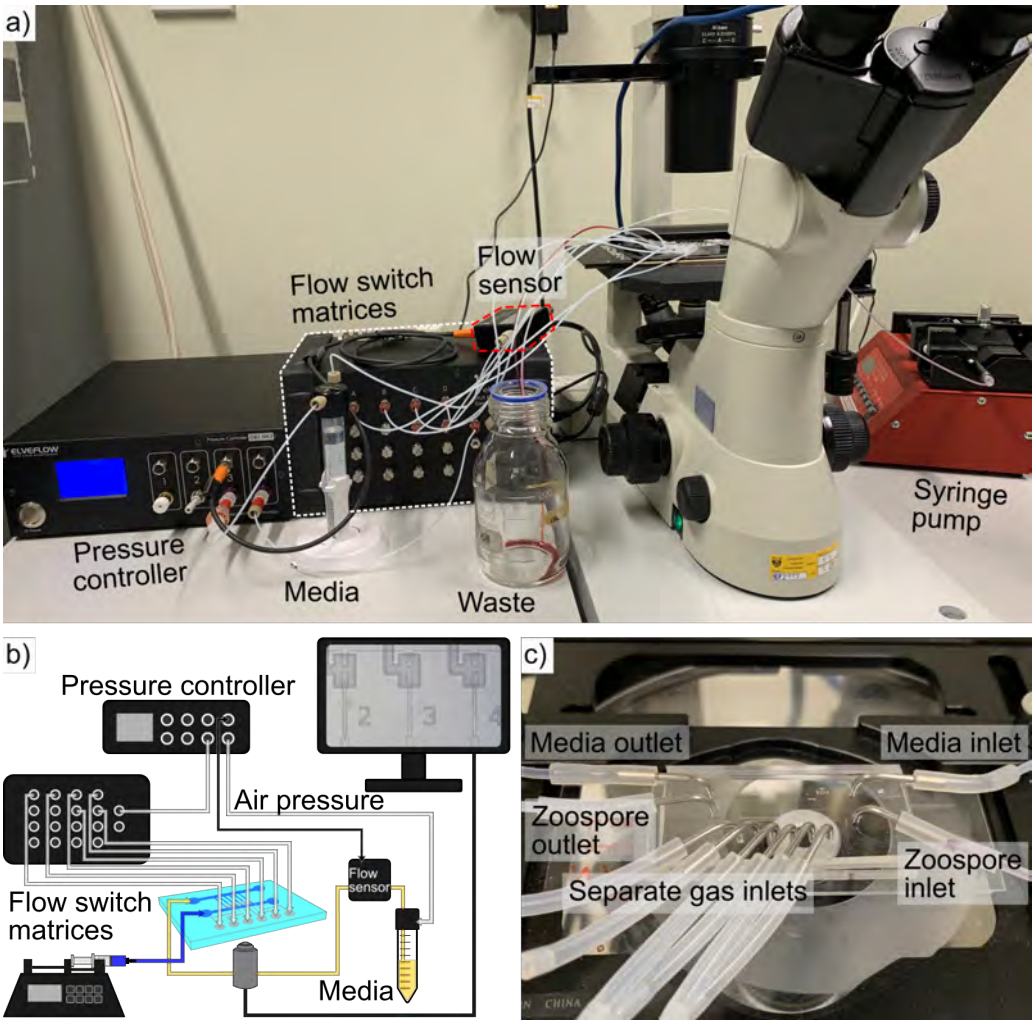


Figure 5.16: Experimental setup for individual microvalve control. (a) Photograph of the setup including a syringe pump for sample injection, microscope with digital camera, a flow sensor, pressure controller for microvalve driving and media supplement, and flow switch matrix for individual microvalve control. (b) Schematic diagram showing the connection of each part. A flow switch matrix was added to achieve independent control of separate microvalves. (c) Photograph of the platform sitting on the microscope, with the inlet and outlet ports connected with tubing.

partially closed (pressure = 0 bar), and completely closed (positive pressure = 1.0 bar). Blunt-end 90 degree bent needle tips (18 gauge) and silicone tubes were utilized to connect inlet and outlet ports to the other equipment to optimize available space between each port. It is important to note that efficient use of external fluid and gas interfaces becomes increasingly important on devices with multiple measurement channels, such as the six side-by-side gas inlets required to control the current platform. This problem is not new or unique to this particular platform [211] though and high-density microfluidic interfacing approaches continue to evolve [212–215].

Similar as in the previous experimental setup, the media inlet was connected to a flow sensor, then a 5 mL reservoir filled with media and pressure controller OB1 to provide constant and continuous flow of media during zoospores culture. The entire experiments were observed and recorded using the inverted microscope TS100 and attached digital colour camera.

The performance of the separately controlled membrane valves was tested using 20 $\mu$m diameter microspheres suspended in DI water coloured with food dye to simulate and visualize zoospore media. The microsphere solution was firstly injected from the zoospore inlet by the syringe pump at a flow rate of 10 $\mu$L/min while all of the microvalves were fully open. For this the pressure applied by OB1 was set to -1.0 bar and all switches of MUX were set to ON in the Elveflow software suite. In the particular example, a single microsphere flowed along the zoospore loading channel, passing over the valve seat and was eventually trapped by the constriction structure as intended (see Fig. 5.17(b), channel No. 2). Then, to demonstrate compartmentalization and retention, only the microvalve of channel No.2 was partially closed and the rest of the valves on the platform were kept open. This was achieved by first keeping the pressure of the OB1 at -1.0 bar and then turning the switch corresponding to the particular microvalve off, which caused the applied pressure to become 0 bar. Similarly, the microvalve of channel No. 3 was partially closed after a microsphere was captured in the trap-site. Since the membrane valves were not completely closed yet, a slow flow continued to be present in the measurement channel, from top to bottom in the Fig. 5.17(f), which resulted in microspheres unceasingly flowing into the measurement channels. However, all these microspheres were successfully stopped by the very small opening space between PDMS membrane and top of the valve seat. This operation was repeated until all six channels had a single microsphere captured, demonstrating the possibility of controlled and selective compartmentalization of zoospores. Compared to previously published work with conidia, valves could be closed individually, allowing for a finer level of control without the need for resist reflow during fabrication [109].

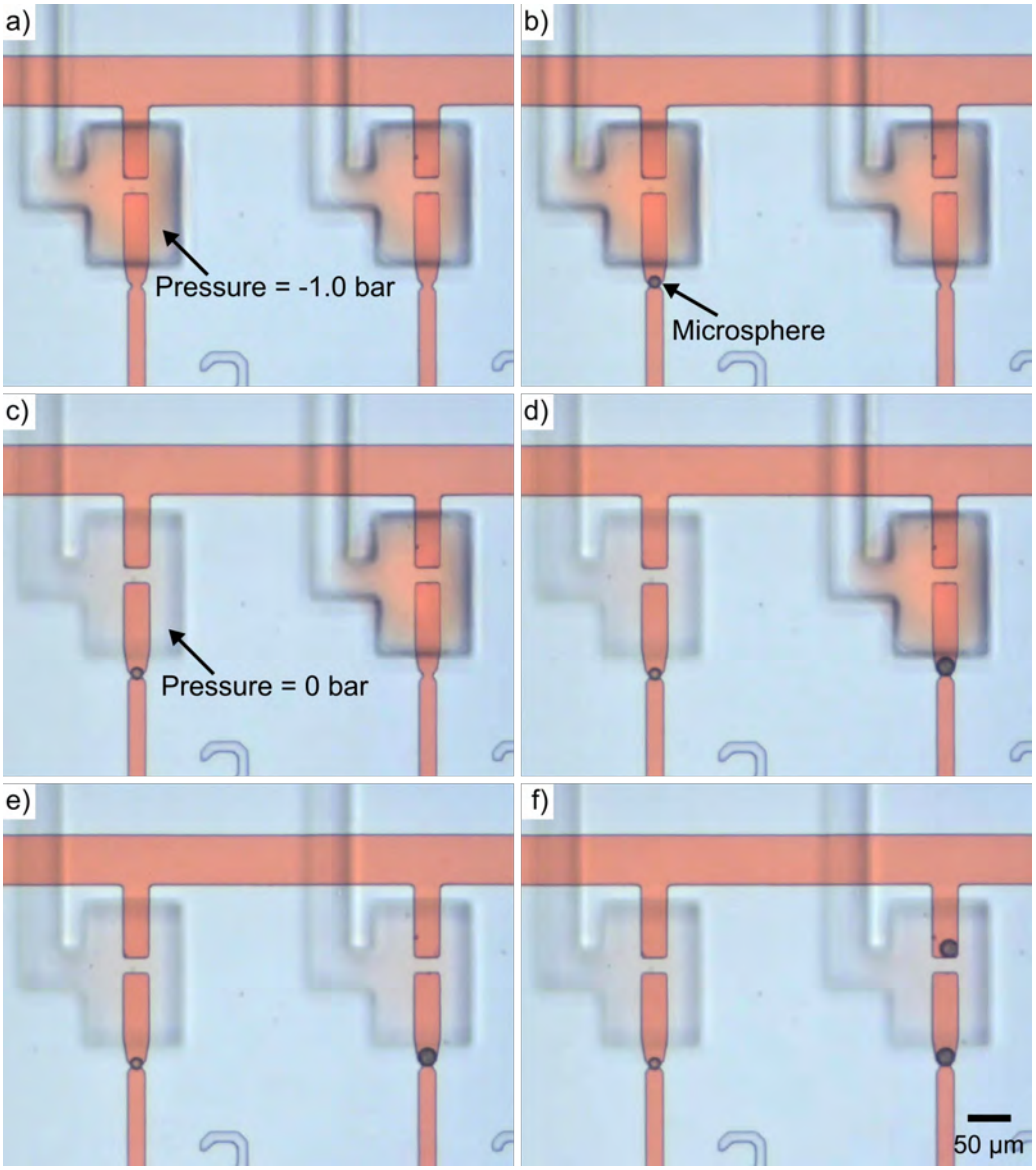


Figure 5.17: Experiments on individual membrane valve closure and microsphere capture. (a - c) Light micrographs showing all microvalves were initially open (vacuum pressure = -1.0 bar), then the microvalve of channel No. 2 was partially closed (pressure = 0 bar) after a microsphere was captured in the trap site of the channel. (d & e) Light micrographs showing another microsphere trapped in measurement channel No. 3, after which the corresponding microvalve was partially closed. (f) Light micrograph showing that microspheres kept flowing into the measurement channels due to the slow flow rate in the channel, but these were stopped by the valve seat.

After microsphere compartmentalization, the sample introduction was stopped and microsphere- and colour-free DI water as media analogue was pumped into the platform at a flow rate of 5 $\mu$L/min via the media channel inlet. This allowed unwanted microspheres located before the valve seats to be flushed away and out of the platform via the zoospore loading channel outlet (see Fig. 5.18(b)). While some of the trapped microspheres moved towards the valve seat during this process, these were successfully retained by the partially closed microvalves. The whole platform became clear, from bottom to top as shown in Fig. 5.18(e), indicating that the media exchange was completed successfully without loss of any of the compartmentalized zoospores. Besides clearing the platform of unwanted zoospores, this process also synchronizes the media conditions in all the six media channels, which may become de-synchronized due to the sequential nature of zoospore loading and subsequent consumption of media components [216]. Finally, the pressure of OB1 was set to 1.0 bar, and all switches of the MUX were set back to ON to make the membrane valves completely close. Then, DI water with red food colouring was injected again from the zoospore inlet. Only the zoospore loading channel became red and the rest of the platform remained clear, demonstrating that there was no leakage through the microvalves while they were in the fully-closed state brought about by application of positive pressure.

### 5.3.3 Flow characteristics of the platform integrated with individual control of normally-closed microvalves.

Biological microorganisms, such as bacteria [217, 218], conidia [219] and zoospores [220, 221], are inherently susceptible to mechanical interactions and may change their morphology or behaviour in response to external inputs [222, 223]. Fluid flow and resulting shear stresses constitute one such potential interaction [224, 225] and it is thus important to characterize what conditions microorganisms may be exposed to on the platform described in this work. Due to the nature of the platform design using hydrodynamic traps, zoospores on the platform are only really exposed to convective flow and shear during the loading process. Once trapped and synchronized behind the closed valves, media exchange to the zoospores is by diffusion only, removing any potential flow effects. Thus, flow rates on the platform were characterized using external flow sensors during the loading procedure and as a function of valve actuation, as shown in Table 5.2.

The experimental setup for this flow characterization was similar as that described in previous Section 5.3.2. Three flow sensors (MFS, Elveflow) were added to the zoospore inlet and outlet, and media outlet each and connected with a sensor reader

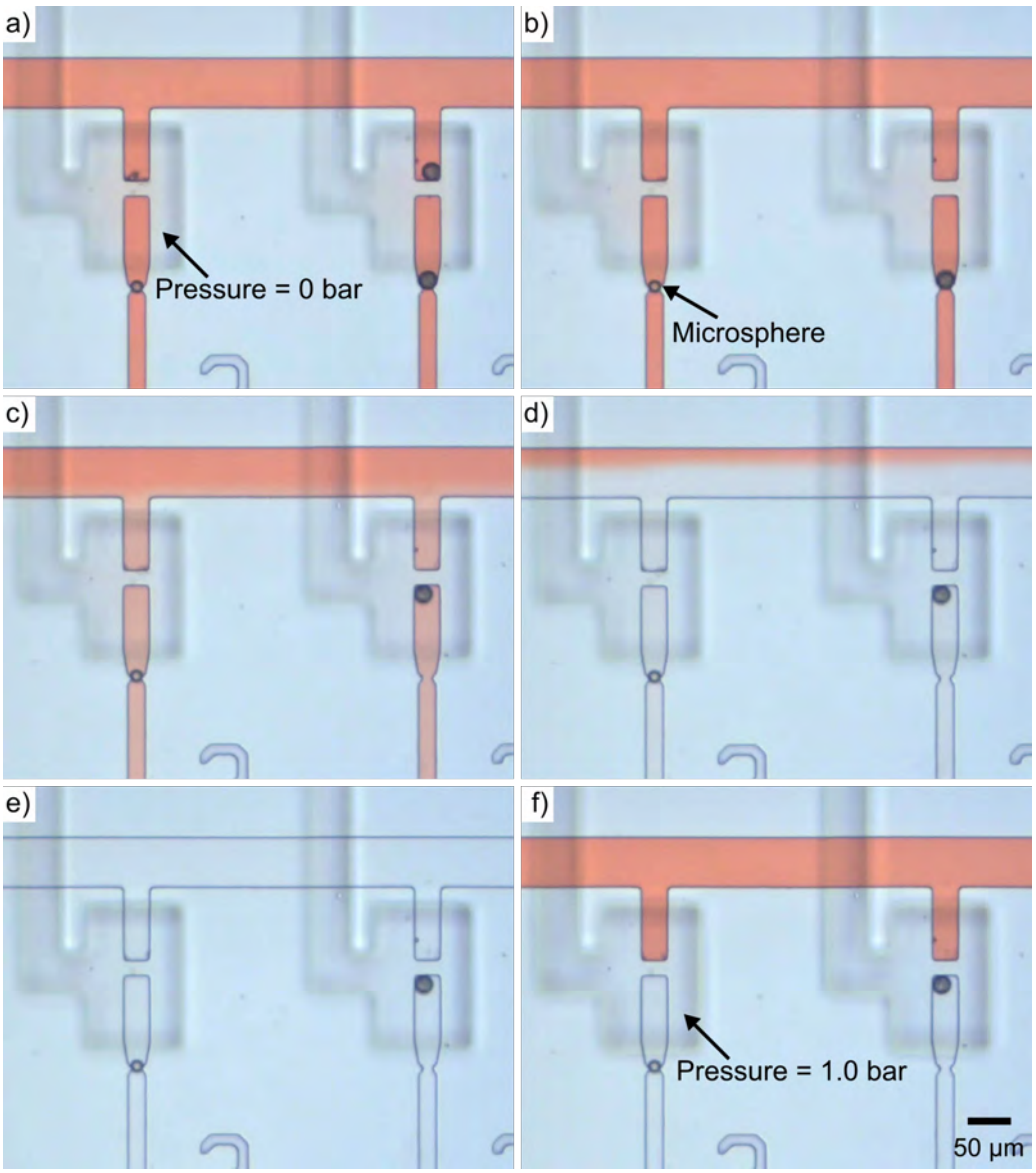


Figure 5.18: Experiments on media exchange and membrane valve complete closure. (a - c) Light micrographs showing the DI water pumped from the media inlet, while the pressure of all the microvalves was 0 bar. The microsphere before the valve seat in channel No. 3 could be flushed out of the channel and the one captured in the trap site moved but remained trapped by the partially closed microvalve. (d & e) Light micrographs showing the red colour in the measurement channels fading from the bottom channel to the zoospore loading channel until the whole platform was filled with clear DI water. (f) Light micrograph showing the membrane valves were completely closed by a positive pressure of 1.0 bar. Red colouring was pumped in again from the zoospore inlet to verify that there was no leakage through the microvalves.

Table 5.2: Operational processes of flow characteristics tests on the platform with independently-controlled, normally-closed microvalves.

| Test | Stage | Pressure applied via OB1 (bar) | Flow switch matrix MUX | Resulting membrane valve status |
|---|---|---|---|---|
| A | I - III | -1.0 ⇒ 0 ⇒ +1.0 | All,* ON | All, FO ⇒ PC ⇒ CC** |
| | IV - VI | +1.0 ⇒ 0 ⇒ -1.0 | All, ON | All, CC ⇒ PC ⇒ FO |
| B | I - III | -1.0 ⇒ 0 ⇒ +1.0 | No.1,* ON | No.1, FO ⇒ PC ⇒ CC |
| | IV - VI | +1.0 ⇒ 0 ⇒ -1.0 | No.6, ON | No.6, CC ⇒ PC ⇒ FO |
| C | I | -1.0 | All, ON ⇒ No.1-6,* OFF | All, FO ⇒ No.1-6,* PC |
| | II | +1.0 | No.1-6, ON | No.1-6, CC |
| | III | -1.0 | All, ON ⇒ No.6-1,* OFF | All, FO ⇒ No.6-1, PC |
| | IV | +1.0 | No.6-1, ON | No.6-1, CC |
| D | I | -1.0 | All, ON ⇒ No.1-6, OFF | All, FO ⇒ No.1-6, PC |
| | II | +1.0 | All, ON | All, CC |

* All: All six switches and membrane microvalves operated simultaneously;
No.1 or 6: Only switch No.1 or 6 were set to ON. Others were set to OFF and corresponding microvalves were kept partially closed;
No.1-6: Switch and corresponding microvalve operated in the sequence from No.1 to No.6;
No.6-1: Switch and corresponding microvalve operated in the sequence from No.6 to No.1
** FO: Fully opened; PC: Partially closed; CC: Completely closed

(MSR, Elveflow) to record the real-time flow rate of each inlet and outlet using the Elveflow software suite. During the test, DI water was continuously pumped into the platform from the zoospore inlet via a syringe pump at the flow rate of 5 $\mu$L/min.
Figure 5.19 shows the flow chart of the first flow characteristics test (A) on the normally-closed microvalve platform. During the experiment, all six switches of the flow switch matrix MUX were set to ON. As a result, six membrane valves were fully opened (vacuum pressure applied = -1.0 bar, (I)) at first, then simultaneously changed to be partially closed (pressure = 0 bar, (II)) and then completely closed (positive pressure applied = +1.0 bar, (III)). Following this, the test was repeated in reverse order (IV - VI). The flow rates of zoospore inlet (Zoo.In, yellow line), zoospore outlet (Zoo.Out, gray line) and media outlet (Med.Out, red line) are plotted as a function of time in Fig. 5.20, together with the pressure applied via the OB1.
As can be observed in Fig. 5.20(a), the flow rates of zoospore and media outlets were almost the same, around 2.5 $\mu$L/min, while all the membrane valves were fully opened (stage I). This was expected, as the fluidic resistance of the two flow paths is comparable in the first approximation when all valves were open, as shown in Appendix C.4. The flow rate of the media outlet decreased slightly after all the microvalves were

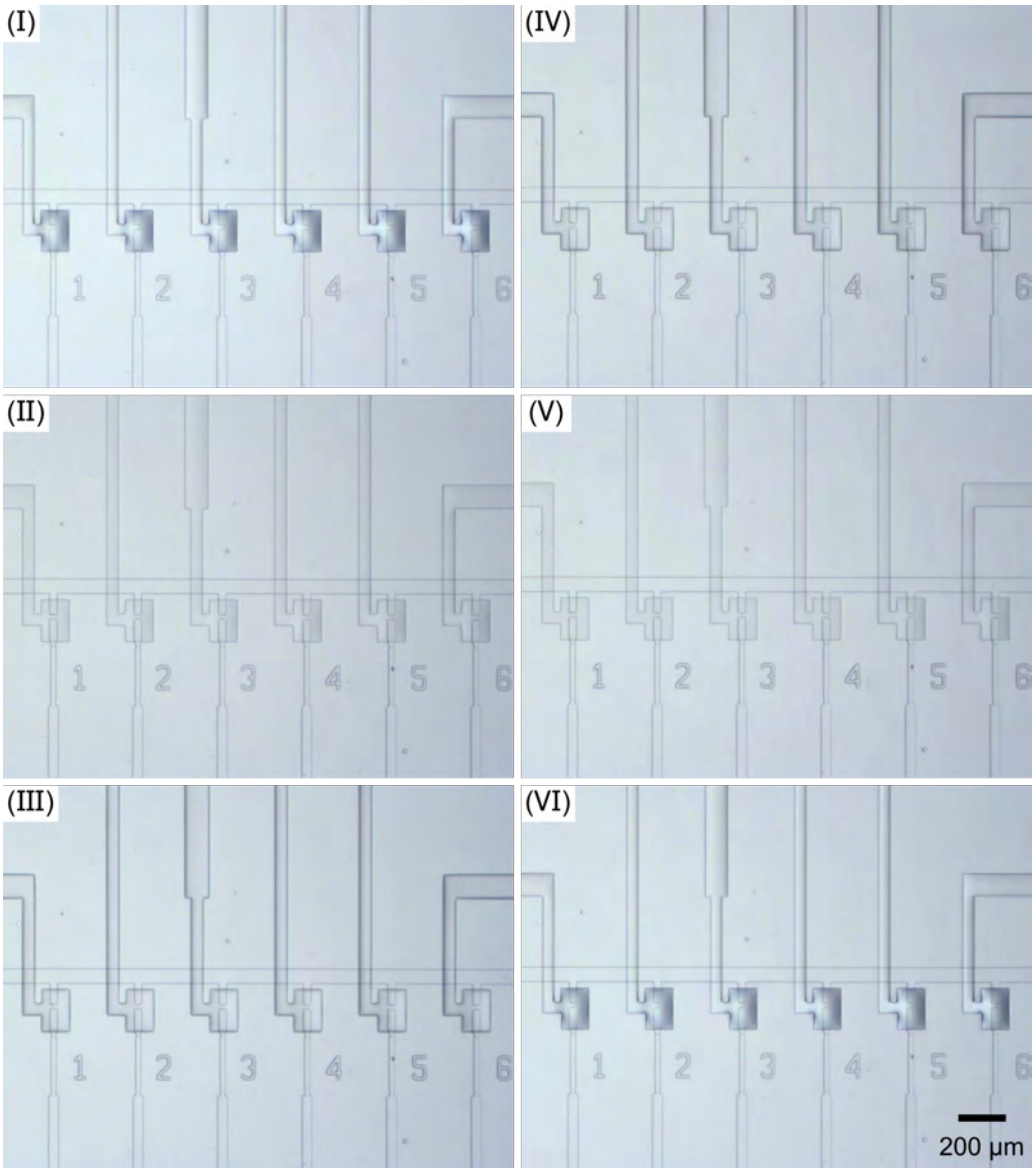


Figure 5.19: Light micrographs of flow characteristics test A. (I - III) All of the six membrane valves were fully opened (vacuum pressure = -1.0 bar), then simultaneously switched to partially-closed (pressure = 0 bar) and completely-closed at last (positive pressure = +1.0 bar). (IV - VI) In reverse order, firstly all of the microvalves were completely closed, then shifted to partially-closed and finally fully opened.

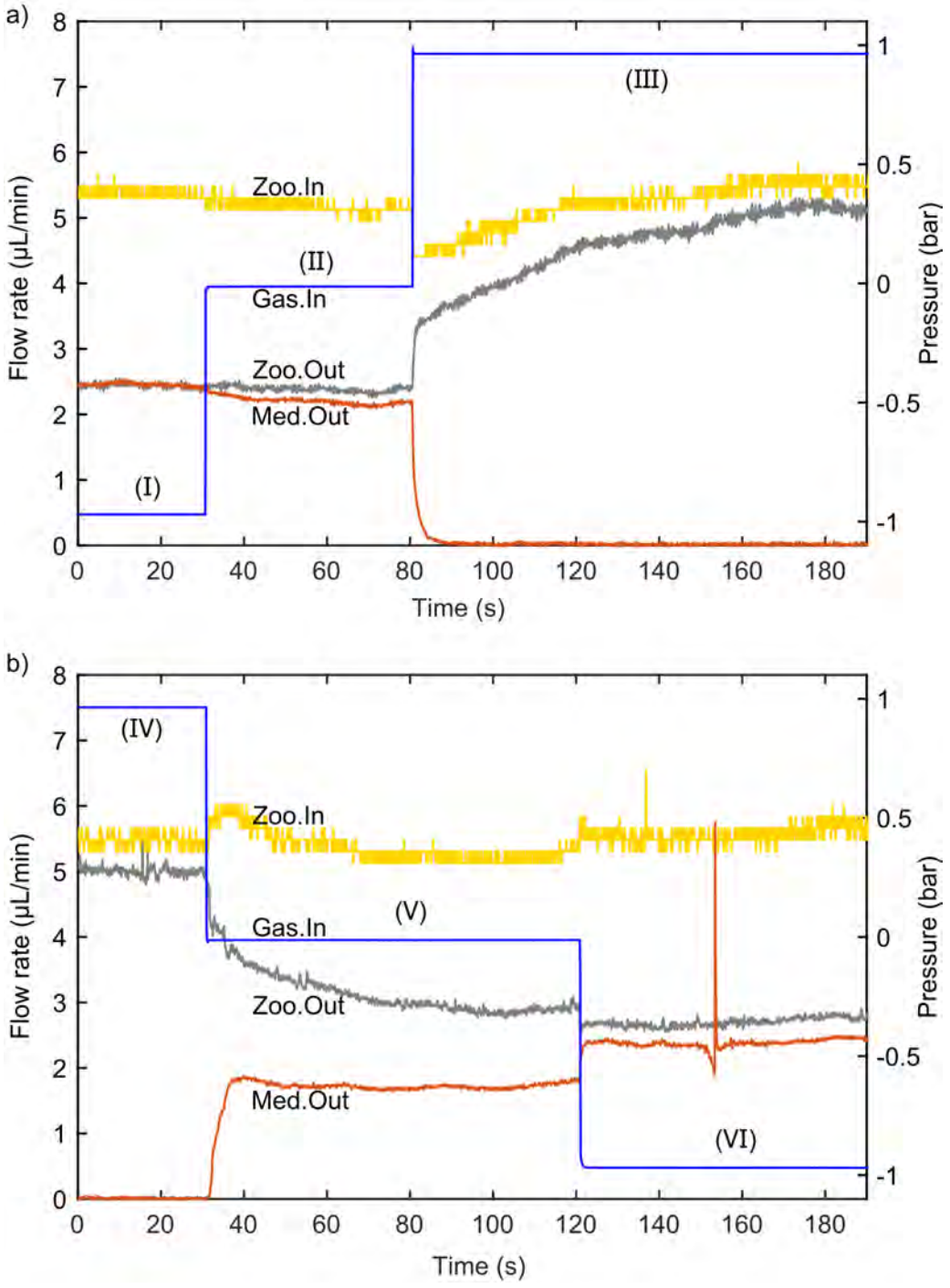


Figure 5.20: Plot of flow characteristics test A. The blue line represents the pressure applied via the pressure controller OB1. The yellow, gray and red lines are the flow rate measured at the zoospore inlet, outlet and media outlet, respectively using the flow sensors. Each stage from (I) to (VI) corresponds to the micrographs shown in Fig. 5.19.

partially closed (stage II). Again, this observation can be explained with an increase in flow resistance in the measurement channels when valves are partially closed, as this flow path only affects the media outlet. Lastly, flow through the media outlet suddenly dropped to zero while all of the valves were completely closed (stage III), a state which, from a flow resistance point of view, renders the media channel connection through the measurement channels and valves open circuit and thus infinite resistance. All the while, the flow rate of the zoospore outlet behaved inversely to this, meaning it increased up to the equivalent, but opposite, flow rate of the zoospore inlet. Almost identical results (see Fig. 5.20(b)) were obtained when all the microvalves were run in the opposite sequence of complete closure, partial closure and then full opening. As before, flow rate changes in both zoospore and media outlets were observed while all the membrane valves were simultaneously switched between the states of partially closed and completely closed.

A difference in flow rate distribution was observed between partially-closed stages II and V, which technically represent the same valve state, but were obtained with differing starting conditions [206, 226]. In brief, the results clearly showed that, in the partially closed state (0 bar pressure) the flow rate distribution through the two flow paths became dependent on whether flow through the valves was already established (II) or previously not present (V). This is most likely due to removal of negative pressure from open to partially-closed state not providing enough closing force against the hydrodynamic pressure of the established flow in state II, together with adhesion and detachment of the membrane from the valve seat [206]. As such, the media outlet flow rate only marginally decreased compared to the zoospore outlet, a result not very representative of this partially-closed state. In state V no flow through the valves was present to start with, so it can be speculated that the membrane does not open as much upon removal of positive pressure, leading to the observed smaller flow out the media outlet and more accurate depiction of the “logic” state the valve is in.

Having demonstrated the suitability of external flow sensors for characterization of platform internal flows, the next test B was implemented to find out the effects of single microvalve on/off switching. Only one switch (channel No. 1 in stage I - III, and channel No. 6 in stage IV - VI) of the MUX was set to ON, which resulted in the other five microvalves being kept partially closed during the experiments (see Appendix C.5). As for test A, the single microvalve was fully opened (pressure = -1.0 bar, I and IV), turned to be partially closed (pressure = 0 bar, II and V) and finally completely closed (pressure = +1.0 bar, III and VI). The results of the flow rate plot, shown in Appendix C.5, confirmed that the sensors attached to each outlet had enough resolution to visualize individual valve closing events. The flow rate of the media outlet

decreased by 0.26 or 0.46 $\mu$L/min when a single microvalve was switched between open, partially or completely closed. Moreover, no significant difference of flow rate change was found between the tests on channel No. 1 and No. 6, suggesting that the position of the operated microvalve does not affect the flow rate of the entire platform. Again, this outcome was expected when a simple flow resistance model was applied to the platform. Within the limit of sensor resolution, this experiment also confirmed that separate valves could be approximated by a common resistance, as dimensional errors introduced during manufacturing influenced flow resistance negligibly.

In test C, the flow characteristics were tested while the membrane valves were partially and completely closed in sequence. In detail, all six microvalves were first fully opened with the negative pressure supplied by OB1 equal to -1.0 bar and all switches of MUX turned on. Then, the latter switches were turned off one-by-one starting from channel No.1 to No.6, one channel every 20 seconds. This resulted in the pressure of corresponding air chambers reducing to 0 bar, and microvalves becoming partially closed (stage I, as shown in Fig. 5.21). In the next stage II, the pressure applied by OB1 was increased to +1.0 bar and switches were turned on in the same order (from channel No.1 to No.6), resulting in the complete closure of the corresponding microvalves, one channel every 20 seconds. Similarly, six microvalves were partially closed and then completely closed in the reverse order (from channel No.6 to No.1, stage III and IV, as shown in Appendix C.6) every 20 seconds. Figure 5.22(a) and Appendix C.6 show the plots of the flow rate of zoospore inlet/outlet and media inlet as a function of time. The difference between the flow rate of the zoospore outlet and that of the media outlet increased gradually while the microvalves were partially closed in sequence (stage I and III). No jump or slump in the flow rates of zoospore or media outlet were evident at the moment of partial closure of the microvalves. On the other hand, a stepped increase and decrease of the flow rates in zoospore and media outlets were observed at the moments that each microvalve was completely closed every 20 seconds (stage II and VI), and the amplitude of both gradually increased with the increase in number of completely closed microvalves.

In order to evaluate the shear stresses acting on trapped zoospores during loading process, the flow rates of each measurement microchannel and fluid induced shear stresses were calculated under the condition that a certain number (ranging from 1 to 6) of microvalves were partially closed and the rest of them were completely closed (stage II in test C). The flow rate of each channel was calculated by dividing the flow rate of the media outlet by the number of partially-closed microvalves. Additionally,

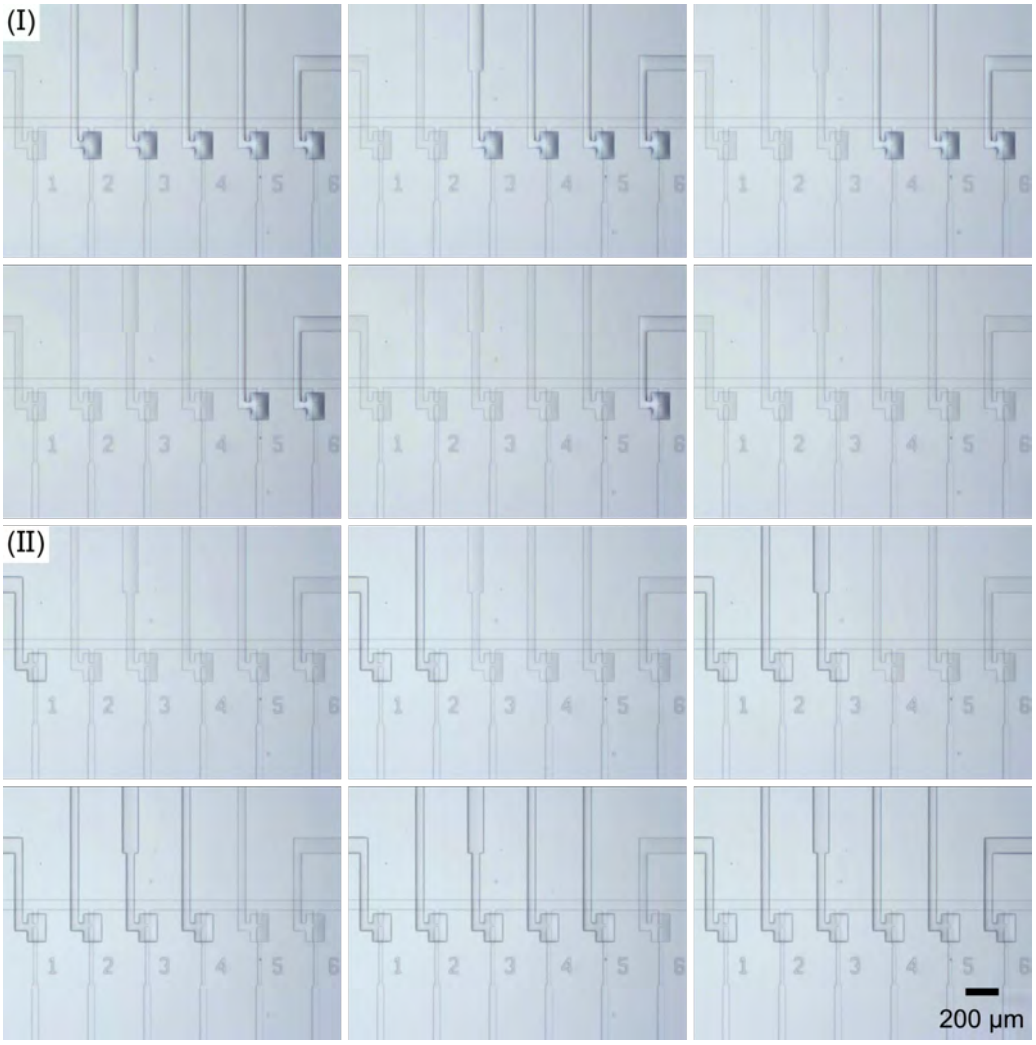


Figure 5.21: Light micrographs of flow characteristics test C. (I) All membrane valves were fully opened (vacuum pressure OB1 = -1.0 bar, all switches of MUX were ON). The switches were then turned off in the sequence from channel No. 1 to No. 6, resulting in the corresponding microvalves becoming partially closed (pressure = 0 bar). (II) The pressure applied by OB1 was set to 1.0 bar and the switches were turned on in the same order (from channel No. 1 to No. 6), resulting in the corresponding microvalves becoming completely closed. Note: DI water was continuously pumped from the zoospore inlet.

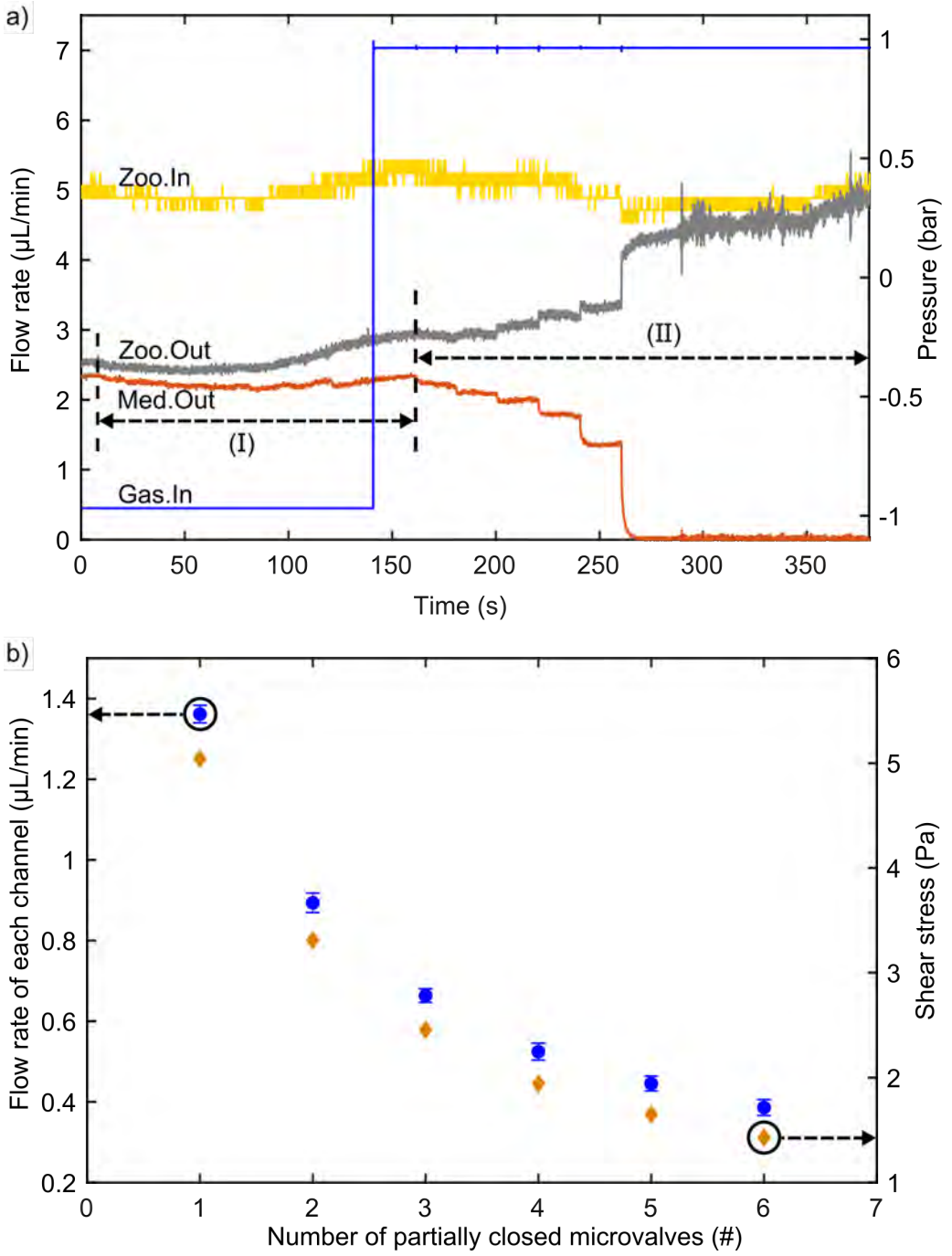


Figure 5.22: Plot of flow characteristics test C. (a) Plot of flow rates of zoospore inlet/outlet and media outlet in stage I and II. The blue line represents the pressure applied by pressure controller OB1. The yellow, gray and red lines are the flow rate measured at the zoospore inlet, outlet and media outlet, respectively by the flow sensor. Stage I and II correspond to the photographs shown in Fig. 5.21. The flow rate of zoospore inlet was set as 5 $\mu$L/min by a syringe pump. (b) Plot of average flow rates of each measurement channel when microvalves were partially closed (blue dot) and corresponding shear stress in each channel (orange diamond), calculated using the flow rate of the media outlet in stage II.

for a rectangular cross-section channel, the wall shear stress $\tau$ is given by [225]:

$$\tau = \frac{6\eta Q}{h^2 W} \tag{5.1}$$

where $\eta$ is the viscosity of the fluid, $Q$ is the flow rate, $h$ and $W$ are the channel height and width, respectively, when the channel length is much larger than its height and width. The results show that, for a flow rate of 5 $\mu$L/min used to load the zoospore solution in this experiment, the minimum flow rate of each measurement channel reached 0.4 $\mu$L/min and the resulting shear stress was 1.4 Pa, while all six microvalves were partially closed (see Fig. 5.22(b)). The shear stresses increased to 5.0 Pa with decreasing number of partially-closed microvalves and corresponding increase of flow rate in each channel up to 1.4 $\mu$L/min. Therefore, rather than completely closing microvalves right after corresponding trap sites were occupied, the zoospores would be exposed to less shear stresses during the loading process when microvalves were partially closed. In comparison, the mean wall shear stress in large arteries of uniform geometry is in the range of 2 - 4 Pa [227]. The growth of *Arabidopsis thaliana* roots was shown to not be affected in the microfluidic chip with shear forces of 1 Pa [92]. Moreover, fluid shear stresses have been used to study bacteria and yeast adhesion to materials or biological surfaces [217, 225, 228]. Li and Palecek used a flow chamber to characterize the attachment of the model yeast *Saccharomyces cerevisiae* to polystyrene surfaces [228]. It was found that the fraction of yeast remaining attached stayed around 60 % within a shear stress of 5 Pa, and decreased linearly from 5 to 35 Pa. In summary, these results show that our system is likely to have little impact on zoospore germination and their germling growth in terms of shear stress. Conversely, if desired, it can be employed to study the adhesion of zoospores by simply adjusting shear stress via the flow rate of the zoospore or media inlet.

Finally, the flow characteristics test D was conducted under the same conditions as the practical operation of the zoospore trapping experiment to simulate and observe the actual performance of the flow rates on the chip. In detail, DI water, as the zoospore solution, was firstly injected from the zoospore inlet at a speed of 5 $\mu$L/min using the syringe pump, while all of the microvalves were fully opened (vacuum pressure applied by OB1 = -1.0 bar, all switches of MUX were set as ON). Six microvalves were partially closed in sequence from channel No.1 to No.6 (corresponding switches were turned off, and pressure in the air chamber became 0 bar) (stage I in Fig. 5.23), after which the syringe pump was then stopped. This stage referred to the zoospore loading process in practical experiments. In the plot of Fig. 5.23, the blue line represents the pressure applied by OB1, while the other lines are the flow rates of zoospore/media

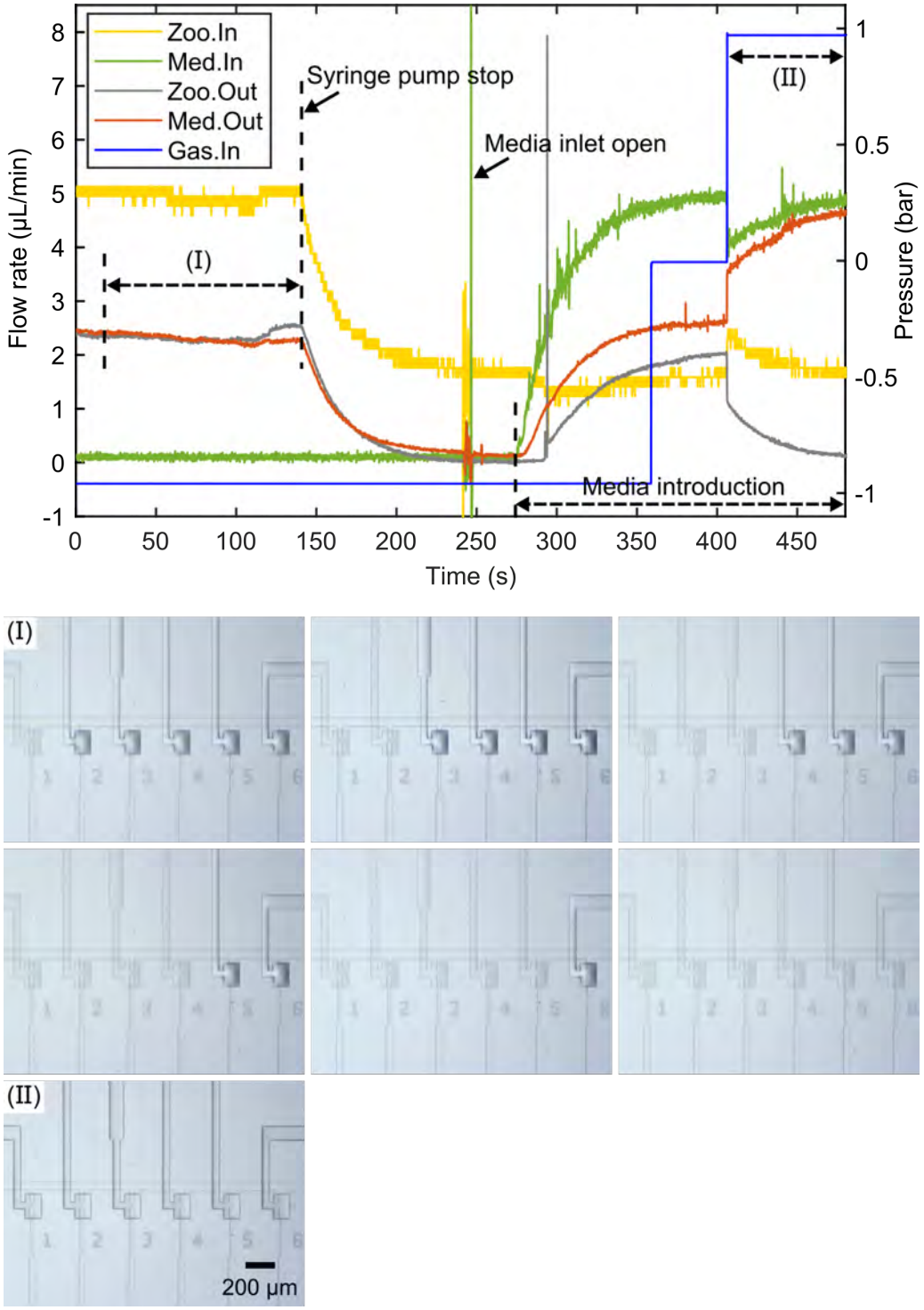


Figure 5.23: Flow characteristics test D, simulation of the practical experiment. The blue line represents the pressure applied by pressure controller OB1. The yellow, green, gray and red lines are the measured flow rate at the zoospore inlet, media inlet, zoospore outlet and media outlet, respectively. Light micrographs showing two stages of microvalve operation. Stage I: six microvalves were partially closed from fully open in the sequence while DI water was pumped from the zoospore inlet. Stage II: all six microvalves were completely closed at same time after injecting DI water from the media inlet, instead of the zoospore inlet.

inlets and zoospore/media outlets, as recorded by the flow sensors. The flow rates of zoospore and media outlets were stable at around 2.5 $\mu$L/min in stage I, which was consistent with the results in test C, and fell rapidly to zero after DI water from the zoospore inlet was stopped. After stabilization of the system (>2 min), DI water, representing media this time, was pumped into the fluidic layer from the media inlet at a flow rate of 5 $\mu$L/min using the pressure controller OB1. The flow rate of media outlet increased again immediately after DI water was injected from the media inlet, while the flow rate of the zoospore outlet started to increase around 20 s later. This indicated that it took media less time to fill the entire chip than by the diffusion process shown previously in Fig. 5.15. Meanwhile, the pressure applied by OB1 was changed to 0 bar, and then increased to 1.0 bar, followed by turning on all the switches of the MUX again, in order to completely close all the microvalves simultaneously (stage II). This was done to prevent trapped zoospores from being exposed to increasing shear stresses when microvalves were completely closed in sequence, as discussed in the flow characteristics test C. The flow rate of media outlet kept increasing and stabilized around 5 $\mu$L/min after all microvalves were completely shut off. Concurrently, the flow rate of the zoospore outlet dropped to zero, indicating that there was no leakage through the closed microvalve. The reason that the flow rate of the zoospore inlet (yellow line) remained around 2 $\mu$L/min after stopping of the syringe pump was attributed to the measurement range of the flow sensor used (MFS3, 2 to 80 $\mu$L/min). Evident noise detected for dozens of seconds from media injection coincided with the point at which the media inlet was opened by turning on a two-way valve.

## 5.4 Conclusion

The development, fabrication and characterization of a triple-layer PDMS-based platform employing normally-closed microvalves for single zoospore capture, compartmentalization, germination and force sensing were shown in this chapter. The device constitutes the first integration of six individually controlled normally-closed microvalves with corresponding force measurement channels, each containing a valve-seat, trap-site with constriction structure and a free-bending force sensing micropillar. Notably, new protocols were developed for chip assembly to avoid the PDMS membrane bonding with the valve-seats in the measurement channels of the fluidic layer. Furthermore, sizes of normally-closed microvalves were optimized to 180 $\mu$m in length and 120 $\mu$m in width for single zoospore transportation and experimentally demonstrated using food coloring and 20 $\mu$m diameter microspheres. Microvalve operation

and flow rates at inlets/outlets were characterized in three operating states, including fully open microvalves at the pressure of -1.0 bar; partially-closed at the pressure of 0 bar, and completely-closed at the pressure of +1.0 bar. The results indicated that the measurement channels could be fully isolated during complete closure, and there were no significant changes of flow rates while the microvalves were partially closed. The shear stresses on the microspheres during the loading process were shown to reach a minimum of 1.4 Pa when all the microvalves were partially closed, compared to if they were completely closed. In the next chapter, the applicability of the optimized platform will be investigated using zoospores of oomycete *A. bisexualis*.

# Chapter 6

# Application of a Normally-closed Valve Platform on *A. bisexualis* Zoospores

The previous chapter described the development of a microfluidic platform with normally-closed valves for concurrent zoospore compartmentalization and force sensing. In this chapter the applicability of this platform is demonstrated via the capture and culture of *Achlya bisexualis* zoospores on the chips. Furthermore, the platform and integrated force sensing pillars were used to measure forces exerted by individual germinated germ tubes at developmental stages.

## 6.1 *Achlya bisexualis* zoospore preparation

Prior to demonstrating force sensing, zoospores of *A. bisexualis* were used to demonstrate the capture and culture function of the platform with integrated normally-closed microvalves. Akin to the work described in Chapter 4, the oomycete *A. bisexualis* was again chosen for this due to its status as model system and the relatively large size of spores and hyphae. The zoospore solution itself was again produced though a starvation cycle of *A. bisexualis* mycelium following the protocol described in Section 4.2.3. In brief, six inoculum plugs from a fresh culture of *A. bisexualis* were evenly spread on a pre-cleaned nappy liner placed on a PYG agar plate. After incubation at 26 °C for 24 hours, the nappy liner with inoculation plugs was peeled off and placed into a flask with 100 mL PYG broth. The PYG broth was exchanged with the mineral salt solution six times and placed overnight on a shaker at 26 °C, followed by another 24 hours of

incubation while being swirled at 150 rpm and 26 °C. The contents of the flask were poured through Kimwipes into centrifuge tubes and centrifuged at 800 rpm for 10 min. Finally, the supernatant of the solution was removed, and collected zoospores were re-suspended in mineral salt solution and stored in a 4 °C fridge. Before experiments, the zoospore solution was mixed with PYG broth (1:1 v/v) and incubated at 26 °C for 2 hours to induce zoospores to germinate and grow larger.

## 6.2 Zoospore capture and maintenance

For demonstration of the capture and culture function of the platform with integrated normally-closed microvalves, the prepared *A. bisexualis* zoospores were loaded into the devices and the liquid handling structures on the chips used to compartmentalize individual zoospores. To achieve this, the platform was first filled with PYG broth as described in detail in Chapter 4, however, this time all the membrane valves were set to their fully-open state (vacuum pressure applied by OB1 set to -1.0 bar, all MUX switches on) individually, rather than via a single control inlet. Pre-cultured zoospore solution was then introduced from the zoospore inlet by a syringe pump at a flow rate of 5 $\mu$L/min. As a result of this, injected zoospores flowed along the zoospore loading channel and were hydrodynamically captured by the constriction structure in the measurement channels.

Figure 6.1(a) shows an example of a zoospore occupying a trap-site after passing through the valve structure. Whether a zoospore entered a trap depended on how close a flow path took the zoospore past a trap. To increase the chance of a trapping event to occur, the width of the zoospore loading channel was decreased in this platform. This was not possible previously, as the loading channel also acted as a valve in the platform with normally-open valves, as also described by Geng et al. [109]. In case of the normally-closed valves, these required a longer distance from the loading channel to the trap-site to provide enough opening space for zoospores to pass by the valve seat, as described in Section 5.3. Due to the use of horizontal-only constriction structures, type B in Section 4.2.1, the flow in the measurement channels was not fully interrupted after one zoospore was captured. These two design constraints together may facilitate the trapping of multiple zoospores before the valves are fully closed. Therefore, to address this issue, once a single zoospore was collected in a trap-site, it was observed using bright-field microscopy and the corresponding microvalve was partially-closed. The latter was achieved by shutting off the switch on the MUX connected to this microvalve, while pressure from OB1 was kept at -1.0 bar. For the

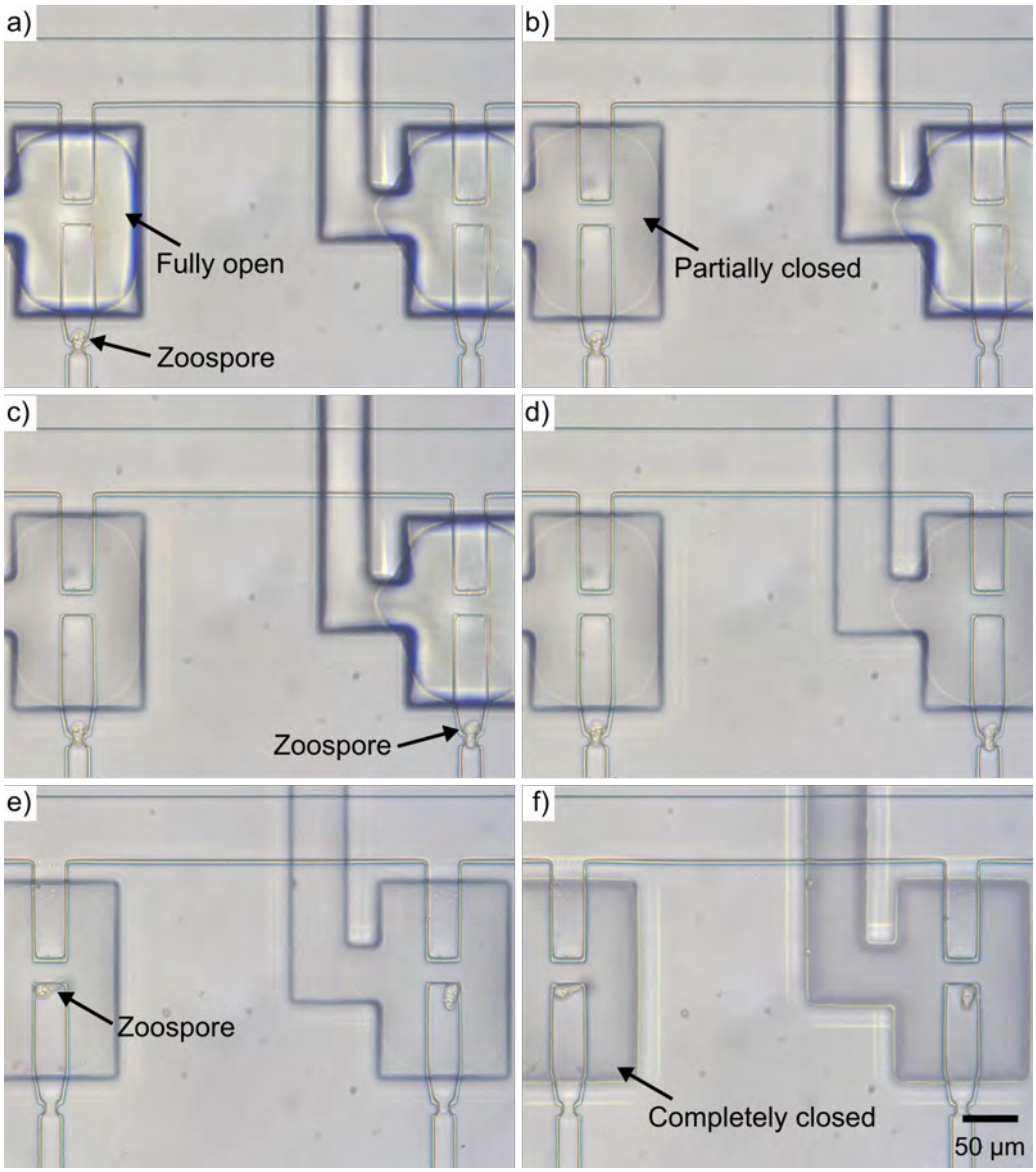


Figure 6.1: A series of light micrographs illustrating the trapping of pre-cultured *A. bisexualis* zoospores using integrated normally-closed microvalves. (a) A single zoospore was hydrodynamically captured in the trap-site of the left measurement channel while all microvalves were fully opening, and (b) the corresponding microvalve was then partially closed, with other valves kept open. (c) Another zoospore was trapped in the right hand side channel and (d) this microvalve also partially closed. This process was repeated until all measurement channels were occupied by one zoospore each. (e) Following this, PYG broth was injected into the fluidic layer of platform from the media inlet at a flow rate of 5 $\mu$L/min, causing some of the trapped zoospores to move towards valve seat. (f) Finally, all microvalves were simultaneously completely-closed.

example zoospore, this state is shown in Fig. 6.1(b). The reason why partial- rather than complete-closure after the capture of zoospores was chosen was that the flow characteristics in Section 5.3 showed the flow rate of media inlet did not decrease dramatically when microvalves were partially-closed from the fully-open stage in sequence. This suggested that, by doing so, subsequently trapped zoospores would not suffer increasing shear forces, something which may happen if the occupied channels were interrupted via complete-closure of corresponding microvalves. In addition, it was demonstrated that partially-closed microvalves successfully stopped any subsequent microspheres before the valve seats. Meanwhile, other unoccupied microvalves were kept in the fully open state. The same operation was repeated (see Fig. 6.1(c & d)) until all the measurement channels had trapped a single zoospore each, after which the zoospore solution was stopped via the external syringe pump. At this point, the system was switched to zoospore maintenance mode, for which the PYG broth was injected into the fluidic layer of platform through the media inlet at a flow rate of 5 $\mu$L/min. In contrast to zoospore loading, the pressure controller OB1 was used for this and continuously supplied media during the entire period of culturing the zoospores on the platform. When the system mode and thus media flows on the platform were switched, some of the captured zoospores were observed to move backwards out of the trap constriction towards the valve seat as a result of the small residual flow through the partially-closed valve. However, as shown by the example in Fig. 6.1(e), all zoospores for which this occurred were successfully retained by the partially-closed state the microvalves were in. This phenomenon suggests zoospores or germlings may be able to attach to the PDMS surfaces, which was also observed for *C. albicans* hyphae by Thomson et al. [229], and, as such, could be used as a feature to estimate zoospore adhesion prior to germ tube extension. As mentioned in Section 5.3.3, the flow shear induced detachment experiments can be implemented on the platform with normally-closed valves during various stages of zoospore germination and germling growth via increasing the flow rate of the media inlet. To conclude trapping and capture, all microvalves were completely closed by applying a positive pressure of 1.0 bar via the OB1 and opening all switches of MUX. All valves were then kept in this state for the entire remaining culture period. Here all microvalves were operated simultaneously to avoid imposing increasing flow rates and shear stresses on zoospores when the microvalves were completely closed one after the other. Moreover, it was demonstrated in the previous Section 5.3, that it took over 1 hour to complete diffusion in the trap-sites from the media inlet when all the microvalves were completely closed. To accelerate this process, the culture media was injected from the media inlet before complete-closure of all microvalves to ensure the measurement channel filling with

media before the valve closed.
In summary, a total of five capture and trapping experiments were conducted, each with one device containing six traps. As part of these experiments, 17 zoospores were successfully captured in measurement channels. In the first two experiments, only two zoospores for each experiment were successfully captured in the trap-sites, mainly because the trap-sites were occupied by empty cysts, which are difficult to avoid in the process of encystment of zoospores using a vortex mixer [230, 231], before zoospores flowed into the measurement channels. This was improved later on by pushing the empty cysts out of the trap-sites via media injection from the media inlet on the other side of the measurement channels. As a result, 3, 5 and 5 zoospores were trapped in the latter three experiments. Of these, 13 zoospores germinated and grew on the platform, resulting in a 76.5 % capture-to-growth success ratio, which was similar to that observed in Chapter 4 for the previous platform with normally-open microvalves. In addition, the morphology of zoospore germination was consistent with controls cultured in a beaker with half-concentrated PYG broth [232]. Germination started after 1 hour of culture at 27 °C, and 50 % and 70 % of the zoospores had produced germ tubes at 2.5 and 3.5 hours, respectively.
Interestingly, three distinct growth patterns could be observed during germination of the zoospores on the platform. In behavior designated type A, of which an example is shown in Fig. 6.2, the germling of the trapped zoospore first extended a germ-tube towards the valve seat. Once it reached the valve seat, the growth direction changed in response to the tip contacting the PDMS valve seat and stopped completely once one of the 90° chamber corners was reached. The directional change of tip growth in this example resembled the thigmotropic response previously observed for hyphae of *C. albicans* [229]. After growth of the initial germ-tube had stopped, the zoospore began to grow a second germ-tube in the opposite direction to the first. The new germ-tube grew through the constriction structure and along the measurement channel, ultimately hitting, deflecting and passing the force sensing micropillar within a period of approximately 3 hours. After 20 hours and more, germlings from each of the six measurement channels had usually reached the media supply channel and begun to grow towards the media inlet.
In the second growth pattern, denoted as type B, the trapped zoospore did not branch during the entire culture. As shown in the example in Fig. 6.3, the germlings grew a single germ-tube directly through the constriction structure, along the measurement channel, finally hitting and passing the force sensing micropillar. The difference in behavior between type A and B could be related to the preferential arrangement and thus polarity of the zoospore after hydrodynamic trapping. Consistent orientation (polarity)

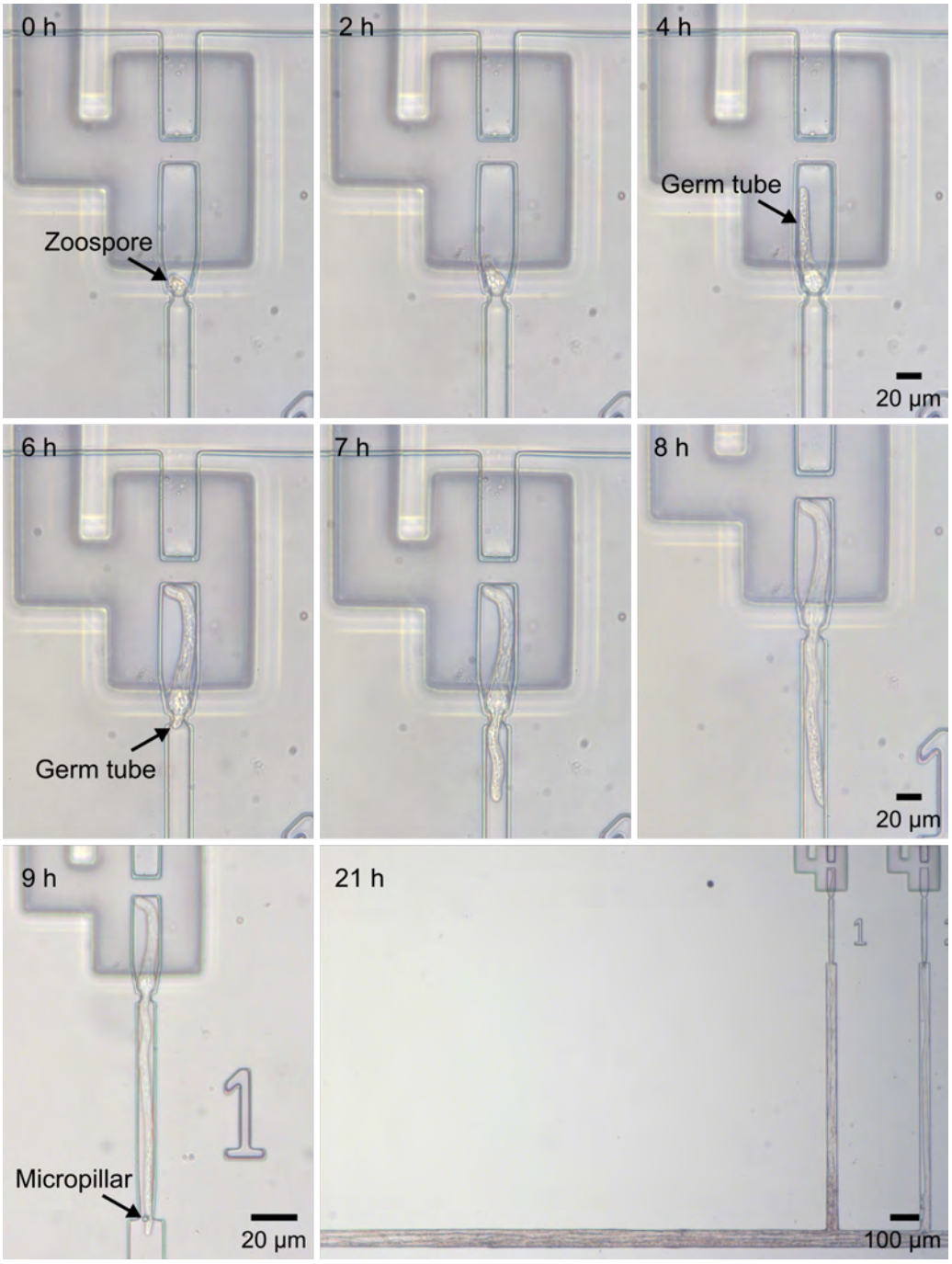


Figure 6.2: A time series of light micrographs showing the first of three specific germination patterns (Type A) exhibited by individual *A. bisexualis* zoospores cultured on the platform over a period of 21 hours. Initially, the germlings of the trapped zoospores grew a germ tube towards the valve seat (0 - 4 hours), made contact with the valve seat and stopped growing. Then they branched and put out a second germ tube in the opposite direction (6 hours). The new germ tube grew through the constriction structure in the measurement channel, ultimately hitting and passing the force sensing micropillar (7 - 9 hours). After 21 hours of continuous culture on the platform, the germ tube had grown into a hyphae and had entered the media supply channel, combining with others originating from the other measurement channels. No growth was observed entering the flow structures beyond the microvalves, such as the zoospore inlet/outlet and loading channel, demonstrating successful and complete compartmentalization.

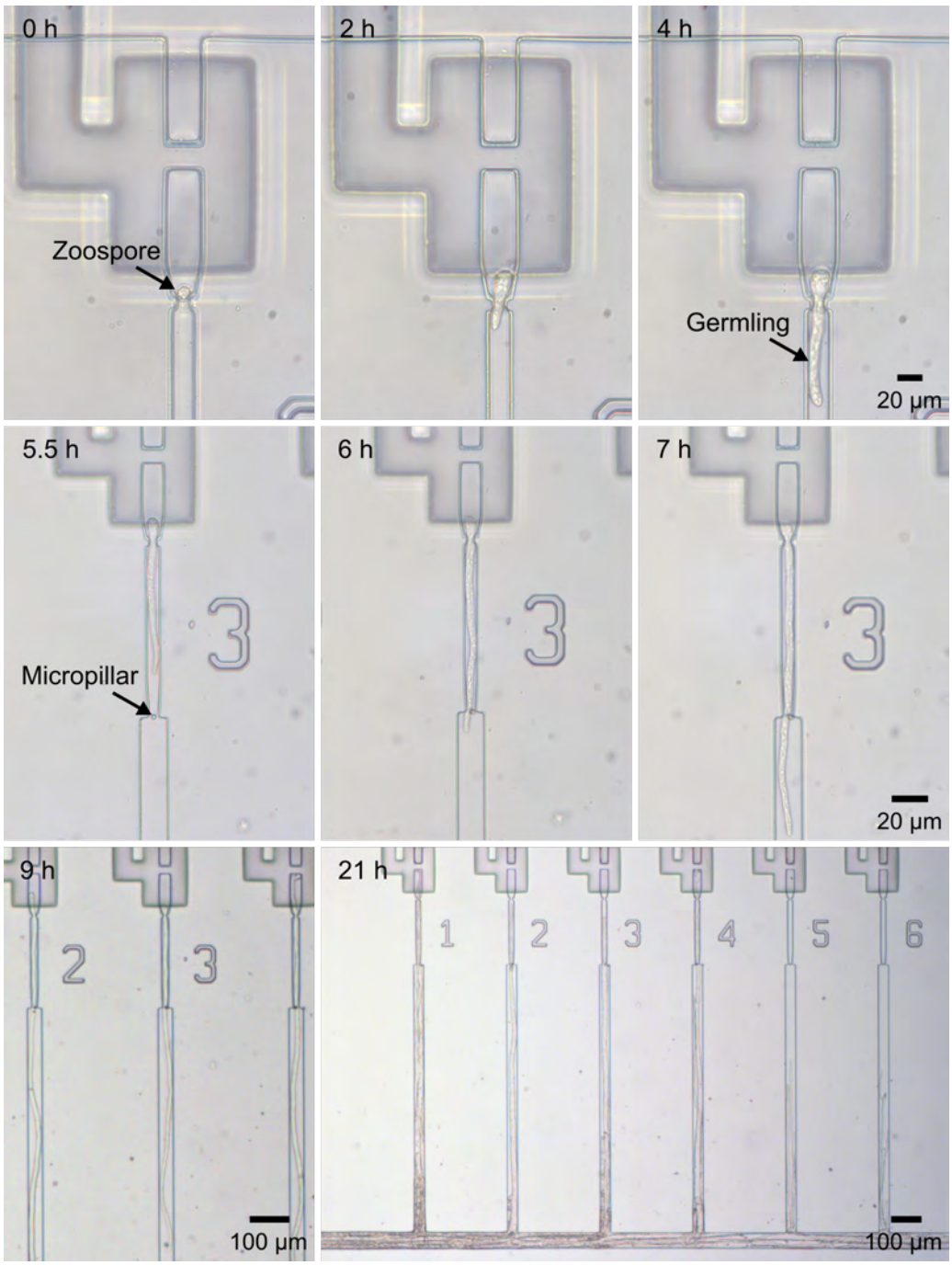


Figure 6.3: A time series of light micrographs showing a second specific germination pattern (Type B) exhibited by *A. bisexualis* zoospores cultured on the platform. The trapped zoospores germinated and the germlings grew a germ tube directly through the constriction structure in the measurement channel (0 - 4 hour). After 6 hours, the tube finally hit and passed the force sensing micropillar. After 21 hours of continuous culture on the platform, the germ tube had grown into a hypha, which merged with others from the neighboring measurement channels in the media supply channel. No hyphae entered the loading area beyond the microvalves.

of zoospore encystment, cyst germination and thus germ-tube growth have been previously observed in, for example, *Catenaria anguillulae*, *Plasmodiophora brassicae*, *Rozella allomycis*, *Pythium* sp, *Phytophthora* and *Saprolegnia* spp. [233, 234].
The third pattern, type C constituted the opposite case to type A. Germlings of trapped zoospores grew germ-tubes through the constriction structures and along the measurement channel first. However, after this first tube had grown a short distance of around 20 $\mu$m, the zoospores started branching and put out a new germ-tube in the opposite direction towards the valve seat. Both of the germ tubes continued to simultaneously grow for a few hours. However, at some stage the germ tubes growing towards the valve seat stopped growing no matter whether they contacted with the valve seats or not, while the germ-tubes towards the micropillars kept growing. Figure 6.4 shows an example of type C where the germ-tube growing towards the valve seat stopped while the other one kept growing, ultimately hitting and passing the micropillar. In summary, the growth pattern of types A and B were observed to occur more frequently, occurring in 6 and 5 samples out of a total of 13 samples respectively, while only 2 trapped zoospores showed type C patterns.
For further comparison, the growth of captured zoospores was observed every hour in the latter three experiments (one chip per experiment, total chip number = 3, trapped zoospore number = 12) and the total length of the germ-tubes growing from each zoospore is summarized in Figure 6.5. The total length in this case was measured from one apex of the germ-tube to the other apex of the germ-tube growing towards the opposite direction in the cases of growth types A and C, or to the zoospore in the case of growth type B. As described in Chapter 4, the constriction type B, which was employed on this platform, provided significantly higher growth success ratios for captured zoospores. However, a pre-culture of zoospores was required for trapping in constriction type B. Therefore, the timeline was counted from the starting-point of zoospore pre-culture, with the zoospore solution injected into the platform after 2 hours of pre-culture. As the data indicate, the majority of germlings grew slowly in the first six hours with a mean growth rate ($\pm$ SEM) of 0.4 $\pm$ 0.07 $\mu$m/min (range = 0.09 - 0.83 $\mu$m/min, n = 12), after which the germ-tube length increased rapidly through the eight hour mark with a mean growth rate ($\pm$ SEM) of 4.1 $\pm$ 0.49 $\mu$m/min (range = 1.07 - 6.11 $\mu$m/min, n = 11). It should be noted that one germling stopped growing after seven hours for unknown reasons. In general, the germlings of type C germination events were observed to grow much slower than other types, possibly due to the additional energy the zoospore needed to grow the second germ-tube. Other work has described the growth rates of hyphae from *A. bisexualis* to be around 8.3 $\mu$m/min on PYG plates [71], albeit for mature hyphae originating from mycelium,

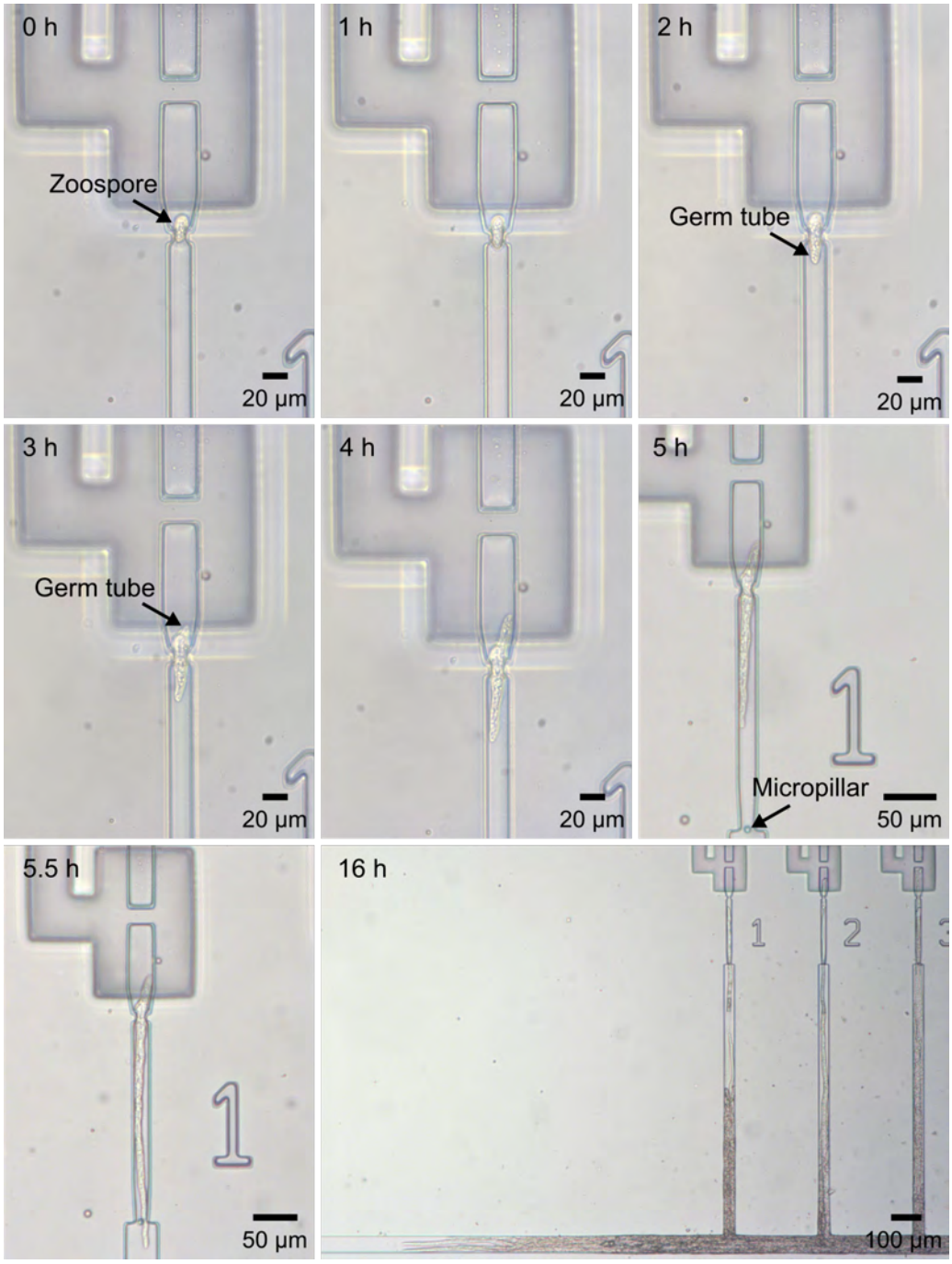


Figure 6.4: A time series of light micrographs showing a third specific germination pattern (Type C) exhibited by *A. bisexualis* zoospores cultured on the platform. The germlings of trapped zoospores grew germ tubes through the constriction structure in the measurement channel towards the force sensing micropillar (0 - 2 hour). However, at this point, germlings branched and put out a new germ tube in the opposite direction towards the valve seat (3 hours). The new germ tubes stopped growing after ∼2 hours, while the former one kept growing and ultimately hit and passed the micropillar (4 - 5.5 hours). After 16 hours of continuous culture on the platform, germ tubes had developed into hyphae and had grown everywhere except for the loading area beyond the microvalves.

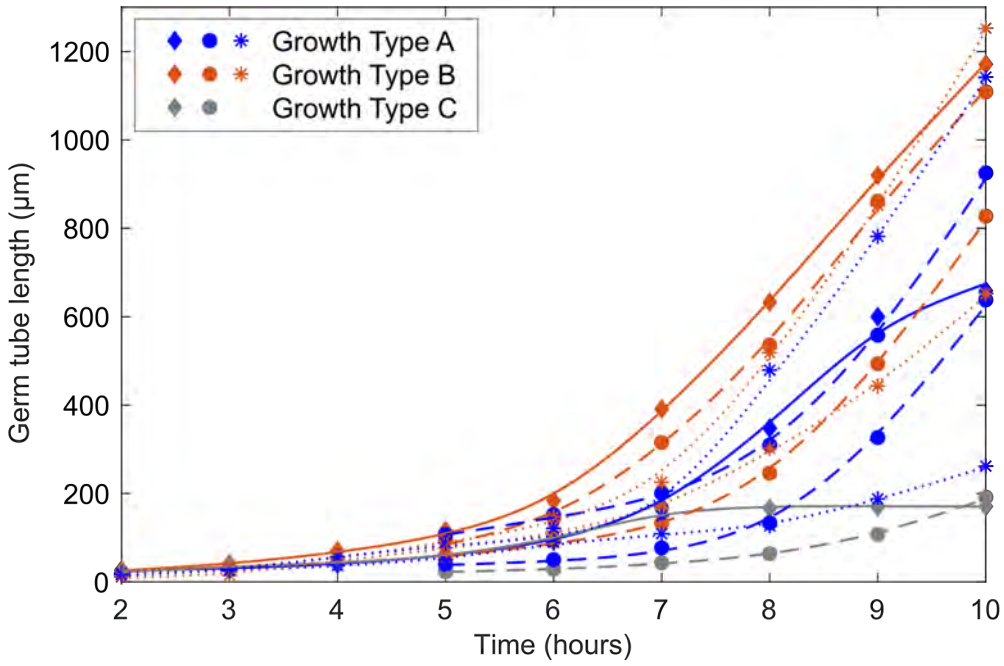


Figure 6.5: Plot of the total length of germlings germinating from individually trapped zoospores (zoospore number = 12) and cultured on the platform. The blue, orange and gray markers represent three pattern types (A, B, and C, respectively) of germ tube growth observed on the platform. The shape of the markers represents the chip they grew on (chip number = 3). The lines are spline-fitted lines of each experimental result. Timelines were synchronized using the start of the pre-culture of zoospores. Zoospore solution was injected into the platform after 2 hours of pre-culture.

and around 6.1 $\mu$m/min in comparable microfluidic channels (35 $\mu$m wide and 30 $\mu$m depth) on previously reported PDMS platform [133]. Both these appear to be slightly higher than those for the germ-tubes originating from zoospores in the current example. However, as mentioned in Chapter 4, Geng et al. observed a growth rate of 20 $\mu$m/h for *N. crassa* germlings, which indicated the germlings were likely to grow slower than mature hyphae [109]. While more comparative data will be needed to draw any conclusions from this, the example shows that the platform can also be used to study growth dynamics and potentially couple these with quantitative force measurements.

## 6.3 Force measurement on single germlings germinated from zoospores

After demonstration and characterization of germination on the platform, forces exerted by germ tubes extending from the compartmentalized zoospores were quantified using the integrated force sensing micro-pillars. Prior to this work, to the best of my knowledge, no force measurements had ever been reported for extending fungal or oomycete germ tubes. All previous measurements documented in the literature, including those of our own group, used mature hyphae, typically growing from a mycelium [24, 80, 84, 133], as these are significantly easier to handle due to their larger size. While some of the force measurement events presented in Chapter 4 could be considered to be initiated by germ tubes, all of the impacting tubes in that example were connected to a larger hyphal network via the outgrowth through the sieve valves. Although the measurements shown here only constitute a proof-of-concept due to their limited sample size, they clearly demonstrate the potential of the platform to contribute to the study of biological processes that have been unexplored to date.

To demonstrate germ tube force sensing, a total of 10 germ tubes were tracked to micropillar impact and deflection. Recordings of the deflection of force sensing micropillars were taken at an elevated frequency (one frame every 2 seconds) to improve the resolution of force plot results, using the inverted microscope and digital camera, while germ tubes grew close to the micropillars. Figure 6.6 shows the moment of impact for all the recorded 10 cases of single germ tubes contacting with their respective force sensing micropillars. Similar to the results obtained using the mycelial platform in Chapter 3, a mixture of direct impact and squeezing interactions between the germ tubes and the measurement pillars could be observed. Two out of a total of 10 micropillar impact events were observed to be direct hit, while remaining 8 were squeezing events. This distribution was consistent with that in the mycelium

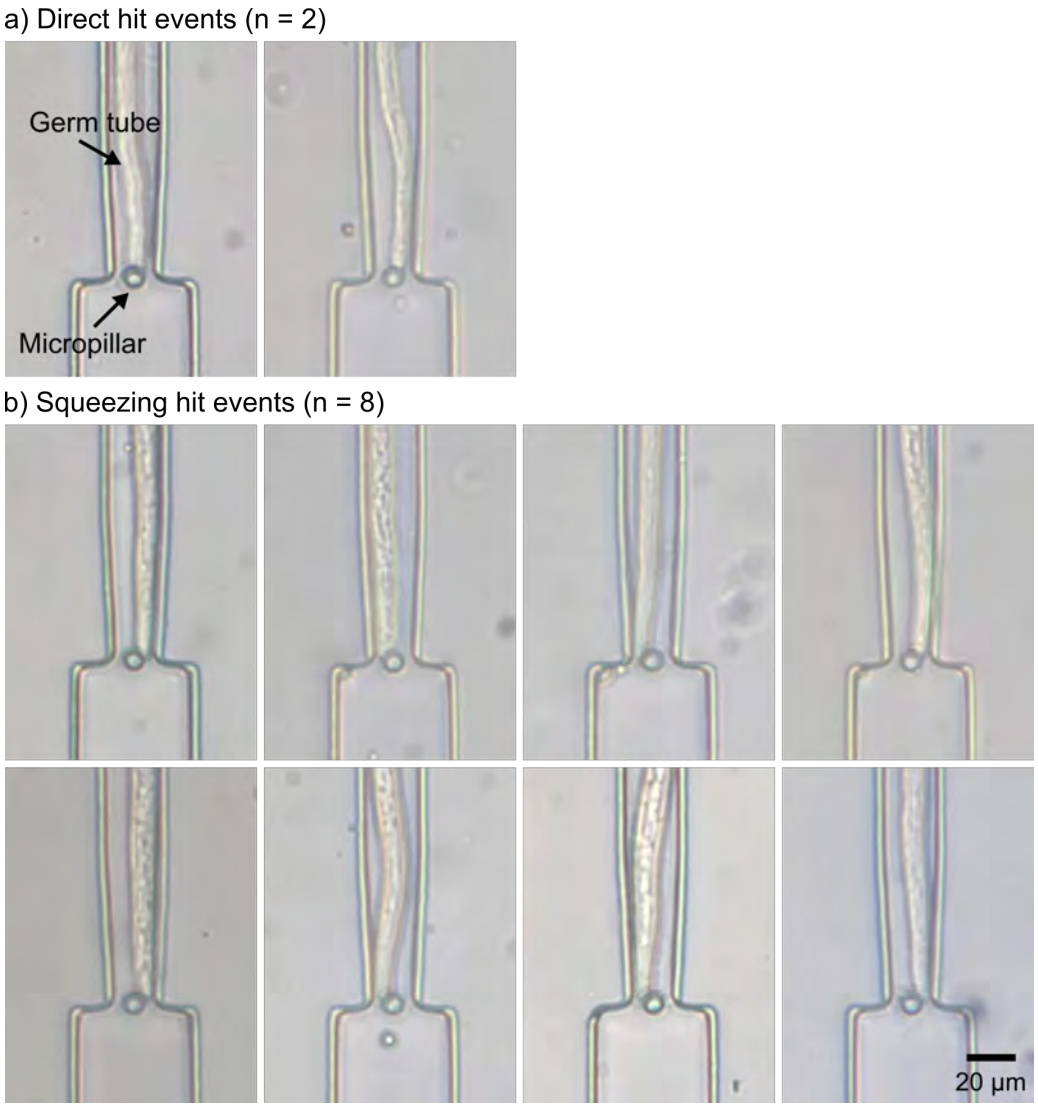


Figure 6.6: Light micrographs showing all the 10 cases where germ tubes originating from single *A. bisexualis* zoospores hit the force sensing micropillars. (a) 2 direct hit and (b) 8 squeezing hit cases out of the total 10 recorded impact cases.

platform for *A. bisexualis* hyphae, where around 18 % of 108 impacts were direct impact [134]. This was again due to the resolution limit of the equipment used for the fabrication process, which restricted how close sensor pillars could be placed next to a channel wall, something which should be improved upon in future platform versions. Moreover, another reason may be that the germ tubes prefer to grow along the walls of channels, something which was observed for most cases of the squeezing hits. Similar morphologies of hyphal growth were also observed for the fungi *N. crassa* [96] and *C. albicans* [229]. In further versions of the platform, one method to improve the number of direct hits to be investigated should be narrowing the width of measurement channels to improve the guidance of germ tubes towards the force sensing micropillar. Image processing to track the movement of the micropillar top was accomplished using ImageJ, and the force was calculated by MATLAB as described in Chapter 3. For a total of 6 out of the 10 recorded impact cases, movement of the pillar top could be tracked using ImageJ. Failure to track the remainder was attributed to limitations of the TrackMate ImageJ plugin [132], which is not currently optimized to track low differential-contrast structures such as was formed by the transparent pillar top rings when recorded with the inverted microscope. Figure 6.7 shows an example of protrusive force measurement on a single germling of the oomycete *A. bisexualis*, which was observed to germinate from a single zoospore and grow following growth pattern type C in the measurement channel before it directly hit the micropillar of 5 $\mu$m diameter. Both force magnitude in x- and y-direction were calculated and plotted as a function of time. The germ tube contacted and directly hit the micropillar at the time point of 1 min, which resulted in the force in y-direction increasing rapidly up to around 0.56 $\mu$N, as indicated by the arrow in the plot. Following this, the germ tube slipped to the right side of the micropillar and continued to grow into the gap between the micropillar and the channel wall (2 - 5 min). As reflected in the force plot, the force magnitude in the y-direction dropped back to around 0.15 $\mu$N, while the force in the x-direction increased consecutively to 0.4 $\mu$N. Considering the low sample number of force measurements on direct hit (n = 1), it is currently not possible to draw any conclusions about the relationship between growth patterns of the germ tubes and generated protrusive forces. However, the force component in hyphal growth direction exerted by the example germ tube was smaller than forces exerted by mature hyphae from mycelium, which were around 2 $\mu$N as mentioned in Chapter 4. One reason might be that the distance from the mycelia seeding area to force sensing micropillars was more than 900 $\mu$m, while the distance from zoospore trap-site to micropillars was only 260 $\mu$m, thus providing reduced mechanical support and less space for hyphae to grow robustly in the germ tube case. Again, as discussed in Chapter 4, with a fully

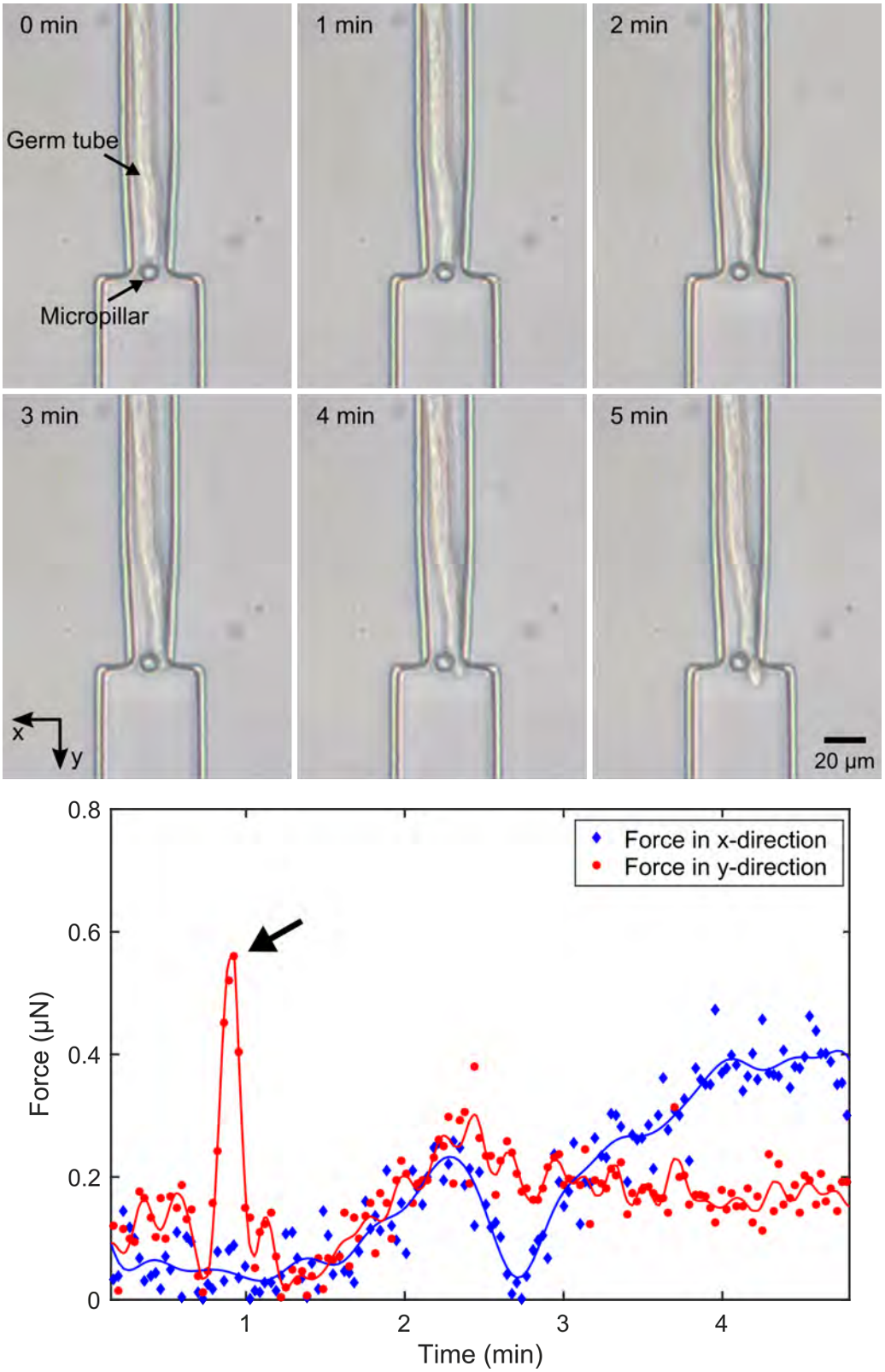


Figure 6.7: Protrusive force measurement on a single germling of the oomycete *A. bisexualis*. (a) A time sequence of micrographs showing the germ tube approaching and directly hitting the force sensing micropillar over a period of 5 min. (b) Plot of the force magnitude in the x- and y-directions as a function of time. The arrow in the plot pointed the moment when the germ tube directly hit the micropillar and obtained the maximum of protrusive force. The lines are spline-fitted lines of force results.

validated platform in place more work now needs to be done on force measurements at different stages of germling growth via placing multiple pillars spaced along the measurement channels. As can be seen in Fig. 6.7, the signal noise was relatively high when small forces under 0.5 $\mu$N were measured, mainly due to the resolution limit of recording images using the inverted microscope. This should be able to be improved on in the future by employing the long working distance microscope objective as discussed in Chapter 7.

Meanwhile, in most cases, the germ tubes originating from single *A. bisexualis* zoospores were observed to grow along the measurement channel walls, squeeze and pass by the micropillar in the gap between it and channel wall. Such an event is shown in Fig. 6.8, where the germ tube grew following growth pattern B. Similar to the direct impact case, squeezing forces exerted by single germ tubes were measured as a function of time and direction. For this example germ tube, the force in x-direction increased to 2.0 $\mu$N, while the force in y-direction only slightly increased to 0.8 $\mu$N within the same time-period of 5 min. The total squeezing forces ranged from 0.2 to 2 $\mu$N, which is smaller than those exerted by the hyphae from mycelia, the latter ranging from 0.5 to 10 $\mu$N [133]. Again, as discussed in previous paragraphs and Chapter 4, having demonstrated its applicability, the platform will now need to be modified to avoid the squeezing impact on the force sensing pillars via an increase of the fabrication resolution or design changes. Efforts towards this are currently underway, including the investment by the University of Canterbury into a two-photon 3D printer, which will enable the fabrication of higher-resolution molds. In the meantime, the current platform has enabled the first compartmentalized screening of zoospore germination and growth morphology of resulting germlings together with protrusive force measurements on germ tubes. The separated normally-closed microvalves not only restrained the backwards growth of germ tubes to the loading channel, but also improved the trapping efficiency of single zoospores.

## 6.4 Conclusion

Zoospores of the oomycete *A. bisexualis* were used to demonstrate the applicability of the platform to germling maintenance and force sensing on germ tubes. Single zoospores, introduced via the zoospore loading channel, were shown to be hydrodynamically-guided, over the valve seats and captured in the trap-sites by the engineered channel constrictions while the microvalves were fully open. Once microvalves corresponding to occupied channels were partially closed, further trapping

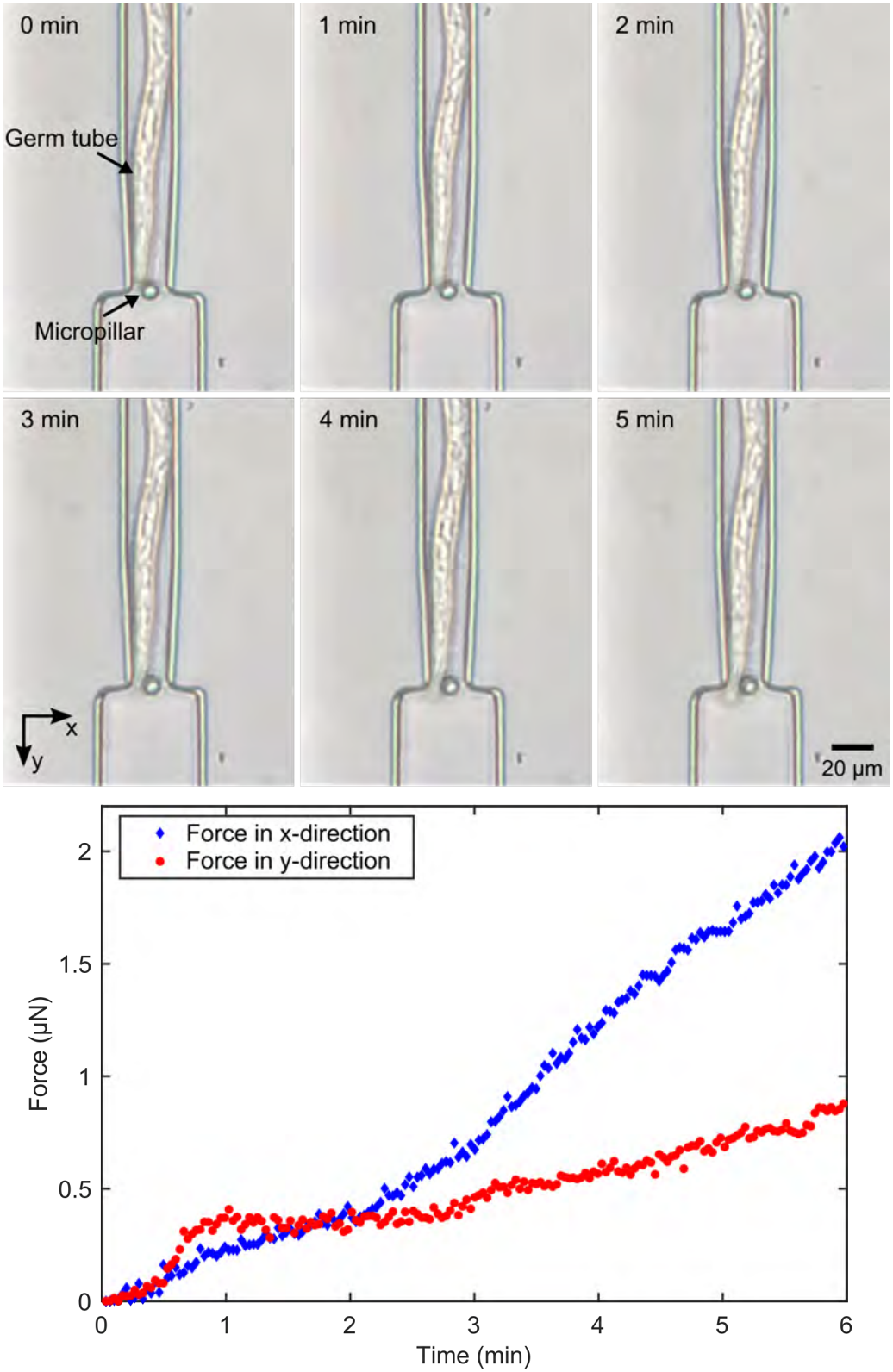


Figure 6.8: Force measurement on a single germling of the oomycete *A. bisexualis*. (a) Time sequence of micrographs of the germ tube approaching the pillar and squeezing past it over a period of 5 min. (b) Plot of the force magnitude in the x- and y-directions as a function of time.

of zoospores in other unoccupied channels continued unhindered.
Following trapping and compartmentalization via full microvalve closure, germination and growth of germ tubes along the measurement channels could be observed. Normally-closed microvalves were able to stop potential reverse growth of germ tubes via the sealed valve seats. During this process, three distinct germ tube growth patterns were observed, the biological basis of which will be further studied in the future. Proof-of-concept force sensing on germ tubes was demonstrated and, similar to work on the mycelial platform in Chapter 3, was found to manifest squeezing and direct hit pillar interaction events. Although preliminary due to the reduced sample set, force magnitudes observed for germ tubes originating from individual zoospore germlings appeared to be on average smaller than for mature hyphae originating from mycelia. In summary, this chapter demonstrates that the integrated platform introduced in Chapter 5, has the potential to enable significant new biological discoveries to be made and inform future development of compounds to combat fungal and oomycete diseases.

# Chapter 7

# Conclusions and Recommendations

This chapter summarizes the work presented in this thesis, highlights the major contributions made and conclusions drawn. Suggestions and recommendations for future work are also given.

## 7.1 Thesis summary and conclusions

The research presented in this thesis contributes to the field by developing a collection of compartmentalization and force sensing LOC platforms for the study of fungal and oomycete hyphae and spores, which could be used to test anti-fungal/oomycete compounds on individual cells. Considering the widespread and severe impact of fungal and oomycete infections, as well as their diversity and drug resistance, increased understanding of biological processes is essential to aid discovery of novel treatments. This research, in particular, provides a tool for parallelized screening on individual hyphae and spores of fungi and oomycetes to help understand the mechanisms of invasive growth and overcome antifungal drug resistance. By inducing single hyphae to grow along parallel microchannels and then contact with free-bending micropillars, morphology analysis and force sensing of invasively growth could be implemented in parallel with cytoskeletal imaging on individual hyphae. Moreover, the development of combined compartmentalization and immobilization of single zoospores enabled parallel observations during various life-cycle stages of fungi and oomycetes, such as spore germination, germling growth and germ tube extension.

The existing LOC platform for the characterization of hyphae originating from fungal and oomycete mycelia was optimized to contain a sequence of parallel microchannels, each housing a single elastomeric micropillar as force sensor. To achieve this, process parameters for a combination of novel negative and positive photoresists were

characterized. The resists were used to fabricate a multi-layer mold with integrated high-aspect ratio pillar cavity inside a channel constriction, and a vertical gap between the micropillar top and the channel lid to allow for free bending. The thickness and corresponding exposure dose of the photoresists were further optimized to acquire high-aspect ratio micropillars adapted to microorganisms with smaller hyphal sizes. Single free-bending micropillars in each channel were successfully fabricated, achieving a minimum diameter of 5 $\mu$m and maximum height-to-diameter aspect ratio of 3.4, close to the resolution limit of the equipment available. The applicability of the optimized mycelial devices was demonstrated using the oomycete *A. bisexualis* and the fungus *N. crassa* with the latter acting as an example of a species with smaller diameter hyphae.

In parallel, a LOC platform for fungal and oomycete spores was developed by integrating the same in-channel micropillar force sensors with a single spore compartmentalization system. For this, hydrodynamic trapping was implemented by adding trap sites with constriction structures at the entrance of each of the parallel measurement channels. Due to their adaptability and compatible fabrication processes, pneumatic membrane valves in the form of normally-open sieve microvalves were first utilized to immobilize captured spores. This resulted in the fabrication of a monolithic device consisting of two PDMS layers, a gas layer and a fluidic layer, separated by a thin PDMS membrane. Individual zoospores of the oomycete *A. bisexualis* were successfully loaded into and retained in the trap sites, and their germination and force exertion by the resulting germ tubes observed. Two types of the constriction structures were evaluated for their impact on zoospore trapping and germination efficacy. The results showed that, although the vertical constriction-only trap could only capture zoospores of larger size, the growth success ratio of zoospores trapped by it was much higher than for the combined horizontal and vertical constriction type. Based on this, vertical constriction-only traps were used for all subsequent devices. The platform was shown to enable the capture of single zoospores of *A. bisexualis*, their germination during long-term culture and force sensing on germ tubes extending from the germlings. In the process, it was observed that germ tubes were able to grow towards and through the normally-open microvalve due to the incomplete seal formed by the sieve valve.

In order to address this issue of backwards growth of germ tubes into the loading channel and also the occasionally observed accumulation of zoospores in the trap sites, independently controlled normally-closed membrane valves were incorporated into measurement channels in substitution of the sieve valve. Due to the complexity of the valve structure, special protocols had to be developed for device assembly. These included the use of a customized PDMS chip aligner to precisely align the gas

and fluidic layers, a continuous vacuum application to prevent PDMS membranes from bonding to valve seats, and keeping the measurement channels fully hydrated to avoid post-alignment valve sticking and micropillars collapse. Air chamber sizes of the normally-closed valves were optimized for single zoospore transportation using microspheres and colored liquid. In addition, the flow characteristics of platform and microvalve operation were characterized, showing that the microvalves were open, partially-closed and completely-closed while under the pressures of -1.0, 0 and 1.0 bar, respectively. Results of these flow experiments also showed that, when the inlet flow rate was set to 5.0 $\mu$L/min, the average flow rate in each channel was 0.4 $\mu$L/min when all six microvalves were partially-closed, which amounted to a quarter of the flow rate in the condition that one microvalve was partially-closed and others were completely-closed. With the partial-closure of all microvalves, the shear stress on trapped zoospore was calculated reaching a minimum of 1.4 Pa using the flow rate of channels.

Finally, zoospores of oomycete *A. bisexualis* were used to demonstrate the applicability of the platform with normally-closed membrane valves. In experiments, once a single zoospore was observed to be captured in the trap site, the corresponding microvalve could be partially closed. This was repeated until all six trap sites were occupied. Then, all the microvalves were completely closed and PYG broth was continuously supplied from media inlet for long-term maintenance and culture. For captured zoospores a growth success ratio (13/17) similar to that of the normally-open sieve valves was obtained. All resulting germlings were observed to grow through the constriction along the measurement channels, however for some this only happened after they had first grown towards the valve seats and then, branched a second germ tube in the opposite direction. All growth of germlings and germ tubes back towards the valve seats was successfully contained by the completely closed microvalves. Analysis of the hyphal growth rates indicated that most of the resulting germ tubes grew slowly during the first 6 hours at an average of $0.4 \pm 0.07$ $\mu$m/min, and then sped up to reach an average of $4.1 \pm 0.49$ $\mu$m/min after 8 hours. Both, direct impact and squeezing interaction between germ tubes and force sensing micropillars, and consequent pillar deflection, could be recorded. The forces exerted by the germ tubes from the zoospores were measured to be smaller on average than those exerted by mature hyphae from a mycelium. However, more biological replicates are required to quantify the protrusive forces generated by germ tubes, and investigate the relationship between growth patterns of germ tubes and their growth rates or protrusive forces. Additional improvements and modifications for future versions of the platforms, which address current issues and expand their applications, will be discussed in the next section.

## 7.2 Recommendations for future work

The first and foremost technical issue that needs to be improved is the tracking of the micropillar deflection. Given the thickness of the two-layer PDMS platform and the space for tubing connection within it, an inverted microscope had to be employed to record the deflection of force sensing pillars from the bottom of the platform. This makes the tracking of the micropillar top extremely difficult at the point when the germ tubes contacted with micropillars, mainly because the top of the micropillar is partially obstructed. One solution to this could be the use of long working distance microscope objective lenses combined with a redesign of the platform, shifting the inlet and outlet port positions away from the measurement channels. Alternatively, connecting the tubes from the side of PDMS platform, as shown in Section 3.2.1, Fig. 3.12, should be considered. In the latter case, the platform fabrication and assembly processes may need to be further optimized, along with enlargement of the device size to enable side tubing connections. These efforts should improve the accuracy of tracking and extend the resolution of force sensing, which will be crucial if the platform is to be used with even smaller diameter species.

Proof-of-concept force sensing on germ tubes of the oomycete *A. bisexualis* was demonstrated in Chapter 6, however, the number of squeezing impact events was significantly higher than that of direct impact events. Given that protrusive forces were sensed by the direct hitting of micropillars, it is important to improve the direct versus squeezing impact hit rate, thus enhancing the efficiency of protrusive force sensing on the platform. As discussed in previous sections, several methods are currently being considered for this, such as increasing the resolution during chip fabrication to place micropillars closer to the channel walls using a new two-photon 3D printer, and horizontal redesign of the measurement channels to better guide germ tubes towards the micropillars. In the meantime, it is imperative to increase biological replicates on the chips in order to evaluate the values of the protrusive forces exerted by germ tubes germinated by zoospores, in particular compared to mature hyphae of mycelium. Later on, extended investigations, such as on the effects of compounds on germ tube growth and protrusive forces, and forces sensing on other microorganisms, should be done using this platform.

One feature of pathogenic fungi and oomycetes, that is worth further investigation on the existing platform is the study of adhesion of the germlings to host surfaces, particularly in the early stages after spore trapping. Cell-substratum adhesion is common in both fungi and oomycetes, and plays an important role in infection, as it secures spores to host surfaces for subsequent penetration [235, 236]. Existing

work has shown that certain enzymes, which degrade the fungal glues, can disrupt adhesion of spores and thus inhibit infections without damage of host plants [45]. This could provide a practicable strategy of infection control of fungal and oomycetes disease. In order to quantify the strength of adhesion to a polystyrene surface, Li and Palecek utilized a parallel plate flow chamber to generate a known shear stress, thus detaching yeast cells from the surface of a Petri dish [228]. The results showed expression of EAP1 in mutant strains of the human fungal pathogen *C. albicans* significantly enhanced attachment to human kidney epithelial cells, HEK293. For the normally-closed microvalve platform developed as part of this thesis, the shear stress in each measurement channel can be calculated and adjusted via the inlet flow rates, as described in Section 5.3.3. Therefore, the adhesion strength of trapped zoospores and germlings in various growth stages could be measured by opening the microvalves and pushing them back towards the valve seats under given flow rates.

Another goal should be the integration of the zoospore trapping and force sensing with on-chip culture of plant roots. This would allow one to observe the invasive growth of individual germlings and hyphae of fungi and oomycetes, as well as penetration of the tissue of plant roots, thus enabling the direct investigation of root-pathogen interactions. For example, germination and growth of *Arabidopsis thaliana* roots, which is a common model for plant biology, have been reported on microfluidic platforms [87, 93, 237]. Grossmann et al. grew *Arabidopsis* seeds in micropipette tips, which were filled with agar and inserted into agar plates, for five days and then plugged the tips into holes on a microfluidic platform [237]. The *Arabidopsis* roots were observed to grow from the pipettes into individual microchannels on the platform. The root growth and cytosolic sugar levels in plants could be monitored during the long-term culture. More recently, Jiang et al. developed a vertical arrangement microfluidic chip for quantitative monitoring of plant phenotypes at the whole organismal stages, including seed germination, root and shoot growth [87]. The *Arabidopsis* seeds were automatically placed in holding sites using a hydrodynamic trapping method and grew gravitropically downward into the tapered channels. *Arabidopsis* plants could be cultured on the chip for up to 11 days and showed a similar morphology and physiology to those grown on conventional agar plates. These methods can be applied to the existing platform for further research on plant-pathogen interactions.

# References


[1] K. J. Willis, "State of the World's Fungi 2018," tech. rep., 2018. https://stateoftheworldsfungi.org/.

[2] M. Thines, "Phylogeny and evolution of plant pathogenic oomycetes-a global overview," *European Journal of Plant Pathology*, vol. 138, no. 3, pp. 431–447, 2014.

[3] J. B. Konopka, A. Casadevall, J. W. Taylor, J. Heitman, and L. Cowen, "One health: fungal pathogens of humans, animals, and plants," tech. rep., 2017.

[4] S. Kamoun, O. Furzer, J. D. Jones, H. S. Judelson, G. S. Ali, R. J. Dalio, S. G. Roy, L. Schena, A. Zambounis, F. Panabières, D. Cahill, M. Ruocco, A. Figueiredo, X. R. Chen, J. Hulvey, R. Stam, K. Lamour, M. Gijzen, B. M. Tyler, N. J. Grünwald, M. S. Mukhtar, D. F. Tomé, M. Tör, G. Van Den Ackerveken, J. Mcdowell, F. Daayf, W. E. Fry, H. Lindqvist-Kreuze, H. J. Meijer, B. Petre, J. Ristaino, K. Yoshida, P. R. Birch, and F. Govers, "The Top 10 oomycete pathogens in molecular plant pathology," *Molecular Plant Pathology*, vol. 16, no. 4, pp. 413–434, 2015.

[5] M. C. Fisher, N. A. R. Gow, and S. J. Gurr, "Tackling emerging fungal threats to animal health, food security and ecosystem resilience," *Philosophical Transactions Royal Society B*, vol. 371, pp. 1–6, 2016.

[6] R. A. Wilson and N. J. Talbot, "Under pressure: investigating the biology of plant infection by *Magnaporthe oryzae*," *Nature Reviews Microbiology*, vol. 7, pp. 185–195, 2009.

[7] R. P. Singh, D. P. Hodson, J. Huerta-Espino, Y. Jin, S. Bhavani, P. Njau, S. Herrera-Foessel, P. K. Singh, S. Singh, and V. Govindan, "The Emergence of Ug99 Races of the Stem Rust Fungus is a Threat to World Wheat Production," *Annual Review of Phytopathology*, vol. 49, no. 1, pp. 465–481, 2011.

[8] J. T. Yorinori, W. M. Paiva, R. D. Frederick, L. M. Costamilan, P. F. Bertagnolli, G. E. Hartman, C. V. Godoy, and J. Nunes, "Epidemics of soybean rust (*Phakopsora pachyrhizi*) in Brazil and Paraguay from 2001 to 2003," *Plant Disease*, vol. 89, no. 6, pp. 675–677, 2005.

[9] M. C. Fisher, D. A. Henk, C. J. Briggs, J. S. Brownstein, L. C. Madoff, S. L. McCraw, and S. J. Gurr, "Emerging fungal threats to animal, plant and ecosystem health," *Nature*, vol. 484, no. 7393, pp. 186–194, 2012.

[10] M. C. Fisher, T. W. Garner, and S. F. Walker, "Global Emergence of *Batrachochytrium dendrobatidis* and Amphibian Chytridiomycosis in Space, Time, and Host," *Annual Review of Microbiology*, vol. 63, pp. 291–310, 2009.

[11] M. Pautasso, G. Aas, V. Queloz, and O. Holdenrieder, "European ash (*Fraxinus excelsior*) dieback - A conservation biology challenge," *Biological Conservation*, vol. 158, pp. 37–49, 2013.

[12] R. E. Bradshaw, S. E. Bellgard, A. Black, B. R. Burns, M. L. Gerth, R. L. Mcdougal, P. M. Scott, N. W. Waipara, B. S. Weir, N. M. Williams, R. C. Winkworth, T. Ashcroft, E. L. Bradley, P. P. Dijkwel, Y. Guo, R. F. Lacey, C. H. Mesarich, P. Panda, and I. J. Horner, "*Phytophthora agathidicida*: research progress, cultural perspectives and knowledge gaps in the control and management of kauri dieback in New Zealand," *Plant Pathology*, pp. 1–14, 2019.

[13] P. J. de Lange, J. R. Rolfe, P. D. Champion, S. P. Courtney, P. B. Heenan, J. W. Barkla, E. K. Cameron, D. A. Norton, and R. A. Hitchmough, "Conservation status of New Zealand indigenous vascular plants, 2017," tech. rep., 2018. http://www.doc.govt.nz/upload/documents/science-and-technical/nztcs3entire.pdf.

[14] B. Havlickova, V. A. Czaika, and M. Friedrich, "Epidemiological trends in skin mycoses worldwide," *Mycoses*, vol. 51, no. Suppl. 4, pp. 2–15, 2008.

[15] G. D. Brown, D. W. Denning, N. A. Gow, S. M. Levitz, M. G. Netea, and T. C. White, "Hidden Killers: Human Fungal Infections," *Science Translational Medicine*, vol. 4, no. 165, pp. 1–9, 2012.

[16] B. J. Park, K. A. Wannemuehler, B. J. Marston, N. Govender, P. G. Pappas, and T. M. Chiller, "Estimation of the current global burden of cryptococcal meningitis among persons living with HIV/AIDS," *AIDS*, vol. 23, pp. 525–530, 2009.

[17] P. K. Anderson, A. A. Cunningham, N. G. Patel, F. J. Morales, P. R. Epstein, and P. Daszak, "Emerging infectious diseases of plants: Pathogen pollution, climate change and agrotechnology drivers," *Trends in Ecology and Evolution*, vol. 19, no. 10, pp. 535–544, 2004.

[18] C. D. Harvell, C. E. Mitchell, J. R. Ward, S. Altizer, A. P. Dobson, R. S. Ostfeld, and M. D. Samuel, "Climate warming and disease risks for terrestrial and marine biota," *Science*, vol. 296, no. 5576, pp. 2158–2162, 2002.

[19] M. C. Fisher, N. J. Hawkins, D. Sanglard, and S. J. Gurr, "Worldwide emergence of resistance to antifungal drugs challenges human health and food security," *Science*, vol. 360, no. 6390, pp. 739–742, 2018.

[20] N. Robbins, T. Caplan, and L. E. Cowen, "Molecular Evolution of Antifungal Drug Resistance," *Annual Review of Microbiology*, vol. 71, no. 1, pp. 753–775, 2017.

[21] M. Bastmeyer, H. B. Deising, and C. Bechinger, "Force Exertion in Fungal Infection," *Annual Review of Biophysics and Biomolecular Structure*, vol. 31, pp. 321–341, 2002.

[22] V. Nock, A. Tayagui, and A. Garrill, "Elastomeric Micropillar Arrays for the Study of Protrusive Forces in Hyphal Invasion," in *19th International Conference on Miniaturized Systems for Chemistry and Life Sciences*, pp. 692–694, 2015.

[23] A. Tayagui, A. Garrill, D. A. Collings, and V. Nock, "On-Chip Measurement of Protrusive Force Exerted By Single Hyphal Tips of Pathogenic Microorganisms," in *20th International Conference on Miniaturized Systems for Chemistry and Life Sciences*, pp. 150–151, 2016.

[24] Y. Sun, A. Tayagui, A. Garrill, and V. Nock, "Fabrication of In-Channel High-Aspect Ratio Sensing Pillars for Protrusive Force Measurements on Fungi and Oomycetes," *Journal of Microelectromechanical Systems*, vol. 27, no. 5, pp. 827–835, 2018.

[25] Y. Sun, A. Tayagui, A. Garrill, and V. Nock, "A Monolithic Polydimethylsiloxane Platform for Zoospore Capture, Germination and Single Hypha Force Sensing," in *20th International Conference on Solid-State Sensors, Actuators and Microsystems & Eurosensors XXXIII (TRANSDUCERS & EUROSENSORS XXXIII)*, pp. 409–412, IEEE, 2019.

[26] A. Stechmann and T. Cavalier-smith, "Rooting the Eukaryote Tree by Using a Derived Gene Fusion," *Science*, vol. 297, no. 5578, pp. 89–91, 2002.

[27] D. L. Hawksworth and R. Lücking, "Fungal Diversity Revisited: 2.2 to 3.8 Million Species," in *The Fungal Kingdom* (J. Heitman, B. J. Howlett, P. W. Crous, E. H. Stukenbrock, T. Y. James, and N. A. Gow, eds.), pp. 79–95, Microbiology spectrum, 2017.

[28] J. Dupont, S. Dequin, T. Giraud, F. L. Tacon, S. Marsit, J. Ropars, F. Richard, and M.-A. Selosse, "Fungi as a Source of Food," in *The Fungal Kingdom* (J. Heitman, B. J. Howlett, P. W. Crous, E. H. Stukenbrock, T. Y. James, and N. A. Gow, eds.), pp. 1063–1085, Microbiology spectrum, 2017.

[29] A. H. Aly, A. Debbab, and P. Proksch, "Fifty years of drug discovery from fungi," *Fungal Diversity*, vol. 50, pp. 3–19, 2011.

[30] M. Imran, Z. Anwar, M. Irshad, M. J. Asad, and H. Ashfaq, "Cellulase Production from Species of Fungi and Bacteria from Agricultural Wastes and Its Utilization in Industry: A Review," *Advances in Enzyme Research*, vol. 4, no. 2, pp. 44–55, 2016.

[31] M. Bhat, "Cellulases and related enzymes in biotechnology," *Biotechnology Advances*, vol. 18, no. 5, pp. 355–383, 2000.

[32] S. E. Smith and D. J. Read, *Mycorrhizal Symbiosis*. London: Academic Press, 3 ed., 2008.

[33] M. G. van der Heijden, F. M. Martin, M. A. Selosse, and I. R. Sanders, "Mycorrhizal ecology and evolution: The past, the present, and the future," *New Phytologist*, vol. 205, no. 4, pp. 1406–1423, 2015.

[34] B. M. Tyler, "Genetics and genomics of the oomycete-host interface," *Trends in Genetics*, vol. 17, no. 11, pp. 611–614, 2001.

[35] G. W. Beakes, S. L. Glockling, and S. Sekimoto, "The evolutionary phylogeny of the oomycete "fungi"," *Protoplasma*, vol. 249, no. 1, pp. 3–19, 2012.

[36] T. A. Richards, J. B. Dacks, J. M. Jenkinson, C. R. Thornton, and N. J. Talbot, "Evolution of Filamentous Plant Pathogens: Gene Exchange across Eukaryotic Kingdoms," *Current Biology*, vol. 16, no. 18, pp. 1857–1864, 2006.

[37] J. Griffith, A. Davis, and B. Grant, "Target sites of fungicides to control oomycetes," in *Target Sites of Fungicide Action* (W. Koeller, ed.), pp. 69–100, CRC Press, 1991.

[38] K. D. Hyde, A. M. Al-Hatmi, B. Andersen, T. Boekhout, W. Buzina, T. L. Dawson, D. C. Eastwood, E. B. Jones, S. de Hoog, Y. Kang, J. E. Longcore, E. H. McKenzie, J. F. Meis, L. Pinson-Gadais, A. R. Rathnayaka, F. Richard-Forget, M. Stadler, B. Theelen, B. Thongbai, and C. K. Tsui, "The world's ten most feared fungi," *Fungal Diversity*, vol. 93, no. 1, pp. 161–194, 2018.

[39] J. Geddes-McAlister and R. S. Shapiro, "New pathogens, new tricks: Emerging, drug-resistant fungal pathogens and future prospects for antifungal therapeutics," *Annals of the New York Academy of Sciences*, vol. 1435, no. 1, pp. 57–78, 2019.

[40] B. A. Sikes, J. L. Bufford, P. E. Hulme, J. A. Cooper, P. R. Johnston, and R. P. Duncan, "Import volumes and biosecurity interventions shape the arrival rate of fungal pathogens," *PLoS Biology*, vol. 16, no. 5, pp. 1–17, 2018.

[41] M. Latijnhouwers, P. J. De Wit, and F. Govers, "Oomycetes and fungi: Similar weaponry to attack plants," *Trends in Microbiology*, vol. 11, no. 10, pp. 462–469, 2003.

[42] P. Gladieux, A. Feurtey, M. E. Hood, A. Snirc, J. Clavel, C. Dutech, M. Roy, and T. Giraud, "The population biology of fungal invasions," *Molecular Ecology*, vol. 24, no. 9, pp. 1969–1986, 2015.

[43] A. R. Hardham, "Cell biology of plant-oomycete interactions," *Cellular Microbiology*, vol. 9, no. 1, pp. 31–39, 2007.

[44] S. Fawke, M. Doumane, and S. Schornack, "Oomycete Interactions with Plants: Infection Strategies and Resistance Principles," *Microbiology and Molecular Biology Reviews*, vol. 79, no. 3, pp. 263–280, 2015.

[45] L. Epstein and R. Nicholson, "Adhesion and adhesives of fungi and oomycetes," in *Biological Adhesives* (A. M. Smith, ed.), pp. 25–55, Springer,Cham, second ed., 2016.

[46] N. Osherov and G. S. May, "The molecular mechanisms of conidial germination," *FEMS Microbiology Letters*, vol. 199, no. 2, pp. 153–160, 2001.

[47] B. Kiefer, M. Riemann, C. Büche, H. H. Kassemeyer, and P. Nick, "The host guides morphogenesis and stomatal targeting in the grapevine pathogen *Plasmopara viticola*," *Planta*, vol. 215, no. 3, pp. 387–393, 2002.

[48] A. C. Sexton and B. J. Howlett, "Parallels in fungal pathogenesis on plant and animal hosts," *Eukaryotic Cell*, vol. 5, no. 12, pp. 1941–1949, 2006.

[49] I. V. Ene and R. J. Bennett, "The cryptic sexual strategies of human fungal pathogens," *Nature Reviews Microbiology*, vol. 12, no. 4, pp. 239–251, 2014.

[50] E. Perez-Nadales, M. F. Almeida Nogueira, C. Baldin, S. Castanheira, M. El Ghalid, E. Grund, K. Lengeler, E. Marchegiani, P. V. Mehrotra, M. Moretti, V. Naik, M. Oses-Ruiz, T. Oskarsson, K. Schäfer, L. Wasserstrom, A. A. Brakhage, N. A. Gow, R. Kahmann, M. H. Lebrun, J. Perez-Martin, A. Di Pietro, N. J. Talbot, V. Toquin, A. Walther, and J. Wendland, "Fungal model systems and the elucidation of pathogenicity determinants," *Fungal Genetics and Biology*, vol. 70, pp. 42–67, 2014.

[51] H. S. Judelson, "Sexual Reproduction in Plant Pathogenic Oomycetes: Biology and Impact on Disease," in *Sex in Fungi* (J. Heitman, J. W. Kronstad, J. W. Taylor, and L. A. Casselton, eds.), pp. 445–458, ASM Press, 2007.

[52] A. L. Fabritius, C. Cvitanich, and H. S. Judelson, "Stage-specific gene expression during sexual development in *Phytophthora infestans*," *Molecular Microbiology*, vol. 45, no. 4, pp. 1057–1066, 2002.

[53] D. Erwin and O. Ribeiro, *Phytophthora diseases worldwide.* St Paul, Minnesota: American Phytopathological Society, 1996.

[54] H. A. Hartmann, R. Kahmann, and M. Bolker, "The pheromone response factor coordinates filamentous growth and pathogenicity in *Ustilago maydis*," *The EMBO Journal*, vol. 15, no. 7, pp. 1632–1641, 1996.

[55] L. Brush and N. P. Money, "Invasive Hyphal Growth in *Wangiella dermatitidis* is induced by Stab Inoculation and Shows Dependence upon Melanin Biosynthesis," *Fungal Genetics and Biology*, vol. 28, pp. 190–200, 1999.

[56] G. Steinberg, M. A. Peñalva, M. Riquelme, H. A. Wösten, and S. D. Harris, "Cell Biology of Hyphal Growth," *Microbiology Spectrum*, vol. 5, no. 2, 2017.

[57] C. J. Alexopoulos, C. W. Mims, and M. M. Blackwell, *Introductory Mycology*. New York, USA: John Wiley and Sons, 4th ed., 1996.

[58] R. Maheshwari, *Fungi: Experimental Methods In Biology*. New York, USA: CRC Press, second ed., 2016.

[59] K. Mendgen, M. Hahn, and H. Deising, "Morphogenesis and Mechanisms of Penetration By Plant Pathogenic Fungi," *Annual Review of Phytopathology*, vol. 34, no. 1, pp. 367–386, 1996.

[60] N. J. Tonukari, J. S. Scott-Craig, and J. D. Walton, "The *Cochliobolus carbonum* SNF1 gene is required for cell wall-degrading enzyme expression and virulence on maize," *Plant Cell*, vol. 12, no. 2, pp. 237–247, 2000.

[61] J. P. Ravishankar, C. M. Davis, D. J. Davis, E. MacDonald, S. D. Makselan, L. Millward, and N. P. Money, "Mechanics of Solid Tissue Invasion by the Mammalian Pathogen *Pythium insidiosum*," *Fungal Genetics and Biology*, vol. 34, pp. 167–175, 2001.

[62] E. MacDonald, L. Millward, J. P. Ravishankar, and N. P. Money, "Biomechanical interaction between hyphae of two *Pythium* species (Oomycota) and host tissues," *Fungal Genetics and Biology*, vol. 37, pp. 245–249, 2002.

[63] N. P. Money, "Wishful Thinking of Turgor Revisited: The Mechanics of Fungal Growth," *Fungal Genetics and Biology*, vol. 21, pp. 173–187, 1997.

[64] R. R. Lew, "How does a hypha grow? The biophysics of pressurized growth in fungi," *Nature*, vol. 9, pp. 509–518, 2011.

[65] A. S. Nezhad and A. Geitmann, "The cellular mechanics of an invasive lifestyle," *Journal of Experimental Botany*, vol. 64, no. 15, pp. 4709–4728, 2013.

[66] N. P. Money, "Measurement of hyphal turgor," *Experimental Mycology*, vol. 14, no. 4, pp. 416–425, 1990.

[67] N. P. Money and F. M. Harold, "Two water molds can grow without measurable turgor pressure," *Planta*, vol. 190, pp. 426–430, 1993.

[68] R. R. Lew, N. N. Levina, S. K. Walker, and A. Garrill, "Turgor regulation in hyphal organisms," *Fungal Genetics and Biology*, vol. 41, pp. 1007–1015, 2004.

[69] P. Fayant, O. Girlanda, Y. Chebli, C. É. Aubin, I. Villemure, and A. Geitmann, "Finite element model of polar growth in pollen tubes," *Plant Cell*, vol. 22, no. 8, pp. 2579–2593, 2010.

[70] N. P. Money, "Biomechanics of Invasive Hyphal Growth," in *Biology of the Fungal Cell* (R. Howard and N. A. Gow, eds.), pp. 237–249, Springer, Berlin, Heidelberg, 2007.

[71] S. K. Walker, K. Chitcholtan, Y. Yu, G. M. Christenhusz, and A. Garrill, "Invasive hyphal growth: An F-actin depleted zone is associated with invasive hyphae of the oomycetes *Achlya bisexualis* and *Phytophthora cinnamomi*," *Fungal Genetics and Biology*, vol. 43, no. 5, pp. 357–365, 2006.

[72] S. Suei and A. Garrill, "An F-actin-depleted zone is present at the hyphal tip of invasive hyphae of *Neurospora crassa*," *Protoplasma*, vol. 232, pp. 165–172, 2008.

[73] R. P. Hertzberg and A. J. Pope, "High-throughput screening: new technology for the 21st century," *Current Opinion in Chemical Biology*, vol. 4, no. 4, pp. 445–451, 2000.

[74] C. J. Henrich and J. A. Beutler, "Matching the power of high throughput screening to the chemical diversity of natural products," *Natural Product Reports*, vol. 30, no. 10, pp. 1284–1298, 2013.

[75] S. S. Wong, L. P. Samaranayake, and C. J. Seneviratne, "In pursuit of the ideal antifungal agent for Candida infections: High-throughput screening of small molecules," *Drug Discovery Today*, vol. 19, no. 11, pp. 1721–1730, 2014.

[76] S. Chaturvedi, S. S. Rajkumar, X. Li, G. J. Hurteau, M. Shtutman, and V. Chaturvedi, "Antifungal testing and high-throughput screening of compound library against geomyces destructans, the etiologic agent of geomycosis (WNS) in bats," *PLoS ONE*, vol. 6, no. 3, 2011.

[77] T. Watamoto, H. Egusa, T. Sawase, and H. Yatani, "Screening of pharmacologically active small molecule compounds identifies antifungal agents against Candida biofilms," *Frontiers in Microbiology*, vol. 6, no. DEC, pp. 1–9, 2015.

[78] S. A. Lawrence, E. J. Burgess, C. Pairama, A. Black, W. M. Patrick, I. Mitchell, N. B. Perry, and M. L. Gerth, "Mātauranga-guided screening of New Zealand native plants reveals flavonoids from kānuka (*Kunzea robusta*) with anti-Phytophthora activity," *Journal of the Royal Society of New Zealand*, vol. 6758, pp. 137–154, 2019.

[79] R. J. Howard, M. A. Ferrari, D. H. Roacht, and N. P. Money, "Penetration of Hard Substrates by a Fungus Employing Enormous Turgor Pressures," *Proceedings of the National Academy of Sciences of the United States of America*, vol. 88, no. 24, pp. 11281–11284, 1991.

[80] G. D. Wright, J. Arlt, W. C. K. Poon, and N. D. Read, "Optical tweezer micromanipulation of filamentous fungi," *Fungal Genetics and Biology*, vol. 44, pp. 1–13, 2007.

[81] G. D. Wright, J. Arlt, W. C. Poon, and N. D. Read, "Experimentally manipulating fungi with optical tweezers," *Mycoscience*, vol. 48, no. 1, pp. 15–19, 2007.

[82] D. R. Burnham, G. D. Wright, N. D. Read, and D. McGloin, "Holographic and single beam optical manipulation of hyphal growth in filamentous fungi," *Journal of Optics A: Pure and Applied Optics*, vol. 9, no. 8, pp. S172–S179, 2007.

[83] S. Johns, C. M. Davis, and N. P. Money, "Pulses in turgor pressure and water potential: resolving the mechanics of hyphal growth," *Microbiological Research*, vol. 154, pp. 225–231, 1999.

[84] N. P. Money, C. M. Davis, and J. P. Ravishankar, "Biomechanical evidence for convergent evolution of the invasive growth process among fungi and oomycete water molds," *Fungal Genetics and Biology*, vol. 41, pp. 872–876, 2004.

[85] A. Spohr, C. Dam-Mikkelsen, M. Carlsen, J. Nielsen, and J. Villadsen, "On-line study of fungal morphology during submerged growth in a small flow-through cell," *Biotechnology and Bioengineering*, vol. 58, no. 5, pp. 541–553, 1998.

[86] A. Sanati Nezhad, "Microfluidic platforms for plant cells studies," *Lab on a Chip*, vol. 14, no. 17, pp. 3262–3274, 2014.

[87] H. Jiang, Z. Xu, M. R. Aluru, and L. Dong, "Plant chip for high-throughput phenotyping of *Arabidopsis*," *Lab on a Chip*, vol. 14, no. 7, pp. 1281–1293, 2014.

[88] K. K. Lee, L. Labiscsak, C. H. Ahn, and C. I. Hong, "Spiral-based microfluidic device for long-term time course imaging of *Neurospora crassa* with single nucleus resolution," *Fungal Genetics and Biology*, vol. 94, pp. 11–14, 2016.

[89] N. Ghanem, C. E. Stanley, H. Harms, A. Chatzinotas, and L. Y. Wick, "Mycelial Effects on Phage Retention during Transport in a Microfluidic Platform," *Environmental Science and Technology*, vol. 53, no. 20, pp. 11755–11763, 2019.

[90] W. Zhou, J. Le, Y. Chen, Y. Cai, Z. Hong, and Y. Chai, "Recent advances in microfluidic devices for bacteria and fungus research," *TrAC - Trends in Analytical Chemistry*, vol. 112, pp. 175–195, 2019.

[91] A. Burmeister and A. Grünberger, "Microfluidic cultivation and analysis tools for interaction studies of microbial co-cultures," *Current Opinion in Biotechnology*, vol. 62, pp. 106–115, 2020.

[92] M. Meier, E. M. Lucchetta, and R. F. Ismagilov, "Chemical stimulation of the *Arabidopsis thaliana* root using multi-laminar flow on a microfluidic chip," *Lab on a Chip*, vol. 10, no. 16, pp. 2147–2153, 2010.

[93] A. Parashar and S. Pandey, "Plant-in-chip: Microfluidic system for studying root growth and pathogenic interactions in Arabidopsis," *Applied Physics Letters*, vol. 98, no. 26, pp. 1–3, 2011.

[94] K. L. Hanson, D. V. Nicolau, L. Filipponi, L. Wang, A. P. Lee, and D. V. Nicolau, "Fungi use efficient algorithms for the exploration of microfluidic networks," *Small*, vol. 2, no. 10, pp. 1212–1220, 2006.

[95] M. Held, A. P. Lee, C. Edwards, and D. V. Nicolau, "Microfluidics structures for probing the dynamic behaviour of filamentous fungi," *Microelectronic Engineering*, vol. 87, no. 5-8, pp. 786–789, 2010.

[96] M. Held, C. Edwards, and D. V. Nicolau, "Probing the growth dynamics of *Neurospora crassa* with microfluidic structures," *Fungal Biology*, vol. 115, no. 6, pp. 493–505, 2011.

[97] S. Demming, B. Sommer, A. Llobera, D. Rasch, R. Krull, and S. Büttgenbach, "Disposable parallel poly(dimethylsiloxane) microbioreactor with integrated readout grid for germination screening of *Aspergillus ochraceus*," *Biomicrofluidics*, vol. 5, no. 1, pp. 1–11, 2011.

[98] C. Mattupalli, J. E. Spraker, E. Berthier, A. O. Charkowski, N. P. Keller, and R. W. Shepherd, "A Microfluidic Assay for Identifying Differential Responses of Plant and Human Fungal Pathogens to Tobacco Phylloplanins," *Plant Health Progress*, vol. 15, no. 3, pp. 130–134, 2014.

[99] A. Grünberger, K. Schöler, C. Probst, G. Kornfeld, T. Hardiman, W. Wiechert, D. Kohlheyer, and S. Noack, "Real-time monitoring of fungal growth and morphogenesis at single-cell resolution," *Engineering in Life Sciences*, vol. 17, no. 1, pp. 86–92, 2017.

[100] J. Marshall, X. Qiao, J. Baumbach, J. Xie, L. Dong, and M. K. Bhattacharyya, "Microfluidic device enabled quantitative time-lapse microscopic-photography for phenotyping vegetative and reproductive phases in *Fusarium virguliforme*, which is pathogenic to soybean," *Scientific Reports*, vol. 7, pp. 1–10, 2017.

[101] H. N. Joensson and H. Andersson Svahn, "Droplet microfluidics-A tool for single-cell analysis," *Angewandte Chemie - International Edition*, vol. 51, no. 49, pp. 12176–12192, 2012.

[102] D. J. Collins, A. Neild, A. DeMello, A. Q. Liu, and Y. Ai, "The Poisson distribution and beyond: Methods for microfluidic droplet production and single cell encapsulation," *Lab on a Chip*, vol. 15, no. 17, pp. 3439–3459, 2015.

[103] J. Clausell-Tormos, D. Lieber, J. C. Baret, A. El-Harrak, O. J. Miller, L. Frenz, J. Blouwolff, K. J. Humphry, S. Köster, H. Duan, C. Holtze, D. A. Weitz, A. D. Griffiths, and C. A. Merten, "Droplet-Based Microfluidic Platforms for the Encapsulation and Screening of Mammalian Cells and Multicellular Organisms," *Chemistry and Biology*, vol. 15, no. 5, pp. 427–437, 2008.

[104] S. Köster, F. E. Angilè, H. Duan, J. J. Agresti, A. Wintner, C. Schmitz, A. C. Rowat, C. A. Merten, D. Pisignano, A. D. Griffiths, and D. A. Weitz, "Drop-based microfluidic devices for encapsulation of single cells," *Lab on a Chip*, vol. 8, no. 7, pp. 1110–1115, 2008.

[105] T. Beneyton, I. P. M. Wijaya, P. Postros, M. Najah, P. Leblond, A. Couvent, E. Mayot, A. D. Griffiths, and A. Drevelle, "High-throughput screening of filamentous fungi using nanoliter-range droplet-based microfluidics," *Scientific Reports*, vol. 6, pp. 1–11, 2016.

[106] H. Yang, X. Qiao, M. K. Bhattacharyya, and L. Dong, "Microfluidic droplet encapsulation of highly motile single zoospores for phenotypic screening of an antioomycete chemical," *Biomicrofluidics*, vol. 5, no. 4, pp. 1–11, 2011.

[107] C. G. Agudelo, A. Sanati, M. Ghanbari, M. Packirisamy, and A. Geitmann, "A microfluidic platform for the investigation of elongation growth in pollen tubes," *Journal of Micromechanics and Microengineering*, vol. 22, no. 11, pp. 1–11, 2012.

[108] M. Ghanbari, A. S. Nezhad, C. G. Agudelo, M. Packirisamy, and A. Geitmann, "Microfluidic positioning of pollen grains in lab-on-a-chip for single cell analysis," *Journal of Bioscience and Bioengineering*, vol. 117, no. 4, pp. 504–511, 2014.

[109] T. Geng, E. L. Bredeweg, C. J. Szymanski, B. Liu, S. E. Baker, G. Orr, J. E. Evans, and R. T. Kelly, "Compartmentalized microchannel array for high-throughput analysis of single cell polarized growth and dynamics," *Scientific Reports*, vol. 5, pp. 1–12, 2015.

[110] L. Xu, H. Lee, D. Jetta, and K. W. Oh, "Vacuum-driven power-free microfluidics utilizing the gas solubility or permeability of polydimethylsiloxane (PDMS)," *Lab on a Chip*, vol. 15, no. 20, pp. 3962–3979, 2015.

[111] L. J. Millet, J. Aufrecht, J. Labbé, J. Uehling, R. Vilgalys, M. L. Estes, C. Miquel Guennoc, A. Deveau, S. Olsson, G. Bonito, M. J. Doktycz, and S. T. Retterer, "Increasing access to microfluidics for studying fungi and other branched biological structures," *Fungal Biology and Biotechnology*, vol. 6, no. 1, pp. 1–14, 2019.

[112] N. Minc, A. Boudaoud, and F. Chang, "Mechanical Forces of Fission Yeast Growth," *Current Biology*, vol. 19, no. 13, pp. 1096–1101, 2009.

[113] A. S. Nezhad, M. Naghavi, M. Packirisamy, R. Bhat, and A. Geitmann, "Quantification of cellular penetrative forces using lab-on-a-chip technology and finite element modeling," *Proceedings of the National Academy of Sciences of the United States of America*, vol. 110, no. 20, pp. 8093–8098, 2013.

[114] J. T. Burri, H. Vogler, N. F. Läubli, C. Hu, U. Grossniklaus, and B. J. Nelson, "Feeling the force: how pollen tubes deal with obstacles," *New Phytologist*, vol. 220, no. 1, pp. 187–195, 2018.

[115] A. Ghanbari, V. Nock, S. Johari, R. Blaikie, X. Chen, and W. Wang, "A micropillar-based on-chip system for continuous force measurement of *C. elegans*," *Journal of Micromechanics and Microengineering*, vol. 22, no. 9, pp. 1–10, 2012.

[116] S. Johari, V. Nock, M. M. Alkaisi, and W. Wang, "On-chip analysis of *C. elegans* muscular forces and locomotion patterns in microstructured environments," *Lab on a Chip*, vol. 13, pp. 1699–1707, 2013.

[117] Z. Qiu, L. Tu, L. Huang, T. Zhu, V. Nock, E. Yu, X. Liu, and W. Wang, "An integrated platform enabling optogenetic illumination of *Caenorhabditis elegans* neurons and muscular force measurement in microstructured environments," *Biomicrofluidics*, vol. 9, no. 1, pp. 1–12, 2015.

[118] A. Ghanbari, V. Nock, R. Blaikie, X. Chen, J. G. Chase, and W. Wang, "Automated vision-based force measurement of moving *C. elegans*," in *6th annual IEEE Conference on Automation Science and Engineering*, pp. 198–203, 2010.

[119] L. Yang, X. Hao, C. Wang, B. Zhang, and W. Wang, "Rapid and low cost replication of complex microfluidic structures with PDMS double casting technology," *Microsystem Technologies*, vol. 20, no. 10-11, pp. 1933–1940, 2014.

[120] P. Rai-Choudhury, *Handbook of Microlithography, Micromachining, and Microfabrication*, vol. 1. Bellingham, Washington, USA: SPIE Optical Engineering Press, 1997.

[121] J. Zhang, M. B. Chan-Park, and S. R. Conner, "Effect of exposure dose on the replication fidelity and profile of very high aspect ratio microchannels in SU-8," *Lab on a Chip*, vol. 4, no. 6, pp. 646–653, 2004.

[122] W.-J. Kang, E. Rabe, S. Kopetz, and A. Neyer, "Novel exposure methods based on reflection and refraction effects in the field of SU-8 lithography," *Journal of Micromechanics and Microengineering*, vol. 16, pp. 821–831, 2006.

[123] "ADEX Epoxy Thin Film Rolls / Sheets Preliminary Data Sheet," tech. rep., 2018. https://djmicrolaminates.com/datasheets/DJ-MicroLaminates-SUEX-Data-Sheet-7142017.pdf.

[124] "AZ40XT-11D Photoresist Data Sheet," tech. rep., 2017. https://microchemicals.com/micro/tds_az_40xt_photoresist.pdf.

[125] M.-C. King and D. H. Berry, "Photolithographic Mask Alignment Using Moire Techniques," *Applied Optics*, vol. 11, no. 11, pp. 2455–2459, 1972.

[126] S. Zhou, Y. Fu, X. Tang, S. Hu, W. Chen, and Y. Yang, "Fourier-based analysis of moiré fringe patterns of superposed gratings in alignment of nanolithography," *Optics Express*, vol. 16, no. 11, pp. 7869–7880, 2008.

[127] F. Schneider, T. Fellner, J. Wilde, and U. Wallrabe, "Mechanical properties of silicones for MEMS," *Journal of Micromechanics and Microengineering*, vol. 18, no. 6, pp. 1–9, 2008.

[128] J. Monahan, A. A. Gewirth, and R. G. Nuzzo, "A method for filling complex polymeric microfluidic devices and arrays," *Analytical Chemistry*, vol. 73, no. 13, pp. 3193–3197, 2001.

[129] S. M. Khare, A. Awasthi, V. Venkataraman, and S. P. Koushika, "Colored polydimethylsiloxane micropillar arrays for high throughput measurements of forces applied by genetic model organisms," *Biomicrofluidics*, vol. 9, no. 1, pp. 1–20, 2015.

[130] "Silc Pig® Product Information." https://www.smooth-on.com/products/silc-pig/.

[131] J. Schindelin, I. Arganda-Carreras, E. Frise, V. Kaynig, M. Longair, T. Pietzsch, S. Preibisch, C. Rueden, S. Saalfeld, B. Schmid, J. Y. Tinevez, D. J. White, V. Hartenstein, K. Eliceiri, P. Tomancak, and A. Cardona, "Fiji: An open-source platform for biological-image analysis," *Nature Methods*, vol. 9, no. 7, pp. 676–682, 2012.

[132] J. Y. Tinevez, N. Perry, J. Schindelin, G. M. Hoopes, G. D. Reynolds, E. Laplantine, S. Y. Bednarek, S. L. Shorte, and K. W. Eliceiri, "TrackMate: An open and extensible platform for single-particle tracking," *Methods*, vol. 115, pp. 80–90, 2017.

[133] A. Tayagui, Y. Sun, D. A. Collings, A. Garrill, and V. Nock, "An elastomeric micropillar platform for the study of protrusive forces in hyphal invasion," *Lab on a Chip*, vol. 17, no. 21, pp. 3643–3653, 2017.

[134] A. B. Tayagui, *Measurement of protrusive forces in hyphae using lab-on-a-chip technology*. PhD thesis, University of Canterbury, 2018.

[135] "AZ 15nXT (115 CPS) Photoresist Data Sheet," tech. rep., 2015. https://www.microchemicals.com/micro/tds_az_15nxt_115cps_photoresist.pdf.

[136] "AZ 12XT-20PL Series Technical Data Sheet," tech. rep., 2016. https://microchemicals.com/micro/tds_az_12xt_photoresist.pdf.

[137] H. Shearer, *The Use of Lab-on-a-chip Devices to Measure the Forces Exerted by Pathogenic Oomycete Species*. PhD thesis, University of Canterbury, 2018.

[138] S. F. Syed Ab Rahman, E. Singh, C. M. Pieterse, and P. M. Schenk, "Emerging microbial biocontrol strategies for plant pathogens," *Plant Science*, vol. 267, pp. 102–111, 2018.

[139] T. Luo, L. Fan, R. Zhu, and D. Sun, "Microfluidic single-cell manipulation and analysis: Methods and applications," *Micromachines*, vol. 10, no. 2, pp. 1–31, 2019.

[140] D. Di Carlo, N. Aghdam, and L. P. Lee, "Single-cell enzyme concentrations, kinetics, and inhibition analysis using high-density hydrodynamic cell isolation arrays," *Analytical Chemistry*, vol. 78, no. 14, pp. 4925–4930, 2006.

[141] D. Di Carlo, L. Y. Wu, and L. P. Lee, "Dynamic single cell culture array," *Lab on a Chip*, vol. 6, pp. 1445–1449, 2006.

[142] S. L. Faley, M. Copland, D. Wlodkowic, W. Kolch, K. T. Seale, J. P. Wikswo, and J. M. Cooper, "Microfluidic single cell arrays to interrogate signalling dynamics of individual, patient-derived hematopoietic stem cells," *Lab on a Chip*, vol. 9, no. 18, pp. 2659–2664, 2009.

[143] D. Wlodkowic, S. Faley, M. Zagnoni, J. P. Wikswo, and J. M. Cooper, "Microfluidic single-cell array cytometry for the analysis of tumor apoptosis," *Analytical Chemistry*, vol. 81, no. 13, pp. 5517–5523, 2009.

[144] A. M. Skelley, O. Kirak, H. Suh, R. Jaenisch, and J. Voldman, "Microfluidic control of cell pairing and fusion," *Nature Methods*, vol. 6, no. 2, pp. 147–152, 2009.

[145] H. Chen, J. Sun, E. Wolvetang, and J. Cooper-White, "High-throughput, deterministic single cell trapping and long-term clonal cell culture in microfluidic devices," *Lab on a Chip*, vol. 15, no. 4, pp. 1072–1083, 2015.

[146] T. Luo, J. Hou, S. Chen, Y. T. Chow, R. Wang, D. Ma, R. Zhu, and D. Sun, "Microfluidic single-cell array platform enabling week-scale clonal expansion under chemical/electrical stimuli," *Biomicrofluidics*, vol. 11, no. 5, pp. 1–11, 2017.

[147] W. H. Tan and S. Takeuchi, "A trap-and-release integrated microfluidic system for dynamic microarray applications," *Proceedings of the National Academy of Sciences of the United States of America*, vol. 104, no. 4, pp. 1146–1151, 2007.

[148] S. Kobel, A. Valero, J. Latt, P. Renaud, and M. Lutolf, "Optimization of microfluidic single cell trapping for long-term on-chip culture," *Lab on a Chip*, vol. 10, no. 7, pp. 857–863, 2010.

[149] I. Kumano, K. Hosoda, H. Suzuki, K. Hirata, and T. Yomo, "Hydrodynamic trapping of *Tetrahymena thermophila* for the long-term monitoring of cell behaviors," *Lab on a Chip*, vol. 12, no. 18, pp. 3451–3457, 2012.

[150] J. P. Frimat, M. Becker, Y. Y. Chiang, U. Marggraf, D. Janasek, J. G. Hengstler, J. Franzke, and J. West, "A microfluidic array with cellular valving for single cell co-culture," *Lab on a Chip*, vol. 11, no. 2, pp. 231–237, 2011.

[151] Y. C. Chen, S. G. Allen, P. N. Ingram, R. Buckanovich, S. D. Merajver, and E. Yoon, "Single-cell migration chip for chemotaxis-based microfluidic selection of heterogeneous cell populations," *Scientific Reports*, vol. 5, pp. 1–14, 2015.

[152] C. G. Agudelo, A. S. Nezhad, M. Ghanbari, M. Naghavi, M. Packirisamy, and A. Geitmann, "TipChip: A modular, MEMS-based platform for experimentation and phenotyping of tip-growing cells," *Plant Journal*, vol. 73, no. 6, pp. 1057–1068, 2013.

[153] A. S. Nezhad, M. Naghavi, M. Packirisamy, R. Bhat, and A. Geitmann, "Quantification of the Young's modulus of the primary plant cell wall using Bending-Lab-On-Chip (BLOC)," *Lab on a Chip*, vol. 13, no. 13, pp. 2599–2608, 2013.

[154] A. M. Malek and S. Izumo, "Mechanism of endothelial cell shape change and cytoskeletal remodeling in response to fluid shear stress," *Journal of Cell Science*, vol. 109, no. 4, pp. 713–726, 1996.

[155] C. R. White and J. A. Frangos, "The shear stress of it all: The cell membrane and mechanochemical transduction," *Philosophical Transactions of the Royal Society B: Biological Sciences*, vol. 362, no. 1484, pp. 1459–1467, 2007.

[156] A. K. Au, H. Lai, B. R. Utela, and A. Folch, "Microvalves and micropumps for BioMEMS," *Micromachines*, vol. 2, pp. 179–220, 2011.

[157] K. W. Oh and C. H. Ahn, "A review of microvalves," *Journal of Micromechanics and Microengineering*, vol. 16, no. 5, pp. 13–39, 2006.

[158] C. Zhang, D. Xing, and Y. Li, "Micropumps, microvalves, and micromixers within PCR microfluidic chips: Advances and trends," *Biotechnology Advances*, vol. 25, no. 5, pp. 483–514, 2007.

[159] M. A. Unger, H.-p. Chou, T. Thorsen, A. Scherer, and S. R. Quake, "Monolithic Microfabricated Valves and Pumps by Multilayer Soft Lithography," *Science*, vol. 288, pp. 113–116, 2000.

[160] C.-C. Lee, G. Sui, A. Elizarov, C. J. Shu, Y.-S. Shin, A. N. Dooley, J. Huang, A. Daridon, P. Wyatt, D. Stout, H. C. Kolb, O. N. Witte, N. Satyamurthy, J. R. Heath, M. E. Phelps, S. R. Quake, and H.-R. Tseng, "Multistep Synthesis of a Radiolabeled Imaging Probe Using Integrated Microfluidics," *Science*, vol. 310, pp. 1793–1796, 2005.

[161] T. Thorsen, S. J. Maerkl, and S. R. Quake, "Microfluidic Large-Scale Integration," *Science*, vol. 298, no. 5593, pp. 580–584, 2002.

[162] A. Y. Fu, H. P. Chou, C. Spence, F. H. Arnold, and S. R. Quake, "An integrated microfabricated cell sorter," *Analytical Chemistry*, vol. 74, no. 11, pp. 2451–2457, 2002.

[163] V. Studer, G. Hang, A. Pandolfi, M. Ortiz, W. F. Anderson, and S. R. Quake, "Scaling properties of a low-actuation pressure microfluidic valve," *Journal of Applied Physics*, vol. 95, no. 1, pp. 393–398, 2004.

[164] P. M. Fordyce, C. A. Diaz-Botia, J. L. Derisi, and R. Gomez-Sjoberg, "Systematic characterization of feature dimensions and closing pressures for microfluidic valves produced via photoresist reflow," *Lab on a Chip*, vol. 12, no. 21, pp. 4287–4295, 2012.

[165] Y. C. Wang, M. H. Choi, and J. Han, "Two-dimensional protein separation with advanced sample and buffer isolation using microfluidic valves," *Analytical Chemistry*, vol. 76, no. 15, pp. 4426–4431, 2004.

[166] J. Dai, S. H. Yoon, H. Y. Sim, Y. S. Yang, T. K. Oh, J. F. Kim, and J. W. Hong, "Charting microbial phenotypes in multiplex nanoliter batch bioreactors," *Analytical Chemistry*, vol. 85, no. 12, pp. 5892–5899, 2013.

[167] M. Mehling, T. Frank, C. Albayrak, and S. Tay, "Real-time tracking, retrieval and gene expression analysis of migrating human T cells," *Lab on a Chip*, vol. 15, no. 5, pp. 1276–1283, 2015.

[168] P. Dettinger, T. Frank, M. Etzrodt, N. Ahmed, A. Reimann, C. Trenzinger, D. Loeffler, K. D. Kokkaliaris, T. Schroeder, and S. Tay, "Automated Microfluidic System for Dynamic Stimulation and Tracking of Single Cells," *Analytical Chemistry*, vol. 90, no. 18, pp. 10695–10700, 2018.

[169] Y. Yang, J. F. Swennenhuis, H. S. Rho, S. Le Gac, and L. W. Terstappen, "Parallel single cancer cell whole genome amplification using button-valve assisted mixing in nanoliter chambers," *PloS ONE*, vol. 9, no. 9, pp. 1–8, 2014.

[170] H. Wu, A. Wheeler, and R. N. Zare, "Chemical cytometry on a picoliter-scale integrated microfluidic chip," *Proceedings of the National Academy of Sciences of the United States of America*, vol. 101, no. 35, pp. 12809–12813, 2004.

[171] T. Xu, H. Fu, Y. Li, X. Chen, W. Cheuk, C. W. Li, H. Zou, W. Yue, S. K. Au, Y. Wang, and M. Yang, "Single cell target gene mutation analysis by arc-edge-channel monolithic valve microfluidic cell isolation and locked nucleic acid-based PCR detection," *Sensors and Actuators, B: Chemical*, vol. 293, pp. 224–234, 2019.

[172] A. R. Wheeler, W. R. Throndset, R. J. Whelan, A. M. Leach, R. N. Zare, Y. H. Liao, K. Farrell, I. D. Manger, and A. Daridon, "Microfluidic device for single-cell analysis," *Analytical Chemistry*, vol. 75, no. 14, pp. 3581–3586, 2003.

[173] Y. Chen, B. Zhang, H. Feng, W. Shu, G. Y. Chen, and J. F. Zhong, "An automated microfluidic device for assessment of mammalian cell genetic stability," *Lab on a Chip*, vol. 12, no. 20, pp. 3930–3935, 2012.

[174] H. Sun, T. Olsen, J. Zhu, J. Tao, B. Ponnaiya, S. A. Amundson, D. J. Brenner, and Q. Lin, "A microfluidic approach to parallelized transcriptional profiling of single cells," *Microfluidics and Nanofluidics*, vol. 19, no. 6, pp. 1429–1440, 2015.

[175] Y. Zhou, S. Basu, K. J. Wohlfahrt, S. F. Lee, D. Klenerman, E. D. Laue, and A. A. Seshia, "A microfluidic platform for trapping, releasing and super-resolution imaging of single cells," *Sensors and Actuators, B: Chemical*, vol. 232, pp. 680–691, 2016.

[176] Fluidigm, "Fluidigm | Products | C1," 2018. https://www.fluidigm.com/products/c1-system.

[177] C. Hu, G. Munglani, H. Vogler, T. Ndinyanka Fabrice, N. Shamsudhin, F. K. Wittel, C. Ringli, U. Grossniklaus, H. J. Herrmann, and B. J. Nelson, "Characterization of size-dependent mechanical properties of tip-growing cells using a lab-on-chip device," *Lab on a Chip*, vol. 17, no. 1, pp. 82–90, 2017.

[178] X. Li, Z. T. F. Yu, D. Geraldo, S. Weng, N. Alve, W. Dun, A. Kini, K. Patel, R. Shu, F. Zhang, G. Li, Q. Jin, and J. Fu, "Desktop aligner for fabrication of multilayer microfluidic devices," *Review of Scientific Instruments*, vol. 86, no. 7, pp. 1–9, 2015.

[179] A. Muralidhar, E. Swadel, M. Spiekerman, S. Suei, M. Fraser, M. Ingerfeld, A. B. Tayagui, and A. Garrill, "A pressure gradient facilitates mass flow in the oomycete *Achlya bisexualis*," *Microbiology*, vol. 162, no. 2, pp. 206–213, 2016.

[180] A. Garrill, G. Findlay, and S. Tyerman, "Mechanosensitive ion channels," in *Membranes: Specialized Functions in Plants* (M. Smallwood, J. Knox, and D. J. Bowles, eds.), pp. 247–257, BIOS Scientific, 1996.

[181] C. A. Walker and P. van West, "Zoospore development in the oomycetes," *Fungal Biology Reviews*, vol. 21, no. 1, pp. 10–18, 2007.

[182] T. Nakagaki, H. Yamada, and Á. Tóth, "Maze-solving by an amoeboid organism," *Nature*, vol. 407, no. 6803, p. 470, 2000.

[183] W. Park, S. Han, and S. Kwon, "Fabrication of membrane-type microvalves in rectangular microfluidic channels via seal photopolymerization," *Lab on a Chip*, vol. 10, no. 20, pp. 2814–2817, 2010.

[184] K. Hosokawa and R. Maeda, "Pneumatically-actuated three-way microvalve fabricated with polydimethylsiloxane using the membrane transfer technique," *Journal of Micromechanics and Microengineering*, vol. 10, no. 3, pp. 415–420, 2000.

[185] W. H. Grover, A. M. Skelley, C. N. Liu, E. T. Lagally, and R. A. Mathies, "Monolithic membrane valves and diaphragm pumps for practical large-scale integration into glass microfluidic devices," *Sensors and Actuators, B: Chemical*, vol. 89, no. 3, pp. 315–323, 2003.

[186] B. R. Schudel, M. Tanyeri, A. Mukherjee, C. M. Schroeder, and P. J. Kenis, "Multiplexed detection of nucleic acids in a combinatorial screening chip," *Lab on a Chip*, vol. 11, no. 11, pp. 1916–1923, 2011.

[187] C. J. Huang, H. C. Chien, T. C. Chou, and G. B. Lee, "Integrated microfluidic system for electrochemical sensing of glycosylated hemoglobin," *Microfluidics and Nanofluidics*, vol. 10, no. 1, pp. 37–45, 2011.

[188] Y. H. Lin, Y. J. Chen, C. S. Lai, Y. T. Chen, C. L. Chen, J. S. Yu, and Y. S. Chang, "A negative-pressure-driven microfluidic chip for the rapid detection of a bladder cancer biomarker in urine using bead-based enzyme-linked immunosorbent assay," *Biomicrofluidics*, vol. 7, no. 2, pp. 1–11, 2013.

[189] C. Szydzik, R. J. Brazilek, K. Khoshmanesh, F. Akbaridoust, M. Knoerzer, P. Thurgood, I. Muir, I. Marusic, H. Nandurkar, A. Mitchell, and W. S. Nesbitt, "Elastomeric microvalve geometry affects haemocompatibility," *Lab on a Chip*, vol. 18, no. 12, pp. 1778–1792, 2018.

[190] E. T. Lagally, S.-H. Lee, and H. T. Soh, "Integrated microsystem for electrokinetic cell concentration and genetic detection," *Lab on a Chip*, vol. 5, pp. 1053–1058, 2005.

[191] S. L. Chen, W. H. Chang, C. H. Wang, H. L. You, J. J. Wu, T. H. Liu, M. S. Lee, and G. B. Lee, "An integrated microfluidic system for live bacteria detection from human joint fluid samples by using ethidium monoazide and loop-mediated isothermal amplification," *Microfluidics and Nanofluidics*, vol. 21, no. 5, pp. 1–12, 2017.

[192] S. B. Huang, Y. Zhao, D. Chen, H. C. Lee, Y. Luo, T. K. Chiu, J. Wang, J. Chen, and M. H. Wu, "A clogging-free microfluidic platform with an incorporated pneumatically driven membrane-based active valve enabling specific membrane capacitance and cytoplasm conductivity characterization of single cells," *Sensors and Actuators, B: Chemical*, vol. 190, pp. 928–936, 2014.

[193] G. Pasirayi, S. M. Scott, M. Islam, L. O'Hare, S. Bateson, and Z. Ali, "Low cost microfluidic cell culture array using normally closed valves for cytotoxicity assay," *Talanta*, vol. 129, pp. 491–498, 2014.

[194] Y. N. Yang, S. K. Hsiung, and G. B. Lee, "A pneumatic micropump incorporated with a normally closed valve capable of generating a high pumping rate and a high back pressure," *Microfluidics and Nanofluidics*, vol. 6, pp. 823–833, 2009.

[195] X. Zhou, X. Zhou, and B. Zheng, "A pneumatic valve controlled microdevice for bioanalysis," *Biomicrofluidics*, vol. 7, no. 5, pp. 1–8, 2013.

[196] B. Mosadegh, M. Agarwal, H. Tavana, T. Bersano-Begey, Y. S. Torisawa, M. Morell, M. J. Wyatt, K. S. O'Shea, K. F. Barald, and S. Takayama, "Uniform cell seeding and generation of overlapping gradient profiles in a multiplexed microchamber device with normally-closed valves," *Lab on a Chip*, vol. 10, no. 21, pp. 2959–2964, 2010.

[197] D. Irimia and M. Toner, "Cell handling using microstructured membranes," *Lab on a Chip*, vol. 6, no. 3, pp. 345–352, 2006.

[198] Y. H. Chang, C. J. Huang, and G. B. Lee, "A tunable microfluidic-based filter modulated by pneumatic pressure for separation of blood cells," *Microfluidics and Nanofluidics*, vol. 12, pp. 85–94, 2012.

[199] N. Li, C. H. Hsu, and A. Folch, "Parallel mixing of photolithographically defined nanoliter volumes using elastomeric microvalve arrays," *Electrophoresis*, vol. 26, no. 19, pp. 3758–3764, 2005.

[200] G. A. Cooksey, C. G. Sip, and A. Folch, "A multi-purpose microfluidic perfusion system with combinatorial choice of inputs, mixtures, gradient patterns, and flow rates," *Lab on a Chip*, vol. 9, no. 3, pp. 417–426, 2009.

[201] J. H. Wang and G. B. Lee, "Formation of Tunable, Emulsion Micro-Droplets Utilizing Flow-Focusing Channels and a Normally-Closed Micro-Valve," *Micromachines*, vol. 4, no. 3, pp. 306–320, 2013.

[202] J. Y. Baek, J. Y. Park, J. I. Ju, T. S. Lee, and S. H. Lee, "A pneumatically controllable flexible and polymeric microfluidic valve fabricated via in situ development," *Journal of Micromechanics and Microengineering*, vol. 15, no. 5, pp. 1015–1020, 2005.

[203] B. Mosadegh, H. Tavana, S. C. Lesher-Perez, and S. Takayama, "High-density fabrication of normally closed microfluidic valves by patterned deactivation of oxidized polydimethylsiloxane," *Lab on a Chip*, vol. 11, no. 4, pp. 738–742, 2011.

[204] "SUEX Epoxy Thick Film Sheets (TDFS) Preliminary Data Sheet," tech. rep., 2018. https://djmicrolaminates.com/datasheets/DJ-MicroLaminates-SUEX-Data-Sheet-7142017.pdf.

[205] H. Lai and A. Folch, "Design and dynamic characterization of "single-stroke" peristaltic PDMS micropumps," *Lab on a Chip*, vol. 11, pp. 336–342, 2011.

[206] R. Mohan, B. R. Schudel, A. V. Desai, J. D. Yearsley, C. A. Apblett, and P. J. Kenis, "Design considerations for elastomeric normally closed microfluidic valves," *Sensors and Actuators, B: Chemical*, vol. 160, no. 1, pp. 1216–1223, 2011.

[207] B. H. Jo, L. M. Van Lerberghe, K. M. Motsegood, and D. J. Beebe, "Three-dimensional micro-channel fabrication in polydimethylsiloxane (PDMS) elastomer," *Journal of Microelectromechanical Systems*, vol. 9, no. 1, pp. 76–81, 2000.

[208] L. Aoun, P. Weiss, A. Laborde, B. Ducommun, V. Lobjois, and C. Vieu, "Microdevice arrays of high aspect ratio poly(dimethylsiloxane) pillars for the investigation of multicellular tumour spheroid mechanical properties," *Lab on a Chip*, vol. 14, no. 13, pp. 2344–2353, 2014.

[209] R. Soffe, A. J. Mach, S. Onal, V. Nock, L. P. Lee, and J. T. Nevill, "Art-on-a-Chip: Preserving Microfluidic Chips for Visualisation and Permanent Display," *Small*, no. 2002035, 2020.

[210] J. R. Raper, "Sexual Hormones in Achlya. I. Indicative Evidence for a Hormonal Coordinating Mechanism," *American Journal of Botany*, vol. 26, no. 8, pp. 639–650, 1939.

[211] A. Pfreundt, K. B. Andersen, M. Dimaki, and W. E. Svendsen, "An easy-to-use microfluidic interconnection system to create quick and reversibly interfaced simple microfluidic devices," *Journal of Micromechanics and Microengineering*, vol. 25, no. 11, pp. 1–10, 2015.

[212] Y. Temiz, R. D. Lovchik, G. V. Kaigala, and E. Delamarche, "Lab-on-a-chip devices: How to close and plug the lab?," *Microelectronic Engineering*, vol. 132, pp. 156–175, 2015.

[213] J. W. Hong, V. Studer, G. Hang, W. F. Anderson, and S. R. Quake, "A nanoliter-scale nucleic acid processor with parallel architecture," *Nature Biotechnology*, vol. 22, no. 4, pp. 435–439, 2004.

[214] A. Scott, A. K. Au, E. Vinckenbosch, and A. Folch, "A microfluidic D-subminiature connector," *Lab on a Chip*, vol. 13, no. 11, pp. 2036–2039, 2013.

[215] D. Van Swaay, J. P. Mächler, C. Stanley, and A. Demello, "A chip-to-world connector with a built-in reservoir for simple small-volume sample injection," *Lab on a Chip*, vol. 14, no. 1, pp. 178–181, 2014.

[216] A. Bosch, R. A. Maronna, and O. M. Yantorno, "A simple descriptive model of filamentous fungi spore germination," *Process Biochemistry*, vol. 30, no. 7, pp. 599–606, 1995.

[217] L. Mascari, P. Ymele-Leki, C. D. Eggleton, P. Speziale, and J. M. Ross, "Fluid shear contributions to bacteria cell detachment initiated by a monoclonal antibody," *Biotechnology and Bioengineering*, vol. 83, no. 1, pp. 65–74, 2003.

[218] A. Persat, C. D. Nadell, M. K. Kim, F. Ingremeau, A. Siryaporn, K. Drescher, N. S. Wingreen, B. L. Bassler, Z. Gitai, and H. A. Stone, "The mechanical world of bacteria," *Cell*, vol. 161, no. 5, pp. 988–997, 2015.

[219] B. J. Moss, Y. Kim, M. P. Nandakumar, and M. R. Marten, "Quantifying metabolic activity of filamentous fungi using a colorimetric XTT assay," *Biotechnology Progress*, vol. 24, no. 3, pp. 780–783, 2008.

[220] D. K. Stoecker, A. Long, S. E. Suttles, and L. P. Sanford, "Effect of small-scale shear on grazing and growth of the dinoflagellate *Pfiesteria piscicida*," *Harmful Algae*, vol. 5, no. 4, pp. 407–418, 2006.

[221] T. J. Banko, P. A. Richardson, and C. X. Hong, "Effects of zoospore concentration and application pressure on foliage blight of *Catharanthus roseus* caused by *Phytophthora nicotianae*," *Plant Disease*, vol. 90, no. 3, pp. 297–301, 2006.

[222] J. B. Joshi, C. B. Elias, and M. S. Patole, "Role of hydrodynamic shear in the cultivation of animal, plant and microbial cells," *Chemical Engineering Journal and the Biochemical Engineering Journal*, vol. 62, no. 2, pp. 121–141, 1996.

[223] L. H. Grimm, S. Kelly, I. I. Völkerding, R. Krull, and D. C. Hempel, "Influence of mechanical stress and surface interaction on the aggregation of *Aspergillus niger* conidia," *Biotechnology and Bioengineering*, vol. 92, no. 7, pp. 879–888, 2005.

[224] S. Kelly, L. H. Grimm, C. Bendig, D. C. Hempel, and R. Krull, "Effects of fluid dynamic induced shear stress on fungal growth and morphology," *Process Biochemistry*, vol. 41, no. 10, pp. 2113–2117, 2006.

[225] G. Guillemot, G. Vaca-Medina, H. Martin-Yken, A. Vernhet, P. Schmitz, and M. Mercier-Bonin, "Shear-flow induced detachment of Saccharomyces cerevisiae from stainless steel: Influence of yeast and solid surface properties," *Colloids and Surfaces B: Biointerfaces*, vol. 49, no. 2, pp. 126–135, 2006.

[226] P. Weerappuli, T. Kojima, S. Takayama, and A. Basu, "Novel monolithic "Slightly-Open doormat" (SOD) valve enables efficient fabrication of highly-scalable microfluidic gas-on-gas multiplexer," *Sensors and Actuators, B: Chemical*, vol. 297, pp. 1–7, 2019.

[227] P. F. Davies, "Flow-Mediated Endothelial Mechanotransduction," *PHYSIOLOGICAL REVIEWS*, vol. 75, no. 3, pp. 1–42, 1995.

[228] F. Li and S. P. Palecek, "EAP1, a *Candida albicans* Gene Involved in Binding Human Epithelial Cells," *Eukaryotic Cell*, vol. 2, no. 6, pp. 1266–1273, 2003.

[229] D. D. Thomson, S. Wehmeier, F. J. Byfield, P. A. Janmey, D. Caballero-Lima, A. Crossley, and A. C. Brand, "Contact-induced apical asymmetry drives the thigmotropic responses of *Candida albicans* hyphae," *Cellular Microbiology*, vol. 17, no. 3, pp. 342–354, 2015.

[230] B. I. Heath and R. L. Harold, "Actin has multiple roles in the formation and architecture of zoospores of the oomycetes, *Saprolegnia ferax* and *Achlya bisexualis*," *Journal of Cell Science*, vol. 102, no. 3, pp. 611–627, 1992.

[231] X. L. Ke, J. G. Wang, Z. M. Gu, M. Li, and X. N. Gong, "Morphological and molecular phylogenetic analysis of two *Saprolegnia sp.* (Oomycetes) isolated from silver crucian carp and zebra fish," *Mycological Research*, vol. 113, no. 5, pp. 637–644, 2009.

[232] H. MacLeod and P. A. Horgen, "Germination of the asexual spores of the aquatic fungus, *Achlya bisexualis*," *Experimental Mycology*, vol. 3, no. 1, pp. 70–82, 1979.

[233] J. W. Deacon and G. Saxena, "Orientated zoospore attachment and cyst germination in *Catenaria anguillulae*, a facultative endoparasite of nematodes," *Mycological Research*, vol. 101, no. 5, pp. 513–522, 1997.

[234] S. K. Walker and A. Garrill, "Actin microfilaments in fungi," *Mycologist*, vol. 20, no. 1, pp. 26–31, 2006.

[235] E. B. Jones, "Fungal adhesion," *Mycological Research*, vol. 98, no. 9, pp. 961–981, 1994.

[236] A. R. Hardham, "Cell Biology of Fungal Infection of Plants," in *Biology of the Fungal Cell*, pp. 91–123, Springer, Berlin, Heidelberg, 2001.

[237] G. Grossmann, W. J. Guo, D. W. Ehrhardt, W. B. Frommer, R. V. Sit, S. R. Quake, and M. Meier, "The Rootchip: An integrated microfluidic chip for plant Science," *Plant Cell*, vol. 23, no. 12, pp. 4234–4240, 2011.

[238] H. Bruus, *Theoretical Microfluidics*. New York, USA: Oxford University Press, 2008.

[239] K. Kryukov, "Resistor Network Solver." http://kirr.homeunix.org/electronics/resistor-network-solver/.

# Appendix A

# Mycelial Force Sensing Platform

## A.1 Formation of air bubbles during spin-coating

Due to the channel patterns on the first layer of photoresist, air bubbles formed during the second layer photoresist spin-coating, as shown in the Fig. A.1. To overcome this problem, a 2-step spin-coating process was utilized on a programmable spin-coater, as described in Section 3.2.1.

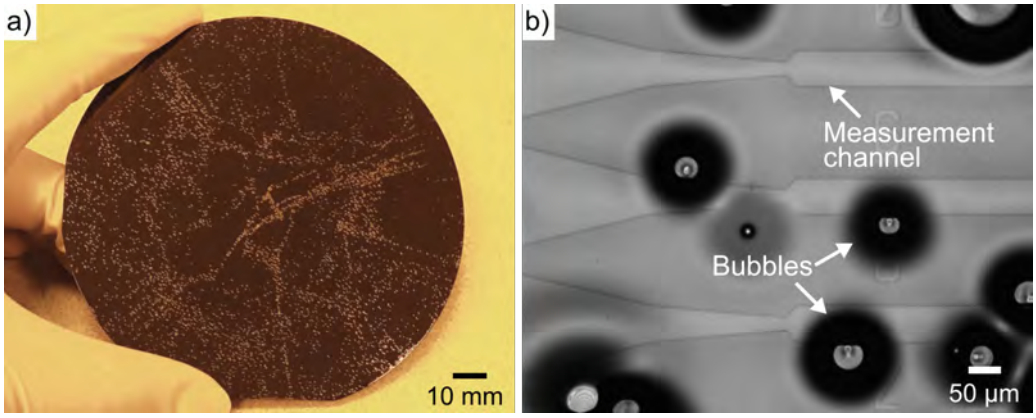


Figure A.1: Photographs of (a) a Si wafer coated with negative photoresist ADEX05 as first layer and positive photoresist AZ 40XT as second layer. (b) Air bubbles were generated during the spin-coating of AZ 40XT at 2000 rpm for 30 sec, preventing further processing.

## A.2 Previous alignment mark

Figure A.2 shows the previously used alignment mark, which contained a large square on the first layer and four small squares on the second layer, overlapping at each corner of the large square. This design made it difficult to align two layers of photoresists with the required precision, especially in the area of the pillar cavity.

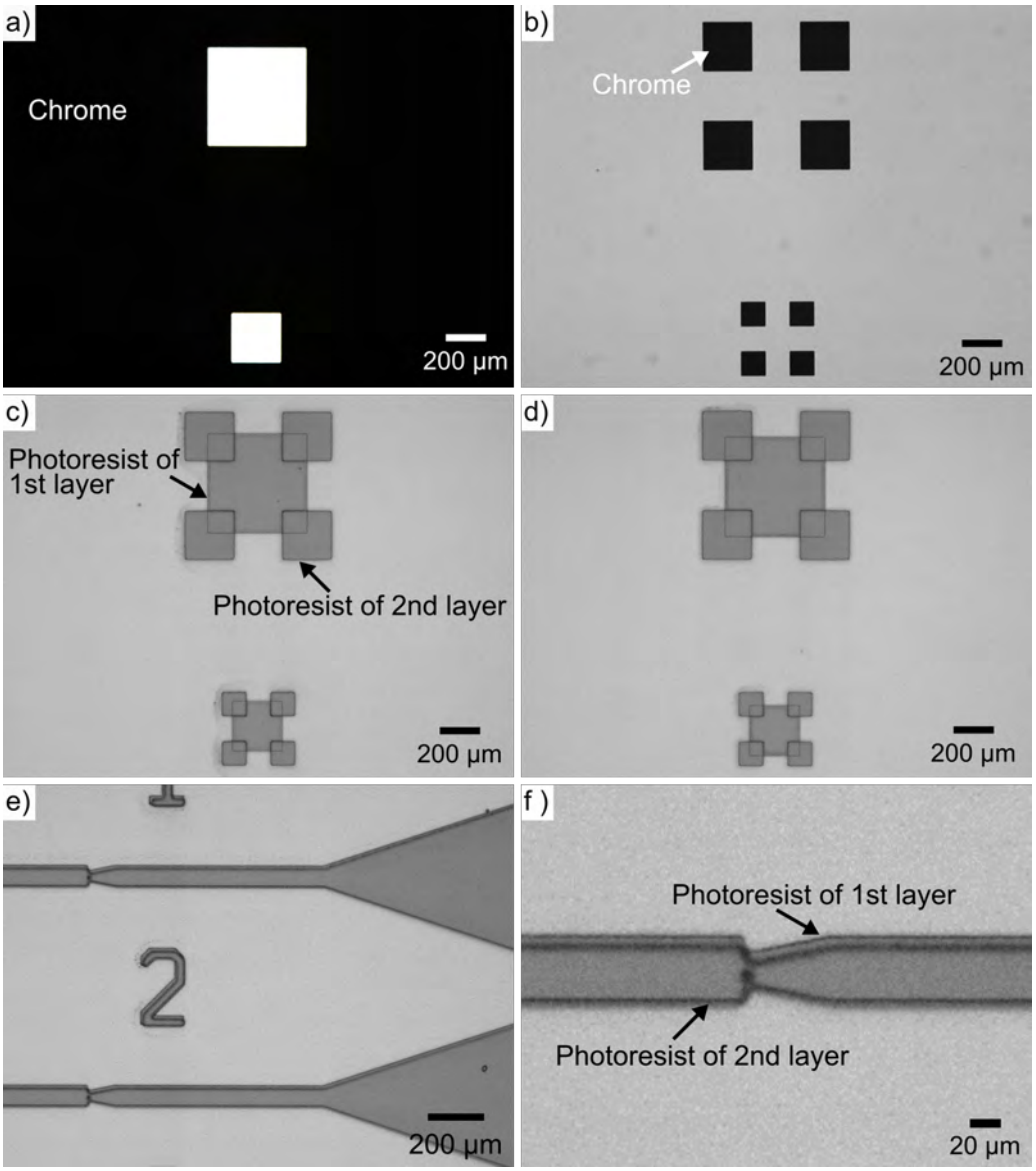


Figure A.2: Optical micrographs of previously-used alignment marks. (a & b) Patterns on the first and second layer masks. (c & d) Fabricated alignment marks on left and right side of the photoresist master indicating sufficient alignment accuracy. (e & f) Images of measurement channels on the same master showing the second layer out of alignment in the constriction area despite the alignment mark overlap.

## A.3 AZ 12XT thickness

Figure A.3 shows the relationship between the spin-coating speed of AZ 12XT, as determined with the pre-processed negative photoresist AZ 15nXT coated to a thickness of 2.6 $\mu$m as the first layer, and the resulting total thickness of the measurement channels. In this arrangement the thickness of measurement channels decreased from 18.6 $\pm$ 0.26 to 10.2 $\pm$ 0.38 $\mu$m, while the speed of spin-coating increased from 1000 to 2000 rpm.

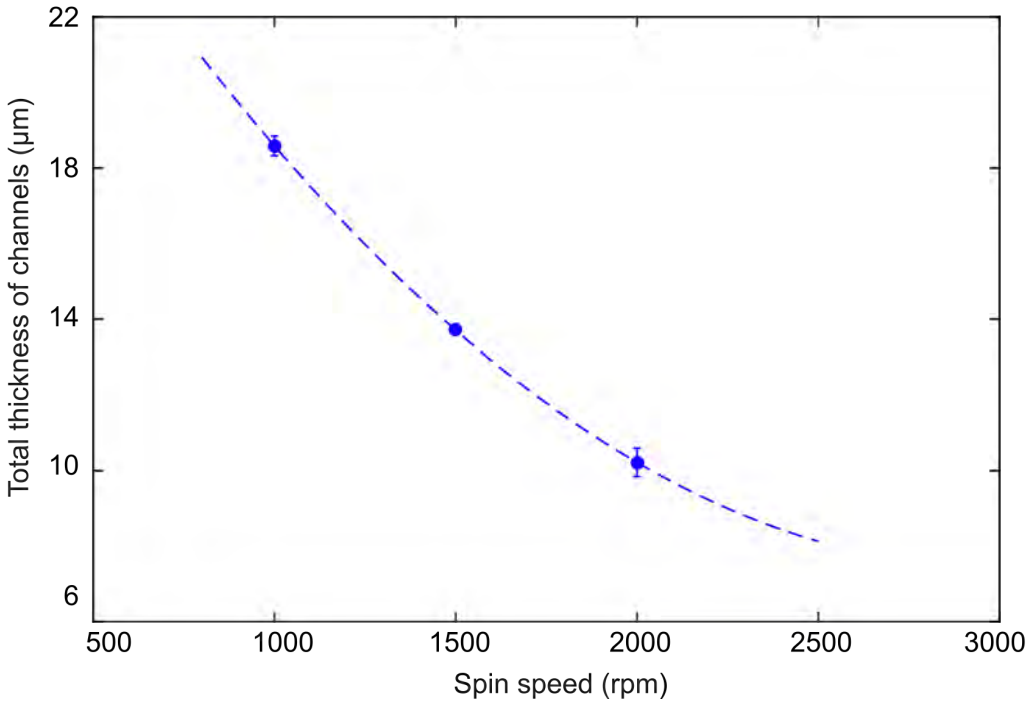


Figure A.3: Plot of the total thickness of measurement channels as a function of the speed of spin-coating of AZ 12XT. A 2.6 $\mu$m thick negative-tone photoresist AZ 15nXT was used as subjacent first layer.

# Appendix B

# Monolithic Platforms with Single Zoospore Capture, Germination and Single Hypha Force Sensing

## B.1 Fabrication process of platform

The PDMS chips of either gas or fluidic layer were fabricated by replica-molding of photoresist masters. As for the mycelial platforms, a two-layer photoresist master was required for the fluidic layer. Figure B.1 shows the two photomasks manufactured for the fluidic layer using $\mu$PG101. The first-layer mask for the negative photoresist contained the outline of channels and constriction structures inside channels, while the second-layer mask for the positive photoresist had additional features of micropillar cavities and vertical obstacle for constriction type A. For the gas layer master, standard photolithography processing was used. Fabricated photomask, photoresist master with 50 $\mu$m high negative photoresist patterns and PDMS-casted chip are shown in Fig. B.2.

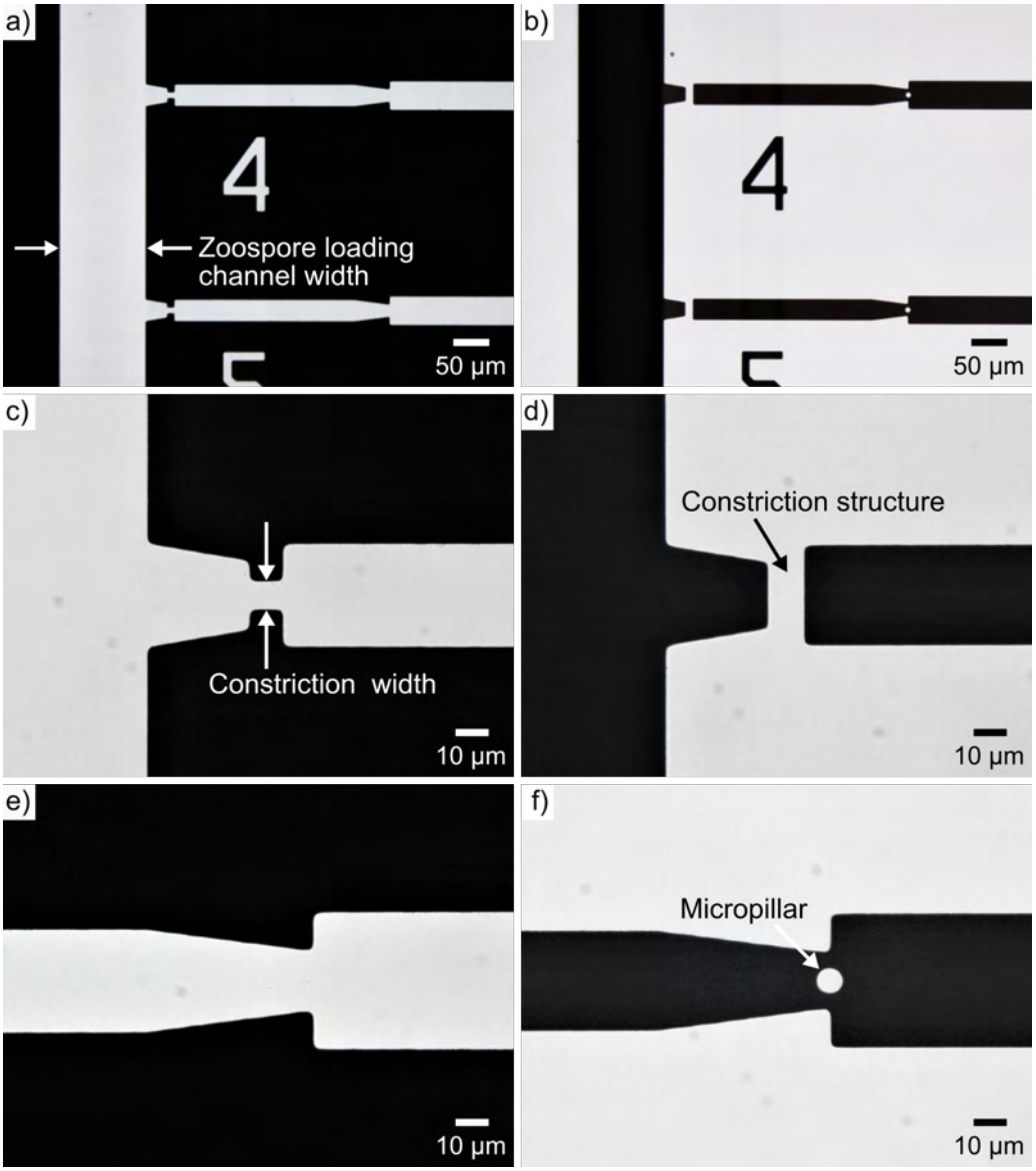


Figure B.1: Optical micrographs of fabricated photomasks for the fluidic layer with constriction type A. (a) First-layer mask for negative photoresist including a 120 $\mu$m wide zoospore loading channel and parallel measurement channels. (b) Second-layer mask for positive photoresist. (c & d) Detailed view of first and second-layer mask in the constriction structure area including a vertical obstacle for constriction type A. (e & f) Detailed view of first and second-layer mask for micropillar cavities.

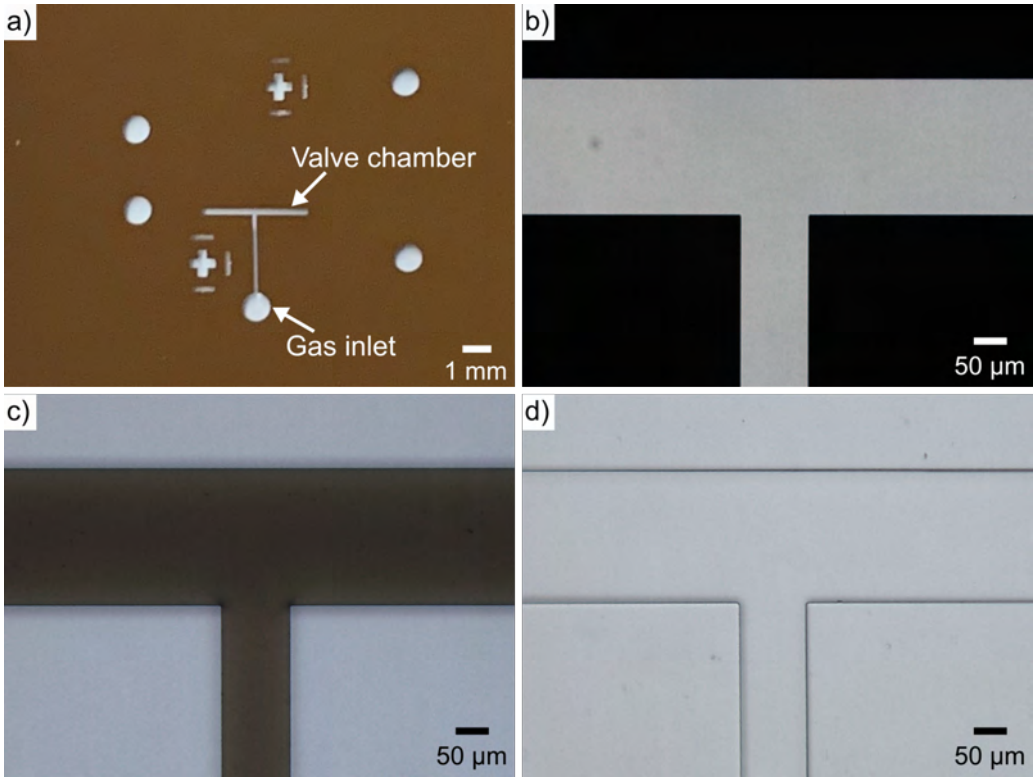


Figure B.2: Optical micrographs of fabricated photomask (a & b), master mold coated with negative photoresist ADEX 50 (c), and PDMS chip (d) for the gas layer.

## B.2 Microsphere capture and retention tests

To optimize the width of the zoospore loading channel, capture and retention tests using 20 $\mu$m diameter microspheres were carried out on the platforms with 60, 120 and 190 $\mu$m wide loading channels. Microsphere suspension was injected into the fluidic layer from the zoospore inlet at a flow rate of 20 $\mu$L/min using the syringe pump. After capture of the microspheres in the trap-sites of the measurement channels was observed, the membrane microvalve was closed by applying the previously determined positive pressure (2.0 bar) to the gas layer of the platform. DI water was then pumped into the fluidic layer from the media inlet at a flow rate of 5 $\mu$L/min using the pressure controller, while sample flow from the zoospore inlet was stopped. Figures B.3 and B.4 show the results of experiments on 60 and 190 $\mu$m wide loading channel platforms.

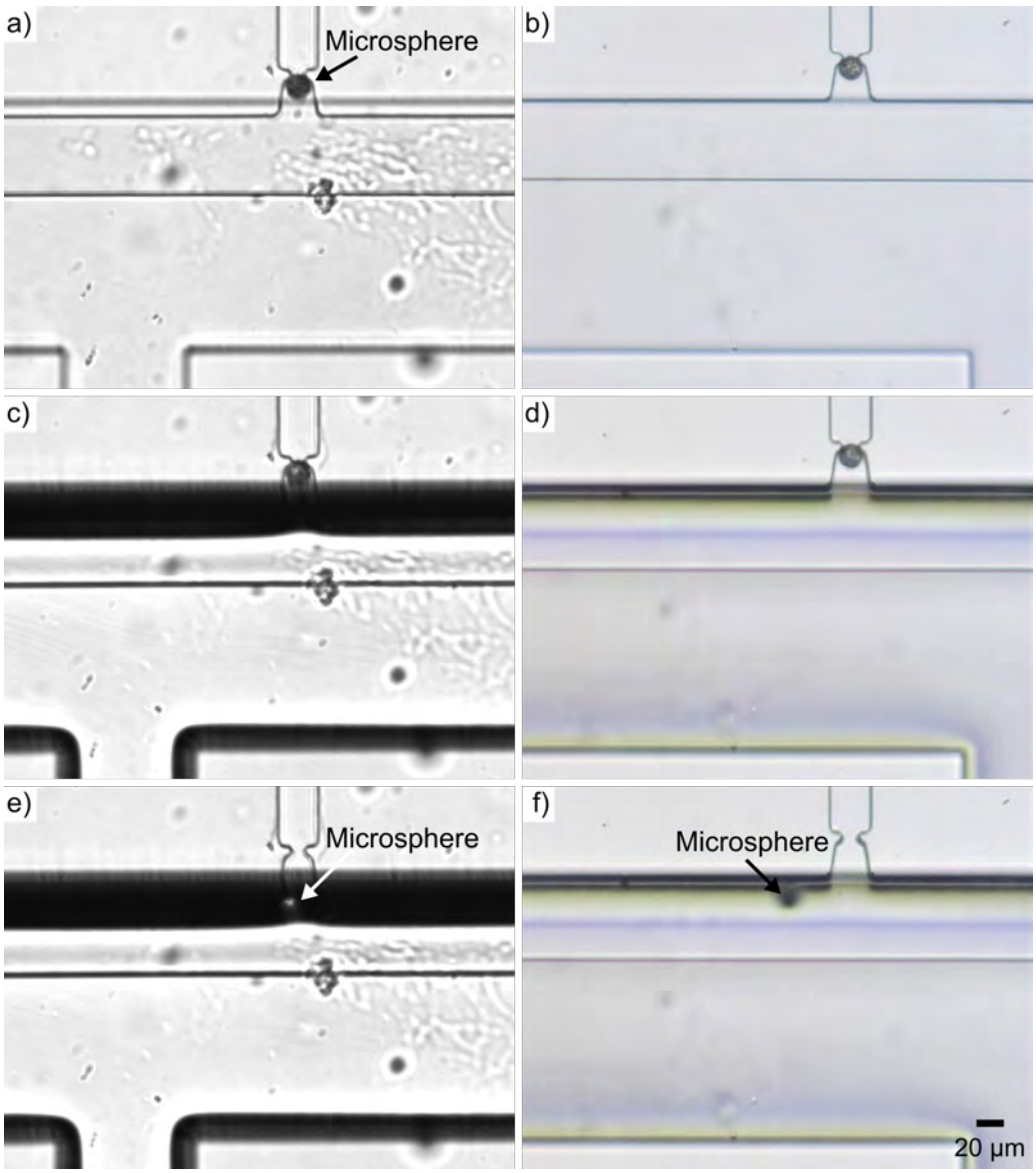


Figure B.3: Microsphere capture and retention tests on the platform with the 60 $\mu$m wide zoospore loading channel. (a, c & d) Optical micrographs showing that, while a single microsphere could be captured in the trap-site of one measurement channel, it could not be retained even if the membrane microvalve was closed at pressure of 2.0 bar. After DI water was pumped from media inlet to simulate perfusion, the microsphere flowed into the corner of the zoospore loading channel. Note, in this example the microvalve chamber was overlapping the zoospore loading channel due to an alignment error. (b, d & f) Optical micrographs showing the same loss of retention, but on a device where the microvalve chamber was more precisely aligned to zoospore loading channel.

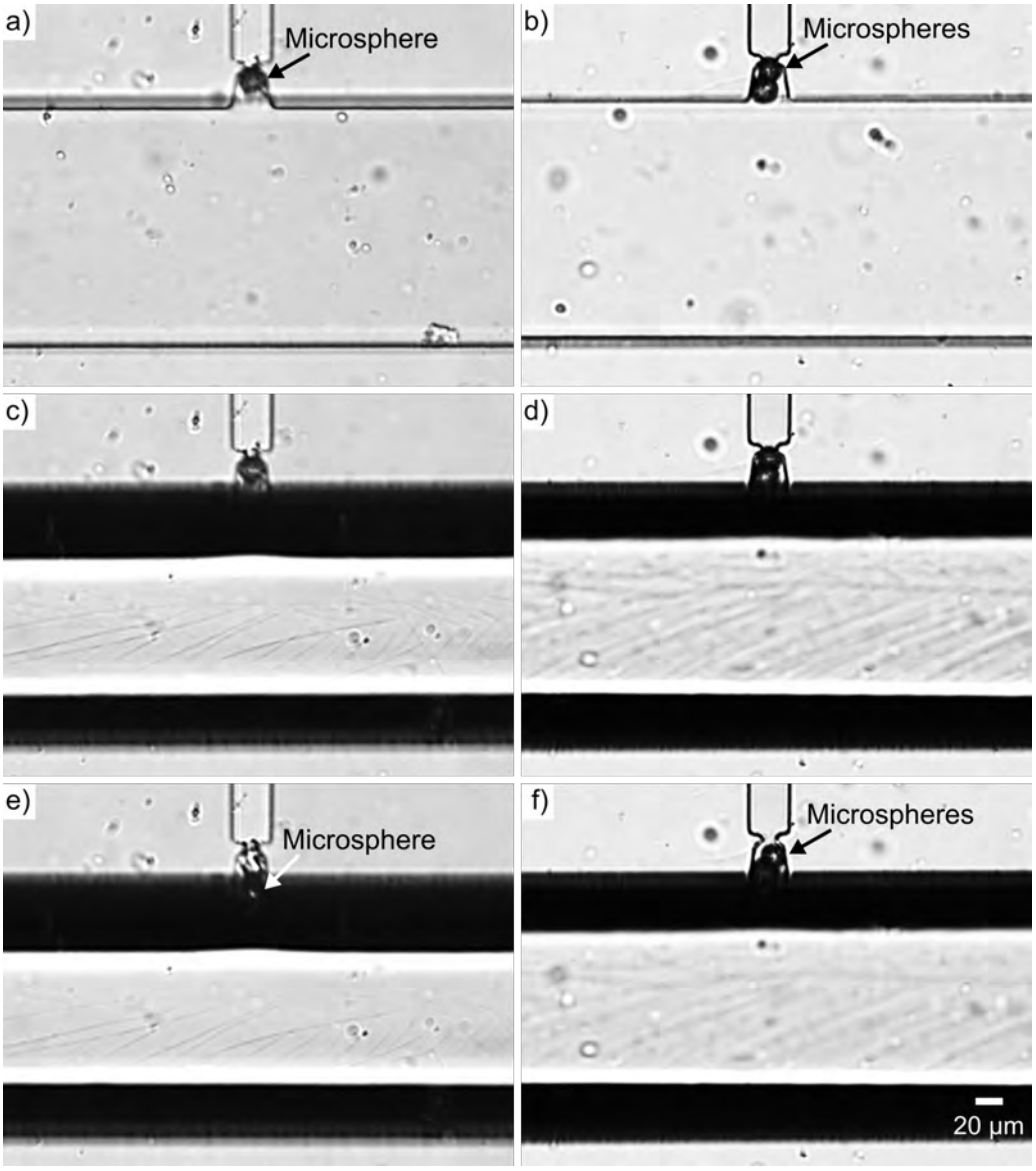


Figure B.4: Microsphere capture and retention tests on the platform with a 190 $\mu$m wide zoospore loading channel. (a, c & d) Optical micrographs showing a single microsphere being captured in the trap-site of one measurement channel, the membrane microvalve being closed at a pressure of 2.0 bar, and the microsphere flowing back against the membrane valve after the DI water was pumped from media inlet. Note, in this example the microvalve chamber was overlapping the zoospore loading channel due to an alignment error. (b, d & f) Optical micrographs showing the same on a device where the microvalve chamber was more precisely aligned to zoospore loading channel.

## B.3 Zoospore trapping test with constriction type B

Single zoospore trapping tests were implemented on the platform with two types of constriction structures. Figure B.5 shows the results for constriction type B, which only constricted in horizontal direction. It was observed that smaller, initially captured zoospores were eventually squeezed and pushed through the trap sites.

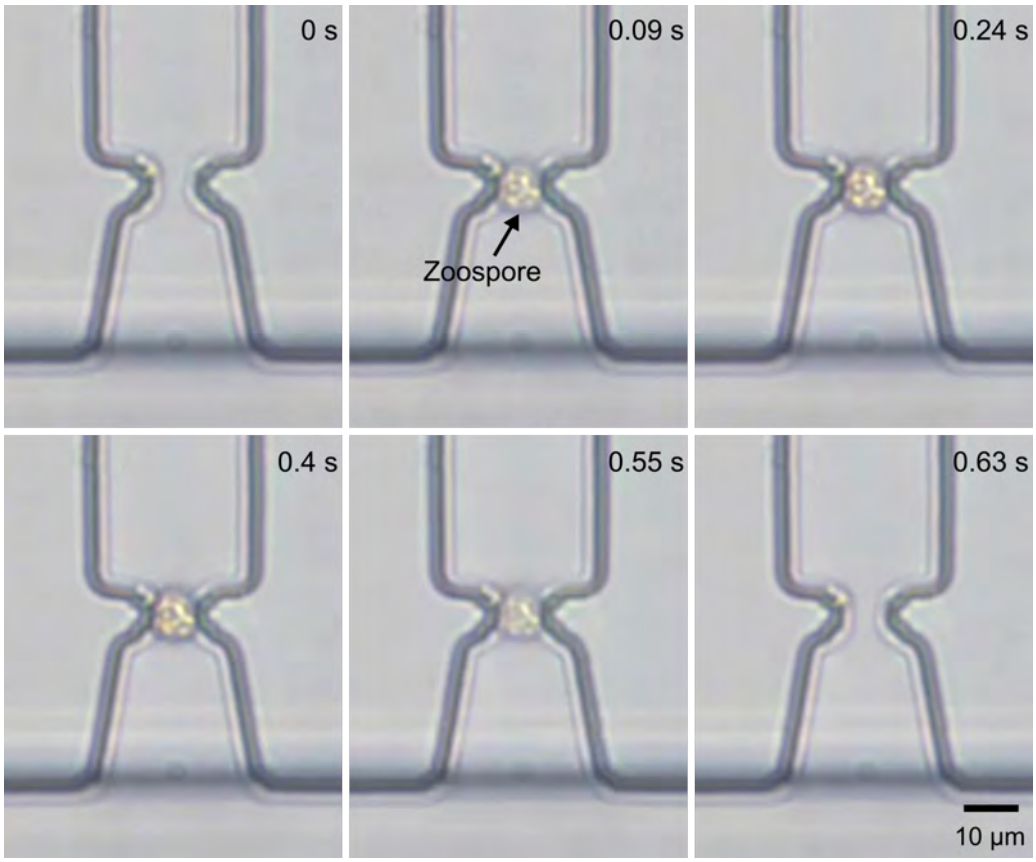


Figure B.5: Single zoospore trapping test on the platform with constriction type B (constriction only in horizontal direction, 8 $\times$ 30 $\mu$m width $\times$ height). Optical micrographs showing a zoospore was captured by the constriction structure in the beginning (0.24 sec), but eventually pushed through the constriction (0.63 sec) due to increased fluid shear.

## B.4 Improved experimental setup

Contamination with bacteria and other undefined organisms growing in the platform were observed during long-term on-chip culture. In order to reduce the occurrence of contamination, the experimental setup was improved, as shown in Fig. B.6. This included the autoclaving of all tubing and containers, assembly of them in a sterile laminar flow hood and adding filters on each channel of the OB1.

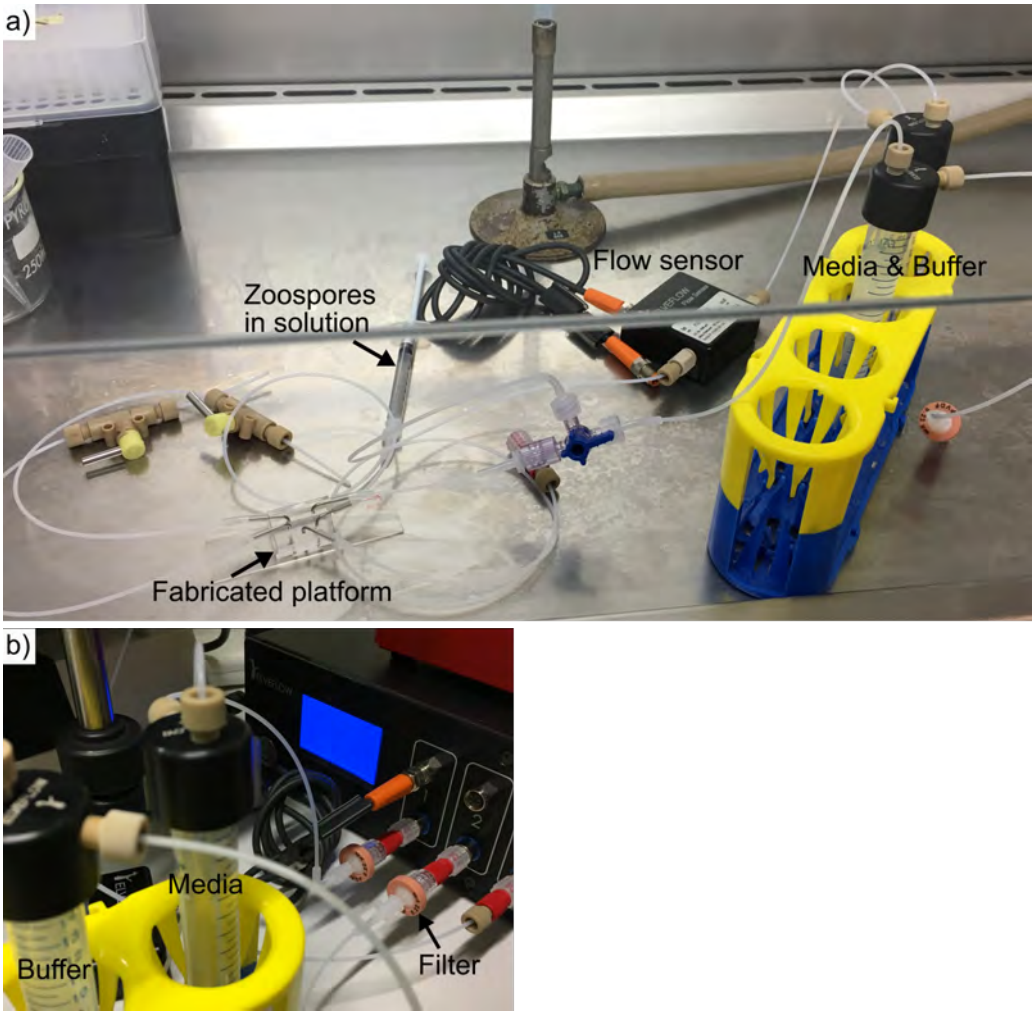


Figure B.6: Photographs of the improved experimental setup to prevent contamination. (a) Fittings and tubings were autoclaved and connected in the laminar flow hood. (b) Filters were added onto the channels of the pressure controller OB1 before the media reservoir.

# Appendix C

# Integration of Normally-Closed Microvalves

## C.1 Fabrication of the LOC platform

Both gas and fluidic layer of the platform were fabricated by PDMS casting from photoresist masters. For the gas layer photoresist master, standard photolithography processing was utilized. Figure C.1 shows the photomask, photoresist master and PDMS chip for the gas layer with various sized air chambers merging to a single gas inlet port. Meanwhile, the photoresist master of the fluidic layer was fabricated as a two-layer master according to the protocol described in Section 3.2.1. Figure C.2 shows two fabricated photomasks for the first negative photoresist layer and second positive photoresist layer of the fluidic layer master.

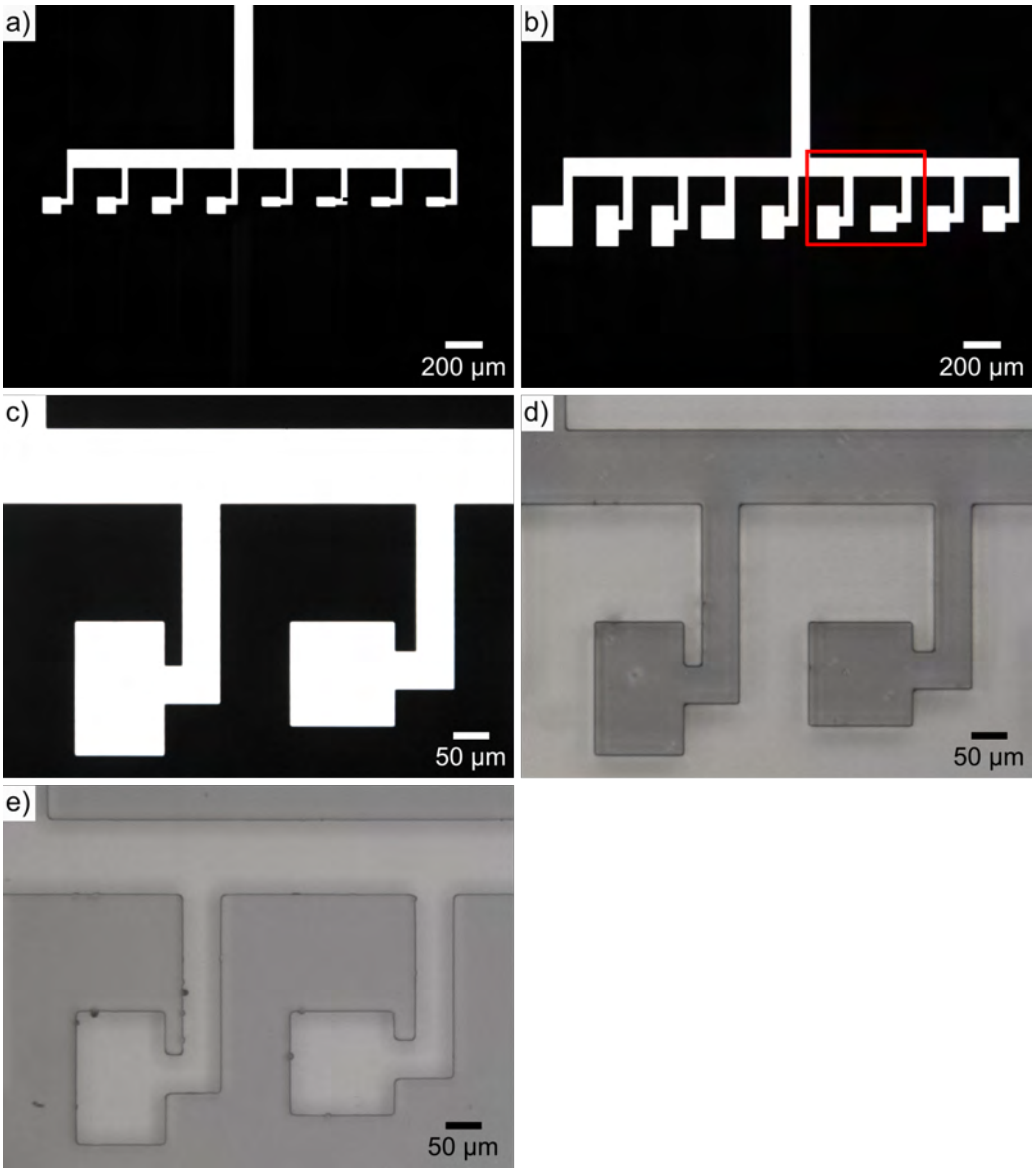


Figure C.1: Optical micrographs of fabricated photomask, photoresist master and PDMS chip for the gas layer. (a - c) Photomask with various air chamber sizes and their detail views. The red box in (b) indicates the example area highlighted in (c - e). (d) Photoresist master wafer with SUEX 100 photoresist coated and (e) replicated PDMS chip.

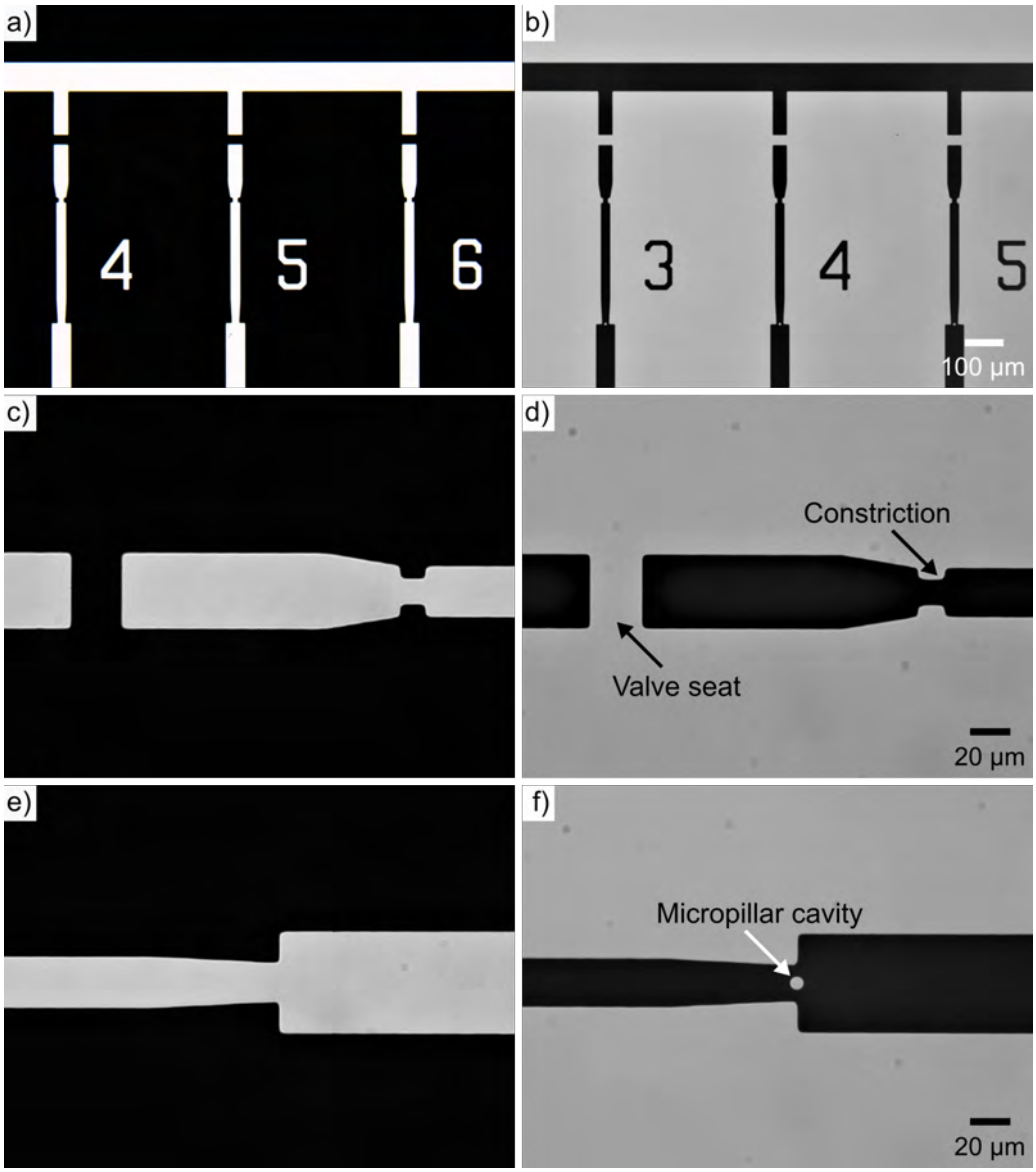


Figure C.2: Fabricated photomasks for the fluidic layer. (a, c & e) Optical micrographs of the first layer photomask for negative photoresist, and detail view of the valve seat and constriction structure. (b, d & f) Optical micrographs of the second layer photomask for positive photoresist and detail view of valve seat, constriction structure and micropillar cavity.

## C.2 Collapse of micropillars

During the chip assembly, DI water was injected into the fluidic layer through the zoospore inlet to prevent the PDMS membrane from permanently contacting with the valve seats. However, as a result of this, the force sensing micropillars in the measurement channels could be observed to collapse in random direction towards the side walls of the channels after the fluidic chip dried out, as shown in Fig. C.3. A $CO_2$ critical point dryer has been proved to avoid pillar collapse during the drying of PDMS [208], which could be a solution in the future.

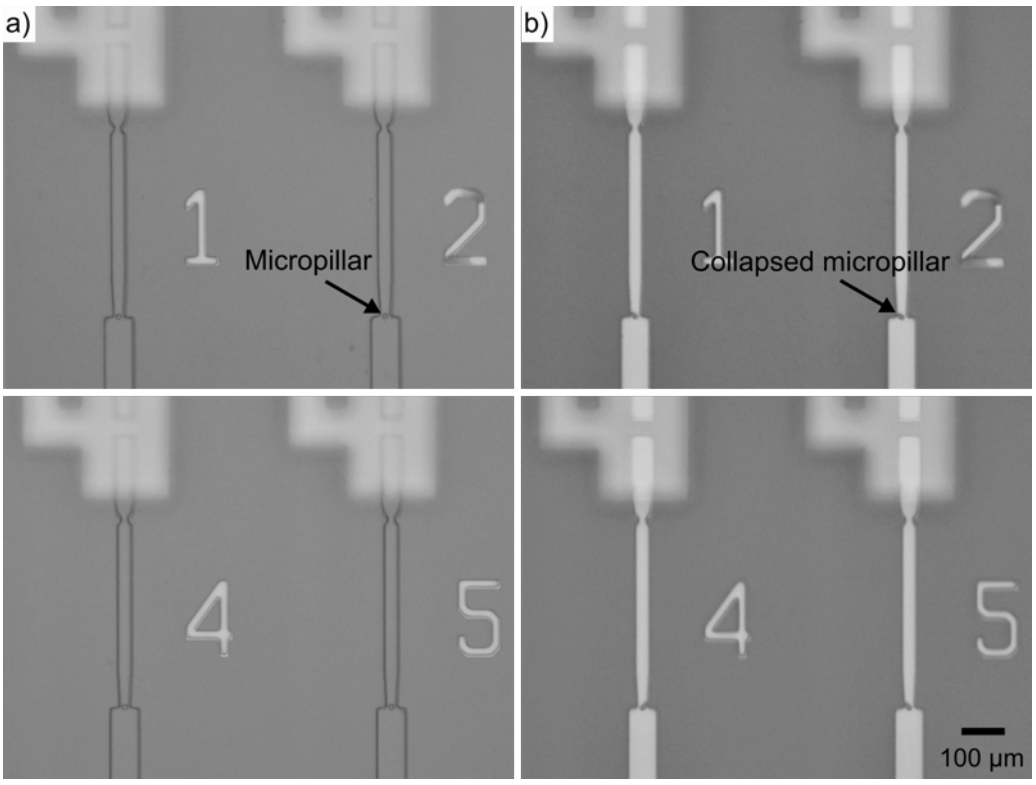


Figure C.3: Optical micrographs of measurement channels containing the force sensing pillars. (a) DI water was filled in the fluidic chip. (b) Drying of the fluidic channels on the chip led to permanent collapse of the micropillars in different directions against the channel walls. This collapsed state could not be recovered by successive filling with media.

## C.3 Gas layer with separate inlet ports

The design of the gas layer was optimized to achieve individual control of the membrane valves for each measurement channel. Figure C.4 shows the fabricated photomask, photoresist master and PDMS chip for the gas layer, in which the air chamber of each valve was connected via a separate gas port, rather than converging at single inlet.

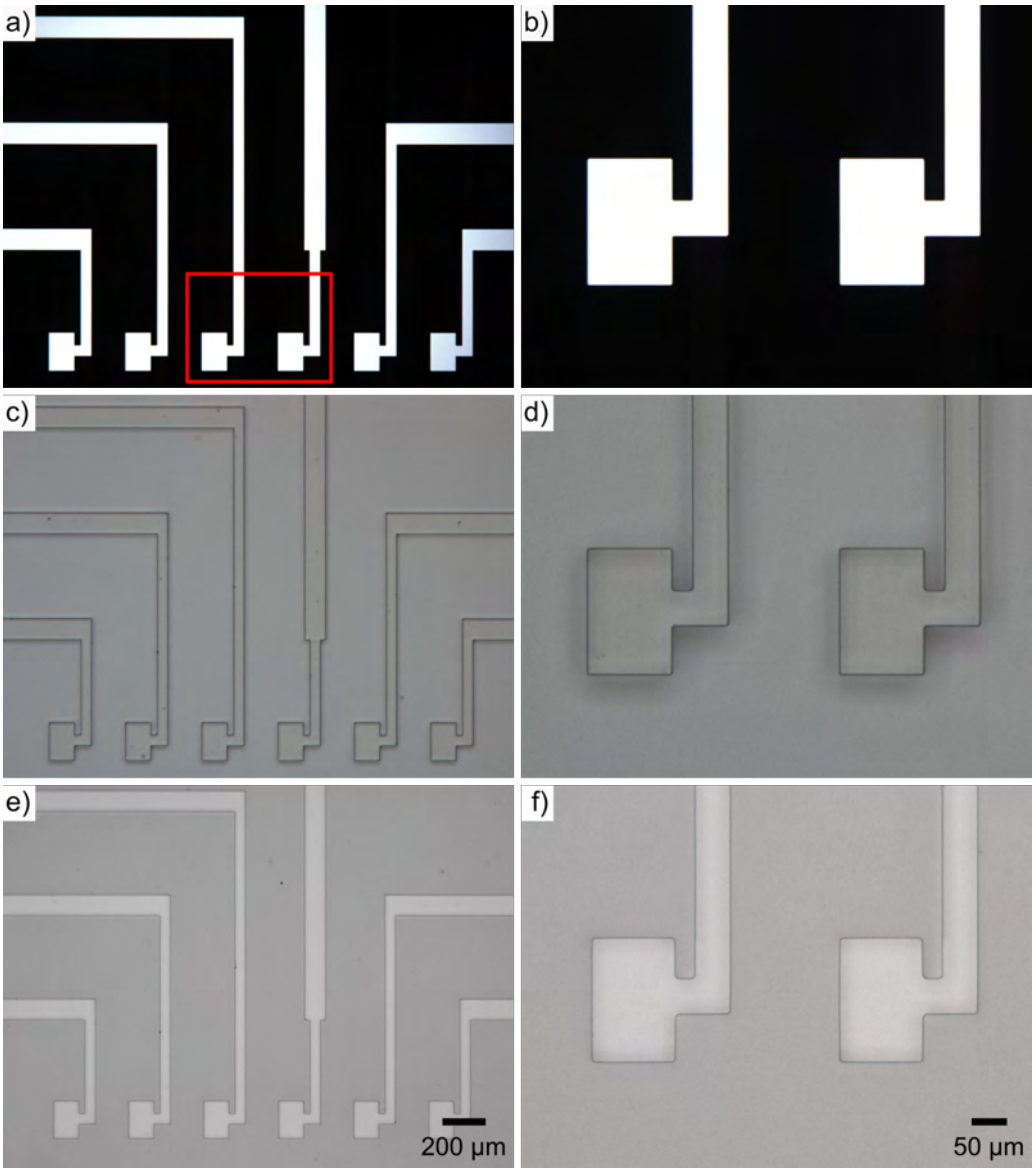


Figure C.4: Optical micrographs of fabricated photomask, photoresist master and PDMS chip of the gas layer for independent microvalve control. (a & b) The photomask with separated inlets for each air chamber and its detail view (red outline). (c & d) The master wafer coated with SUEX 100 photoresist. (e & f) The same detail on the fabricated PDMS chip.

## C.4 Fluidic resistance

Equivalent to Ohm's law, $\Delta V = RI$ for an electrical potential drop $\Delta V$ along a wire, a pressure drop $\Delta P$ through a straight channel can be summarized as [238]:

$$\Delta P = R_F Q \tag{C.1}$$

where $R_F$ is the fluidic resistance and $Q$ is the flow rate. For channels with rectangular cross-section, the fluidic resistance can be expressed as:

$$R_F = \frac{12\eta L}{wh^3(1-0.63h/w)} \tag{C.2}$$

where $\eta$ is the fluidic viscosity, $w$ and $h$ are the width and height of the channel. Therefore, when all the microvalves are open, the fluidic layer of the platform could be approximated as shown in Fig. C.5(a & b). Each part of the channel was considered as a fluidic resistance and calculated using equation C.2 with the valve section modeled by a straight rectangular channel in first approximation. Then the fluidic resistances of two flow paths, from Zoo.In to Zoo.Out and from Zoo.In to Med.Out, were calculated as 185 and 197 TΩ using an online resistor network tool created by Kirill Kryukov [239].

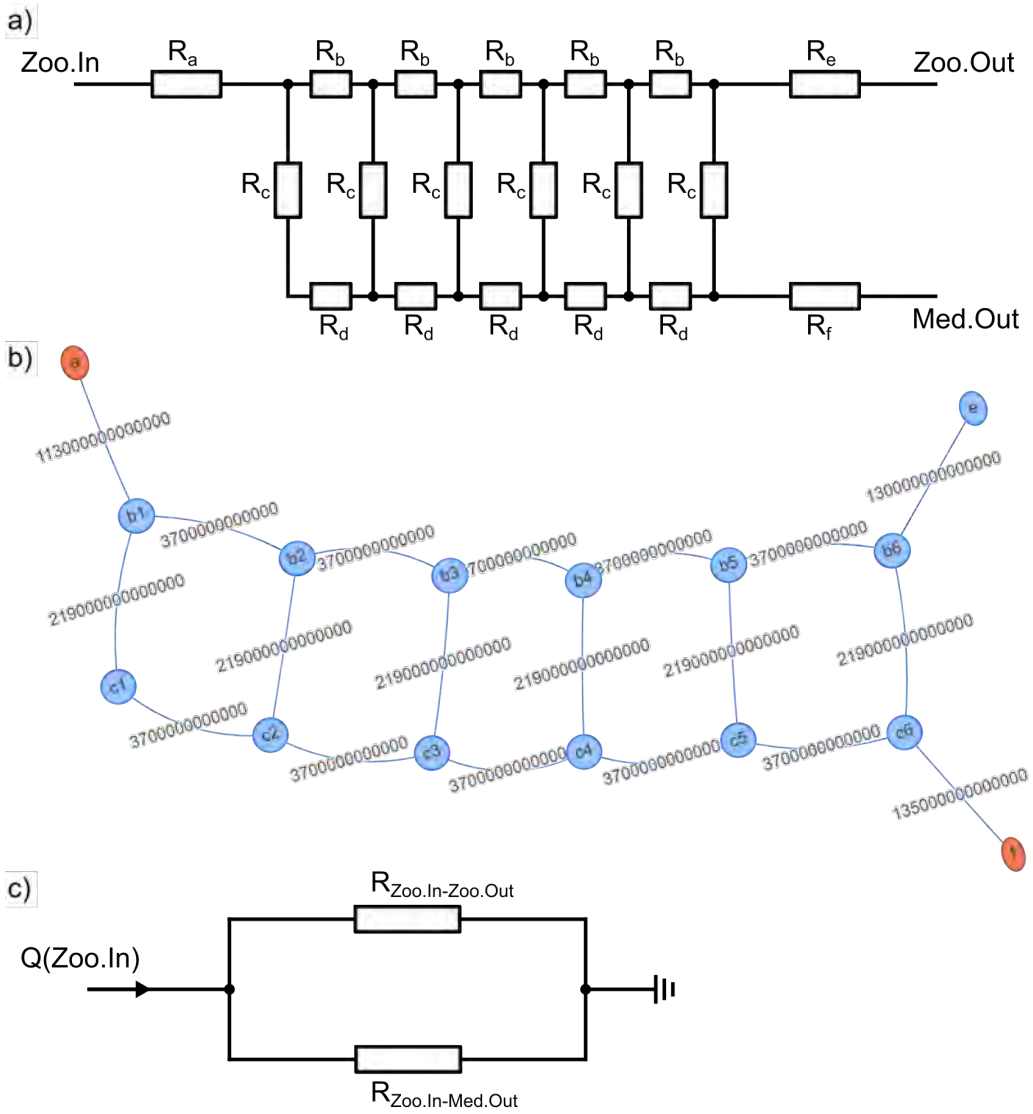


Figure C.5: Fluidic resistance estimation for the fluidic layer when all microvalves are open. (a) Schematic showing each part of the channel being considered as a fluidic resistance. (b) Network diagram showing calculated results of fluidic resistances for each part of the channels using equation C.2, as displayed by the online resistor network tool. (c) Schematic showing two flow paths, from Zoo.In to Zoo.Out and from Zoo.In to Med.Out, whose fluidic resistances were calculated using the online tool.

## C.5 Flow characteristics test B

In test B, only one switch (channel No. 1 in stage I - III, or channel No. 6 in stage IV - VI) of the MUX was set to ON during the experiments, as shown in Fig. C.6. This resulted in the single valve turning from fully opened (pressure = -1.0 bar, I and IV) to partially closed (pressure = 0 bar, II and V) and finally to completely closed (pressure = +1.0 bar, III and VI), while the other five microvalves were kept partially closed. Figure C.7 shows the plot of the flow rates for test B, with the decrease in flow rate for the media outlet could be observed at the point of partial or complete closure of the valve. This indicated that the sensors attached to each outlet had sufficient resolution to visualize individual valve closing events.

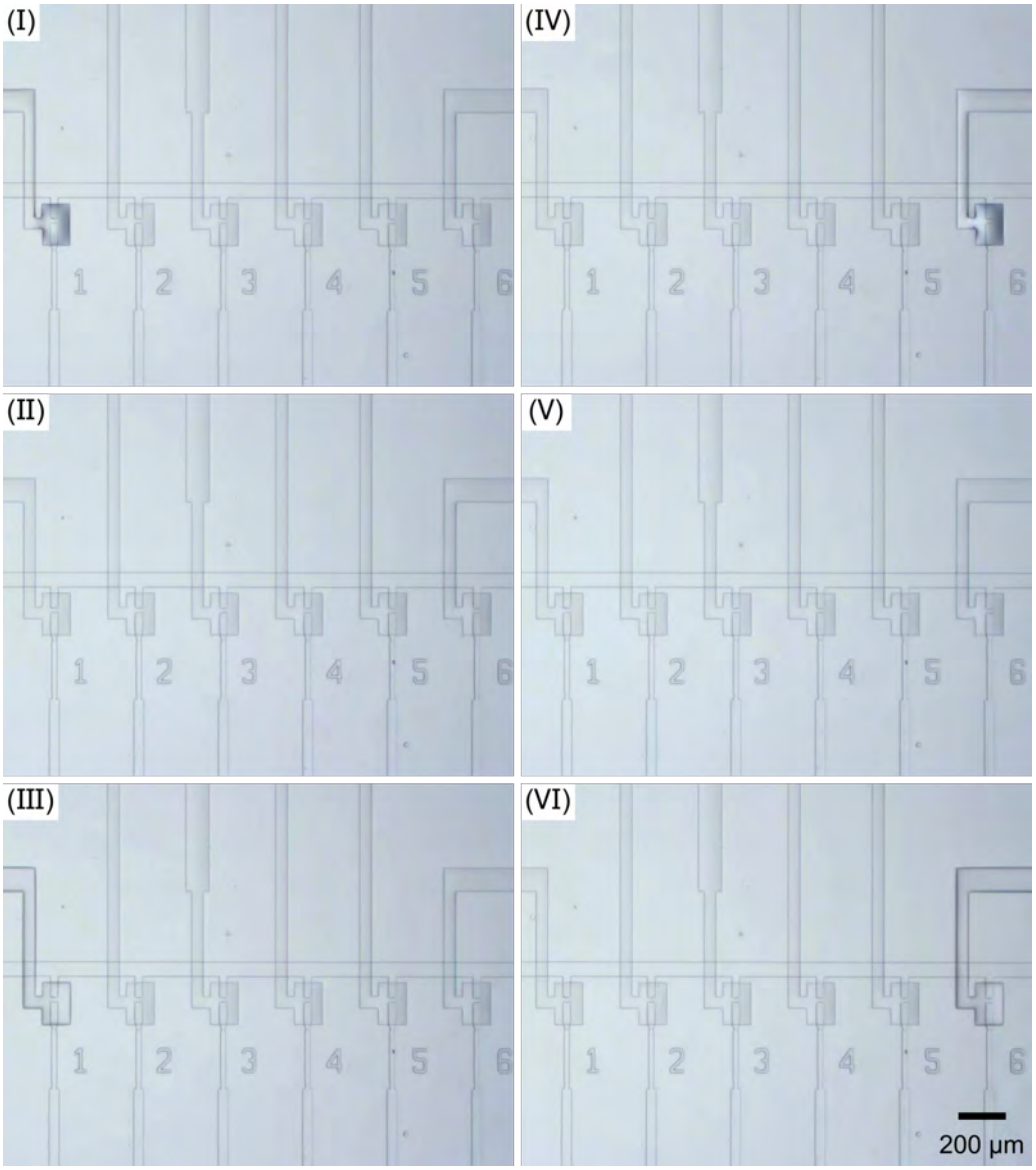


Figure C.6: Optical micrographs of flow characteristics test B, for which only one switch of the MUX was set to ON (channel No. 1 or No. 6) and the other five switches were kept OFF during the test. (I - III) Only the switch of channel No.1 was set to ON. The membrane valve of channel No. 1 was fully opened (vacuum pressure = -1.0 bar) first, then changed to partially closed (pressure = 0 bar) and completely closed at last (positive pressure = 1.0 bar). (IV - VI) Only the switch of channel No. 6 was set to ON. Similarly, the valve was firstly fully opened, then partially closed and finally completely closed.

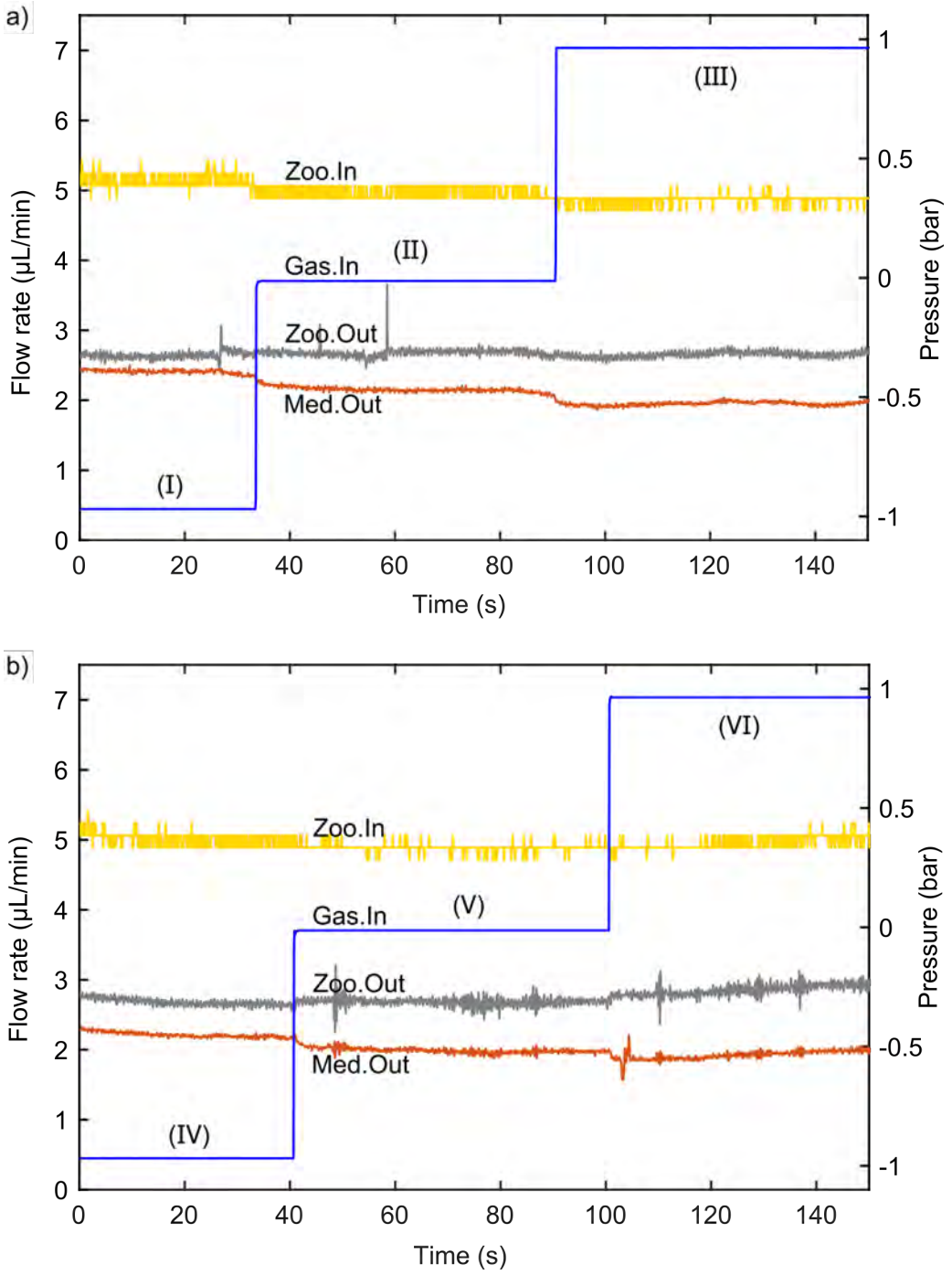


Figure C.7: Plot of flow characteristics test B. The blue line represents the pressure applied by the pressure controller OB1. The yellow, gray and red lines are the flow rate measured at the zoospore inlet, outlet and media outlet, respectively, using the flow sensors. Each stage from (I) to (VI) corresponds to the photographs shown in Fig. C.6.

## C.6 Flow characteristics test C

In test C, the flow characteristics were tested while the membrane valves were partially and completely closed in two sequences. Figure C.8 shows the case when valves were operated in the reverse order of stage I and II (from channel No.6 to No.1), which was described in Section 5.3.3. In detail, all six microvalves were first fully opened, then became partially closed one-by-one from channel No.6 to No.1 (stage III). In the next stage IV, microvalves were completely closed in the same order. The flow rates of zoospore inlet/outlet and media inlet are plotted in Fig. C.8, showing no significant difference in flow rate behaviour between these two cases of microvalve operation (from channel No.1 to No.6 or from channel No.6 to No.1).

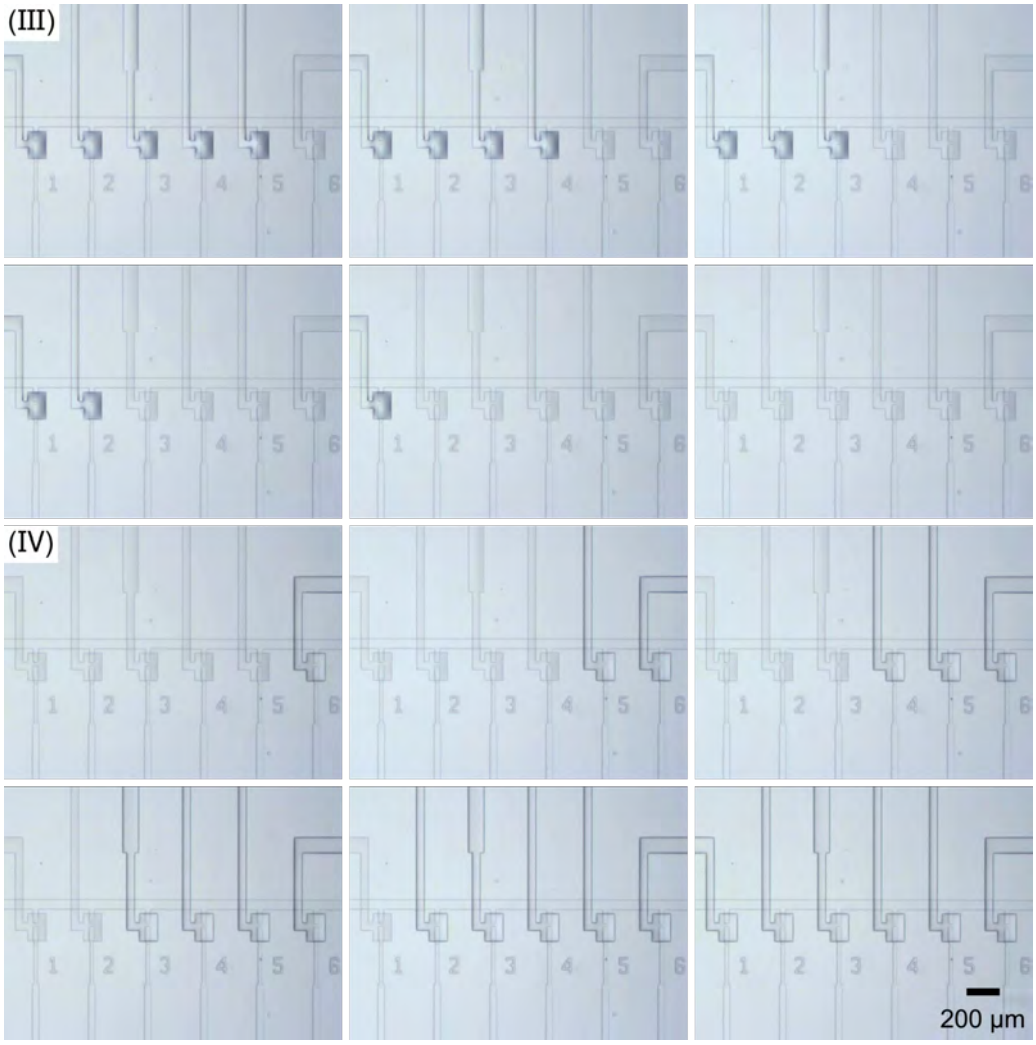


Figure C.8: Optical micrographs of the repeat flow characteristics test C (2). (III) All of the membrane valves were fully opened (vacuum pressure = -1.0 bar, all switches of MUX were ON) firstly. The switches were then turned off in reverse from channel No. 6 to No. 1, resulting in the corresponding microvalves becoming partially closed (pressure = 0 bar). (II) Thirdly, the pressure applied by OB1 was set to 1.0 bar and the switches were turned on in the same order (from channel No. 6 to No. 1). This resulted in the corresponding microvalves becoming completely closed. Note: DI water was continuously pumped from the zoospore inlet.

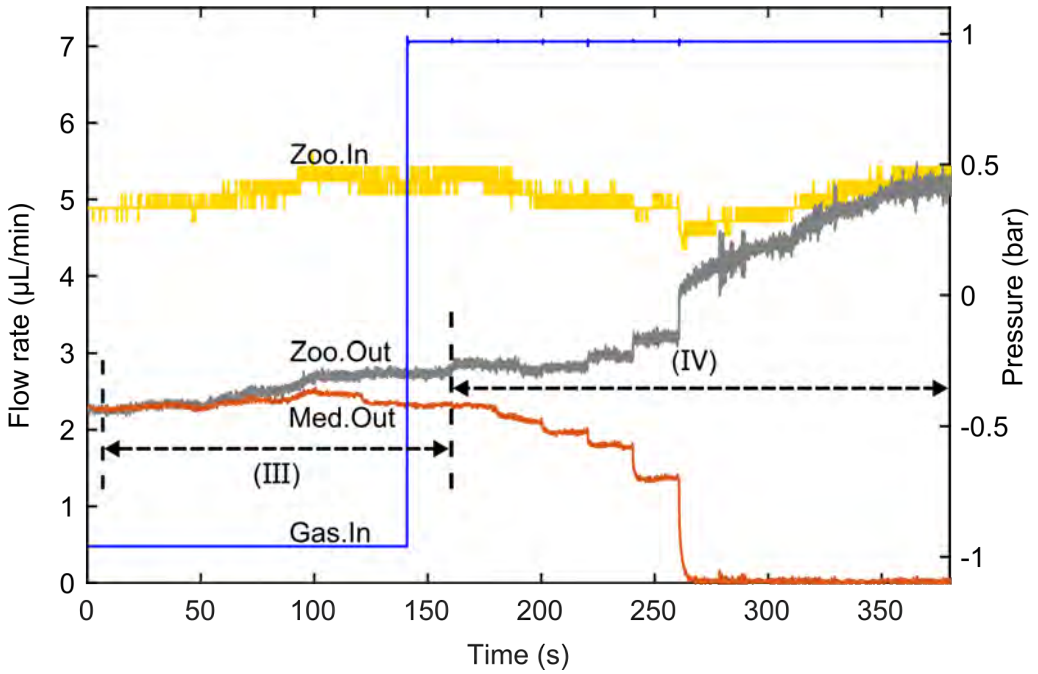


Figure C.9: Plot of flow characteristics test C. The blue line represents the pressure applied by the pressure controller OB1. The yellow, gray and red lines are the flow rate measured at the zoospore inlet, outlet and media outlet, respectively, using the flow sensors. Stages III and IV correspond to the photographs shown in Fig. C.8. The flow rate of zoospore inlet was set to 5 $\mu$L/min by a syringe pump.